Effect of Component Geometry and Build Orientation on the Microstructure and Mechanical Properties of Nickel Superalloys Manufactured with Laser Powder Bed Fusion

A Thesis submitted to the Faculty of Mechanical Engineering of the Technical University of Darmstadt in Fulfilment of the Requirements For the Degree Doctor of Engineering (Dr.-Ing.)

DISSERTATION

by

Sandra Mustafa Megahed, M.Sc.

Supervisor:	Prof. Dr.-Ing Matthias Oechsner
Co-Supervisor:	Prof. Dr.-Ing Thomas Niendorf

Date of Submission:	04.12.2023
Date of Oral Exam:	28.02.2024

Darmstadt 2024

D17

Megahed, Sandra Mustafa: Effect of Component Geometry and Build Orientation on the Microstructure and Mechanical Properties of Nickel Superalloys Manufactured with Laser Powder Bed Fusion,
Darmstadt, Technical University of Darmstadt,

Published on TUprints: 2024
Date of oral exam: 28.02.2024

Published under CC BY-SA 4.0 International

https://creativecommons.org/licenses/

Per Ardua Ad Alta

Acknowledgements

This thesis was written during my time as a research associate at the Institute for Materials Technology at the Technical University Darmstadt.

I would like to express my sincere gratitude to Prof. Dr.-Ing. Matthias Oechsner, without whom this thesis would not have been possible. Your time, supervision, fruitful discussions as well as your trust under the given circumstances are greatly appreciated.

I thank the entire team of the *High Temperature Materials* competence division. Special thanks go to the team leader, Dr.-Ing. Christian Kontermann for his trust, for always asking “why” and taking the time whenever I needed feedback.

I would also like to thank Dr.-Ing Michael Krämer for all his guidance, support and very thorough feedback.

Without the expertise, trust and encouraging words of you three (Prof. Oechsner, Christian, Michael), this thesis would not exist.

My thanks also go to Prof. Dr.-Ing. Thomas Niendorf for agreeing to be my co-supervisor.

Thanks to the staff of the mechanical workshop, the laboratories and all colleagues, whose expertise has ensured the quality of the experimental results documented in this thesis.

I thank the Federal Ministry for Economic Affairs and Climate Action, the German Federation of Industrial Research Associations (AiF e.V.) and the FVV e.V. for both their financial and administrative support of the underlying research project.

I would also like to thank the staff of the Materials Testing Institute at the University of Stuttgart for their support, especially Dr.-Ing Annett Udoh.

Thanks also go to Dr.-Ing. Christoph Heinze, Siemens Energy, and Dr.-Ing. Roland Herzog, MAN Energy Solutions, for providing the samples and their unwavering support in my work.

On a personal note: Words cannot express my gratitude for the support of my family, without whom I would not be the person I am.

My niece for always asking for my undivided attention.

My brother, whom I always find in my rear-view mirror.

My parents for all their support and guidance, always and unconditionally no matter what.

Erklärung

Hiermit erkläre ich, dass ich die vorliegende Arbeit, abgesehen von den in ihr ausdrücklich genannten Hilfen, selbständig verfasst habe.

04.12.2023

(Datum)

(Unterschrift)

Kurzfassung

Selektives Laserstrahlschmelzen metallischer Materialien (engl.: Metal Laser Powder Bed Fusion; PBF-LB/M) ermöglicht durch den schichtweisen Bauteilaufbau hohe geometrische Freiheitsgrade. Die resultierende PBF-LB/M-Mikrostruktur hängt dabei von mehreren Faktoren ab, darunter Prozessparameter, Bauteilgeometrie, Aufbauorientierung sowie Nachbearbeitungsprozesse (bspw. Wärmebehandlung). Insbesondere für den zuverlässigen Einsatz von Hochtemperaturwerkstoffen aus PBF-LB/M-Prozessen fehlt es derzeit sowohl an einer zuverlässig übertragbaren Datenbasis als auch an reproduzierbaren Prüfvorschriften.

Da sich die Geometrie realer Bauteile von zur Kennwertermittlung standardmäßig verwendeten zylinderförmigen Proben unterscheidet, muss untersucht werden, ob direkt gedruckte PBF-LB/M fertigungsbegleitende Proben vergleichbare Materialeigenschaften aufweisen, als aus Bauteilen entnommene Proben. Zu diesem Zweck wurde ein generisches Bauteil entworfen. Das generische Bauteil repräsentiert anwendungsrelevante geometrische Merkmale, wie bspw. Überhänge, Querschnittsänderungen usw. Weiterhin wurden fertigungsbegleitende Proben innerhalb des generischen Bauteils integriert. Die Kombination aus fertigungsbegleitenden Proben und generischen Bauteil bildet das Probeentnahmebauteil. Die Proben haben relativ zur Baurichtung folgende Orientierungen: 0°, 45° und 90°. Um den Einfluss der geometrischen Merkmale beurteilen zu können, wurden zum Vergleich fertigungsbegleitende Proben in denselben Bauorientierungen gefertigt. Die entnommenen Proben wurden mikrostrukturell untersucht, auf ihre mechanischen Eigenschaften geprüft und mit den Ergebnissen der fertigungsbegleitenden Proben verglichen.

Als Werkstoffe wurden die Legierungen IN718 und IN738LC verwendet. Die Ni Superlegierung IN738LC ist aufgrund der Rissanfälligkeit herausfordernd mittels PBF-LB/M zu verarbeiten. Obwohl die mechanischen Eigenschaften für Hochtemperaturanwendungen vielversprechend sind, ist PBF-LB/M IN738LC noch kein gängiges Einsatzmaterial. Im Gegensatz wird IN718 aus additiver Fertigung bereits in Hochtemperaturanwendungen verwendet.

Mikrostrukturelle Unterschiede in Phasenbildung und -verteilung zwischen fertigungsbegleitenden Proben und entnommenen Proben lassen sich auf den PBF-LB/M-Prozess zurückführen. Die Korngrößen unterscheiden sich zwischen den Geometrien, wobei die aus dem Probenentnahmebauteil entnommenen Proben kleinere Körner aufzeigen. Durch den Unterschied in den Korngrößen werden auch Unterschiede in den mechanischen Eigenschaften hervorgerufen. Entnommene Proben zeigen höhere Vickershärten im Vergleich zu fertigungsbegleitenden Proben auf. Die Zugfestigkeit und die Streckgrenze der entnommenen Proben liegen deutlich über denen der fertigungsbegleitenden Proben. Die IN738LC Kriecheigenschaften unterscheiden sich von denen von IN718, was auf die Phasenbildung und unterschiedliche Kriechdeformationsmechanismen zurückzuführen ist.

Abstract

Metal laser powder bed fusion (PBF-LB/M) enables high geometric design freedom. However, the resulting PBF-LB/M microstructure depends on several factors, including process parameters, part geometry, build orientation and post-processing (e.g. heat treatment) etc. The correlation between the PBF-LB/M microstructure and the influencing factors is not yet sufficiently researched or understood. Thus, there is currently a lack of transferable databases and reproducible test procedures, especially for high temperature materials.

Since the geometry of components used in applications generally differs from standard witness samples, it must be investigated whether directly printed PBF-LB/M witness samples exhibit comparable material properties to samples extracted from components. Within the scope of this thesis, a generic component was designed with application-relevant geometric features, such as overhangs, changes in cross-section, etc. Witness samples were integrated within the generic component, which combined, form the Sample Extraction Component (SEC). The (witness) samples are manufactured in three build orientations: 0° (perpendicular to the build direction), 45° and 90° (parallel to the build direction). The samples extracted from the SEC are microstructurally and mechanically characterized and compared to the results of witness samples.

The materials used were IN718 and IN738LC. The Ni superalloy IN738LC is challenging to process using PBF-LB/M due to its crack susceptibility. Although the mechanical properties are promising for high temperature applications, PBF-LB/M IN738LC is not yet commonly used in application. In comparison, PBF-LB/M IN718 is already used in high temperature applications.

Microstructural differences regarding phase formation and distribution were found between witness and extracted samples and are attributed to the difference in solidification conditions during the PBF-LB/M process itself. The grain sizes differ, with the largest grain size found in the witness samples. The samples extracted from the SEC show smaller grains. The difference in grain sizes also causes differences in mechanical properties. The Vickers hardness of extracted samples is higher compared to witness samples. The tensile and yield strengths of the extracted samples are significantly higher than those of witness samples. The IN738LC creep properties differ from those of IN718 due to phase formation and different creep deformation mechanisms taking place.

Table of Contents

1 Introduction

One of the most common application examples for high temperature materials are turbine blades in a jet engine. The gas flow route within a typical jet engine can be broken down into the cold and hot section. In the cold section, average temperatures ranging from ambient to 550 °C can be reached [1]. Components in the cold section can therefore be made of light weight and high-strength Titanium (Ti)-alloys. The hot section consists of the region from the combustion chamber to the exhaust nozzle exit. The materials used in the combustion chamber and in the turbine must endure temperature rises at metallic surfaces between 650 °C to 1250 °C [1].

Materials used in the hot section must therefore fulfill the following:

- Maintain mechanical properties under operating temperatures close to their melting temperatures ($\frac{T_{Operating}}{T_{Melting}} > 0.6$),
- Resist mechanical degradation caused by mechanical and thermal loading over extended periods of time (i.e. creep resistance),
- Resist corrosion and oxidation due to the operation environment within the combustion exhaust.

The higher the turbine inlet temperature, the higher the achievable efficiency. It is therefore important to continue optimizing alloys to withstand even higher operating conditions. The lifetime of turbine components in the hot section is limited by the exposure duration to high thermal and mechanical stresses, repeated loading and environmental factors [2]. The expected lifetime for a blade in a stationary gas turbine until first revision corresponds to more than 25,000 h [3]. Ni superalloys are commonly used for turbine blades and nozzles due to their mechanical properties and high temperature resistance.

High temperatures combined with high mechanical stresses lead to gradual blade damage. Integrating conformal cooling channels can prolong the lifetime of components used in high temperature applications by reducing the component temperatures. Additive Manufacturing (AM), especially Metal Laser Powder Bed Fusion (PBF-LB/M), is a promising manufacturing route that allows for such innovate cooling concepts [4].

AM is defined as a digital technology that creates objects using the CAD representation of the required component by successive addition of materials [5–7]. Several technologies are classified as AM processes, including Direct Energy Deposition (DED), Electron Beam Melting (PBF-EB/M), PBF-LB/M, Laminate Object Manufacturing (LOM), Stereolithography (SLA) etc. The differences between AM technologies lie in the heat source, the feedstock (e.g. wire, powder, sheets etc.), the feedstock delivery method (e.g. nozzle, powder bed etc.) and the required post-processing.

All AM technologies are nevertheless based on the following process steps:

1. A three-dimensional CAD model of the product is adapted to account for AM manufacturing constraints.
2. Using respective build preprocessors, the CAD file is sliced into 2D layers with a predefined layer thickness.
3. The component is manufactured layer-by-layer until completed.

The PBF-LB/M process is one of the most prevalent AM processes for the manufacturing of complex metallic components and is considered a potentially feasible manufacturing route in aerospace and stationary gas turbine industries [8]. The PBF-LB/M process allows for increased functionality due to the high design freedom. Furthermore, weight reduction via topology optimization is possible with PBF-LB/M which reduces costs and increases efficiency even further.

Although complex Ni-superalloy demonstrator components can already be manufactured in the required quality, experimentally secured process parameters and concepts for a robust determination of key enabling parameters do not exist yet. The large number of (PBF-LB/M) process parameters as well as locally varying thermal conditions and individual design features are among the most important factors leading to the lack of repeatable manufacturing quality.

The Ni superalloy IN718 is a common alloy used in high temperature applications due to its good weldability. However, the maximum application temperature for IN718 is limited to 650 °C. On the other hand, IN738LC can maintain its mechanical properties up to 950 °C, however its weldability and crack susceptibility prohibits its use in application.

The correlation of Ni superalloys properties and creep behavior to AM process parameters (and resulting microstructure) is yet to be understood [9]. In the time between 2007 and 2017, more than 1980 journal papers were published on various alloys used in AM; Only 8.8% of these papers studied Ni superalloys [10]. Since then, publications on AM of Ni alloys have increased. In 2021, 290 publications were analyzed by Sanchez et al. [11]: It was reported that 68% studied powder bed fusion of IN718, while only 3% focus on powder bed fusion of IN738LC [11].

Considering that across 290 papers on powder bed fusion papers of Ni alloys only 7% investigate creep behavior, it can be summarized that knowledge on creep behavior of PBF-LB/M Ni superalloys is limited [11,12]. Long-term PBF-LB/M creep results are scarce in literature. This can be explained by the extensive experimental series required by DIN EN ISO 204 [13]. This requirement and the large number of PBF-LB/M process parameters lead to an increase in the number of required PBF-LB/M samples by several folds (almost prohibitively) in comparison to conventional manufacturing (e.g., casting, forging etc.). In depth creep

analysis is nevertheless necessary for PBF-LB/M components to be considered for high temperature applications.

When manufacturing components with PBF-LB/M, witness samples are often printed simultaneously. Witness samples are simple test geometries, such as cylinders, that allow mechanical testing without destructively investigating the manufactured components. Witness samples are hence used as a comparative reference.

According to the qualification standard (DIN EN ISO/ASTM 52920 [14]), witness samples should be manufactured alongside large components for characterization and qualification purposes. It is generally accepted that the microstructure and thus mechanical properties of witness samples are representative of those of printed components, which will be used in applications. The transferability of witness sample properties to components is however largely unexplored, despite being an important step to qualify PBF-LB/M components for service. The first research question pursued in this thesis is therefore:

1. **To what extent are microstructural and mechanical properties of witness samples representative of large-scale components?**

Components used in application are usually irregular in shape and generally not comparable in terms of surface area to volume ratio with witness samples. It should therefore be investigated whether microstructural and mechanical differences exist between witness samples and components. To ensure that the results are not dependent on a specific build orientation, different build orientations are to be considered.

The influence of build orientation is not discussed in the aforementioned standard, especially not in the context of long-term mechanical properties, thus defining the second research question:

2. **How do build orientation and microstructure affect creep mechanisms?**

The sparse literature on creep behavior of Ni superalloys includes limited information about how the build orientation affects long term mechanical behavior of PBF-LB/M parts. Since it is presumed that the extremes of 0° and 90° build orientation show the largest microstructural differences and thus long-term mechanical properties, it is generally assumed that these build orientations represent the best- and worst-case scenarios. However, arbitrary build orientations (e.g. 45°) are barely researched leaving a major gap in knowledge of Ni superalloy creep behavior. It is therefore possible, that these arbitrary build orientations (e.g. 45°) are even worse and thus the impact of build orientation needs to be investigated.

This thesis is arranged as follows: Chapter 2 discusses published literature and the state of the art concerning PBF-LB/M, Ni superalloys, their microstructure and creep behavior. Knowledge gaps are identified to build the foundation for Chapter 3, where detailed research goals and objectives are formulated. The experimental procedure and material characterization methods are described in Chapter 4. Chapter 5 and 6 present and discuss the results of the two research questions. Chapter 7 summarizes the conclusions and outlines recommendations for future research.

2 Theoretical Background and Literature Review

Ni superalloys and their metallurgical strengthening mechanisms are first considered before introducing PBF-LB/M and how the specific processing procedure affects the resulting Ni superalloy properties, potential defects, microstructures and creep behavior.

2.1 Introduction to Ni Superalloys

There are several definitions for the term superalloy. Most superalloy definitions describe alloys which can maintain their microstructural integrity and mechanical properties over time at elevated temperatures of up to 85% of their absolute melting temperature [15]. Some describe superalloys as alloys with at least two phases, one of which is ordered and the other one is disordered [16]. Others describe superalloys as alloys that offer high temperature tensile strength, stress rupture and creep properties, fatigue strength, oxidation and corrosion resistance and microstructural stability at elevated temperatures of 600 °C and above [17,18].

As mentioned in Chapter 1, Ni superalloys encompass the majority of currently used blade alloys [19] due to their mechanical properties. The microstructure, specifically the phases contained in Ni superalloys, is the root cause for the mechanical properties.

Typical phases and the respective crystal structures of Ni superalloys are shown in Figure 1. The γ–phase solid solution is the matrix of Ni superalloys and exhibits a face center cubic (fcc) crystal structure. The γ'–phase (Ni_3Al) is an intermetallic strengthening phase with an L_{12}-fcc crystal structure [2]. Due to the fcc crystal structures, the γ– and γ'-phases are fully coherent. The γ'-phase is usually cubic shaped. Another strengthening phase is the meta-stable γ''-phase (Ni_3Nb), which exhibits a body center tetragonal crystal (bct) structure. The bct structure is semi-coherent with the γ-phase causing strain (ε) on the lattice, leading to a larger strengthening effect of γ'' compared to γ'. The strain on the lattice is compensated with a distortion within the lattice. The distortion within the lattice, leads to a disc-shaped γ''-phase since it is energetically more favourable. At temperatures ranging between 650 °C to 980 °C, the γ''–phase decomposes into the stable δ-Phase (Ni_3Nb). The orthorhombic crystal structure of the δ-phase is incoherent within the γ–matrix reducing ductility.

In IN738LC the η-phase (Ni_3Ti or Ni_3Ta) with a hexagonal close packed (hcp) crystal structure forms when exposed to temperatures ranging between 850 °C and 950 °C [20,21]. The η-phase forms when MC carbides (i.e. TiC, TaC) decompose. When MC carbides decompose, grain boundaries are enriched with Ti and Ta [20]. The η-phase must form near MC carbides, since those are the source of Ti and Ta during thermal exposure.

Carbides (MC, M_2C_3, M_6C, M_7C_6, $M_{23}C_6$) and borides can be found in Ni superalloys [4,22]. Depending on the location (e.g. grain boundaries), composition (e.g. MC, M_2C_3, M_6C, M_7C_6,

$M_{23}C_6$) and shape (e.g. needle, lath, disc etc.), carbides increase or decrease mechanical properties. High concentrations of refractory metals and Cr are required to withstand high temperatures in a jet engine, as they maintain oxidation resistance and their solid solution strengthening effect at elevated temperatures and can increase the melting temperature. However, refractory metals and Cr promote the formation of Topological Closed Packed (TCP) phases, such as Laves (e.g. TaV_2)-, σ (e.g. MoFe)- or μ (e.g. W_6Fe_7)-phases [23,24]. These phases exhibit high atomic packing densities due to complex crystal structures [23]. Many of the TCP-phases show wide ranges of stoichiometry and can form different morphologies [19]. TCP-phases commonly precipitate after long thermal exposure at elevated temperatures or in some superalloys, such as IN718 and IN738LC, form during solidification [25]. TCP-phases usually accumulate at grain boundaries [26], thereby embrittling grain boundaries reducing mechanical and creep properties [23,27–31]. Another disadvantage is that TCP-phases deplete the Ni-matrix of refractory metals (i.e. solid solution strengtheners). In order to avoid TCP-phases, the content of refractory metals is reduced, however, since refractory metals are required for high temperature resistance, they cannot be avoided completely.

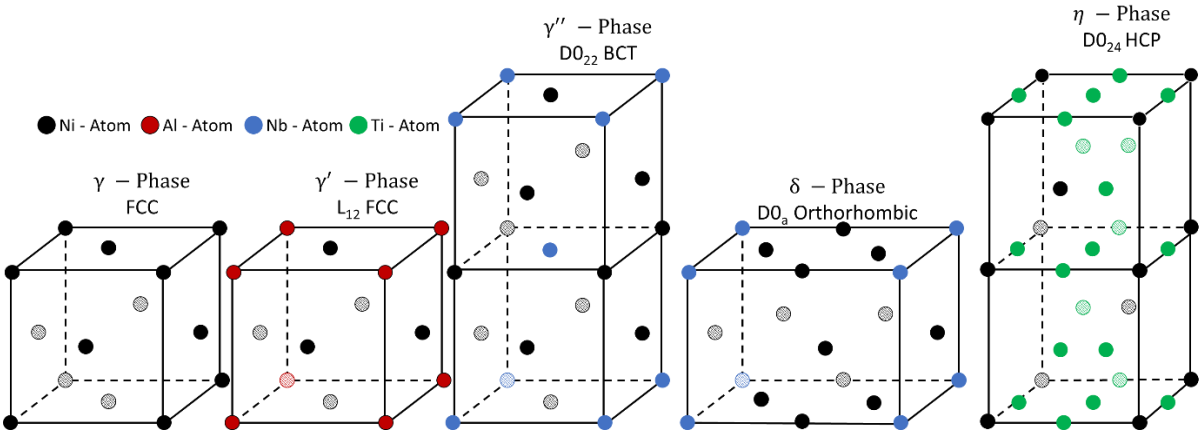

Figure 1 Phases of Ni superalloys and their respective crystal structures, reproduced from [4,32–34]

Ni superalloys can be categorized depending on their strengthening mechanism, as follows:

- Precipitation strengthened Ni superalloys [32]
  - γ′ strengthened

    Hardened by the precipitation of the coherent γ′ phase typically heat treated to form a cuboidal structure.
  - γ′′ strengthened

    γ′′ phase is precipitated as semi-coherent disc shaped particles [35]. γ′ strengthening can occur in addition to that provided by γ′′.
- Solid-solution strengthened Ni superalloys

  Material strength is achieved through solid-solution strengthening elements (e.g. Co, Cr, Fe, Mo, W, Ta, Re) [32]

The Ni superalloys investigated in this thesis, IN718 and IN738LC, are both precipitation strengthened. IN718 (nominal composition shown in Table 1) is one of the most studied Ni superalloys and is considered suitable for service temperatures up to 650 °C. In this research, IN718 is considered as a reference alloy since a relatively large amount of information is available in literature. IN738LC (nominal composition shown in Table 1) is chosen as a representative alloy supporting even higher service temperatures of up to 950 °C, which is not well studied to date. The role of the individual alloying elements can be seen in Appendix A.

Table 1 Nominal material compositions of IN18 and IN738LC [4,8,32,36–39]

	Al	**B**	**C**	**Co**	**Cr**	**Cu**	**Fe**	**Mn**
IN718	0.8	0.0015	0.08	1	21	0.3	11.14	0.35
IN738LC	3.7	0.012	0.13	9	16.3	0	0.05	0.02
	Mo	**Nb**	**Ni**	**Si**	**Ta**	**Ti**	**W**	**Zr**
IN718	3.3	5	55	0.35	0.05	1.15	-	-
IN738LC	2	0.9	58.6	0.3	1.75	3.7	2.8	0.08

2.1.1 Introduction to Ni Superalloy IN718

IN718 is a frequently used precipitation strengthened Ni superalloy in, for example, the aerospace industry as a turbine disk material due to its good high-temperature strength and corrosion and oxidation resistance [40]. IN718 is characterized by very good weldability and is thus suited for processing by PBF-LB/M [41,42]. Surplus Nb leads to embrittling segregations which are frequently found in forged and cast IN718 [43,44]. Their elimination or minimization during manufacturing poses a great challenge. IN718 is therefore exclusively used in a heat-treated condition. Heat treatments for IN718 can be divided into:

1. Solution heat treatment step with the aim of dissolving brittle phases and
2. Ageing step with the aim of homogeneous and complete precipitation of the strengthening γ’ and γ’’-phases [45].

While the main strengthening phases (~20 vol.% [46]), γ’ and γ’’, are beneficial to creep-rupture properties [12], once γ’’ decomposes into the δ-phase between 650 °C and 980 °C, the mechanical properties, especially creep resistance, of IN718 decline significantly [47]. It is generally accepted that the δ-phase is responsible for IN718 notch sensitivity at elevated temperatures [48–51]. Especially when formed at grain boundaries, the creep rupture strength of IN718 has been found to significantly reduce when δ is present [48].

2.1.2 Introduction to Ni Superalloy IN738LC

IN738LC is a γ’ (~40 vol%)-precipitation strengthened Ni superalloy developed for turbine blades [52]; LC stands for Low Carbon. It is a derivative of IN738 for improved castability.

IN738LC has a reduced concentration of C and Zr as well as a reduced tolerance for B in order to reduce crack susceptibility due to segregation at grain boundaries [8,53–56]. The expected phases in IN738LC include γ, γ′ and TCP Phases [8].

The heat treatment for cast IN738LC can be divided into the following steps [10, 56]

- Solution Annealing
- Precipitation hardening
- Hot Isostatic Pressing (HIP) is often carried out to close porosity after casting [57–59].

2.2 Introduction to Metal Laser Powder Bed Fusion (PBF-LB/M)

PBF-LB/M describes the process in which thin layers of powder are deposited on a substrate, and then selectively melted by a laser according to the slices of a 3D CAD model [5–7]. The process steps can be summarized as follows:

1. Thin powder layer is spread across the substrate plate.
2. Laser selectively scans the powder layer according to sliced geometry being processed thus densifying the material.
3. Powder platform moves up, and the build platform moves down.
4. Fresh layer of powder is spread on the previously processed layer.
5. Repeat steps 2 to 4 until the component is completed.

The PBF-LB/M process usually takes place under an inert gas atmosphere, usually Argon (Ar), to reduce powder oxidation. A brief overview of PBF-LB/M powder characteristics can be found in Appendix B.

Figure 2a shows the PBF-LB/M machine setup and Figure 2b defines the coordinate system commonly used and also adopted throughout this thesis.

The direction in which the component is built is referred to as the build direction and corresponds to the Z-direction, as shown in Figure 2b. The X- and Y-directions are perpendicular to the build direction.

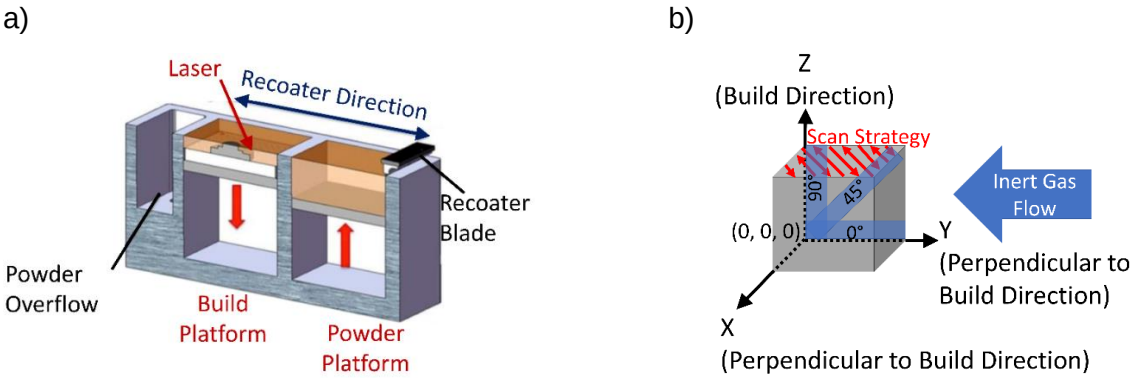

Figure 2 a) Schematic representation of PBF-LB/M machine [60], b) PBF-LB/M coordinate system used throughout this thesis [61]

The high cooling rate during PBF-LB/M of roughly 10^6 K/s [62] is the main difference between PBF-LB/M solidification and conventional manufacturing routes [104]. Comparatively, cooling rates for casting can reach up to 10 K/s. Equilibrium solidification and thus equilibrium phase diagrams can therefore not be used to accurately describe PBF-LB/M solidification. Instead, non-equilibrium conditions need to be accounted for, which is best considered under the Scheil-Gulliver solidification conditions [63,64] (for more details see Chapter 2.2.4.1).

Figure 3 compares equilibrium and non-equilibrium solidification for IN718. While for both solidification conditions γ-, γ'-, δ-phase and MC form, the σ-phase forms additionally under Scheil-Gulliver conditions. The gradient of the Scheil-Gulliver solidification curve is steeper compared to equilibrium. A rapid shift in gradient along the curve indicates crack susceptibility since segregations and TCP-phases form when the distribution of alloying elements is not homogeneous. Hence phase formation and distribution are affected by solidification conditions.

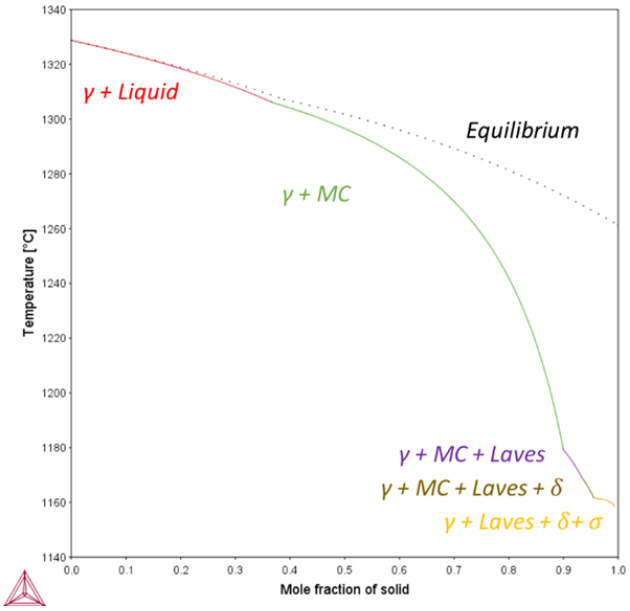

Figure 3 IN718 phase diagram calculated using ThermoCalc for equilibrium and Scheil-Gulliver solidification conditions [65]

The PBF-LB/M microstructure is mostly oriented in build direction, which can be attributed to grains growing in the direction of the thermal gradient [66].

For 90° and 0° build orientation (refer to Figure 2b for the coordinate system being used) the conditions for each layer (i.e. amount of surrounding powder and solid material etc.) are similar, as seen in Figure 4a and c. In the case of the 45° build direction, the conditions are comparatively more complex as schematically demonstrated in Figure 4b, meaning that the amount of powder and solidified material surrounding the area to be melted varies for each layer, increasing the thermal gradients [67]. Additionally, due to the overhang of the 45° build orientation, powder particles from powder layers underneath could partially melt onto the overhanging surface increasing surface roughness. According to Sanchez et al. [67], assuming a robust set of process parameters, the difference in porosity between the build orientations is insignificant.

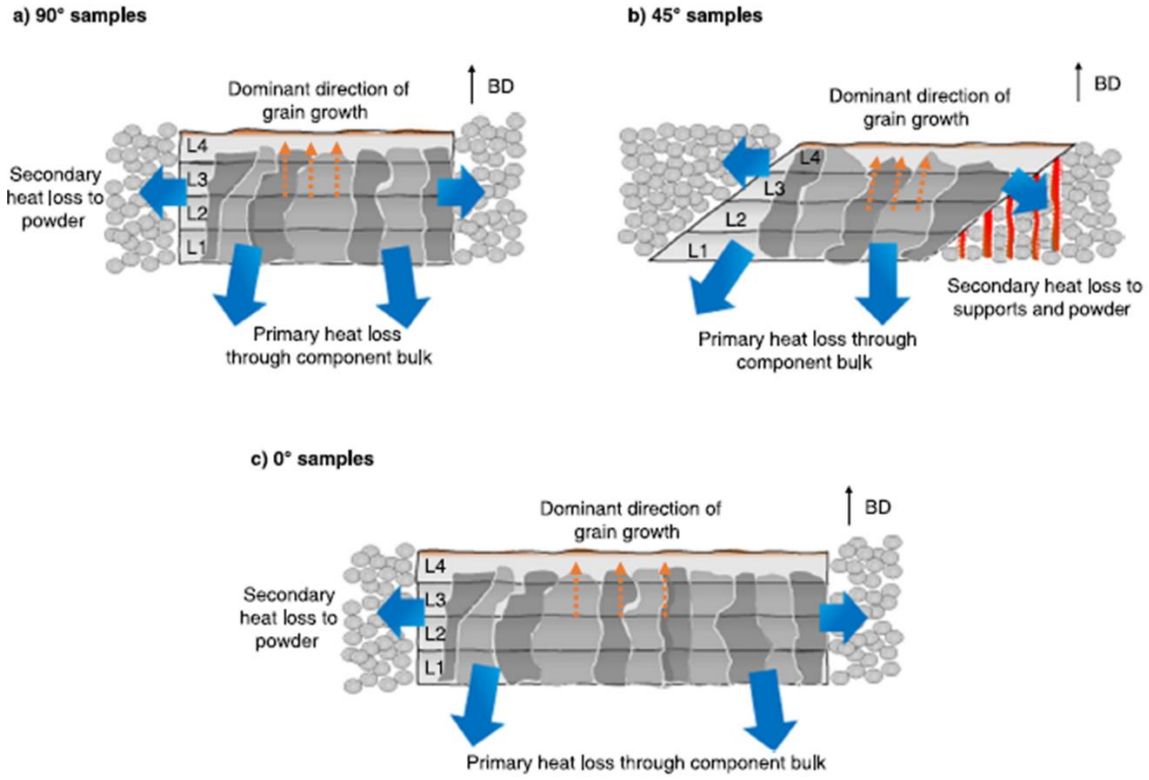

Figure 4 Schematic representation of heat loss and grain growth for a) 90° b) 45° and c) 0° build orientation [67]

2.2.1 Process Parameters

While PBF-LB/M has many advantages, material porosity, cracking and residual stresses are particularly challenging to improve [4]. Finding the right combination of process parameters is usually the focus of large experimental campaigns to avoid PBF-LB/M defects.

Yadroitsev discussed more than 100 process parameters that can influence PBF-LB/M material properties [68]. The majority of research work dedicated to the understanding the effect of process parameters focuses on laser power, scan speed, hatch spacing, layer

thickness and preheating temperature [69–73]. Whereas the list of parameters is thus drastically reduced from Yadroitsev's list, the studied parameters still present a very large search space for the optimum process window [74–79]. Linear, area or volume energy densities (Equation 1) are used to join multiple process parameters into one value that can be used to characterize the process behavior [62,80]. Although this is an oversimplified representation of non-linear phenomena as discussed by Bertoli et al. [81], it offers a means of identifying trends. While the optimum energy density differs for each material, all materials show similar trends [82]. Energy density affects grain size, precipitate and defect density [67,83].

Linear Energy Density (E_L)	Area Energy Density (E_A)	Volume Energy Density (E_V)	
$E_L = \frac{P_L}{v}$	$E_A = \frac{P_L}{v \cdot h}$	$E_V = \frac{P_L}{v \cdot h \cdot y}$	***Equation 1 Linear, area and volume energy density***

Where:

- E_L = Linear energy (J/m)
- E_A = Area energy density (J/m^2)
- E_V = Volume energy density (J/m^3)
- P_L = Laser power (W)
- v = Laser scan velocity (m/s)
- y = The distance between two consecutive and parallel laser tracks (m)
- h = Powder layer thickness (m)

In addition to the process parameters briefly discussed above, the laser profile and scan strategy play a large role in reducing defects and improving as-built mechanical properties, since they affect the overall sample/component thermal history.

The large number of PBF-LB/M process parameters [68] as well as locally varying thermal conditions and individual design features are crucial factors affecting manufacturability and repeatable build quality [9,84,85]. The correlation between PBF-LB/M processing and resulting microstructures has been investigated in several studies [86–88], but the results are not generalizable across all alloys or transferrable from one part to the other.

Microstructural and mechanical transferability from one sample to the other is not guaranteed in PBF-LB/M, even when manufactured with the same process parameters. According to DIN EN ISO/ASTM 52920, witness samples should be manufactured alongside large components to confirm build quality and for qualification purposes. However, studies on the transferability

of microstructure and mechanical properties of witness samples to components (and vice versa) could not be found in literature.

It is expected that microstructure and hence mechanical properties depend on the geometry due to differences in thermal histories caused by differences in volumes and cross-sections being manufactured. An example of geometric influences on material and part quality is thin-walled structures, that require different process parameters as compared to voluminous structures [89–91]. It is thus questionable whether witness samples can indeed be used to qualify thin wall properties or – in a more generic formulation– complex geometries.

2.2.2 PBF-LB/M of Ni Superalloys

Generally, the manufacturability of Ni superalloys with PBF-LB/M correlates with their individual weldability (see Appendix C). This is largely governed by their aluminum and titanium content. These elements are involved in a number of strengthening mechanisms.

While IN718 is easy to weld and can therefore be readily processed with AM technologies, IN738LC is difficult to process due to its susceptibility to hot cracking [55,92–95].

Hot cracks formed during solidification, tend to be about 1 µm long with a sharp tip that increases local stresses within a component. Hot cracks are difficult to detect using Non-Destructive Testing methods (NDT; such as µCT), due to their size and the Ni density, inhibiting X-Ray penetration into the component.

2.2.2.1 PBF-LB/M of IN718

As IN718 is a widely used Ni superalloy [96], several studies have been carried out on processing IN718 with PBF-LB/M. IN718 is readily weldable. Huynh et al. defined the corresponding process window for the manufacture of pore and crack-free IN718 and correlated the resulting microstructures to the process conditions [97]. An overview of the process parameter range with corresponding volume energy densities is listed in Appendix D. Reported IN718 mechanical properties are shown in Table 2 and Table 3 for as-built (AB) and as heat-treated (HT) condition. As can be seen, the yield strength and ultimate tensile strength of heat-treated samples can be up to twice as high compared to as-built condition due to precipitation. Elongation is heavily dependent on heat treatment and tends to reach lower values with increasing heat treatment temperature or time due to formation of the δ-phase. In terms of Vickers hardness, 0° samples show higher values compared to 90° build orientation. Machining does not show a significant effect on hardness.

2.2.2.2 PBF-LB/M of IN738LC

Prior to 2013, there was no public literature on PBF-LB/M of IN738(LC) [57]. Although IN738(LC) has generally poor weldability (see Appendix C), Rickenbacher et al. produced IN738LC parts via PBF-LB/M with ~0.5% porosity and a ”few micro-cracks” [57]. The authors

did not publish the utilized processing parameters; it is therefore impossible to verify their claims. Kunze et al. [98] reported similar results. Since the authors are from the same company, it is assumed that the same, unpublished, process parameters were used. Since then, the research in processing IN738(LC) with PBF-LB/M has increased, as can be seen in the review by Sanchez et al. [11]. The research focus remains on the correlation between process parameters, reducing crack density, microstructure and mechanical properties. Several studies have reported crack-free processing of IN738LC; however, the repeatability of this result still poses a challenge. The process parameters used for simple small cubes (e.g. 10 x 10 x 10 mm^3) cannot easily be transferred to more voluminous samples with complex geometries. A summary of process parameters used for IN738LC is shown in Appendix D. Corresponding mechanical properties for IN738LC are listed in Table 4. It can be readily seen that the number of properties listed is reduced compared to IN718, which is attributed to the limited amount of publicly published IN738LC research. However, a similar trend to that seen in IN718 can be identified. The yield strength and ultimate tensile strength values are increased in heat treated condition due to precipitation compared to as-built condition. The 0° build orientation shows higher strength values compared to the 90° build orientation. The elongation increases with increasing heat treatment temperature and/or time.

Table 2 Overview of IN718 mechanical properties found in literature, reproduced from [11]

Material	Standard	Test condition	Sample Condition	Yield strength [MPa]	Tensile strength [MPa]	Elongation [%]	Young's modulus [GPa]
IN718	-	Strain rate $4.25 \cdot 10^{-4}\ s^{-1}$	AB Room Temperature (RT)	677	1023	28.1	-
			HT / RT	1271	1425	18.6	-
			AB / 650 °C	594	862	25.1	-
			HT / 650 °C	1042	1142	10.1	-
IN718	ASTM-E8/E8M	Strain rate 2 mm/min	AB	596 ± 30	943 ± 8	35 ± 1	170 ± 9
			HT A	924 ± 11	1186 ± 2	25 ± 5	158 ± 17
			HT B	951 ± 3	1210 ± 23	23 ± 1	195 ± 2
			HT C	1158 ± 14	1339 ± 30	7 ± 1	138 ± 6
			HT D	558 ± 7	933 ± 3	43 ± 1	170 ± 7
IN718		Strain rate $10^{-3}\ s^{-1}$	Homogenization + AMS 5663 Solution Treatment and Ageing (STA)	1211 ± 24	1406 ± 21	13.6 ± 4	191 ± 3.1

Table 3 Overview of IN718 hardness found in literature, reproduced and adjusted from [11]

Material	Standard	Sample condition	Hardness
IN718	Vickers hardness	90° / AB	269 ± 5 HV
		0° / AB	310 ± 5 HV
		90° / HT	452 ± 5 HV
		0° / HT	457 ± 5 HV
		90° / machined / HT	441 ± 5 HV
		0° / machined / HT	454 ± 5 HV

Table 4 Overview of IN738LC mechanical properties found in literature, reproduced from [11]

Material	Standard	Test condition	Sample Condition	Yield strength [MPa]	Tensile strength [MPa]	Elongation [%]	Young's modulus [GPa]
IN738LC	ISO 6892	Strain rate ~4%/min	0° / RT	933 ± 8	1184 ± 112	8.4 ± 4.6	233 ± 9
			90° / RT	786 ± 4	1162 ± 35	11.2 ± 1.9	158 ± 3
			0° / 850 °C	610 ± 1	716 ± 1	8.0 ± 1.2	157 ± 4
			90° / 850 °C	503 ± 2	688 ± 7	14.2 ± 3.9	110 ± 2
IN738LC	-	Strain rate $4 \cdot 10^{-3}$ s^{-1}	90° / HT	981 ± 12	1450 ± 16	14 ± 1.1	-
			90° / HIP + HT	932 ± 4	1350 ± 22	14 ± 1.3	-

2.2.3 Common PBF-LB/M Defects

As briefly mentioned above, there are many defects that can occur during PBF-LB/M processing. An overview is shown in Figure 5. As can be seen, defects can be divided into process-related defects and material defects. The defects highlighted in green are easily controllable and are not further considered in this thesis. Similarly, due to the condition and geometry-specific complexity of distortion and oxidation defects, the grey highlighted defects are also excluded from this study. Focus is placed on the consequences of heat distribution (i.e. residual stresses, element distribution) and different types of porosity.

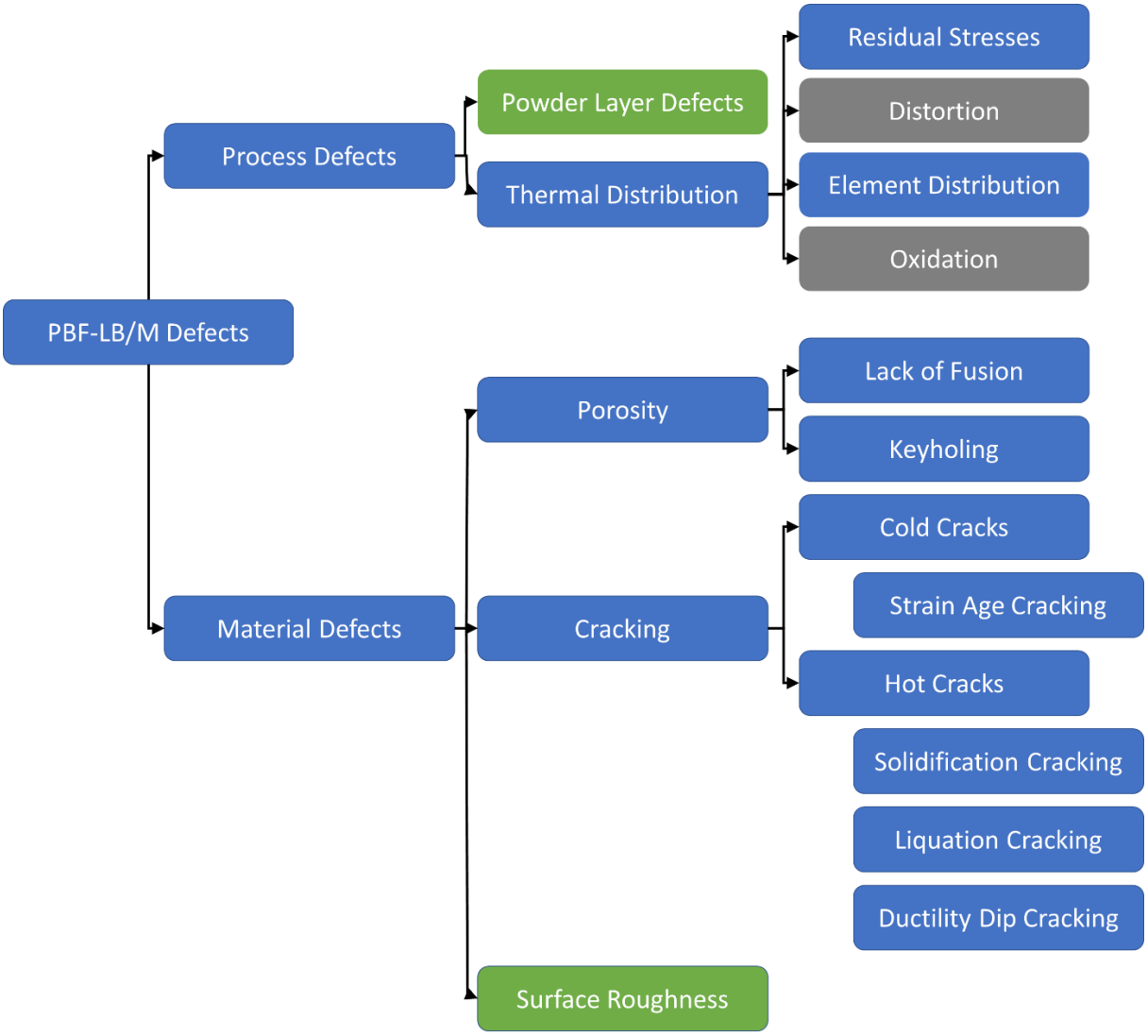

Figure 5 Overview of common PBF-LB/M defects

Cracks can be categorized into cold and hot cracking [63]. Cold cracks occur in entirely solid state, for example due to excessive stresses, and can usually be seen with the naked eye [63]. Hot cracking occurs in the mushy zone during solidification [63,99]. A detailed overview of the typical crack types can be found in Appendix E.

2.2.3.1 Porosity

Porosity is a common defect in AM of metals in general [100,101].

Too low energy densities lead to unconsolidated powder particles. In this case, there is not enough energy to fully melt and bond the layers together, i.e. Lack of Fusion (LOF) [102], shown in Figure 6a. Too high energy density, on the other hand, leads to keyhole porosity [103], shown in Figure 6b. The high laser energy evaporates material at the surface of the melt pool causing a dip (keyhole) leading to direct heating of lower layers. Reflected laser rays are captured by the opposite side of the keyhole, increasing the energy up-take and increasing evaporation. As the keyhole grows, the melt pool stability declines until the keyhole collapses trapping vapor as spherical pores in the solidifying material. [125]. In spite of the understanding of how the energy density may affect porosity, they are no clear guidelines or recommendations to achieve dense material for any of the materials used for PBF-LB/M – confirming the drawbacks reported in [104].

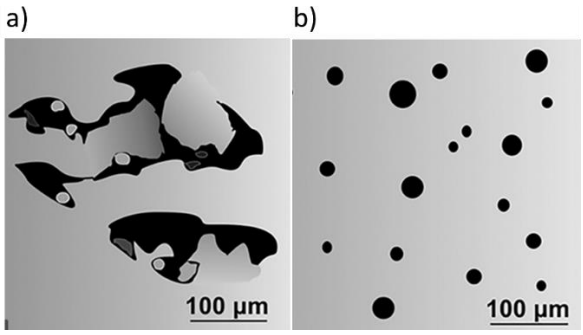

Figure 6 Common porosity in PBF-LB/M a) LOF; b) Keyhole porosity adapted from [103,105]

Hot Isostatic Pressing (HIP) is a common post-processing method for additively manufactured components, especially for the aerospace industry [106]. This process reduces, in particular, closed coalesced porosities [84]. However, pore regrowth was found in samples, that were heat treated after HIP (see Figure 7). While the porosity count is less than prior to HIP, with increased exposure to high temperatures, the pores expand affecting mechanical properties [106].

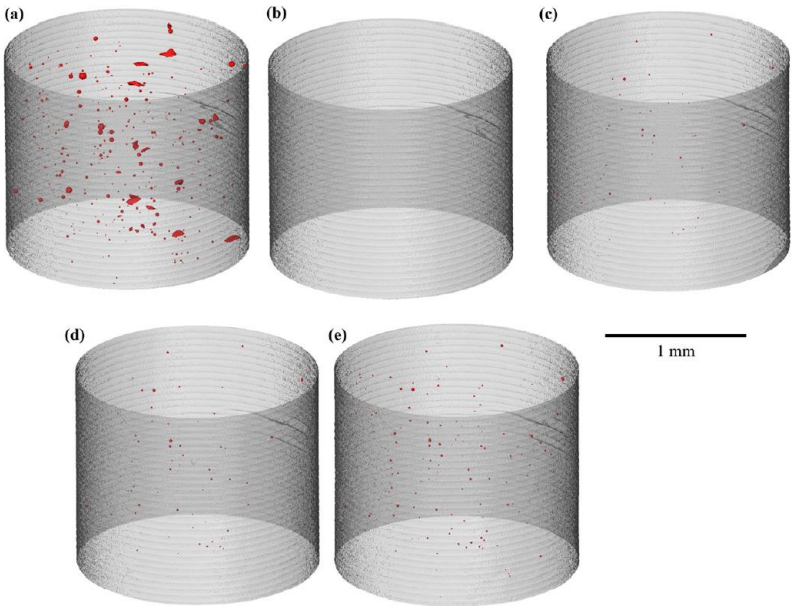

Figure 7 CT scans of cylindrical sample: a) as-built; b) with HIPing; (c) with HIPing followed by 10 min at 1035 °C; d) with HIPing followed by 10 h at 1035 °C; e) with HIPing followed by 10 min at 1200 °C [106]

2.2.3.2 Residual Stresses

Residual stress is a stationary stress at equilibrium within a material [107,108].

Multiscale residual stresses are categorized as follows:

- Type I Macro-stresses vary over the geometric dimensions of the component
- Type II Micro-stresses span grain dimensions
- Type III forms at the atomic scale [107,109]

Residual stresses are introduced during AM due to the layer-by-layer processing and are known to be distributed throughout the manufactured part in a complex manner [110]. During heating, the material surrounding the melt pool expands. Due to the larger expansion of the heated layer as compared to the cooler lower layers, the material bends away from the laser (compressive stress in the upper layer). When the laser moves on, the upper layer cools down and the material shrinks leading to tensile stresses in the upper layers (see Figure 8).

The material below the layer being processed is mechanically constrained, the above mentioned stresses are in balance leading to a complex stress distribution in the part. The residual stresses lead to deformation of the part (deviation from original design) and could lead to delamination, cold cracking and reduced mechanical properties [111].

Theoretical and experimental studies of AM components show that the magnitude of residual stress is dependent on material properties (i.e. coefficient of thermal expansion, thermal diffusivity, thermal conductivity) [112–114], phase transformation or precipitation [115], component geometry [116,117], position of specimen on the substrate plate, process parameters [118,119], scan strategy [108,112,115,120,121] and substrate plate used

[108,122]. It was found that reducing the thermal gradient by e.g. substrate preheating, reduces residual stresses [108,123].

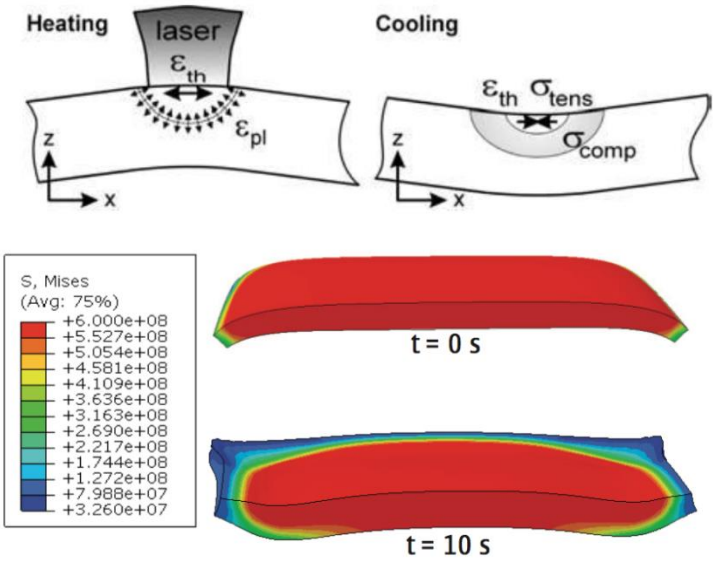

Figure 8 Residual stress formation of a single layer [108,124]

Ding et al. [125] reported that tensile stresses along the deposited material (at the layer being processed) are highest – usually reaching a magnitude corresponding to the as-built yield stress. Once the substrate plate is unclamped significant distortion and redistribution of the stresses was observed. Therefore, stress relieving is often carried out prior to removing samples from the substrate.

2.2.4 PBF-LB/M Thermal Modelling

For a faster determination and qualification of process parameters, multiscale and multi-physics numerical models are often applied [126]. Models resolving the laser interaction with the powder and detailed thermomechanical modelling are computationally expensive. On the other hand, quick analytical models are of limited reliability due to the underlying assumptions made (e.g. neglecting latent heat of fusion) [127].

Process models predicting the build thermal history with temperature dependent material properties seem to be a good compromise between both approaches [128].

Several solutions have been suggested in literature that resolve the deposition path [129–133]. The computational effort, however, remains high and a key prerequisite is knowledge of the scan file format that drives the heat source motion. The advantages of layer-wise thermal models, that do not resolve scan strategy, are computational speed and accuracy of the overall thermal history as demonstrated by Zielinski et al. [134] However, these models are not able to resolve directional grain growth due to tailored deposition paths as demonstrated by Attard et al. [88].

2.2.4.1 CALculating PHAse Diagrams (CALPHAD)

A phase diagram shows the regions where phases are stable and regions where two or more of them coexist for a given composition in temperature - concentration space. CALPHAD uses elemental and phase thermodynamic properties to determine which phases are formed during solidification.

As discussed above, equilibrium phase diagrams cannot be used to simulate PBF-LB/M solidification. Instead, non-equilibrium conditions should be considered, such as the Scheil-Gulliver-conditions [63,64]. The assumptions of the Scheil-Gulliver solidification include [135,136]:

- No diffusion occurs in solid phases once they are formed.
- Infinitely fast diffusion occurs in the liquid at all temperatures.
- Equilibrium exists at the solid-liquid interface.

The difference in chemical composition achieved in equilibrium and non-equilibrium (i.e. Scheil-Gulliver) conditions is schematically shown in Figure 9. Under equilibrium conditions, the chemical composition remains constant since sufficient time allows for complete diffusion. Under Scheil-Gulliver conditions, whatever is solidified does not undergo any further diffusion. Therefore, the chemical composition in the fully diffused liquid is constantly altered.

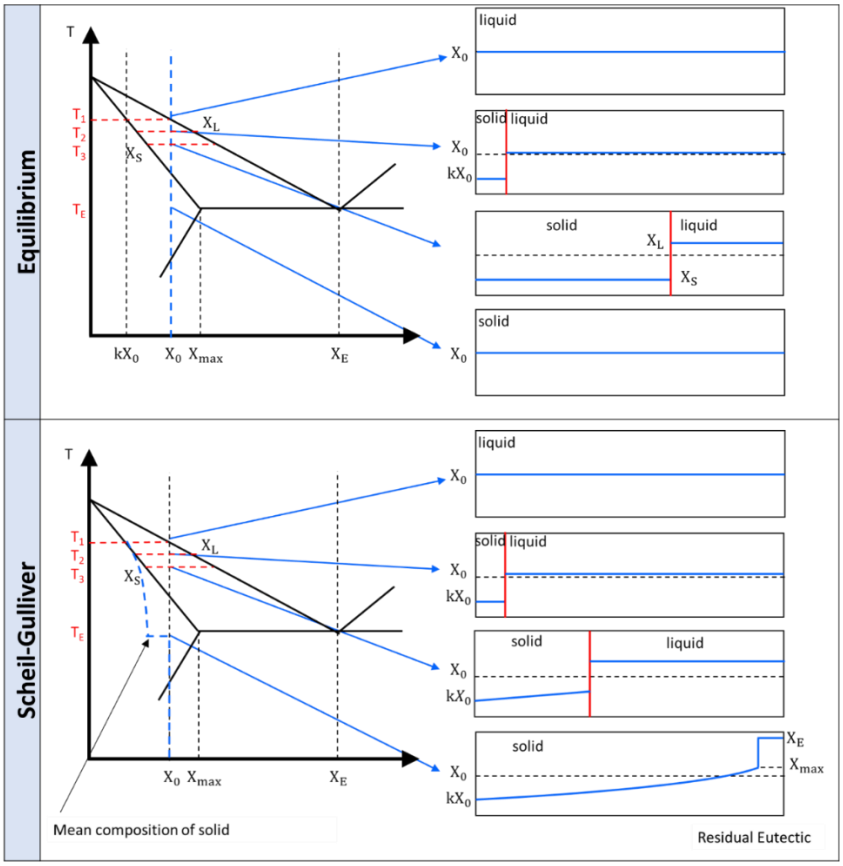

Figure 9 Comparison of equilibrium and non-equilibrium (i.e., Scheil-Gulliver) solidification in terms of composition, reproduced from [63]

2.2.5 PBF-LB/M Microstructures of Ni Superalloys

An example of the PBF-LB/M IN718 microstructure manufactured with an E_V between 60 – 70 J/mm^3 is shown in Figure 10. Similar microstructures are reported in [73,137–140]. The microstructure in XY-plane (see Figure 2b) is circular, while the microstructure in the XZ-plane is oriented in build direction. Rickenbacher et al. [57], Kunze et al. [98] and Carter et al. [141] found similar oriented microstructures in IN738LC. The difference in microstructure in different planes leads to anisotropic properties, which is typical for PBF-LB/M.

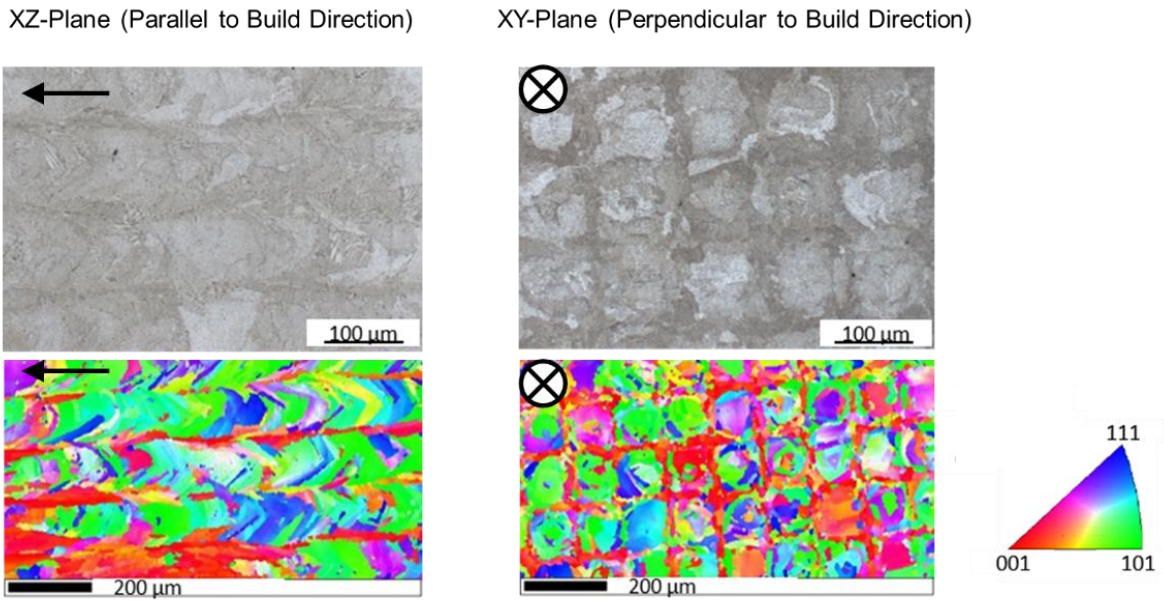

Figure 10 Characteristic microstructure of IN718 from PBF-LB/M processing: Micrographs (above) and inverse pole figures (IPF; below) parallel and perpendicular to build-up direction [142]

Depending on the build orientation and energy density used, microstructures develop from equiaxed to clearly textured grains (see Figure 11) [143]. When comparing microstructures of all build orientations (0°, 45° and 90°), the 45° grain shape and grain size for all energy densities differ significantly compared to the other two build orientations (0° and 90°). In the 45° build orientation, the grains are neither columnar nor spherical, which can be correlated to the secondary heat loss to support structures and surrounding powder causing unique thermal distribution among different build orientations (see Figure 4b).

Besides the grain shape and size, the grains of the 45° sample shown in Figure 11 are oriented mostly in [111] and [101] directions. A predominant [111] grain orientation for the 45° build orientation is also found by Sanchez-Mata et al. [144]. A mixture of the [111] and [101] grain orientations leads to large grain boundary angles (grain boundary misorientation >15° are referred to as High Angle Grain Boundaries; HAGBs), straining the crystal lattice.

The strain induced into the lattice caused by the misorientation increases strength, since dislocation movement is hindered. A dislocation pile-up at HAGBs can be seen in Figure 12a. While the strength is increased, the plasticity and thereby ductility of the material is reduced

significantly. Compared to the HAGBs, no dislocation pile-up can be seen at Low Angle Grain Boundaries (LAGBs <15°; refer to Figure 12b).

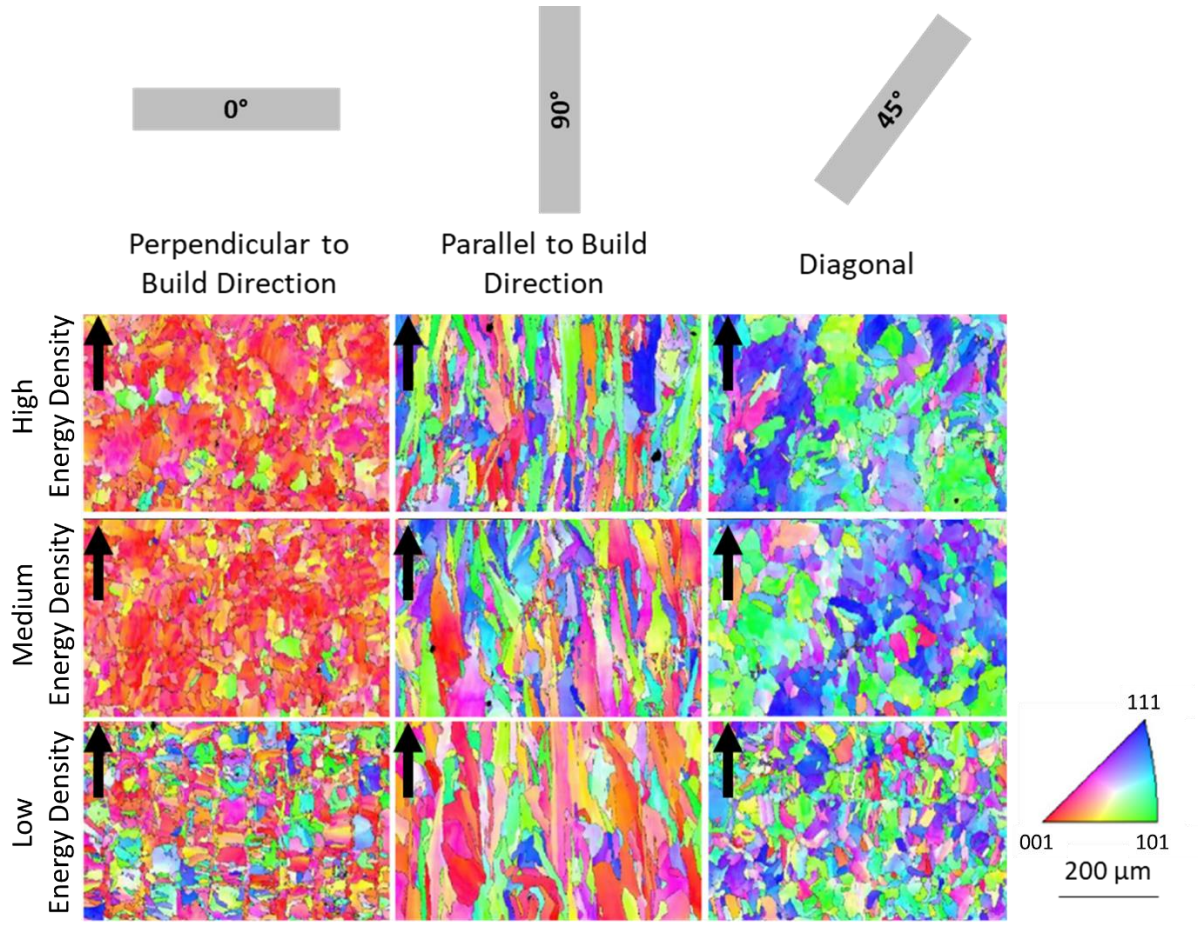

Figure 11 EBSD results for 0°, 45° and 90° build orientation for low, medium and high linear energy densities, adjusted from [143]

a) b)

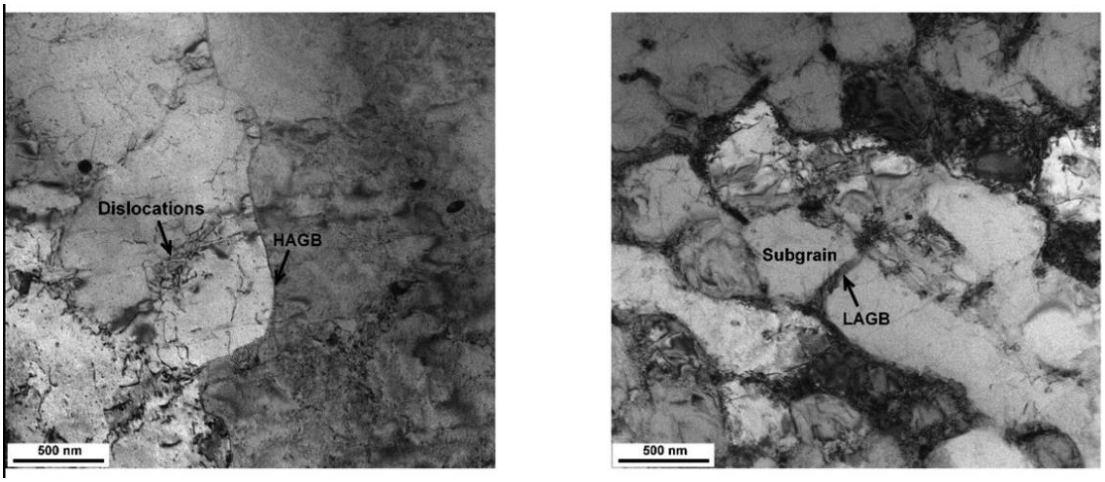

Figure 12 TEM images of Hastelloy-X samples a) Higher amount of dislocations accumulating at HAGBs; b) TEM image of subgrains and LAGBs [145]

Twinning is frequently reported in Ni superalloys and is found in additively manufactured IN718 and IN738LC [33,146–149].

Figure 13 compares slip and twinning deformation. When comparing a slip to a twin the following differences can be drawn:

- For slip [150]
  - The crystallographic orientation above and below the slip plane is the same before and after the deformation.
  - Slip occurs in distinct atomic spacing multiples.
- For twinning (in general) [150]
  - There is a crystallographic reorientation across the twin plane allowing for new slip systems.
  - The shear deformation is homogeneous.
  - Atomic displacement is less than the interatomic separation.

The amount of bulk plastic deformation from twinning is normally small relative to that resulting from slip [150]. It is generally accepted that materials with high stacking fault energies (SFE) deform by slip, whereas materials with low SFE deform by twinning.

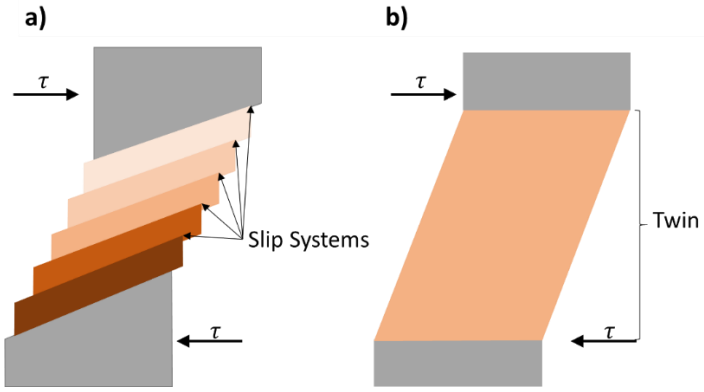

Figure 13a) Deformation by slip [150]; b) Deformation by twinning, reproduced from [150]

Twins result from atomic displacements that are produced from applied mechanical shear forces (mechanical twins) and also during annealing heat treatment (annealing twins) [150]. Twinning occurs on a definite crystallographic plane and in a specific direction, both of which depend on the crystal structure. Mechanical twins are found in hcp crystal structures, while annealing twins are typically found in fcc crystal structures [150]. Even though fcc and hcp structures have low SFE, fcc structures have a sufficient number of slip systems (namely 12) for slip deformation to occur. Comparatively, hcp structures only have three slip systems, which is why mechanical twins form mostly in hcp rather than fcc.

Sanchez-Mata et al. found extensive twinning in the 45° build orientation compared to 90° build orientation after tensile testing [144]. The twins are identified as deformation twins in [111]-

direction after tensile testing (see Figure 14a and b) [144]. Twinning was predominantly found in 45° and 0° build orientations. Sanchez-Mata et al. found the required stress for twin formation in 0° and 45° samples to be lower than the yield stress, while for the 90° samples the required stress lies above the UTS, leading to reduced twin formation in 90° samples [144].

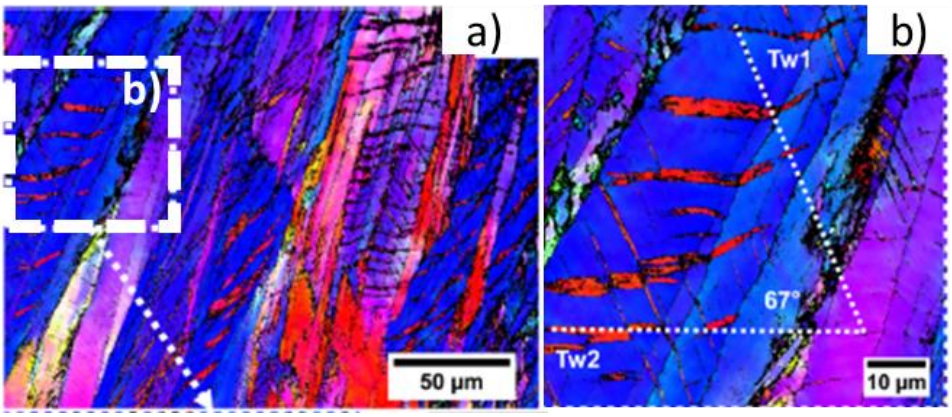

Figure 14 EBSD analysis of 45° build orientation Ni superalloy sample after tensile fracture: a) IPF map, b) Selected enlarged region highlighting twins (Tw1, Tw2) and the angle between them; adjusted from [144]

In the rarest of cases, PBF-LB/M-produced, metallic components are used in as-built condition. Cooling processes during the printing process introduce significant residual stresses, which must be reduced at least by stress relief and/or annealing [84]. The typical microstructural anisotropy is reflected in mechanical properties (see Table 2) and significantly affects short- and long-term behavior [142,151]. Therefore, the microstructure is additionally adjusted to the required quality by means of heat treatment. Heat treatments can be used to create an equiaxed microstructure, increase grain size, dissolve detrimental phases (such as TCP- or Laves-phases) and to form strengthening precipitates (such as γ'-phase and carbides) [152]. Table 5 shows the effect PBF-LB/M processing and heat treatment have on phase formation and phase distribution in IN718.

Conclusively it can be said that clear anisotropy is to be expected in PBF-LB/M samples and components. This anisotropy is also observed when comparing different build orientations. Deformation is achieved via twinning and slip in IN718 and IN738LC. Which type of deformation occurs is dependent on the microstructure and phases present, which in turn depends on PBF-LB/M processing itself and the subsequent heat treatment.

Table 5 Effect of processing and heat treatment on phase distribution in IN718, reproduced from [11,153]

Sample Condition	Phases	Vol. %
Original Powder	γ - Ni	90
	γ'- Ni_3Al	3.5 – 3.9
	γ'' – Ni_3Nb	4.3 – 4.5
	δ – Ni_3Nb	1.8 – 2.0
AB	γ - Ni	86.6
	γ'- Ni_3Al	1.9
	γ'' – Ni_3Nb	8.0
	δ – N_i3Nb	3.3
Homogenisation	γ – Ni	90.1
	γ'- Ni_3Al	1.9
	γ'' – Ni_3Nb	8.0
Homogenisation + Ageing	γ – Ni	67.3
	γ'- Ni_3(Al, Ti)	8
	γ'' – Ni_3Nb	4
	δ – Ni_3Nb	3.5
	γ'- Ni_3Al (nano-scale)	17.2

2.3 Creep Behavior

2.3.1 Introduction to Creep

In a jet engine, materials used within the hot section are exposed to elevated temperatures and static mechanical stresses over prolonged periods of time. The permanent deformation caused by exposure to loads below the yield limit for prolonged periods of time is called creep deformation or creep [150]. Creep deformation is time-dependent and is often the limiting factor in the lifetime of a component within the high temperature industry. For metals, creep must be considered under operating conditions where constant temperatures of at least 40% of the homologous melting temperature are expected [150].

A typical creep test entails subjecting a sample to a constant stress while held at constant elevated temperature [154]. Deformation and/or strain are simultaneously measured and plotted against test duration. A schematic representation of a resulting creep curve is shown in Figure 15.

Creep can be divided into three stages, ignoring the elastic range [155–157], shown in Figure 15. In Stage I (primary creep stage), the strain rate is high, but decreases with increasing time and strain due to strain hardening. The dislocation density increases and a sub-grain morphology forms [158]. In the secondary creep stage (Stage II), the strain rate is constant since an equilibrium between strain hardening and thermal softening is reached. It should be noted that various microstructural processes take place during this stage. The strain rate increases in the tertiary creep stage (Stage III) until rupture [157] due to the formation of voids.

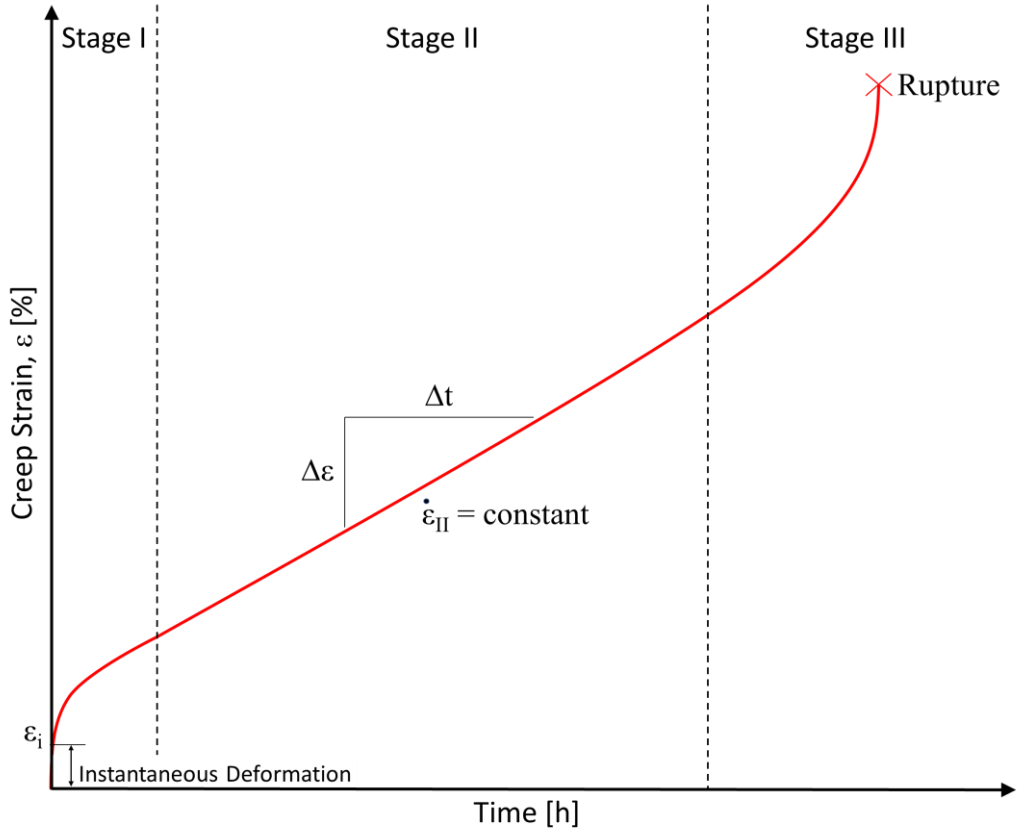

Figure 15 Schematic creep curve highlighting the three creep stages, reproduced from [150]

As shown in the deformation mechanism map (see Figure 16), creep can further be divided into the following types [157,159]:

- Dislocation creep
  - Core Creep
  - Bulk Diffusion
- Diffusion Creep
  - Coble Creep
  - Nabarro-Herring Creep

These creep types are related to different microstructural mechanisms.

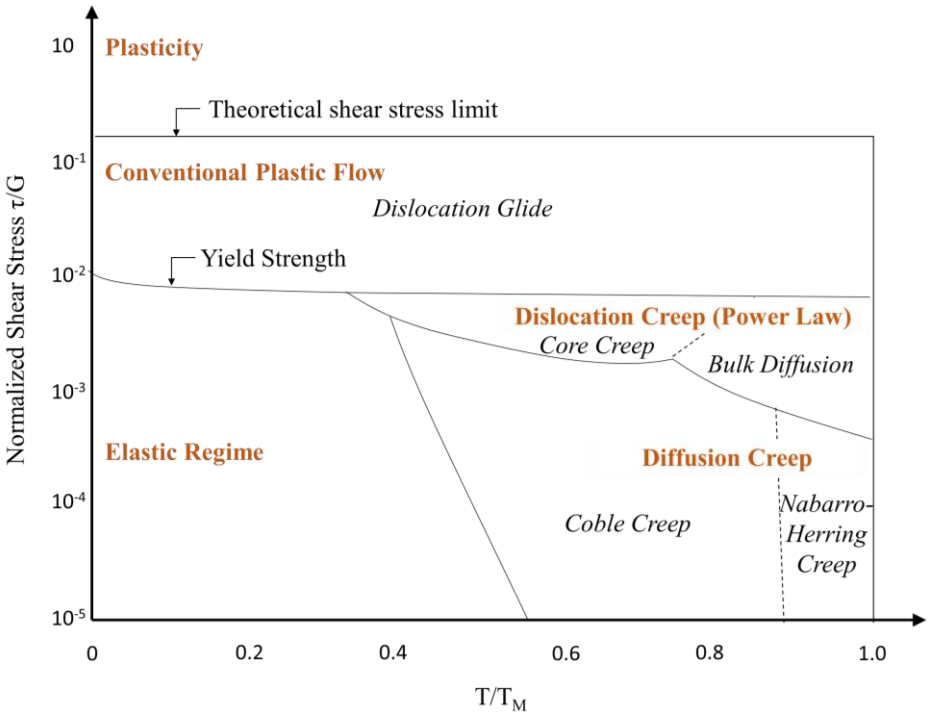

Figure 16 Creep deformation mechanism map, reproduced from [160,161], where τ is shear stress, G is shear modulus, T is material temperature and T_M is melting temperature

Microstructural creep deformation mechanisms in polycrystalline Ni superalloys are complex [162,163]. The deformation mechanism depends on load, microstructure and crystallography [164]. In Figure 17, the dislocation behavior during creep is shown. Different dislocation-based shearing processes occur at temperatures below 650 °C. At temperatures above 850 °C, creep deformation is governed by Orowan looping and cross-slip mechanisms [165]. Deformation mechanisms in temperatures ranging between 650 °C and 800 °C include Anti-Phase Boundary (APB)[1] shearing, continuous faults[2] and micro-twinning [164] (see Figure 17).

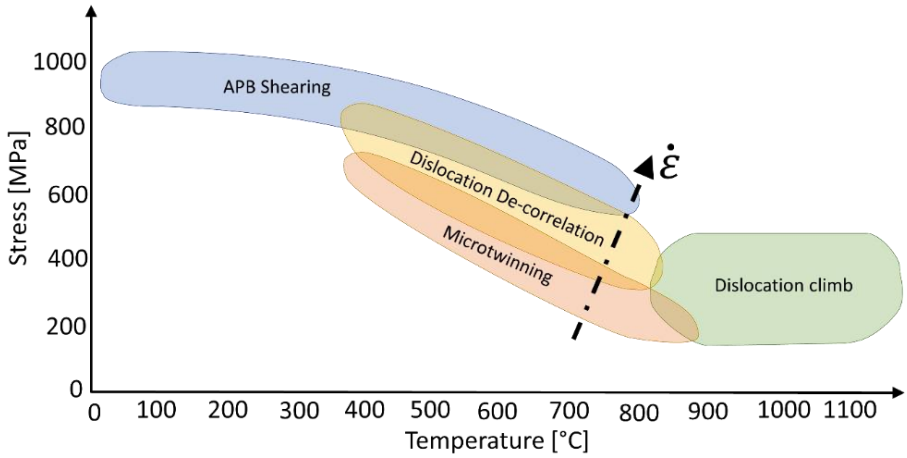

Figure 17 Deformation map for a Ni superalloy, reproduced from [166,167]

[1] An APB is a displacement boundary in ordered crystal structure by half of the lattice constant.
[2] Continuous faults refer to stacking fault shearing [166].

Kear et al. first introduced micro-twinning as a possible deformation mechanism in Ni superalloys [168]. Since then, numerous studies concerning the formation and verification of micro-twins were carried out on single and polycrystalline Ni superalloys [163,168–170]. Special focus lies on the formation boundary conditions, i.e., temperatures and loads. The adopted theory by Kear et al. [168] involves localized atomic diffusion.

Micro-twins are strongly connected to the L_{12} crystal structure; therefore, micro-twins do not form in the γ phase, but in the γ' phase. Should an a/3 <112> dislocation meet a L_{12}-structure, the shear would cause the L_{12} structure to break. Therefore, micro-twins are formed by a/6 <112> Shockley partials, since they keep the L_{12}-FCC structure intact. Dislocation partition can leave high energy (approx. 300 mg./mm^2 [166]) Complex Stacking Faults (CSF) behind.

The formation of the CSF causes wrong atom neighbors in the lattice. Localized atomic diffusion allows for a low energy perfect crystal structure with the correct atom neighbors, with a 60° rotation with respect to the parent crystal (i.e. micro-twin) [166].

Micro-twins have been found preferentially at Superlattice Intrinsic Stacking Faults (SISF)[3] and Superlattice Extrinsic Stacking Faults (SESF) within the γ' phase [167,171,172]. This was also confirmed by Smith et al. [173], who additionally found high-density Co/Cr atmospheres around stacking faults. Segregations of Co, Cr, W and Ta lead to SISFs and SESFs [174]. Barba et al. established a compositional dependency of micro-twin formation to segregations of Co, Cr, Nb, W and Ta [172]. A microstructural dependency has also been reported by Titus et al. [174].

Brittle material behavior has been found in relation to micro-twins [166]. Micro-twins lead to a dislocation pile up, since the slip systems are limited to <111> bands. These dislocations pile-ups can eventually cause stress concentrations which can lead to (cold) crack initiation and propagation along the twin-parent interfaces.

Due to the small sizes of micro-twins (usually span between 7 – 12 atomic planes), they are often mistaken for deformation twins.

[3] A schematic representation of SISF and SESF in comparison to a perfect lattice and a twin is shown in Figure 18.

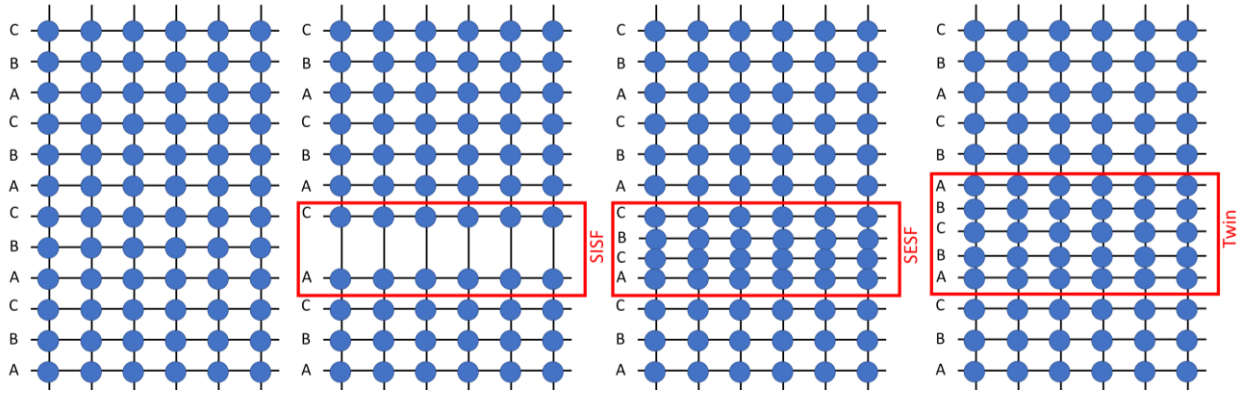

Figure 18 Schematic representation of a) Perfect lattice, reproduced from [150]; b) SISF, reproduced and adjusted from [175]; c) SESF, reproduced and adjusted from [175] and d) Twin, reproduced and adjusted from [150]

2.3.2 Creep of PBF-LB/M Ni Superalloys

For creep testing, Xu et al. found that wrought IN718 samples outperform heat-treated PBF-LB/M ones by 33% [176]. It was shown that defects contained within the PBF-LB/M samples are the root cause for increased creep rates and shorter times to rupture in comparison to conventionally manufactured Ni superalloys. Sanchez et al. investigated the effect of scan strategy and heat treatment of defect-free PBF-LB/M IN718 samples and found comparable creep rates and a 24% longer creep life of PBF-LB/M samples compared to wrought samples [12]. The choice of scan strategy and heat treatment affects phase formation. It was found that the density, shape and orientation of the δ-phase significantly affect creep life, in that they impede void coalescence, thereby reducing the creep rate [12].

Figure 19 shows the creep curves for IN718 in 0°, 45° and 90° build orientation as reported by Sanchez et al. [67]. The 0° samples show the lowest test durations and creep strains. While the difference between the 0° and 45° samples is small, the 45° samples do show larger strains and test durations. A significant increase in both duration and strain is to be seen for the 90° build orientation. The tertiary stage of the 90° samples is significantly different compared to the other two build orientations. The reason behind this creep behavior discussed in literature is linked to the mixed mode failure, caused by the different build orientations, combined with the stress state of the samples [67]. It was found that the 0° samples failed across the highest number of PBF-LB/M layers, while the 45° samples fail across the smallest number of layers [67]. While differing scan strategies did not show a significant effect on creep properties [67], using multiple lasers was found to increase times to rupture. Multiple lasers increase the heat induced into the material, leading to coarser grains, which reduces the risk for grain boundary sliding. Applying differing heat treatments has also shown to affect creep properties [177]. Higher solution heat treatment temperatures can reduce the PBF-LB/M anisotropy and the columnar grain structure, thereby inhibiting intergranular crack growth. Additionally grain

boundary carbides were found to be the dominant strengthening mechanism in terms of creep [177].

In IN718, it was found that the embrittling effect of the δ phase is correlated to the location of the δ phase (i.e. at grain boundaries) and the load direction [47,178,179]. Kuo et al. found a higher amount of δ-phase in 0°-samples than in 90° samples. Due to the grain orientation in the 45° samples, the δ-phase location does not play a predominant role in determining the creep rate, but rather sample geometry and PBF-LB/M process parameters [180].

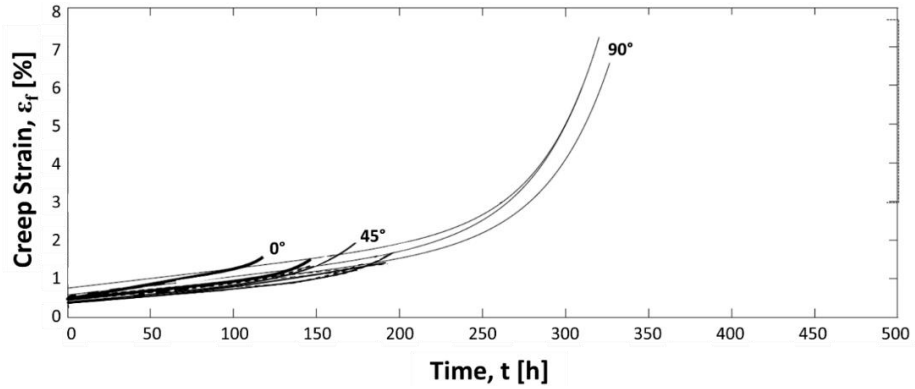

Figure 19 IN718 creep curves tested at 650 °C and 600 MPa for 90°, 45° and 0° build orientation, recompiled from [67]

Rickenbacher et al. [57] showed that the creep strength of 90° PBF-LB/M-manufactured IN738LC clearly lies above the creep strength of 0° samples (see Figure 20). Similar results were found by [98,147].

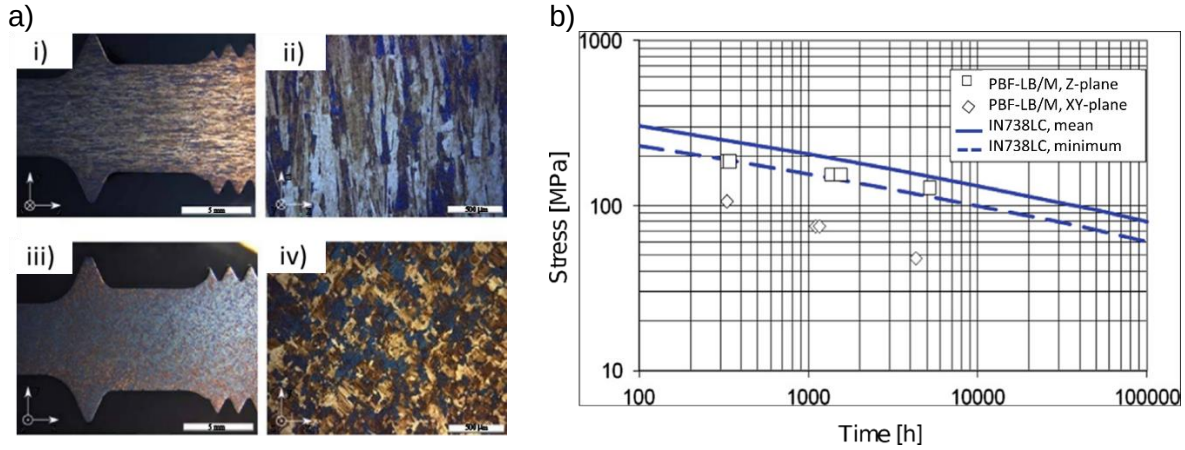

Figure 20 a) i) & ii) Cross-sections of 90° oriented tensile specimens; iii) & iv) Cross-sections of 0° oriented tensile specimens; b) Comparison of short-term 1% proof stresses of cast and PBF-LB/M manufactured IN738 LC, adjusted from [57]

From the surveyed literature, it is apparent that a very small number of papers study creep behavior of PBF-LB/M materials. The general understanding of the creep performance of PBF-LB/M materials is therefore limited [12]. The large number of process parameters, the complicated experimental procedure to measure creep and the influence of PBF-LB/M build orientation on mechanical behavior, makes drawing generalized conclusions challenging.

3 Aims and Objectives

As can be deduced from Chapter 2, there is a strong connection between the PBF-LB/M solidification conditions (affected by process parameters, support structures etc.) and resulting material properties. The large number of parameters and the corresponding property range – even within one build job or one component - poses a serious challenge for thorough material qualification. The build orientation and post-processing methods alter the microstructure, which affect the mechanical properties, especially concerning creep.

For the purpose of this thesis, the process parameters for the PBF-LB/M manufacturing of both Ni superalloys, IN718 and IN738LC, are fixed. The manufacturing routes were optimized with regards to relative density. This also includes scan strategy and thermal post-processing steps.

As reported in Chapter 2, the PBF-LB/M microstructure significantly differs when processing conditions besides process parameters vary. It is thus hypothesized that component geometry as well as build orientations affect the microstructure and thus long-term mechanical properties. The overall goal of this research is thus to identify correlations between the distinct PBF-LB/M microstructure and long-term mechanical properties of IN718 and IN738LC for the reliable use of Ni superalloys in applications. This entails a microstructural and mechanical comparison of witness samples and samples extracted from components as well as a study on the effect of build orientation on creep properties (see Figure 21).

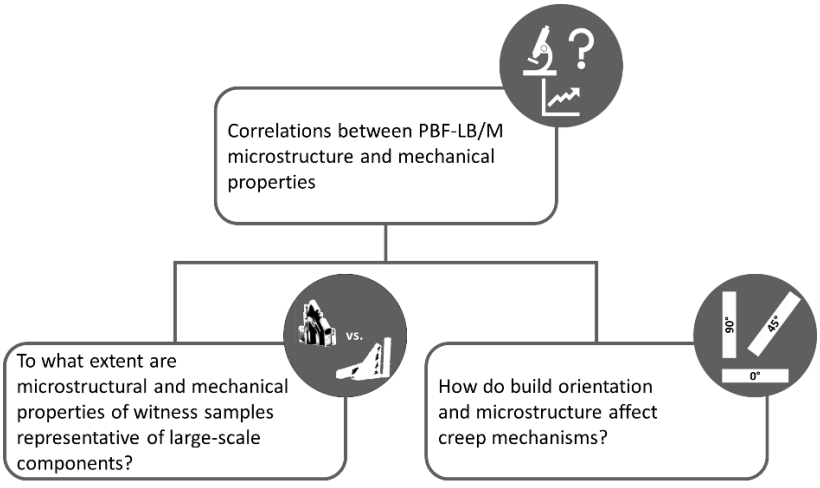

Figure 21 Research goal and research questions of dissertation

1. **To what extent are microstructural and mechanical properties of witness samples representative of large-scale components?**

The solidification conditions during the PBF-LB/M process play a key role in the resulting microstructure, phase formation and mechanical properties. Therefore, it hypothesized, that different component geometries lead to different solidification conditions and hence microstructures and mechanical properties. For this purpose, a generic component with integrated samples oriented in 0°, 45° and 90° is manufactured and compared to witness

samples (i.e., cylinders oriented in 0°, 45° and 90°). The following sub-goals are defined for research question 1:

- How is the thermal history of components and witness samples affected by the difference in component geometry during the PBF-LB/M process?
    - For this sub-goal, numerical simulations are performed to investigate the thermal distribution for different sample geometries as well as for different build orientations. The effective cooling rates are quantified for each sample and correlated to residual stresses and microstructures, specifically grain sizes.
- How do Vickers hardness values correlate to component geometry?
- What is the effect of component geometry on the tensile properties?

The effective cooling rates are used to explain the mechanisms behind potential differences in microstructure and mechanical properties. The results are quantitively and qualitatively correlated to microstructures.

Qualitative correlations are critically assessed using the following evaluation matrix:

Strong correlation	++
Correlation	+
Weak Correlation	0
No correlation	-

2. How do build orientation and microstructure affect creep mechanisms?

Since heat transfer depends on the build orientation under consideration, differences in solidification behavior during PBF-LB/M are expected. The difference in microstructure for different build orientations would therefore lead to different mechanical properties. The extent of the expected differences is to be identified. Additionally, it should be investigated whether the commonly tested extremes (0° and 90° build orientation) are sufficient to describe creep properties of intermediate orientation angles. The effect of creep test parameters (i.e. test temperature and applied net stress) is also considered for 0°, 45° and 90° build orientation.

The following sub-goals are investigated:

- What is the effect of different creep test parameters?
- How do build orientation affect creep deformation mechanisms?
- Is the creep behavior of witness and extracted samples comparable?

Based on a creep deformation mechanism map, the expected creep mechanisms for the three considered build orientations are discussed and correlated to microstructures.

4 Materials and Experimental Methods

This chapter documents alloy composition, manufacturing process parameters, post processing steps, computational models and material characterization methods utilized throughout this research. This documentation not only provides the foundation to assess the quality and accuracy of results obtained but also allows the repetition of all research steps for verification and validation purposes.

4.1 Materials

Gas atomized IN718 and IN738LC powders were used to manufacture samples required to study the microstructure, tensile and creep behavior of both Ni superalloys. Chemical analysis of the Ni superalloys was carried out according to ASTM E1835 [181]. The respective powder suppliers and the powder compositions of the respective alloys are shown in Table 6. An oxygen content below 0.015 wt.% was measured for IN718 and 0.007 wt.% oxygen content was measured for IN738LC. The oxygen content for both powders is considered low enough to avoid oxidation. The content of B, P, S, H and N were measured to be below 0.01 wt.% for both Ni superalloys.

In order to achieve a successful PBF-LB/M build, powder flowability must be ensured. A Hall Flowmeter funnel is used according to ASTM B213-20 to determine the Hausner Ratio (Equation 2). A value below a maximum of 1.25 indicates good flowability.

$$\text{Hausner Ratio} = \frac{Tapped\ Density\ (\frac{g}{cm^3})}{Apparent\ Density\ (\frac{g}{cm^3})} \qquad \textit{Equation 2 Hausner Ratio}$$

To ensure uniform powder spreading on the substrate plate, powder particles should be spherical in shape with no satellites. The powder particle morphology was assessed using a scanning electron microscope (SEM; Zeiss Auriga). The sphericity was characterized using ImageJ. Powder particle surfaces were studied by sticking loose powder to conductive tape.

SEM images of the IN738LC powder are shown in Figure 22. As can be seen, the powder is mostly spherical (sphericity 0.96) with limited porosity. Some satellites are visible. A Hausner ratio of 1.02 confirms excellent flowability. Similar characteristics are found for the IN718 powder.

The Powder Particle Size Distribution (PSD) was carried out according to ASTM B214-16 (sieving) and ASTM B822-17 (laser diffraction). For IN718, the $D_{10\text{-}90}$[4] range corresponds to 17 µm – 54 µm (see Figure 23). The IN738LC $D_{10\text{-}90}$ range corresponds to 22 µm – 49 µm (see Figure 23).

[4] D_{10}, D_{50} and D_{90} values indicate the percentiles (10%, 50%, 90%) of the cumulative powder distribution (i.e. 10% of the cumulative powder distribution lie below the D_{10} value).

Table 6 Powder composition of IN718 and IN738LC

	IN718		**IN738LC**	
Manufacturer Material Name	Ni-Alloy IN718		VDM® Powder 738 LC	
D_{10} – D_{90} Range	17 µm – 54 µm		22 µm – 49 µm	
Supplier	SLM Solutions®		VDM Metals	
Chemical Composition	**Nominal [182]**	**Powder (measured)**	**Nominal [183]**	**Powder (measured)**
Ni	50 - 55	54.37	58.6	61.65
Al	0.2 – 0.8	0.46	3.7	3.47
B	<0.01	0.002		0.01
C	Max. 0.08	0.03	0.09 – 0.13	0.09
Co	Max. 1	0.16	3 - 9	8.31
Cr	17 - 21	19.33	15.7 - 16.3	15.83
Cu	Max. 0.3	0.01	-	0.002
Fe	11 - 22.5	16.015	Max. 0.05	0.09
H	Not specified	<0.01	Not specified	<0.002
Hf	-	-	-	0.07
Mn	Max. 0.35	0.01	Max. 0.02	0.001
Mo	2.8 – 3.3	3.17	1.5 - 2	1.78
N	Not specified	0.01	Not specified	0.002
O	Not specified	0.02	Not specified	0.007
P	Max. 0.015	0.002	Max. 0.015	0.002
S	Max. 0.015	0.001	Max. 0.015	0.0005
Si	Max. 0.35	0.03	Max. 0.3	0.04
Ta	Max. 0.05	0.11	1.5 - 2	1.87
Nb	4.75 - 5.5	5	0.6 – 1.1	0.9
Ti	0.65 - 1.15	0.99	3.2 – 3.7	3.35
V	-	-	-	0.003
W	-	-	2.4 - 2.8	2.57
Zr	-	-	0.03 - 0.08	0.0016

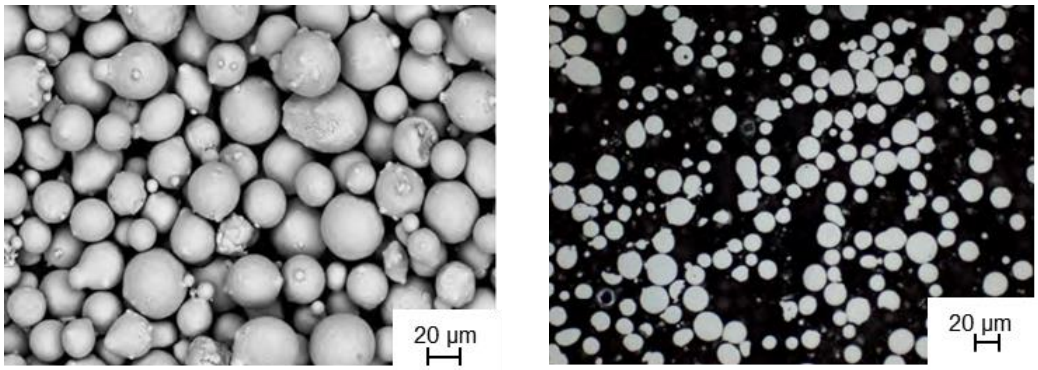

Figure 22 SEM images of virgin IN738LC powder. Similar powder characteristics are found for IN718

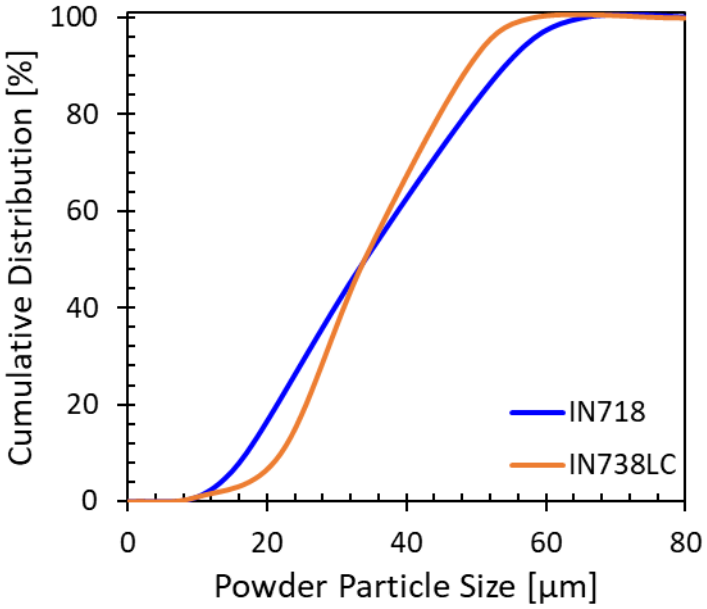

Figure 23 PSD for IN718 (blue) and IN738LC (orange) virgin powder

4.2 PBF-LB/M Manufacturing

The qualification standard (DIN EN ISO/ASTM 52920 [14]) states that witness samples should be manufactured alongside the component to be used in application. The witness samples are to be analyzed to qualify the manufacturing process (e.g. ensure relative density, static and/or dynamic properties) and eventually for qualification of the product.

PBF-LB/M components usually differ geometrically from the witness samples. For example, sudden cross-sectional changes and/or undercuts are usually found in components but not in witness samples, which are usually composed of simple geometries, such as round bars or cubes.

For this purpose, the generic component shown in Figure 24a was designed to resemble and include geometric features expected in turbomachinery components. Witness samples (see Figure 24b) were integrated in the generic component design, which combined form the

Sample Extraction Component (SEC) - see Figure 24c. The SEC allows the extraction of three samples (one in each of the build orientation 0°, 45°, 90°) to compare their characteristics with those of standard witness samples.

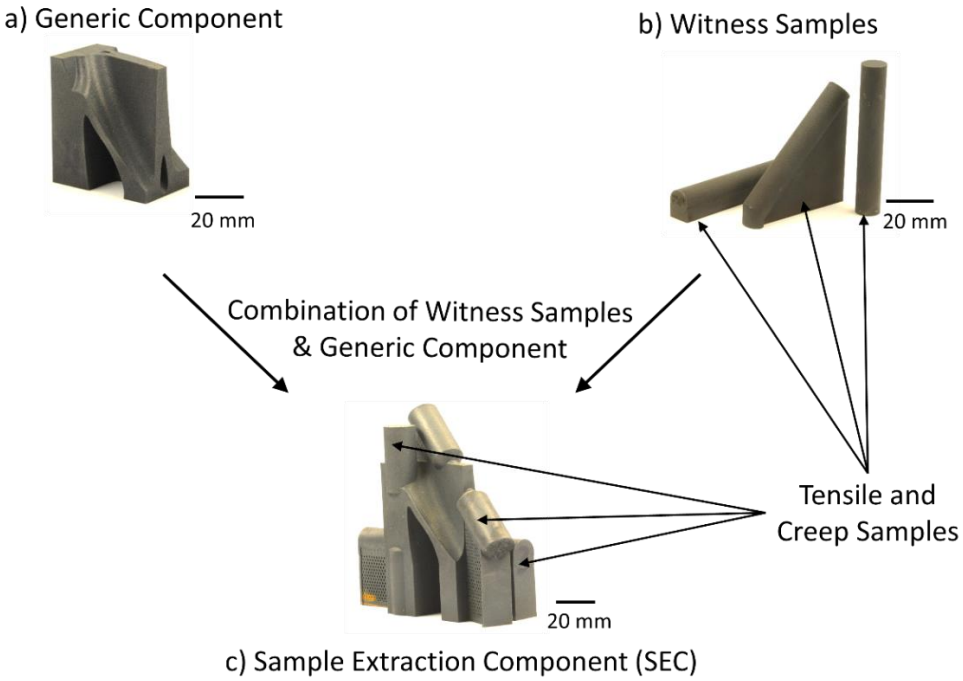

Figure 24 Overview of test geometries: a) Generic component based on industrial design; b) Witness samples oriented in 0°, 45° and 90°; c) Sample Extraction Component (SEC; combines generic component and witness samples)

The witness samples are cylinders with a diameter of ∅13 mm and height of 79 mm oriented in 0°, 45° and 90°. For an overview of the build orientations refer to Figure 2b. The 0° and 45° samples were printed on support structures to avoid build failure due to excessive warpage.

Details regarding the PBF-LB/M process parameters and subsequent sample post processing are listed in Table 7. The sample placement on the substrate plate is shown in Figure 26. The sample numbers indicate the scanning order.

All samples are mechanically tested and characterized in standard post-processed condition (IN718: heat treated; IN738LC: HIP and heat treated) unless otherwise specified.

Table 7 Manufacturing routes for IN718 and IN738LC

	IN718	IN738LC
Machine	SLM280 HL twin	EOS M290
Preheating	20 °C	80 °C
E_V	62 J/mm³ (refer to Appendix D for process parameters)	69 J/mm³ (refer to Appendix D for process parameters)
Laser Spot Diameter	80 µm – 115 µm	100 µm
Layer thickness	30 µm	40 µm
Post-processing	AMS 5663 (see Figure 25, only air cooling was applied) Under Ar atmosphere	110–1230 °C, air cooling 840 °C for 24 h, air cooling Under Ar atmosphere
	No HIP	HIP
Samples manufactured and post-processed by	MAN Energy Solutions	Siemens Energy

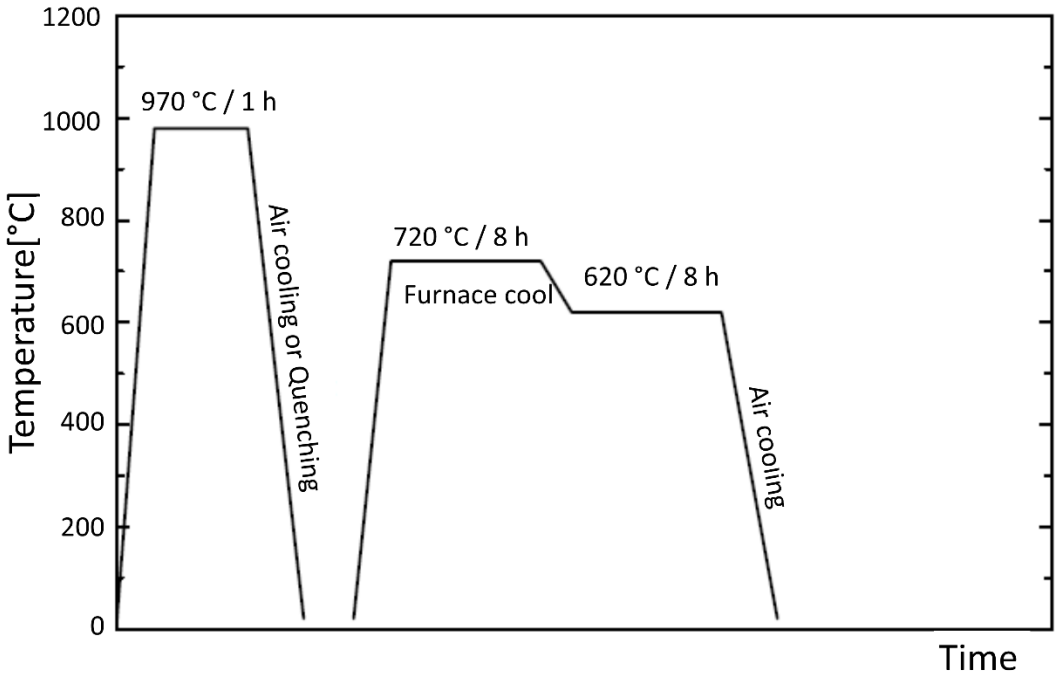

Figure 25 AMS5663 heat treatment applied to IN718 samples

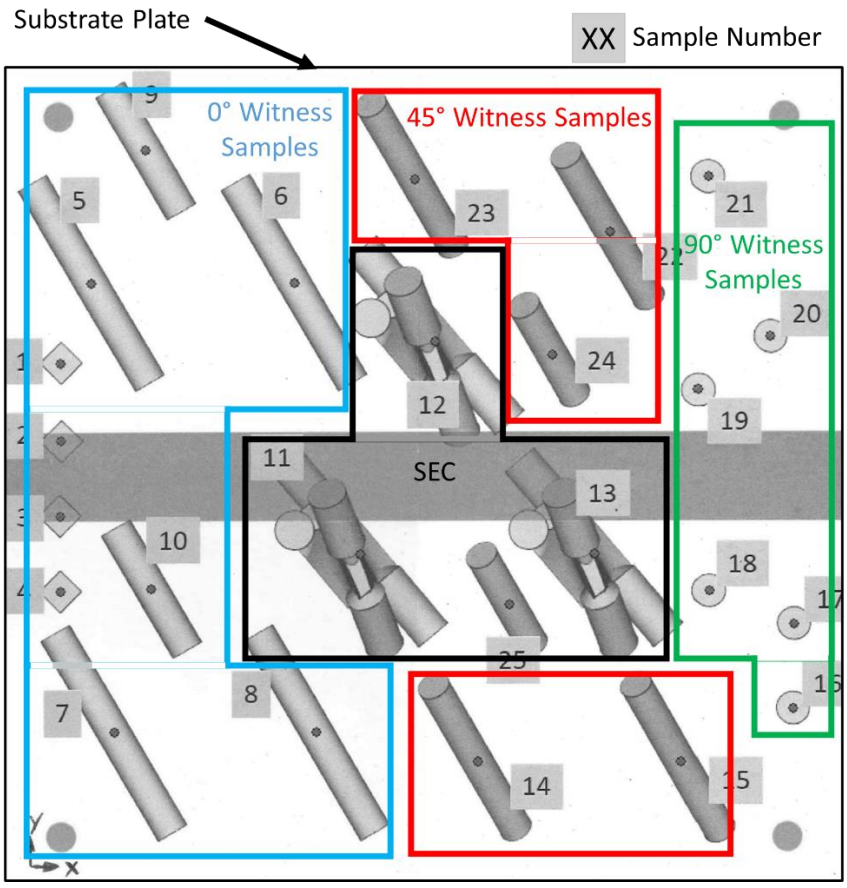

Figure 26 Sample placement on substrate plate

4.3 Theoretical Modelling

4.3.1 PBF-LB/M Process Modelling

As discussed in Chapter 2, the microstructure of the samples manufactured with PBF-LB/M is heavily dependent on the solidification conditions throughout the process. Therefore, numerical calculations were undertaken to describe and quantify the thermal history of the manufactured samples.

The conduction equation (Equation 3) is applied in OpenFOAM to obtain the thermal history for the witness samples and SEC. Equation 3 is cast into a transient volume formulation and is solved iteratively until a quasi-steady solution of the temperature field is reached.

$$\rho c_p \frac{dT}{dt} = \nabla \cdot (\lambda \nabla T) + Q_v$$

Equation 3 Transient Fourier's Law

Where:

- ρ is the density,
- c_p is the specific heat,
- T is temperature,
- t is time,

- λ is thermal conductivity,
- Q_v is volumetric heat source.

Equation 3 neglects melt pool dynamics in favour of accelerating the computation. Within the solidification range (temperature range from $T_{solidus}$ to $T_{liquidus}$), the solution is held constant until the latent heat is consumed or released depending on whether the alloy is melting or solidifying respectively. The maximum temperature is limited to the nickel boiling temperature (i.e. 3200 K). In order to reduce the computational effort (time and memory), 100 powder layers are lumped together. The volume energy density is applied to the layer or a lump of layers under consideration. The duration of energy input corresponds to the build rate[5] (in mm^3/s) and the volume being processed within that layer or lump. After that, the heat source is switched off and heat is allowed to diffuse during the recoating time, which is 10 seconds [184]. When a lump is considered, the recoating time in the thermal model corresponds to the sum of all recoating times of lumped layers. After the recoating time, the next layer/lump is activated and the whole process is repeated.

In this research, the effect of scan strategy is not investigated and was kept constant throughout the build for all samples. Since the difference in solidification between witness and SEC should be analyzed, layer wise comparison of the thermal history is considered to be sufficiently accurate.

Further assumptions of the model include [128]:

- The bottom surface of the substrate plate is assumed to be connected to the respective PBF-LB/M machine which is considered a large heat sink and remains at constant ambient temperature.
- The substrate plate sides exchanges heat with the environment. The heat transfer coefficient is assumed to be 10 $\frac{W}{m \cdot K}$ [185].
- The top of the substrate plate and the sample sides in contact with powder are assumed to have a heat transfer coefficient of 5 $\frac{W}{m \cdot K}$ [185].

The boundary conditions used in this study were adopted from [128]. Lumping layers to reduce computational speed affects the temperature prediction accuracy, which will be discussed in Chapter 5.2.

The respective Ni superalloy properties ρ, c_p and λ are temperature dependent as reported in [186,187] for IN718 and [183] for IN738LC.

[5] Build rate = Scan speed · Hatch distance · Layer height

4.3.2 CALculation of PHAse Diagrams (CALPHAD)

As previously discussed, the solidification conditions during PBF-LB/M do not allow for phase prediction under equilibrium conditions. Thus, CALPHAD was used to predict the phase formation under Scheil-Gulliver solidification.

Within the scope of this thesis, *Thermo-Calc*, a commercial software package, was used to simulate the solidification for IN718 and IN738LC using the Scheil-Gulliver method and the TCNI8 database. For comparison, equilibrium conditions are also calculated.

4.4 Mechanical Testing

All samples (for all build orientations: 0°, 45°, 90°) are destructively tested to determine mechanical properties, including Vickers hardness, tensile and creep properties. Details about the exact procedures are outlined below.

4.4.1 Vickers Hardness

Vickers hardness (HV30) is measured for all materials on separate samples from tensile and creep specimens. Vickers hardness measurements are carried out according to EN ISO 6507-1 [188]. Up to ten (10), minimum three (3), measurements were taken along the build direction in the center of the XZ-plane of the samples.

4.4.2 Tensile Testing

Tensile tests are carried out according to DIN EN ISO 6892-1 [189]. The printed cylinders were milled into the geometry shown in Figure 27. A Zwick-Roell machine is used with a 3-zone convection oven with a max. temperature of 1100 °C. The test temperature for IN718 sample lies at 650 °C, while IN738LC samples were tested at 850 °C. For IN718, the strain rates lie at 0.42 %/min. within the elastic regime and at 8.4 %/min. in the plastic regime. For IN738LC, the strain rates lie at 0.5 %/min. within the elastic regime and at 5 %/min. in the plastic regime.

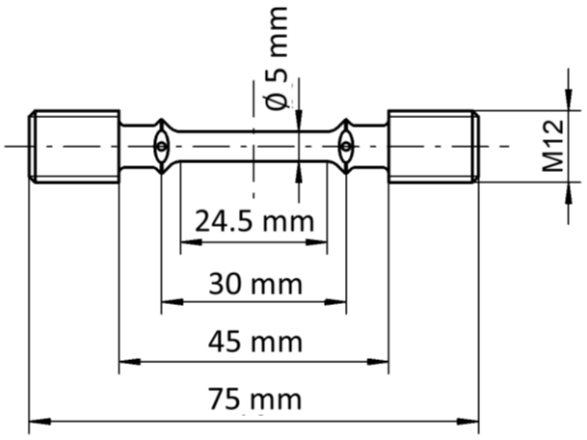

Figure 27 Tensile and creep sample geometry

4.4.3 Creep Testing

Similar to the tensile samples, the printed cylinders were processed into the geometry shown in Figure 27.

Since creep testing has already been carried out for IN718 (see Chapter 2.3), only literature data will be used to discuss the differences in material behavior between IN718 and IN738LC. The IN718 samples from literature [12] were manufactured using PBF-LB/M with a similar volume energy density as in this study, followed by a AMS5662 heat treatment (see Figure 28). The samples were subsequently machined into an ASTM E8/E8M uniaxial specimen to be creep tested at 650 °C and an applied net stress of 600 MPa according to the ASTM E139 standard [154] using a Dension constant load creep machine.

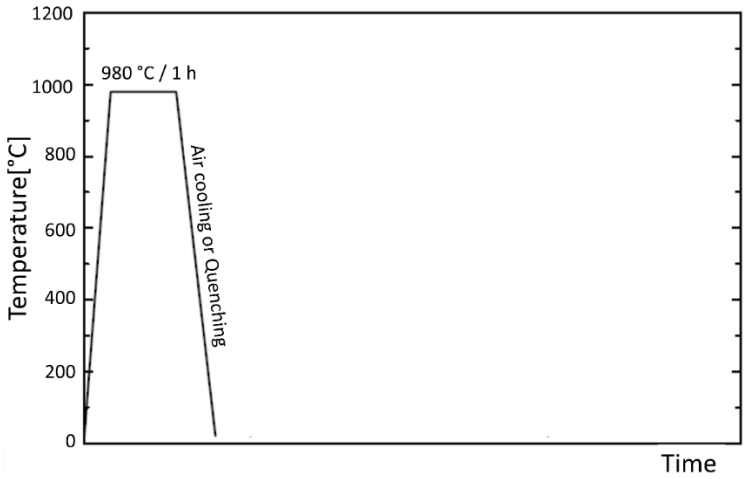

Figure 28 AMS 5662 heat treatment

IN738LC creep tests are carried out according to DIN EN ISO 204 [13]. Creep tests are carried out at temperatures ranging between 750 °C and 850 °C with applied net stresses varying between 150 MPa and 350 MPa using a lever loaded single specimen test machine with a 3-zone convection oven. Each creep test was performed once. An axial ceramic extensometer was used to measure specimen elongation. Three type S thermocouples were tied onto the sample surface with ceramic threads to measure and control the temperature along the sample and grippings. The creep test parameters were chosen based on the conditions for the intended application (gas industry).

4.5 Sample Analysis

All samples were microstructurally analyzed. This includes residual stresses, X-ray diffractometry (XRD), relative density measurement, Scanning Electron Microscopic (SEM)-, Electron Backscatter Diffraction (EBSD)- and Transmission Electron Microscopic (TEM) analysis. Details about the exact procedure of each of these metrics are outlined below.

4.5.1 Residual Stresses

Residual stresses were characterized according to DIN EN 15305 [190] using a Co cathode in a Strechtech G3R machine. Negative values indicate compressive stresses and positive values indicate tensile stresses.

Measurements were carried out at room temperature on polished surfaces prior to mechanical testing on the final sample geometries (as shown in Figure 27). Residual stresses parallel and perpendicular to build direction (i.e., XZ and XY-plane; see Figure 2b) were measured at the centre of the respective planes. Three measurements were taken per plane and an average was calculated. A standard deviation is determined.

4.5.2 X-Ray Diffractometry (XRD)

In order to validate the phases predicted with Thermo-Calc (see Chapter 4.3.2), phases were identified via X-Ray Diffractometry (XRD) using a Co cathode and machine Rigaku SmartLab SE. Measurements were carried out at room temperature. XRD spectra were taken parallel to build direction (i.e., XZ-plane; see Figure 2b) for witness and extracted samples for both Ni superalloys.

4.5.3 Relative Density

The relative density of all samples was determined by first sectioning the sample in the XZ- and XY-planes (refer to Figure 2b). The sectioned samples were hot mounted in bakelite, and ground using sandpaper grade 80 up to 4000, followed by polishing with 3 µm and 1 µm diamond polishing solution. Five images were taken of the prepared cross-sections using a light microscope (Leitz Aristomet) at 50x magnification (2 mm x 1.5 mm field) parallel and perpendicular to the build direction. The relative density was calculated based on image contrast using ImageJ. A threshold for all macrographs was applied to produce a binary image of porosity (see Figure 29). The percentage porosity in the image was then found by summing the area of the pores and dividing by the original area of the image.

The relative density is additionally confirmed using µCT-scans. A voxel size of 34 µm was utilized for the µCT, resolving a minimum defect size of 0.5 µm, which is considered to be the maximum allowed defect size in many applications. The scans were taken for the entire length and front of the samples.

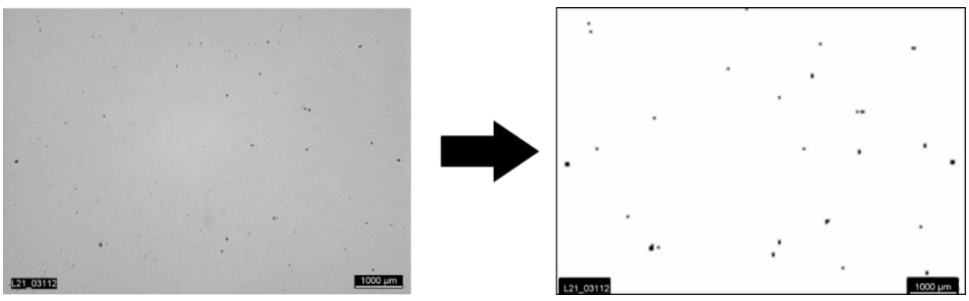

Figure 29 Example of a binary image of IN718 cross-section characterized by ImageJ

4.5.4 Microstructure

Microstructural investigations are carried out on a polished and etched surfaces in XY- and XZ-planes. The used etch solution for the Ni superalloys is V2A-etchant.

The scanning electron microscopic (SEM) investigations was carried out on a Zeiss SEM microscope (Zeiss Auriga) with EDAX software. EBSD analysis was carried out at the sample thread to determine the microstructure prior to creep and close to the fracture surface of creep samples.

EBSD analysis was carried out at the sample thread and close to the fracture surface of creep samples to determine grain orientation using Inverse Pole Figures (IPF-Z). The cross-sectional grain width and length for all grains were measured in the EBSD scan and an average grain size was determined from all measurements of the respective sample. The cross-sectional grain size was also measured with light microscopy. Again, grain width and length were measured for the same size field used in EBSD and an average grain size was determined.

EBSD analysis was also used to determine grain boundary angles. Low Angle Grain Boundaries (LAGBs) were defined to lie below 12° and High Angle Grain Boundaries (HAGBs) above 12°. Schmid factor frequency maps were developed based on Euler angles. All EBSD analyses were taken in the XZ-plane. Energy-dispersive X-Ray (EDX) spectroscopy was run simultaneously.

Since twinning was frequently reported in literature (see Chapters 2.2.5 and 2.3), twin density and twin thickness were determined from EBSD-scans using ImageJ. An average of 7 measurements of the twin thickness was taken. To determine the twin density, twins were manually counted five times per image and divided by the area of the image. The standard deviation indicates the reliability of the results.

Transmission Electron Microscopy (TEM) was carried out on metal foils to analyze grain boundaries and dislocation structures. Dislocation density was measured by means of the line intercept method during TEM analysis. The metal foils were prepared by cutting discs of approximately ~0.4 mm thickness from a 3 mm diameter cylinder extracted from the PBF-LB/M samples by means of spark erosion. The discs are mechanically ground on both sides to achieve 0.1 mm thickness. Further thickness reduction to obtain an end thickness of 50 – 200 nm was achieved by electrochemical thinning. A JEOL JEM 2000 FX (200 KV accelerating voltage) transmission electron microscope was used, which is equipped with an energy dispersive X-Ray system, model Tracor Northern, USA (TN-5500).

SEM and TEM analysis was conducted by the University of Stuttgart Materials Testing Institute in Stuttgart, Germany.

5 Results and Discussion for Research Question 1: To What Extent are Microstructural and Mechanical Properties of Witness Samples Representative of Large-Scale Components?

This chapter presents and discusses correlations between the PBF-LB/M processing, microstructure and mechanical properties of IN718 and IN738LC.

Mechanical properties and creep behavior cannot be fully understood without considering the complete process chain in detail. It is for this reason that the following subchapters are arranged in such a way that the build quality is studied first so as to provide the foundation for interpreting characterization results and observed material behavior.

Before diving into the details, the samples are inspected and analyzed to ensure that no major defects exist that might affect mechanical properties. After confirming the samples' quality, the research questions are pursued considering IN718 first, followed by IN738LC. There is a large pool of researchers investigating PBF-LB/M IN718 covering processing details, material characterization and creep. The results obtained throughout this research are compared to literature to position this research in the overall understanding of IN718 behavior. Open domain knowledge, especially pertaining to IN718 creep behavior is complemented to close knowledge gaps. In a second step, the behavior of IN738LC is also studied. If the behavior identified differs to that of IN718, the root cause is investigated and documented accordingly.

5.1 Sample Quality Assurance

Visual inspection of the sample showed no surface defects or large deformation of the geometry that would negatively influence further analysis of the witness samples or samples extracted from the SEC (refer to Figure 30).

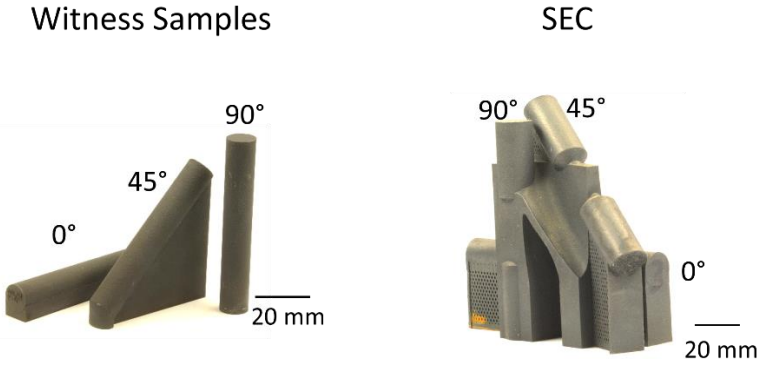

Figure 30 PBF-LB/M samples used for visual inspection

Figure 31a shows a schematic of the 45° witness sample and the support structure upon which it is built. The schematic also shows the planes in which µCT scans of IN718 PBF-LB/M were taken. The scans are shown in Figure 31b and Figure 31c. The voxel size of these scans is 34 µm, which is considered to be fine enough to capture maximum allowable defects. As can

be seen, neither porosity nor cracks are detected at the front of the sample or the along the sample length.

Since the penetration depth of X-rays is limited for Ni superalloys, representative light microscopic images parallel to the build direction (i.e. XZ-plane) and perpendicular to the build direction (i.e. XY-plane) of PBF-LB/M IN718 witness and extracted samples are shown in Figure 32. Limited porosity can be seen for both planes and a relative density of 99.92% was determined for both witness samples and extracted samples.

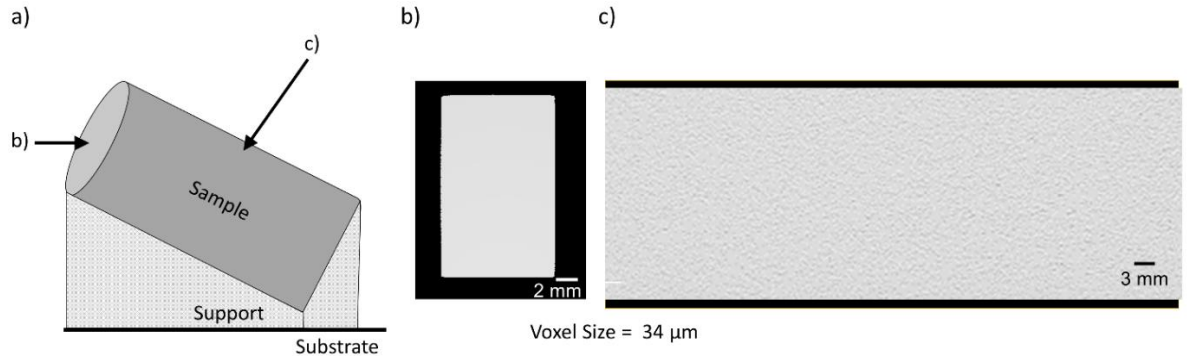

Figure 31 µCT Scans of a 45° IN718 PBF-LB/M sample: a) Schematic to show where scans were taken; b) Scan of sample front; c) Scan of sample length

The achieved relative density (i.e. 99.92%) is comparable to values (> 99.9%) reported in literature, see for example [11,97,191]. Although the applied volume energy density of 62 J/mm^3 fits into the process window for IN718 [97], the sphericity of the pores indicates keyhole porosity. The average pore sphericity in this study is 0.89 (measured using ImageJ).

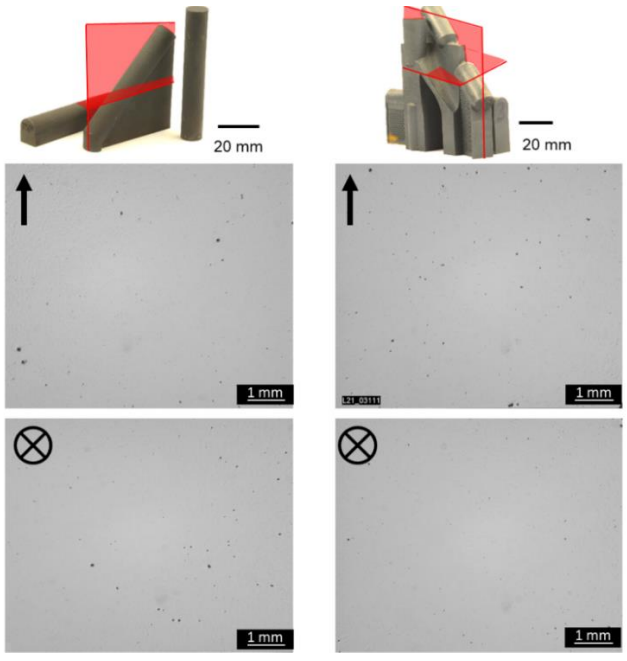

Figure 32 Cross-sections of IN718 PBF-LB/M witness and extracted samples in XZ-plane (top) and in XY-plane (bottom)

The µCT scans of PBF-LB/M IN738LC witness samples are also analyzed (see Figure 33) showing a defect that was not observed for IN718: Figure 33b and 3c show cracks (indicated by the red circle and arrows) at the interface between sample and support structures. The µCT-scan in Figure 33d shows a top view of the entire sample length. The cracks between sample and support structures are highlighted in red.

The cracks are attributed to IN738LC welding difficulties, discussed in Chapter 2. Hot cracking occurs during solidification providing initiation sites for cold cracking due to residual stresses. The residual stresses tend to increase near sudden geometric changes similar to the transition line between straight support structures and curved cylindrical samples.

Prior to further testing the support structure must be removed in any case and the samples must be machined to the final sample geometry for mechanical testing. This step allows for the removal of all cracks as can be seen in Figure 33e. Thus, for the final samples used for mechanical testing, no cracks remain.

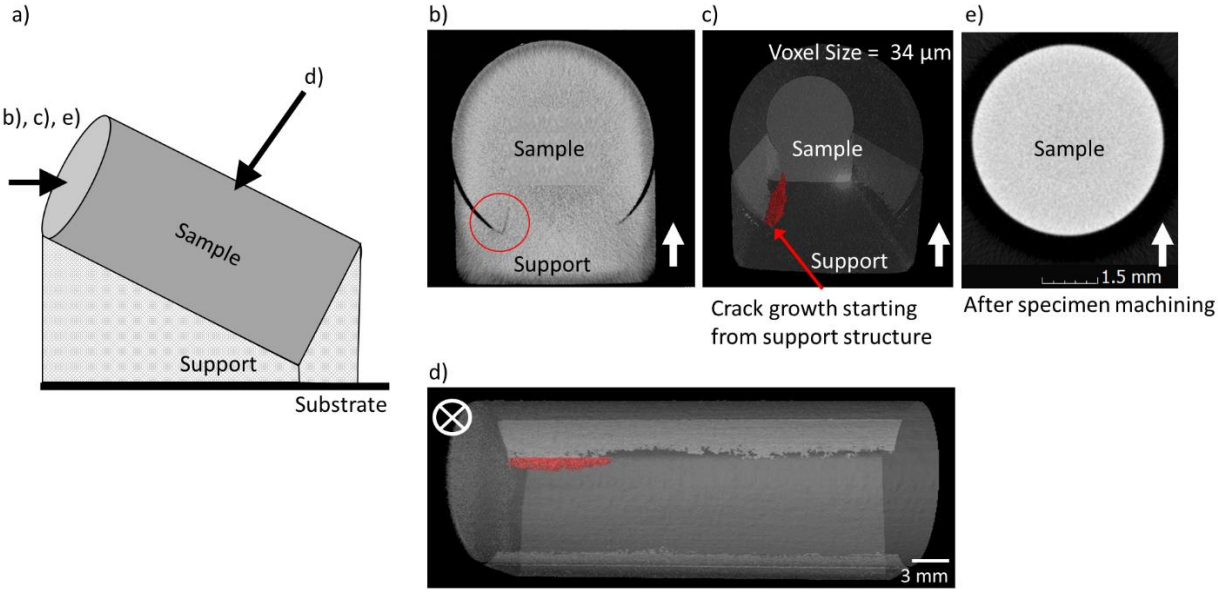

Figure 33 µCT Scans of a 45° IN738LC PBF-LB/M sample: a) Schematic to show where scans were taken; b&c) Scan at the front of sample showing delamination and a crack between sample and supports; d) Scan of sample length; e) Scan showing sample after specimen machining

Representative cross-sections of the HIP and heat-treated samples confirm the absence of cracks from samples to be used in mechanical characterization (see Figure 34). As can be seen from the images, little to no defects are visible. A relative density of 99.98% was determined for both witness and extracted samples. Similar relative densities were reported in literature [8,57,67,98,192].

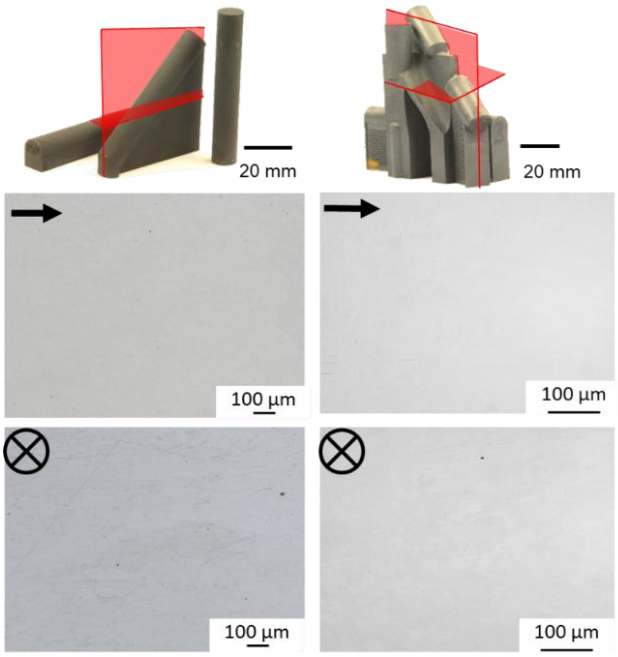

Figure 34 Light microscopic analysis for extracted and witness samples: parallel to build direction (top) and perpendicular to build direction (bottom)

It can be concluded that both IN718 and IN738LC samples are free of significant defects that might affect the accuracy of subsequent characterization and analysis.

5.2 Thermal History

As mentioned in the introduction, the behavior of PBF-LB/M components cannot be explained without considering the manufacturing conditions and especially the thermal history of the printed parts. A cartesian computational grid is developed to represent the substrate plate, the SEC, the witness samples as well as the support structures used for all printed test geometries (see Figure 35). The XY-planes are resolved using 170 x 170 cells, in the Z-direction 5 cells are used to represent the substrate plate thickness and 68 cells are distributed over the maximum height of the geometries (for the 90° witness sample including support structure below it = 79 mm). A total of 2,080,000 cells are thus used to represent the geometry of all samples involved in the PBF-LB/M manufacturing process.

The used layer thickness for IN718 is 30 µm. One hundred layers are combined (lumped) to create a numerical layer corresponding to a printed height of 3 mm. Each numerical layer (lump) is numerically activated by applying 100 x 62 J/mm^3 (i.e. 6200 J/mm^3) for a duration corresponding to the time required for the laser to process all 100 layers. After concluding the scan duration, the application of thermal energy is stopped for a duration corresponding to the recoating time (100 x 10 s). The next lumped layer is then activated and so on.

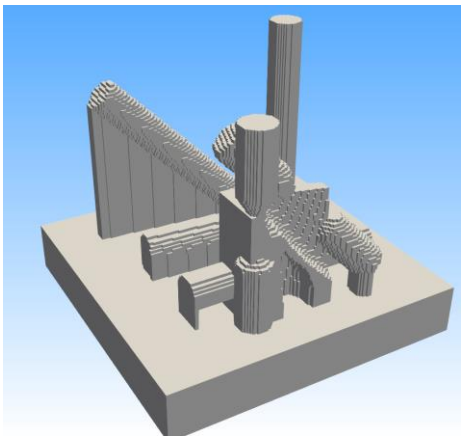

Figure 35 A cartesian mesh is used to represent the substrate plate, the SEC and the witness samples. A total of 2,080,000 cells is used

The thermal boundary conditions are adopted from literature [134], where it is assumed that the substrate plate is connected to a very large metallic volume hence retaining the bottom face of the substrate plate at a constant temperature of 300 K (≈ 25 °C). The substrate plate sides lose thermal energy via convection to the surrounding environment. The heat transfer coefficient is 10 W/mK. The printed samples lose heat energy to the surrounding powder at 5 W/mK. The upper surface of the active layer loses energy via radiation to the surroundings. The emissivity is assumed to be 0.5.

Figure 36 shows the PBF-LB/M temperature evolution of the IN718 witness samples and the SEC. It is important to note that the grid resolution is not fine enough to resolve the melt pool. The temperatures shown are averaged across each computation cell. The temperature scale was adjusted to make the differences in temperatures clearer. Temperatures exceeding 1000 K are also shown in red (boundary condition for max. temperature was set at 3200 K).

Activated layers near the substrate plate do not exhibit high temperatures since they cool down relatively quickly due to their proximity to the substrate plate. As the PBF-LB/M process progresses, the activated layers show higher temperatures, and the manufactured samples cool down slower compared to the initial stages of the PBF-LB/M process. The temperature distribution within the samples is not uniform, as can be identified for example in supported parts after 5109 s and 7059 s. At 5109 s and 7059 s, the supported regions of the SEC show higher temperatures as compared to SEC regions that are directly connected to the substrate plate and as compared to the witness samples.

Manufacturing of the 0° witness sample concluded after about 8000 s. The laser no longer processes this region allowing the 0° witness sample to cool down while the remaining samples continue to be built. Considering the temperature distribution after 19929 s, the 0°witness sample has reached ambient conditions, while the 45° and 90° samples show the highest temperatures when activated. At the end of the PBF-LB/M process simulation a cool down

period is accounted for, showing that the 90° sample requires the longest to reach ambient conditions.

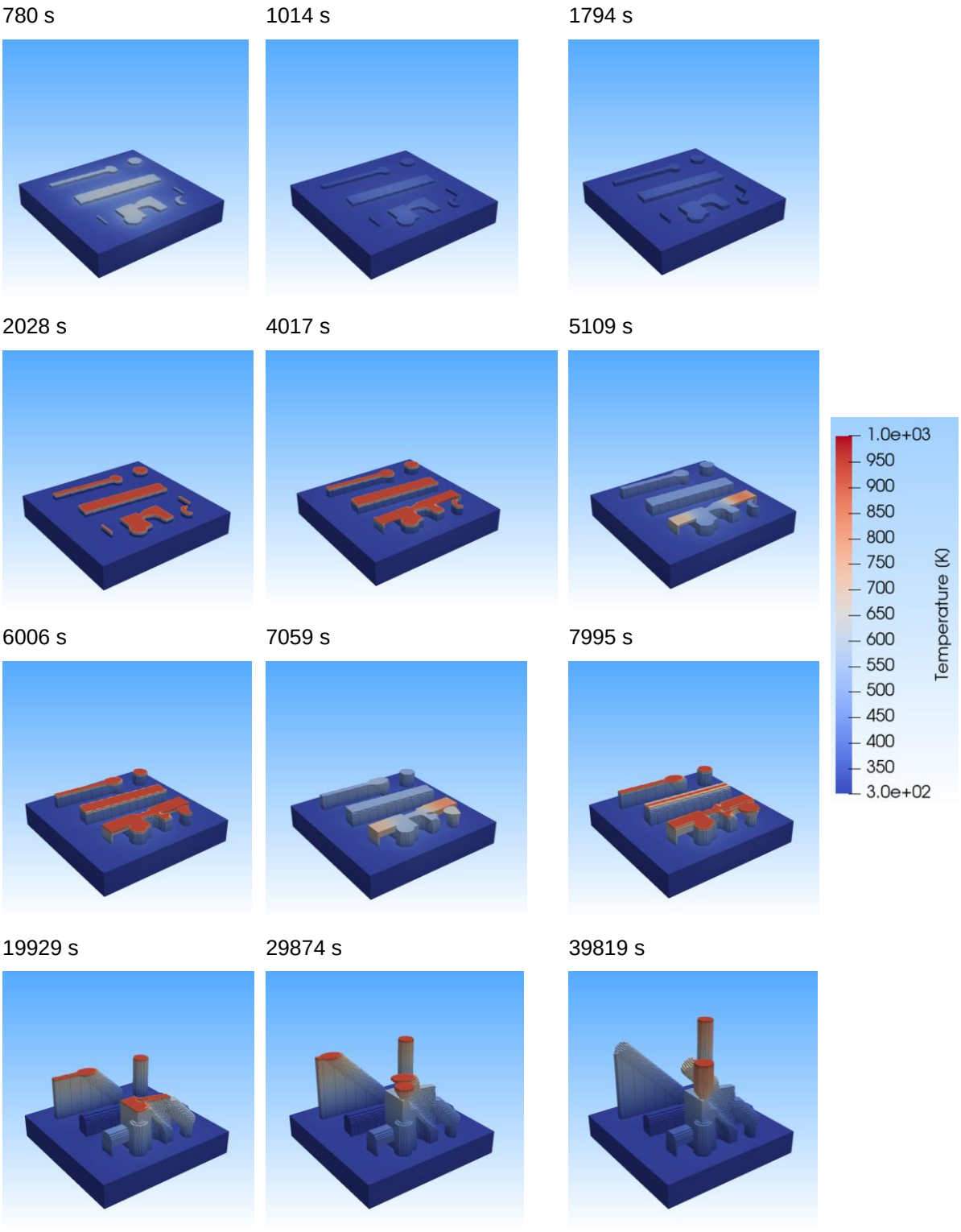

Figure 36 Sequence of images showing the temperature distribution throughout the PBF-LB/M IN718 printed parts and its evolution in time. Images were taken after applying processing energy, except the images at 5109 s and 7059 s to highlight the effect of support structures. The temperature scale was adjusted to make the differences in temperatures clearer. Temperatures exceeding 1000 K are also shown in red.

The thermal history at the center of each of the samples is extracted using monitor points providing information about solidification conditions in the region where the highest stresses and strains are expected during mechanical testing (i.e. during tensile and creep testing). The thermal histories for IN718 and IN738LC witness and extracted samples are shown in Figure 37a and b respectively. The temperatures are extracted for every time step showing how the temperature increases during layer processing and how the temperature decreases during recoating times. The first temperature peak is the highest compared to the subsequent peaks, representing direct energy input into a 100 layer-lump. Once the processing is concluded and recoating starts, the heat diffuses towards the substrate plate. As the activated layer moves upward away from the monitor point the peak temperature decreases until the print job is concluded and the component as a whole begins to cool down.

The temperature evolution at the respective IN718 sample centers is shown in Figure 37a. The first peak reaches over 3200 K (i.e. the nickel boiling temperature). Evaporation is a common phenomenon during PBF-LB/M [193–196]. However due to the short interaction between laser and metal powder, resulting in cooling rates of roughly 10^6 K/s [197], only limited evaporation of alloying elements occurs, which causes the smoke production during the PBF-LB/M process. The first and highest peak is shown when the energy is induced in the layer containing the monitor point. The low thermal conductivity of IN718 does not allow for the heat to readily diffuse towards the heat sink (i.e. substrate plate). The sample therefore retains some heat. Once the next layer lump is applied and the energy is induced, some heat diffuses downwards towards the heat sink past the monitor point, increasing the heat, causing the second peak. The second peak is therefore lower compared to the first. This process continues with the temperature peaks reducing, since the distance to the monitor point increases, reducing the direct energy input to the monitor point.

Figure 37b shows similar temperature trends for the IN738LC witness and extracted samples. The IN718 temperatures are roughly twice as high as those reached by IN738LC, which is attributed to the inferior thermal conductivity of IN718 as compared to that of IN738LC [70,183]. The IN718 thermal conductivity inhibits rapid heat flow towards the heat sink (i.e. substrate plate), the IN718 samples therefore retain more of the heat compared to IN738LC. The IN738LC thermal conductivity is superior compared to IN718 allowing for the heat to diffuse rapidly towards the heat sink, lowering the overall sample temperatures.

a)

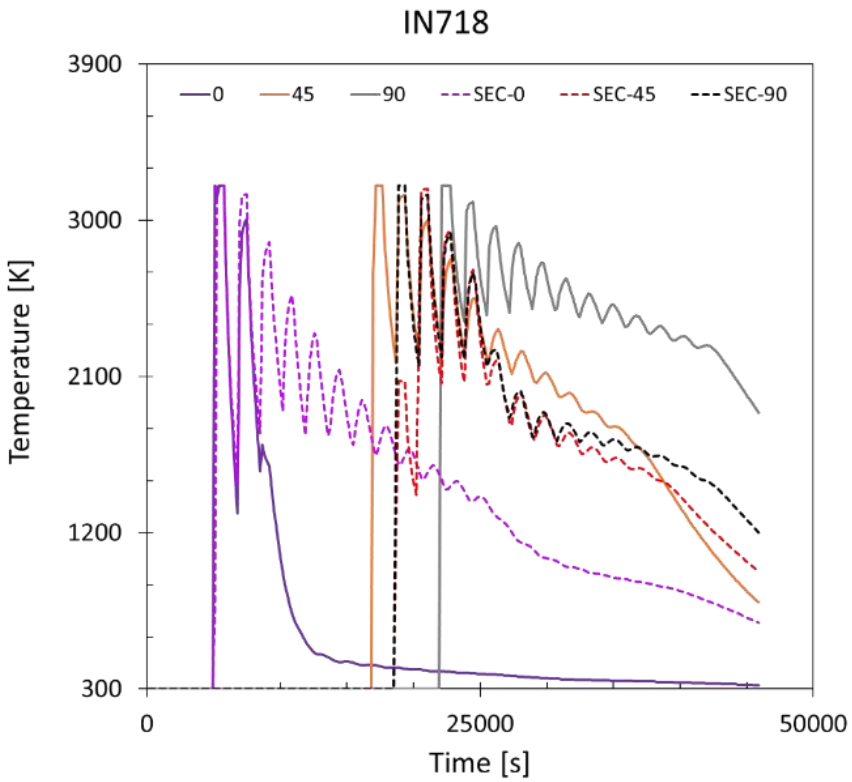

b)

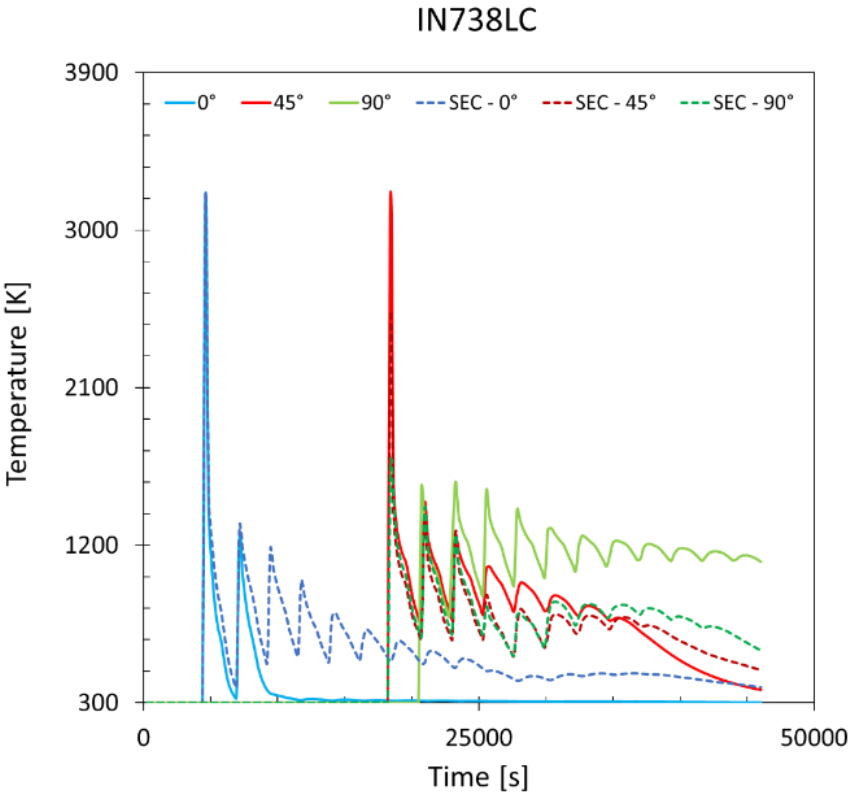

Figure 37 Thermal history at the center of each sample for a) IN718 and b) IN738LC

During the PBF-LB/M process, the cooling rate of individual melt pools within one powder layer is in the order of 10^6 K/s (see Figure 38a). The melt pool cooling rate affects grain size, grain orientation and phase formation. When considering a component, there are multiple layers (and melt pools) to be considered, as shown in Figure 38b. The effective cooling rate is defined

as the temperature gradient between the maximum process temperature and the final process temperature. Besides grain size and phase formation the effective cooling rate also affects mechanical properties.

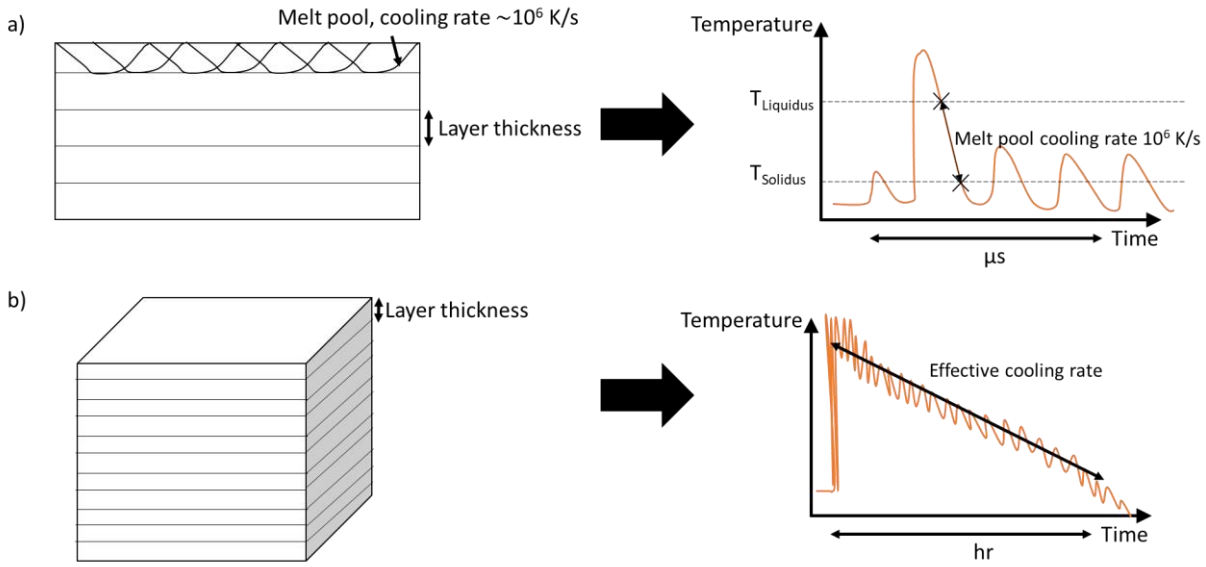

Figure 38 Melt pool cooling rate (a) vs. effective cooling rate (b)

The effective cooling rates extracted from Figure 37 are shown in Figure 39. The IN718 effective cooling rates (see Figure 39a) are slower compared to those experienced by the IN738LC samples (see Figure 39b).

The effective cooling rates of the SEC and the 0° witness samples are significantly higher compared to the 45° and 90° witness samples for both Ni superalloys.

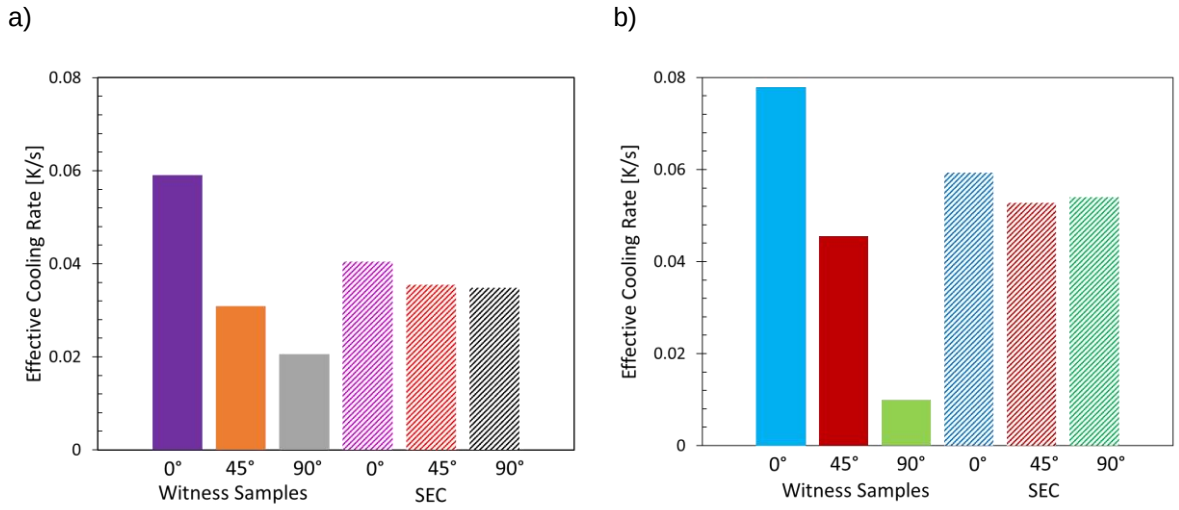

Figure 39 Effective ccoling rates for witness and extracted samples for a) IN718 and b) IN738LC

Regarding the thermal history of witness samples, the 90° build orientation retains considerably higher temperatures throughout the PBF-LB/M process compared to the 0° and 45° samples (see Figure 37 for both IN718 and IN738LC). This can be explained by the

samples' height, where the upper layers of the 90° samples are farthest away from the substrate plate and thus experiencing a higher thermal resistivity to dissipate the heat to the substrate plate. Consequently, the effective cooling rate of the 90° witness samples is the lowest of all samples.

The 45° witness samples are similar in height as the 90° samples, but they are built on a block support structure with an interface area of 270 mm^2 to the substrate plate, which is much larger than the 133 mm^2 for the 90° sample. The heat diffusion for the 45° sample is thus larger allowing the inclined samples to cool down faster.

The 0° witness sample is the shortest sample. It is built on a block support with an interface area of 1500 mm^2. The short processing duration and the large interface area lead to the highest effective cooling rate among all samples.

Considering the 90° sample extracted from the SEC, it can be seen that the effective cooling rate is much higher than those of the 90° witness samples. The difference stems from the significantly different component volume and the difference in interface area between the part and the substrate plate, which is the main heat sink. The interface area of the 90° witness sample is 133 mm^2. The SEC interface area is 663 mm^2 and is approximately 5 times larger than that of the 90° witness samples allowing for the dissipation of larger amounts of energy in shorter periods of time.

The thermal history of the SEC demonstrates the challenges encountered during the production planning stage of complex PBF-LB/M components. Supported structures cause non-uniform thermal conditions, as seen for example in Figure 36. Further thermal inhomogeneities are caused by changes in cross-section, overhangs, and corresponding shapes of the interface area to the substrate plate. The interfacial area of the SEC to the substrate plate being 663 mm^2 allows for a higher effective cooling rate compared to the 90° and 45° witness samples. The 0° sample integrated within the SEC however shows a slower cooling rate as compared to the 0° witness sample, because it is built on a thin support structure prohibiting heat dissipation to the substrate plate (see for example Figure 36 at 7069 s).

It can be summarized that the thermal history is a complex characteristic of the PBF-LB/M process. It is affected by process parameters, geometric details and alloy properties. Due to the large geometric differences between witness samples and the SEC, large differences in temperature levels and effective cooling rates are predicted.

5.2.1 Correlation between Effective Cooling Rate and Residual Stresses

Using XRD, the residual stresses are measured on the surface of the sample centers. The residual stresses are shown in Figure 40a and b for IN718 and IN738LC respectively. All three orientations of the witness and extracted samples are compared for each of the studied alloys. The results parallel to build direction (indicated by the arrow) and perpendicular to the build direction (indicated by the x) are shown. Positive values indicate tensile stresses, negative values are compressive stresses. The standard deviation was calculated based on the three measurements taken for each plane.

Due to the uncertainty of the measurement the residual stress results should be viewed as trends rather than considering the absolute shown values.

When considering the residual stresses shown in Figure 40, it is noticeable that the IN718 samples show more tensile stresses compared to the IN738LC samples, which show mostly compressive stresses. This can be attributed to the X-ray penetration depth of IN718 and IN738LC. In general, for PBF-LB/M samples, tensile stresses are expected at the surface of PBF-LB/M samples, while compressive stresses are expected within the volume of the sample [198]. The penetration depth of IN718 is limited [198] compared to that of IN738LC [199], due to the difference in chemical composition. The residual stress results in IN718 are from the sample surface, whereas the IN738LC results are from the volume of the samples.

While the residual stresses in IN718 (see Figure 40a) are scattered, the IN738LC residual stresses (see Figure 40b) of extracted samples are higher compared to witness samples. The faster effective cooling rates experienced by the extracted samples does not allow for residual stress dissolution. The residual stresses in extracted samples are thus higher and can even reach the tensile regime. In comparison, the witness samples (90° and 45°) are exposed to an in-situ heat treatment, which reduces residual stresses partially.

Note that the same standard heat treatments (e.g. AMS5663 for IN718) were carried out for witness and extracted samples for the respective Ni superalloys. Since the process specific effective cooling rates are still affecting the residual stress magnitudes, it can be concluded that the as-built differences are not entirely eliminated by standard heat treatments – a PBF-LB/M specific heat treatment is required to eliminate process specific differences.

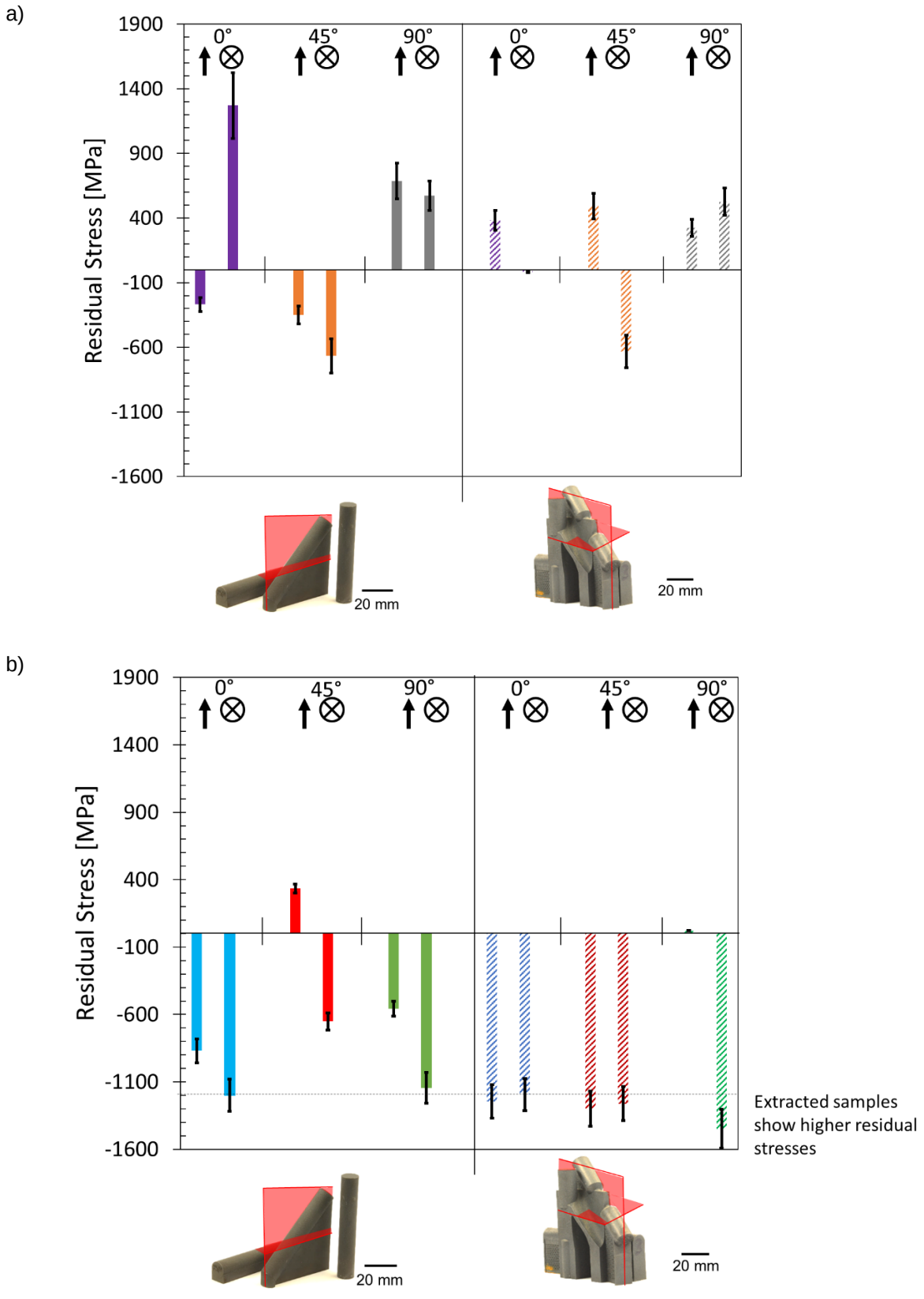

Figure 40 Residual stresses in a) IN718 and b) IN738LC witness samples and extracted samples parallel and perpendicular to build direction

5.2.1.1 Correlation Evaluation

In order to assess the strength of correlation between numerically predicted cooling rates and measured residual rates, the effective cooling rates are normalized using the value of the 0° witness sample (Figure 41).

As can be seen in Figure 41a, if the IN718 sample shows a dominant residual stress within the tensile regime (positive values, due to limited X-ray penetration depth) the normalized effective cooling rates are above 0.55. Normalized effective cooling rates below 0.55 show dominant compressive stresses.

For IN738LC (see Figure 41b), mostly compressive stresses are measured due to the X-ray penetration depth reaching deeper within the sample volume. Normalized effective cooling rates above 0.6 show average (of both planes) residual stresses above -1000 MPa. Normalized effective cooling rates below 0.6 show average residual stresses below 1000 MPa.

A correlation evaluation is shown in Table 8. The correlation legend was presented in Chapter 3.

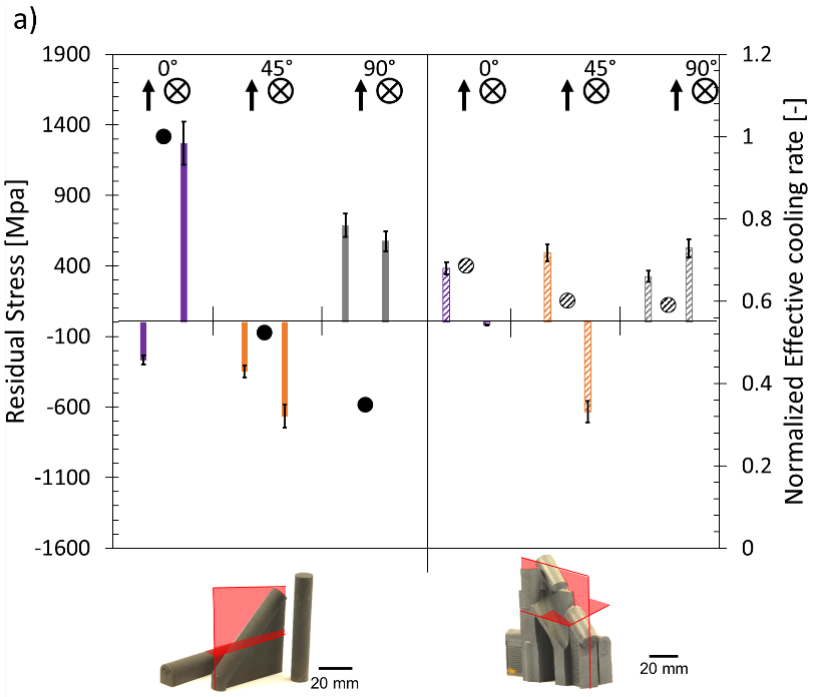

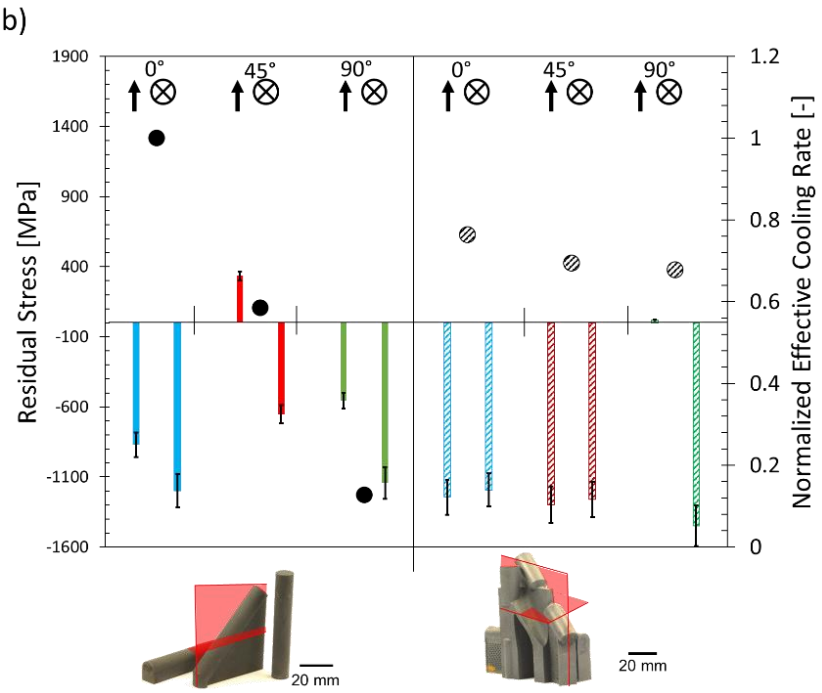

Figure 41 Correlation between residual stresses and normalized effective cooling rate: a) IN718; b) IN738LC. The bars show the residual stresses and the points represent the normalized effective cooling rates

Table 8 Correlation evaluation of residual stresses and normalized effective cooling rates

Factors	Strength of Correlation
Normalized effective cooling rate and residual stress magnitude	0
Normalized effective cooling rate and type of residual stress (tensile or compressive)	+

5.2.2 Correlation between Effective Cooling Rate and Microstructures

5.2.2.1 IN718 Microstructure

The microstructures of witness samples, the generic component and the SEC parallel and perpendicular to the build direction are shown in Figure 42. The grains show no significant differences. The microstructure in build direction (indicated by the arrow) shows oriented grains parallel to Z-direction, while the microstructure perpendicular to the build direction shows circular grain cross-sections.

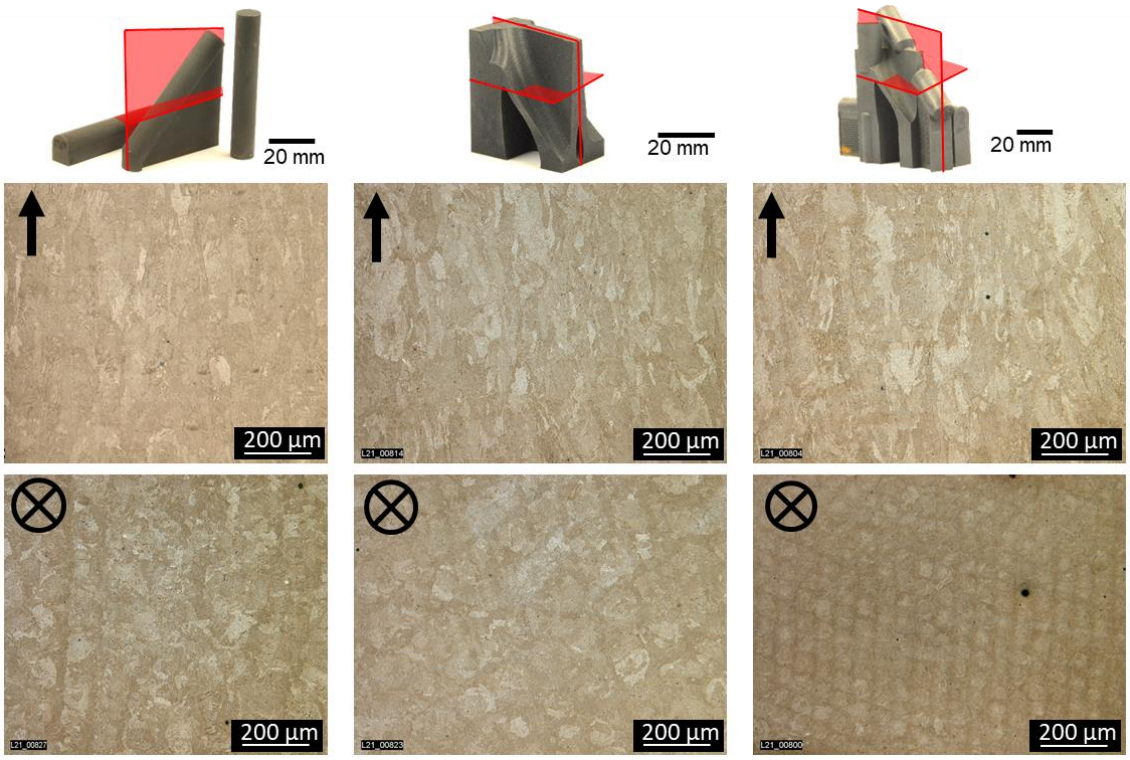

Figure 42 IN718 microstructure for witness samples (left), the generic component (middle) and SEC (right) parallel (top) and perpendicular (bottom) to build direction

As mentioned in the introduction, the microstructure of IN718 consists mostly of the fcc matrix γ and the strengthening fcc phases γ' and γ''. The decomposition of the metastable γ''-phase into the thermodynamically stable δ-phase depends on the process parameters used and the heat treatment applied.

Scheil-Gulliver CALPHAD calculations represent non-equilibrium solidification conditions predicting phases in as-built condition (see Figure 43). Both Scheil-Gulliver and equilibrium solidification curves are displayed for comparison. The δ-phase is predicted for non-equilibrium conditions as well as several detrimental TCP phases towards the end of the solidification process.

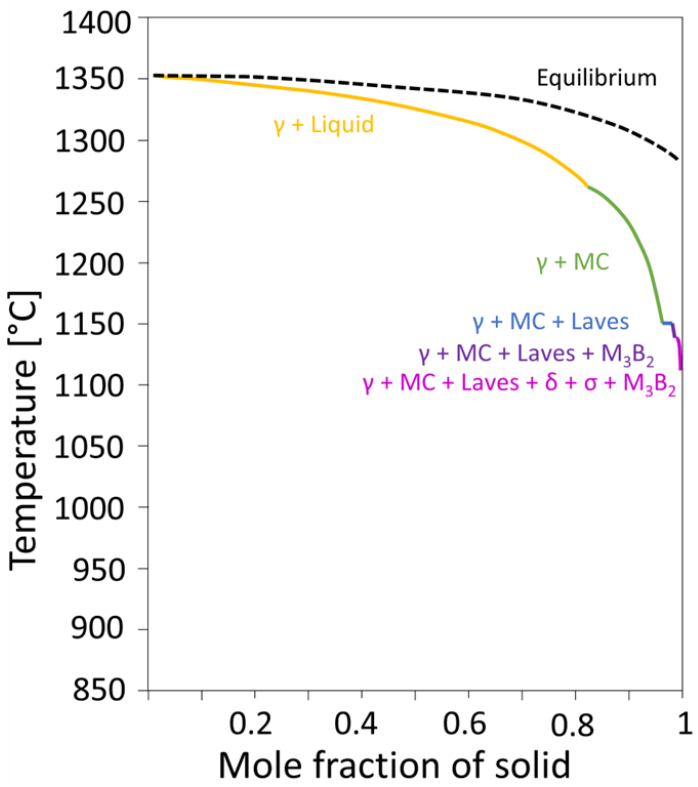

Figure 43 Scheil-Gulliver phase diagram for IN718 using TCNI8 database

To assess the effect of solidification conditions on phase formation beyond CALPHAD predictions (see Figure 43), XRD measurements were undertaken for witness and extracted samples. As can clearly be identified, the 90° and 45° witness samples show an additional Mo peak. Mo is contained in the σ-phase [200] as well as in carbides, which are both predicted in the Scheil-Gulliver phase diagram (see Figure 43). The extracted samples and the 0° witness sample (i.e. the samples, that experience a faster effective cooling rate) do not show peaks for refractory metals. Since refractory metals have relatively large atomic radii, their movement requires temperature and time. The in-situ heat treatment of the 90° and 45° witness samples allows for refractory metal movement due to the comparable slow effective cooling rate. Phase development therefore differs between witness and extracted samples. It is assumed that the in-situ heat treatment leads to continuous phase evolution towards equilibrium conditions in witness samples (90° and 45°).

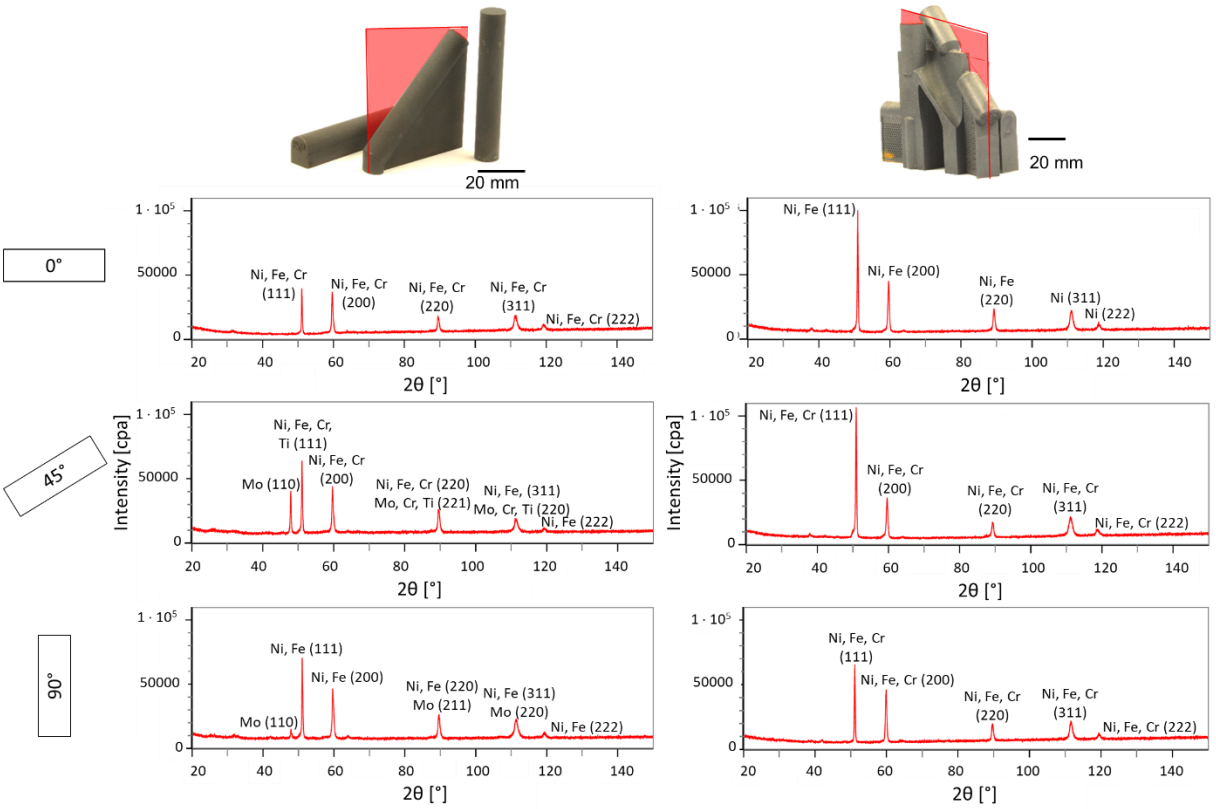

Figure 44 XRD phase identification for IN718 witness and extracted samples in XZ-plane

Figure 45 shows representative microstructures of IN718. In Figure 45, the δ-phase can be identified due to its size and shape. It is embedded in the γ-phase. The γ''-phase forms at a smaller scale (nanometers) and is thus not readily visible at the shown resolution.

As can be seen in Figure 45 for all build orientations, acquired at a resolution of 1 μm, the precipitated δ-phase is finer and differently shaped in the extracted samples compared to the witness samples. In the 0° witness sample, the δ-phase is located as needle-like precipitates along the grain boundaries. While the δ-phase forms a continuous film along the grain boundaries in the witness samples (45° and 90°), the needle-like δ-phase is homogeneously distributed in the extracted samples (all build orientations). This is attributed to the faster effective cooling rates predicted for the extracted samples (see Figure 39). The faster effective cooling rates in the extracted samples do not allow sufficient time for the δ-phase to coarsen and diffuse towards grain boundaries. Even though all build orientations of the extracted samples show these needle-shaped δ-phase, the thickness of the needles decreases from 0° to 45° to 90°, meaning that the 90° sample shows the thinnest needle-shaped δ-phase.

The faster effective cooling rates in the extracted samples are also the reason for the difference in average grain sizes, shown in Figure 46. The extracted samples show grain sizes, which are up to one half of those found in witness samples.

Considering the individual thermal histories of the respective build orientations (see Figure 37) and the average grain sizes (shown in Figure 46), the 90° witness sample experiences the slowest effective cooling rate. Therefore, the grain size measured is the largest compared to all other samples.

Considering the extracted samples, the 90° and 45° samples show similar effective cooling rates, which lead to similar grain sizes. The 0° samples (witness and extracted) showed the fastest effective cooling rates, leading to the smallest grain sizes for the respective sample conditions.

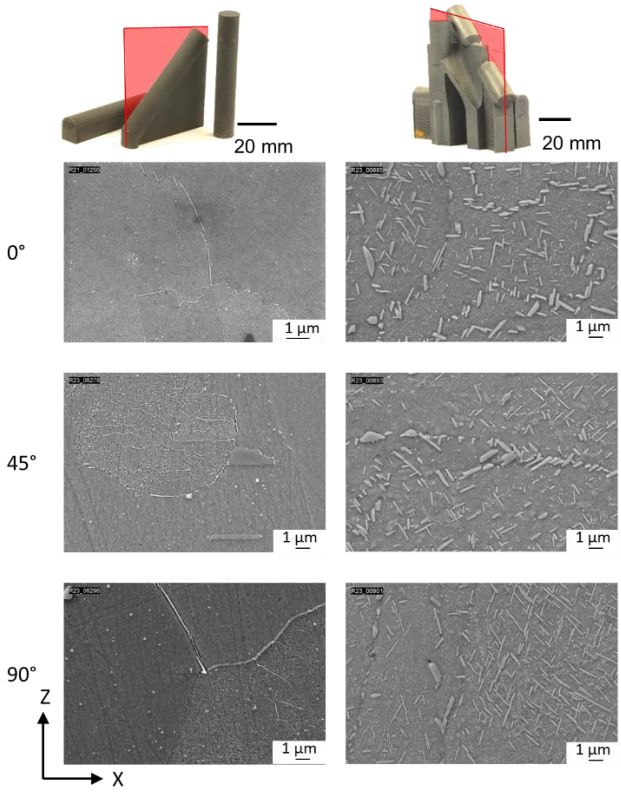

Figure 45 SEM images of the witness samples and extracted samples microstructre for all build orientations (0°, 45°, 90°)

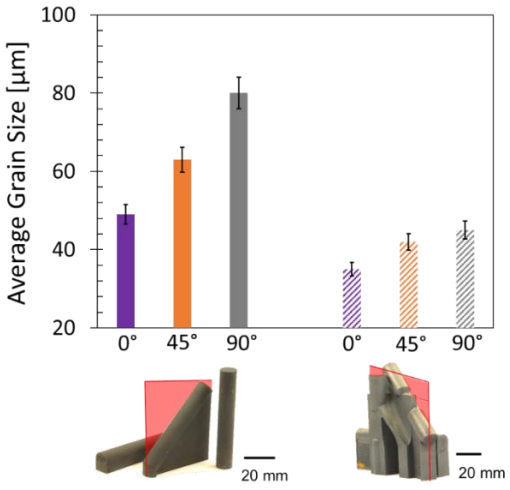

Figure 46 IN718 grain sizes for witness samples and extracted samples in all build orientations (0°, 45° and 90°)

The difference in average grain sizes is also clearly visible when comparing the EBSD scans for the witness and extracted samples (see Figure 47). Whereas the melt pool boundaries are still clearly visible with no dominant grain orientation in the extracted samples, the grains in the witness samples are pronounced and show a favorable grain orientation combination of [111] and [101].

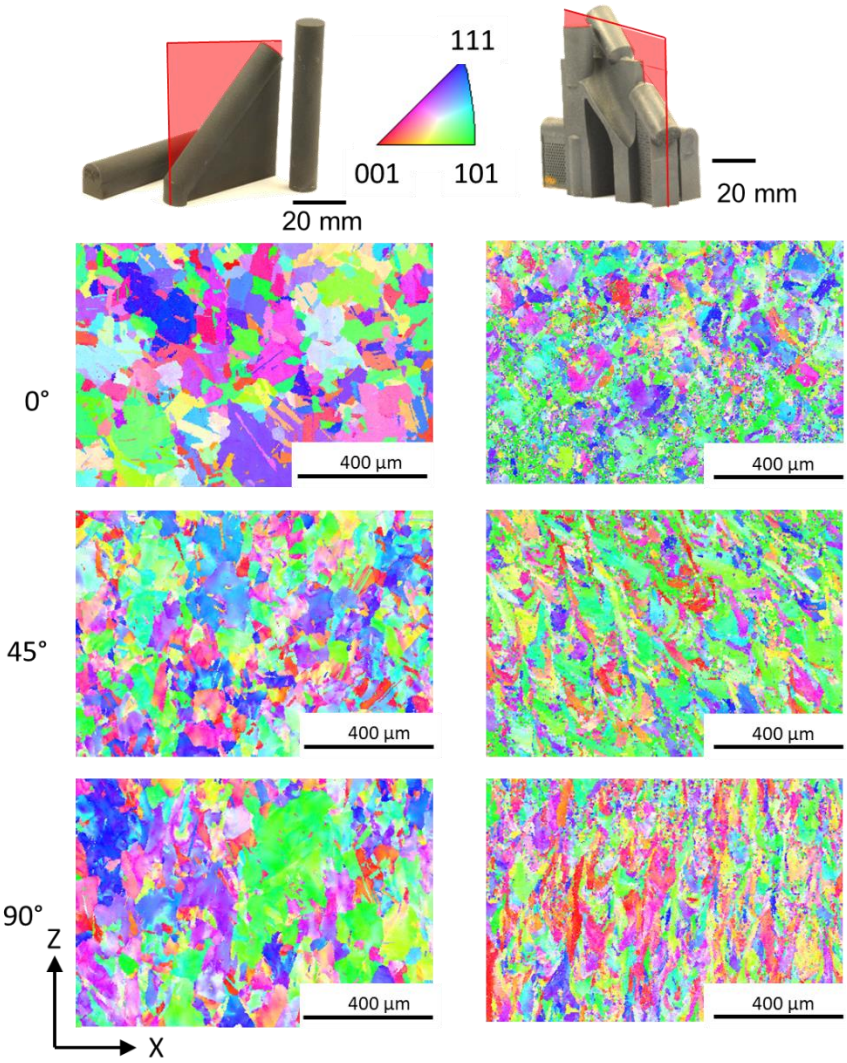

Figure 47 IN718 EBSD analysis (IPF-Z) of the witness samples and extracted samples microstructre for all build orientations (0°, 45°, 90°)

Correlation Evaluation

It was seen that microstructural differences exist between witness and extracted samples, as predicted based on the numerical results. The extracted samples show needle-like δ-phase evenly distributed within the microstructure, whereas the 45° and 90° witness samples show a continuous δ-phase film along the grain boundaries. The 0° witness sample showed a needle-like δ-phase shape concentrating at the grain boundaries. The faster effective cooling rates of the 0° witness samples and all extracted samples therefore lead to the needle-like shape as

compared to the continuous film seen in witness samples (45° and 90°) exposed to slower effective cooling rates. This strong correlation is documented in Table 9.

Further, the correlation between average grain size and normalized effective cooling rate is evaluated in Figure 48. As can be seen slower effective cooling rates lead to larger average grain sizes. However, the 0° witness sample experienced the fastest effective cooling rate among all samples (witness and extracted) but doesn't show the smallest grain size. This discrepancy requires further analysis. The effect of the subsequent heat treatment leading to grain coarsening with a greater effect on the 0° build orientation than 45° and 90° witness samples should be analyzed. The difference in phase formation between the witness samples might lead to a different degree of grain coarsening. This identified correlation is documented in Table 9.

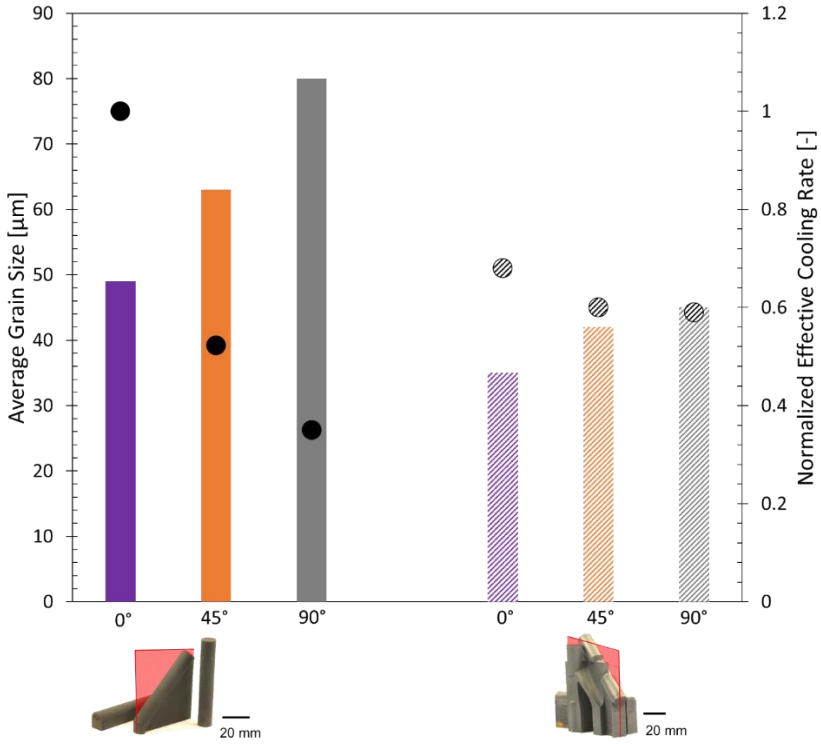

Figure 48 Correlation IN718 grain size and normalized effective cooling rate

Table 9 Correlation evaluation of IN718 microstructure and normalized effective cooling rates

Factors	Strength of Correlation
Normalized effective cooling rate and phase formation	++
Normalized effective cooling rate and grain size	+

5.2.2.2 IN738LC Microstructure

The IN738LC microstructure of witness and extracted samples is shown in Figure 49. Similar to IN718, grains oriented parallel to build direction can be seen. This is due to the layer wise build-up of components during the PBF-LB/M process, causing grains to grow in the direction of the thermal gradient [66]. Perpendicular to build direction, the grain cross-sections are circular in shape. Twins can be seen parallel and perpendicular to build direction in both witness and extracted samples.

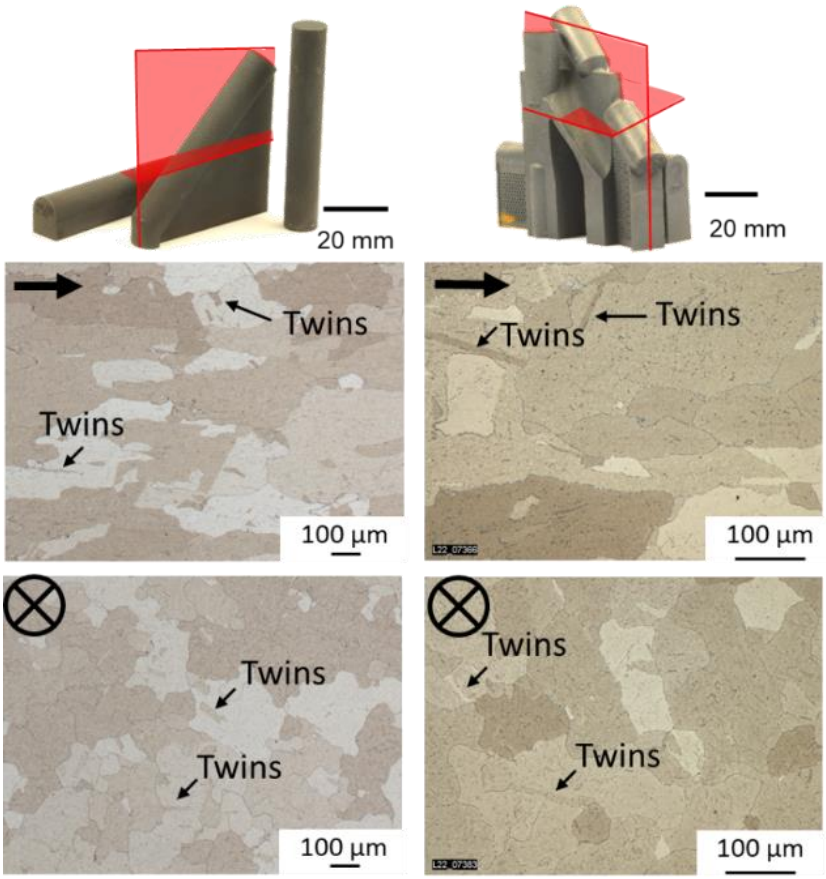

Figure 49 IN738LC microstructural analysis for witness and extracted samples: Parallel to build direction (top) and perpendicular to build direction (bottom)

The Scheil-Gulliver phase diagram for IN738LC is shown in Figure 50. The dashed curve shows equilibrium solidification conditions for comparison. The solidification range under equilibrium conditions is approximately 130 °C. Therefore, the equilibrium solidification range is much smaller than that of non-equilibrium solidification. Towards the end of solidification, phases such as σ- and Laves-phases become visible under Scheil-Gulliver conditions. These types of phases segregate to grain boundaries embrittling and pinning them down and thereby increasing strength but reducing ductility by potentially acting as crack initiation sites. These types of phases also have low melting temperatures increasing the risk of liquation cracking (the definition of liquation cracking can be found in Appendix E).

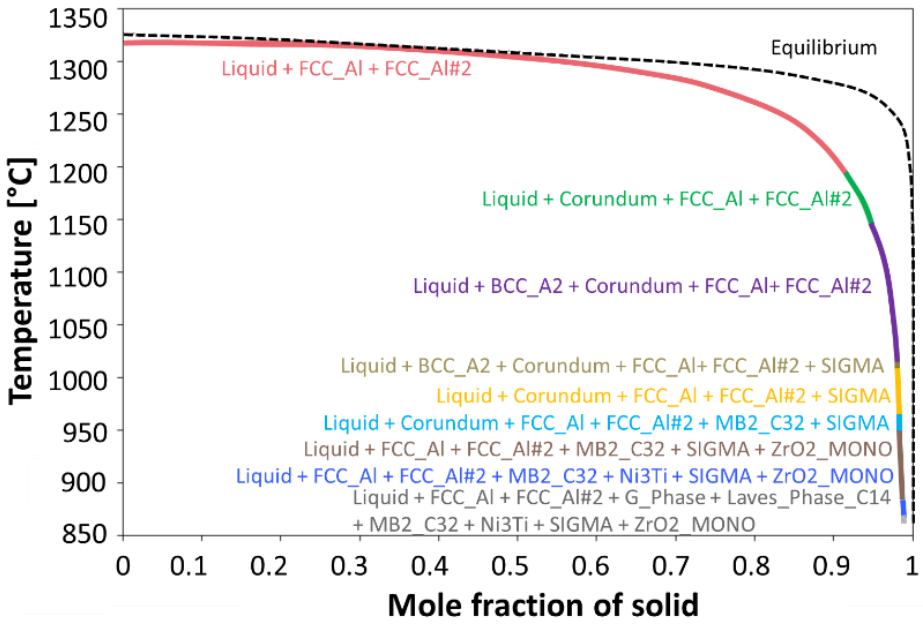

Figure 50 Scheil-Gulliver phase diagram for IN738LC using TCNi8 database

The phases formed during equilibrium and non-equilibrium solidification are compared in Table 10. Segregating phases such as oxides, Laves- and TCP phases, formed due to inhomogeneously distributed alloying elements, are found under non-equilibrium (Scheil-Gulliver) solidification conditions only. For equilibrium conditions, $M_{23}C_6$ carbides form with a strong embrittling effect.

Table 10 Predicted phases for IN738LC Scheil-Gulliver and equilibrium solidification

Scheil-Gulliver	Equilibrium
Liquid	Liquid
FCC_AL	MC
FCC _AL #2	FCC
Corundum	L_{12}_FCC
BCC_A2	M_7C_3
SIGMA	$M_{23}C_6$
MB_2_C_{32}	MB_2
ZrO_2_MONO	
Ni_3Ti	
G-Phase	
Laves_Phase_C_{14}	

XRD measurements were taken to assess the effect of solidification conditions on phase formation. Similar to IN718, the witness samples show an additional refractory metal peak. In the case of IN738LC this peak corresponds to Nb. Similar to Mo (found in IN718), Nb is a carbide former and is contained within the σ-phase. Phase development therefore differs between witness and extracted samples in both Ni superalloys.

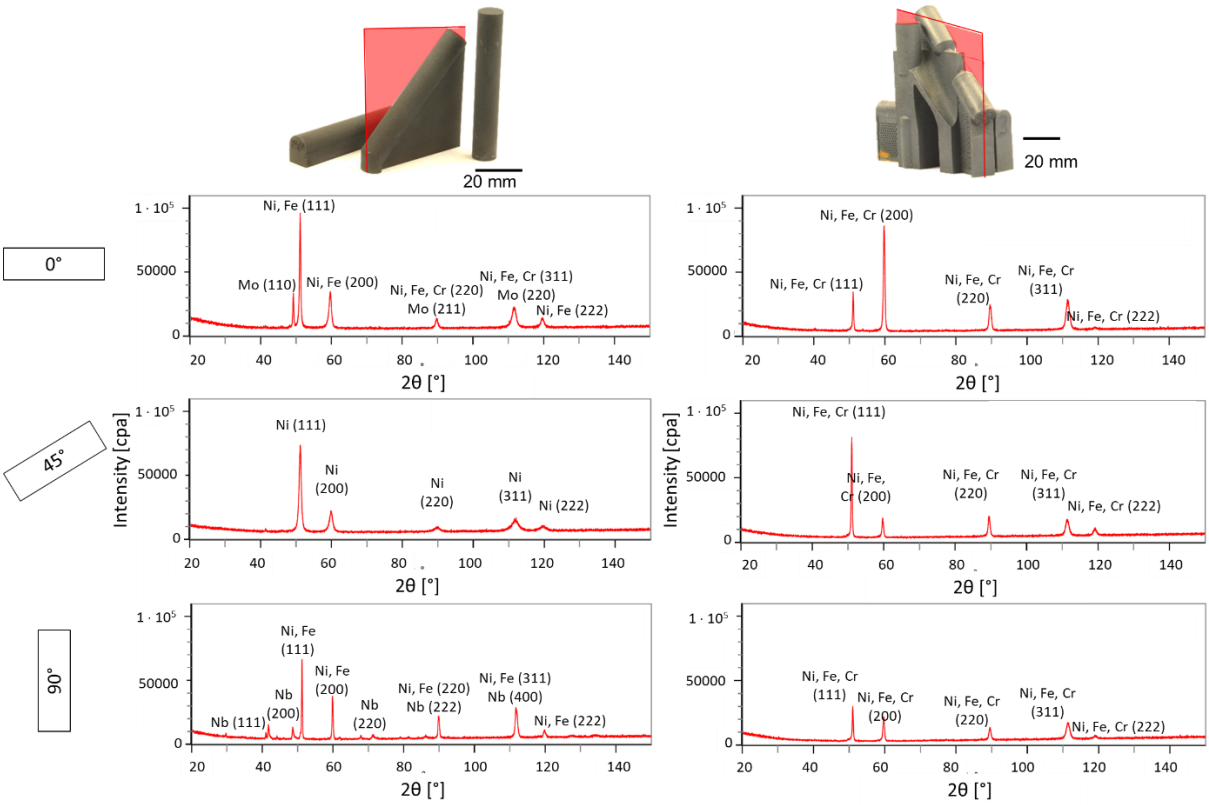

Figure 51 XRD phase identification for IN738LC witness and extracted samples in XZ-plane

Figure 52 shows representative microstructures of IN738LC and Figure 53 shows images at a higher resolution of 1 µm. As can be seen, the microstructures for all build orientations significantly differ between witness and extracted samples. While the microstructure for extracted samples is more refined compared to witness samples, the extracted samples do not show any carbides.

On the other hand, witness samples show a significant amount of carbides accumulating at grain boundaries.

The shape of the γ'-phase also differs between extracted and witness samples. The shape of the γ'-phase dictates the strengthening effect and is usually controlled by heat treatment. Figure 53 shows enlarged microstructural images for witness and extracted samples. Nano-scale precipitates and TCP-phases (indicated by the red arrows) can be identified in the extracted samples. Similar to the IN718 microstructure discussed above, the IN738LC thermal histories (refer to Figure 37b and Figure 39b) can be used to explain the difference in precipitation behavior. The faster effective cooling rate of the extracted samples does not allow sufficient time for precipitates to form and concentrate at the grain boundaries as in the case of witness samples. In the detailed microstructure images shown in Figure 53, nano-scale precipitates are observed in the extracted samples. The small size is attributed to the limited precipitation time available during SEC solidification.

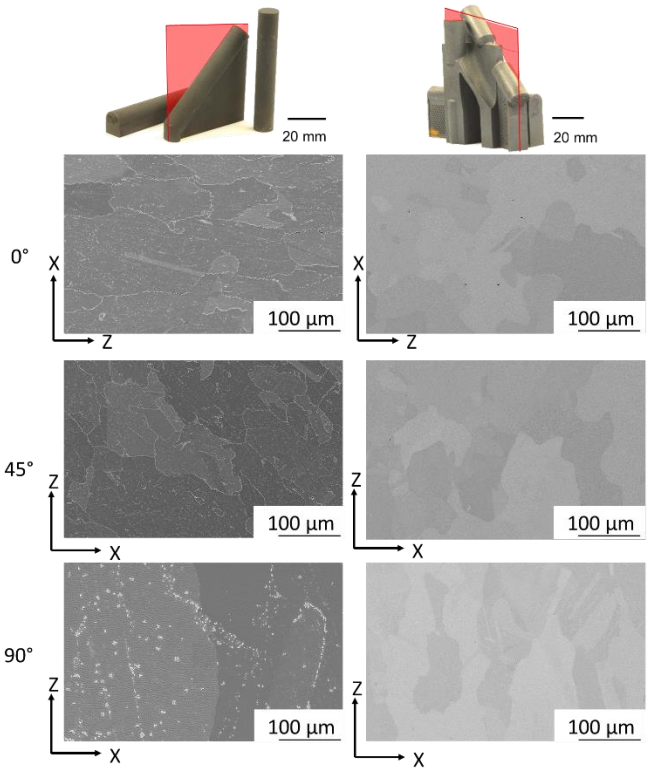

Figure 52 SEM images of IN738LC microstructure for witness and extracted samples for all build orientations (0°, 45°, 90°)

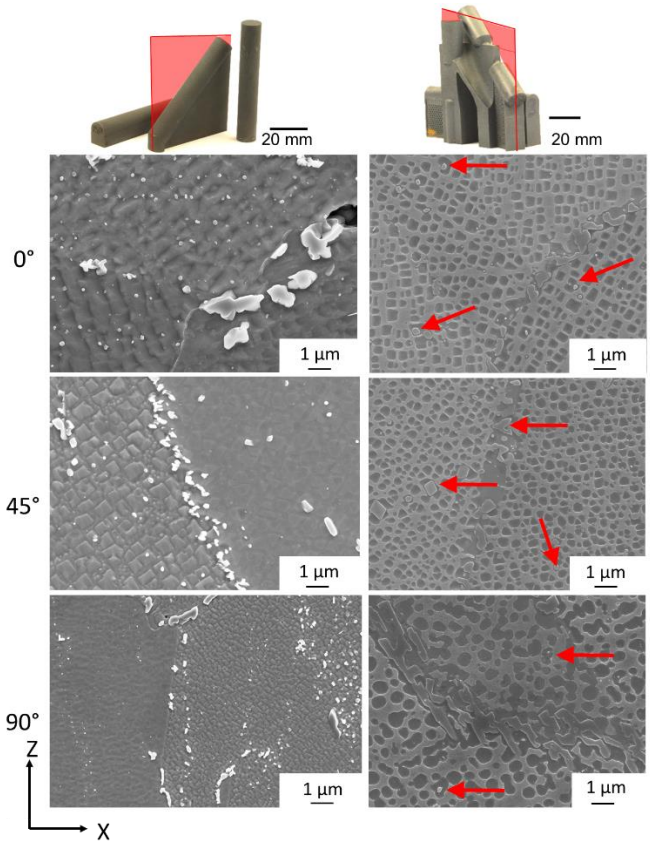

Figure 53 Detailed SEM images of IN738LC microstructure for witness and extracted samples for all build orientations (0°, 45°, 90°). The red arrows point at precipitations and TCP-phases

Similar to IN718, the average grain sizes of IN738LC extracted samples are smaller compared to witness samples (Figure 54). The difference in IN738LC grain size is up to 37.5%.

The standard deviation measured in the grain sizes for all IN738LC witness samples overlap, meaning that the differences are not substantial, and that further testing is necessary. For the extracted samples, the 45° and 90° thermal histories are similar leading to similar grain sizes.

Similar to IN718, the heat treatment does not eliminate process specific effects on microstructure.

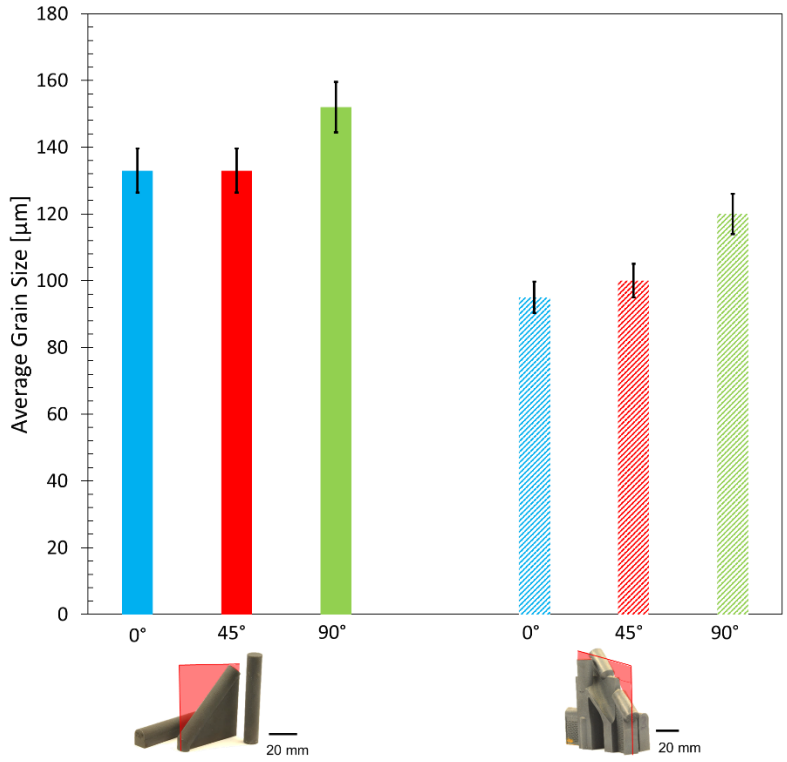

Figure 54 IN738LC average grain sizes for extracted and witness samples in 0°, 45° and 90° build orientation

Correlation Evaluation

Different phases, phase shapes and sizes formed during solidification in IN738LC witness and extracted samples. While witness samples show carbides at the grain boundaries, the extracted samples do not show carbide formation, but nano-scale TCP-phases.

Carbide formation requires time for the carbon to diffuse towards grain boundaries. This correlates well with the lower effective cooling rates of the 45° and 90° witness samples. The 0° witness sample does not show a continuous film of carbides along the grain boundaries. It does however show limited carbide formation along grain boundaries. Nano-scale TCP-phases form with fast cooling [201], which correlates well with the faster effective cooling rates of the extracted samples. Even though the 0° witness samples show a faster normalized effective

cooling rate, no TCP-phases can be identified. The strength of the correlation between effective cooling rate and phase formation is shown in Table 11.

Similar to IN718, the correlation between average grain size and normalized effective cooling rate is evaluated in Figure 55. Slower effective cooling rates lead to larger average grain sizes. As is the case as IN718, the 0° witness sample experienced the fastest effective cooling rate among all samples (witness and extracted) but doesn't show the smallest grain size. Again, this discrepancy requires further analysis. This correlation is documented in Table 11.

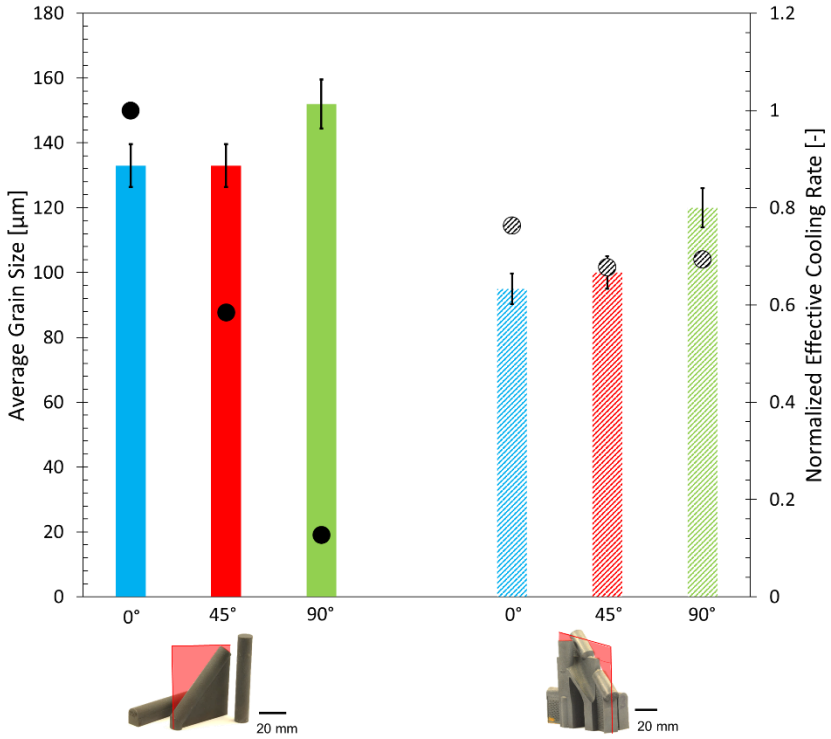

Figure 55 Correlation IN738LC grain size and normalized effective cooling rate

Table 11 Correlation evaluation of IN738LC microstructure and normalized effective cooling rates

Factors	Strength of Correlation
Normalized effective cooling rate and phase formation	+
Normalized effective cooling rate and grain size	+

5.2.3 Critical Assessment of Effective Cooling Rates

The numerical simulation is a simplified model neglecting several phenomena such as shield gas flow, melt pool dynamics and preferential evaporation. The boundary conditions used in this study were not confirmed or validated[6]; they were adopted from the validation study reported by [134]. Also, the use of lumped layers to reduce the computational effort leads to a reduction in resolution and an overall reduction of prediction accuracy. The goal is to obtain quantitative thermal histories to complement experimental results.

Using residual stress measurements and microstructure characterization it has been shown that the numerical results correlate with experimental findings. While there is still further research required (i.e. average grain size 0° witness sample and the respective effective cooling rate), the numerically predicted trends differentiate between manufactured samples and components taking their geometric features, their connection to the substrate plate and process parameters into account.

It can therefore be concluded that while the numerically predicted absolute values may not be quantitatively accurate, they are still sufficient to capture the trends, to explain and to compare different aspects of PBF-LB/M samples.

5.2.4 Analytical Analysis of Thermal Conditions

As seen in the chapters above, the PBF-LB/M thermal conditions significantly affect the microstructure. In order to enable a quicker assessment of the solidification conditions, the build average temperature seems to be a good metric that is worth further investigation. To estimate the average build temperature without numerical models, the conduction equation (Fourier's law) is reformulated as shown below (see Equation 4). Taking the amount of energy supplied by the laser (ΔQ), the build time (Δt), alloy thermal conductivity (λ), the interface area between the sample/component and the substrate plate (A), the sample/component height (H) and the temperature difference between average build temperature and chamber temperature (ΔT), the following equation can be obtained:

[6] Refinement of the boundary conditions would have required detailed manufacturing details, which were not readily available due to proprietary reasons.

$$\frac{\Delta Q}{\Delta t} = \lambda \cdot A \cdot \frac{\Delta T}{H},$$

Using the volume energy density, sample volume and the temperatures defining the temperature difference:

$$\frac{\Delta Q}{\Delta t} = \frac{E_v \cdot V}{\Delta t} \text{ and } \Delta T = T_{ave} - T_{Chamber}$$

Equation 4 Derivation of analytical model using Fourier's Law

The equation can be solved for average build temperature:

$$\frac{E_v \cdot V}{\Delta t} = \lambda \cdot A \cdot \frac{T_{ave} - T_{Chamber}}{H}$$

$$\Rightarrow \quad T_{ave} = \frac{E_v \cdot V \cdot H}{\Delta t \cdot \lambda \cdot A} + T_{Chamber}$$

The geometric values for witness samples, SEC as well as the IN718 and IN738LC properties are listed in Table 12. The calculated average build temperatures for IN718 and IN738LC are shown in Figure 56.

For IN718, the results of the analytical model predict that the 0° witness sample is exposed to the lowest average build temperature. The 45° and 90° witness samples show higher average build temperatures, where the 90° is exposed to the highest temperature. This correlates well with thermal history curves, discussed in Chapter 5.2. The SEC, similar to the 0° witness sample, also experiences relatively cold average build temperatures, but it still higher than the 0° witness sample due to its volume and the larger amount of energy and time required to process the complete volume.

The average build temperature observations of extracted samples are challenging to verify, since the analytical model does not consider the build history for each of the extracted samples separately as in case of the numerical model. However, it can be generally said that the extracted samples are exposed to colder average build temperatures, which would be in agreement with observations discussed above.

Table 12 Variables and input used for the analytical model based on Fourier's Law to determine the average build temperature for IN718 and IN738LC using Equation 4

Variable	Ni superalloy	Abbreviation	Unit	Witness sample			SEC
				0°	45°	90°	
E_V	IN718	E_V	J/m^3	6.20 E+10	6.20 E+10	6.20 E+10	6.20 E+10
E_V	IN738LC	E_V	J/m^3	6.90 E+10	6.90 E+10	6.90 E+10	6.90 E+10
Part volume	Both	V	m^3	3.85 E-05	1.02 E-05	1.87 E-05	1.41 E-05
Part height	Both	H	m	7.60 E-02	7.90 E-02	6.59 E-02	1.60 E-02
Build rate	IN718		m^3/s	4.68 E-09	4.68 E-09	4.68 E-09	4.68 E-09
Build rate	IN738LC		m^3/s	3.24 E-09	3.24 E-09	3.24 E-09	3.24 E-09
Build time	IN718	t	s	8.22 E+03	2.18 E+03	4.01 E+03	3.01 E+03
Build time	IN738LC	t	s	1.19 E+04	3.15 E+03	5.79 E+03	4.34 E+03
Solid thermal conductivity*	IN718	λ	W/mK	9.5	9.5	9.5	9.5
Solid thermal conductivity**	IN738LC	λ	W/mK	19.6	19.6	19.6	19.6
Interface area	Both	A	mm^2	6.63 E-06	2.70 E-06	1.33 E-06	1.50 E-05
Preheating temperature	IN718	$T_{Chamber}$	K	293.15	293.15	293.15	293.15
Preheating temperature	IN738LC	T_{Ch}	K	353.15	353.15	353.15	353.15

*Average calculated using [70]**;** **Average calculated using [183]

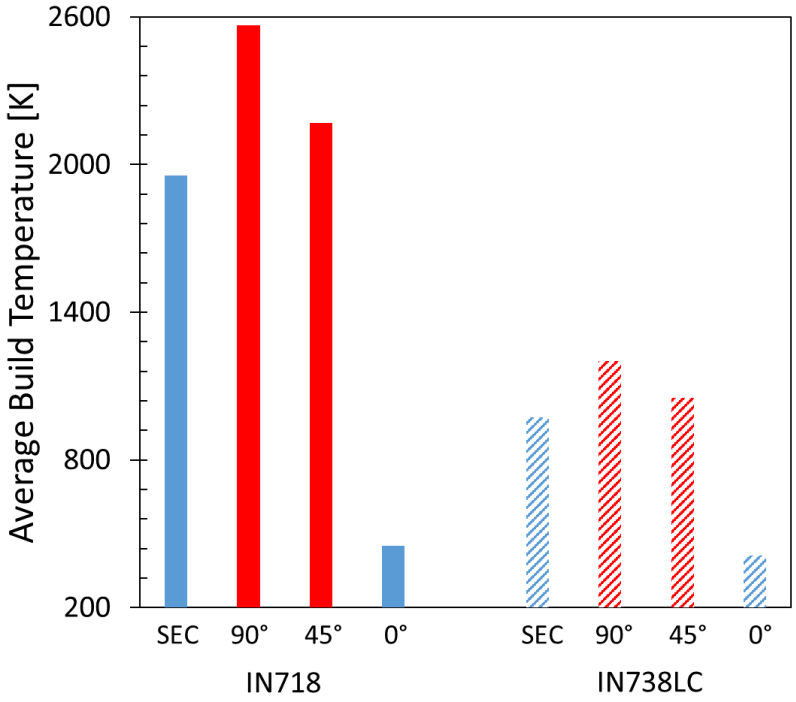

Figure 56 Calculated IN78 and IN738LC average build temperatures for the SEC and all build orientations for the witness samples (0°, 45° and 90°)

For IN738LC, lower average build temperatures compared to IN718 are calculated. Again, the difference in thermal conductivity and the difference in preheating temperatures considered explain this result. The analytically predicted IN738LC average build temperatures follow similar trends as those for IN718. The 0° witness sample and SEC show low average build temperatures, while the 45° and 90° witness samples show hotter average build temperatures.

While the exact temperatures cannot be extracted from the analytical model due to the oversimplification of the complex PBF-LB/M processing conditions, the analytical results seem to provide a quick means to explore thermal trends of the different parts considered.

The analytical model has not been tested for geometries or materials beyond this thesis, it is therefore not verified to be a generally applicable tool. The results presented and the speed of response are however intriguing and might be sufficient justification to explore this simple model further with the goal of establishing a quick and reliable method to compare and assess solidification conditions of different parts.

5.3 Mechanical Properties

5.3.1 Vickers Hardness

The IN718 and IN738LC Vickers hardness values for all witness and extracted samples are shown in Figure 57a and b respectively.

The average hardness of the IN718 SEC is 445 HV and that of the witness samples lies at approximately 424 HV. This is equivalent to an average hardness difference between witness and extracted samples of 5%. This result follows roughly the measured differences in average grain sizes shown in Figure 46. The lower average build temperature and the faster effective cooling rate experienced by the SEC (see Figure 37a) leads to grain refinement and an increase in grain boundary area. Since grain boundaries hinder dislocation movement, the hardness increases [202,203].

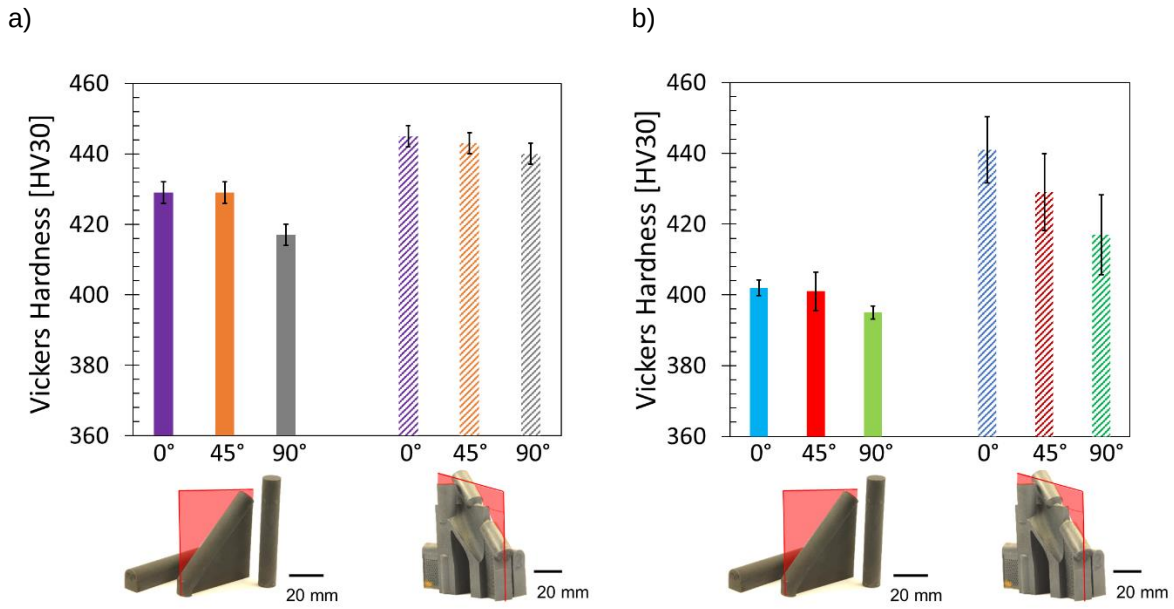

Figure 57 Vickers hardness for a) IN718 and b) IN738LC witness and extracted sample in all build orientations (0°, 45° and 90°)

Comparing the IN738LC witness and SEC samples, a similar behavior is observed, where the hardness of witness samples is on average 5% lower than that of the extracted samples.

The behavior of 0° to 45° to 90° build orientations is also similar between both alloys. The 90° witness samples show the slowest effective cooling rate, thus leading to the lowest hardness values. In comparison to the 90° build orientation, the 0°and 45° samples show slower effective cooling rates leading to smaller average grain sizes and therefore higher hardness.

5.3.1.1 Correlation Evaluation

The correlation between Vickers hardness and normalized effective cooling rate is characterized, as shown in Figure 58. As can be seen for both alloys, with slower effective

cooling rates the hardness decreases. This can be correlated to the fact, that slower cooling rates allow for grain coarsening, leading to larger grains and therefore lower hardness. On the other hand, faster cooling rates, as in the case of the 0° witness sample and all extracted samples, lead to smaller grains and therefore higher hardness. The same strong correlation is shown in Figure 59 regarding Vickers hardness and average grain size. The correlation evaluation is summarized in Table 13.

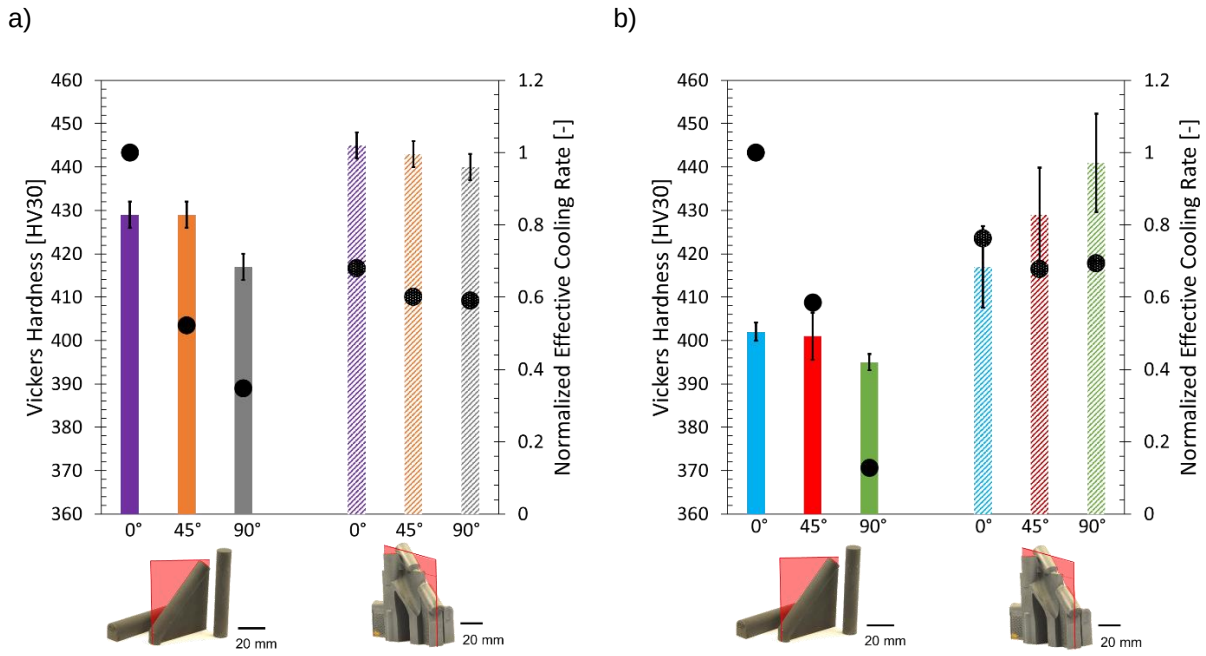

Figure 58 Correlation Vickers hardness and normalized effective cooling rate: a) IN718; b) IN738LC

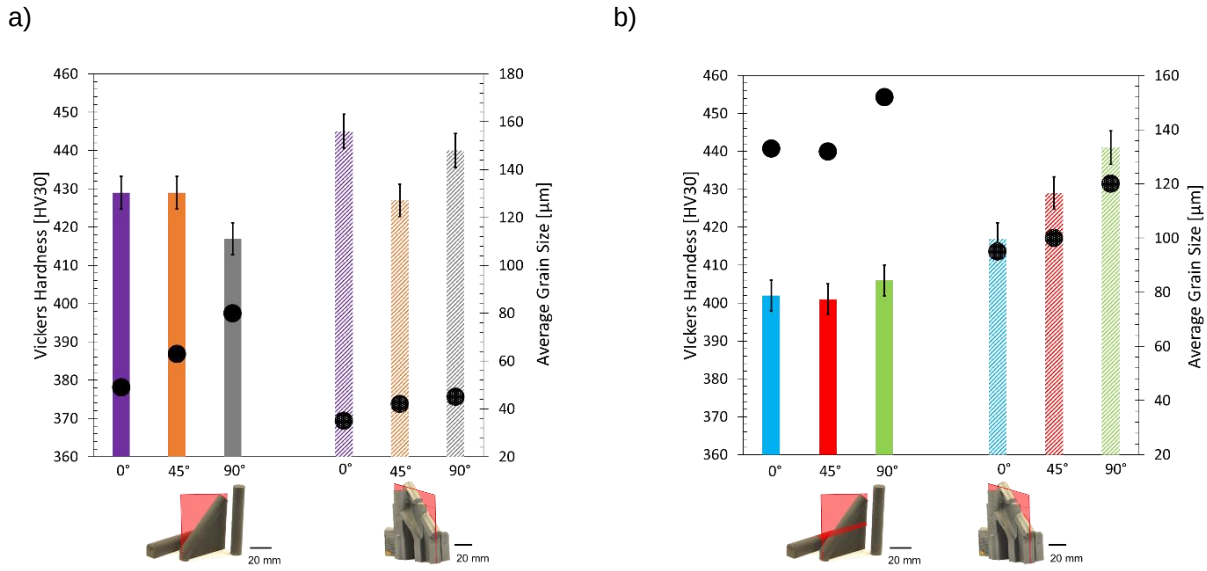

Figure 59 Correlation Vickers hardness and average grain size: a) IN718; b) IN738LC

Table 13 Correlation evaluation of Vickers hardness, normalized effective cooling rates and average grain size

Factors	Strength of Correlation
Normalized effective cooling rate and Vickers hardness	++
Grain size and Vickers hardness	++

5.3.2 Tensile Properties

5.3.2.1 IN718 Tensile Properties

Figure 60 shows the IN718 tensile behavior at 650 °C. Both witness and extracted samples are studied for all three build orientations: 0°, 45° and 90°. As per DIN EN ISO 6892, the strain rate is increased from 0.42 %/min to 8.4 %/min once the strain reaches 1.5%. The change in strain rate causes the sudden increase in stresses observed in all curves [13]. While the tensile tests were carried out according to the same norm and under the same conditions, the witness samples were tested at the Technical University of Darmstadt, Institute for Materials and Technology, whereas the extracted samples were tested at the University of Stuttgart, Materials Testing Institute. It is assumed that the extent of the stress increase due to the change in strain rate is caused by the different testing locations.

Based on literature [11,57], it is expected that the 90° build orientation shows the largest strain but lower strengths compared to the 0° build direction. The 45° build orientation is expected to lie within the bounds of 0° and 90° build orientations. The IN718 results shown in Figure 60 follow this expectation.

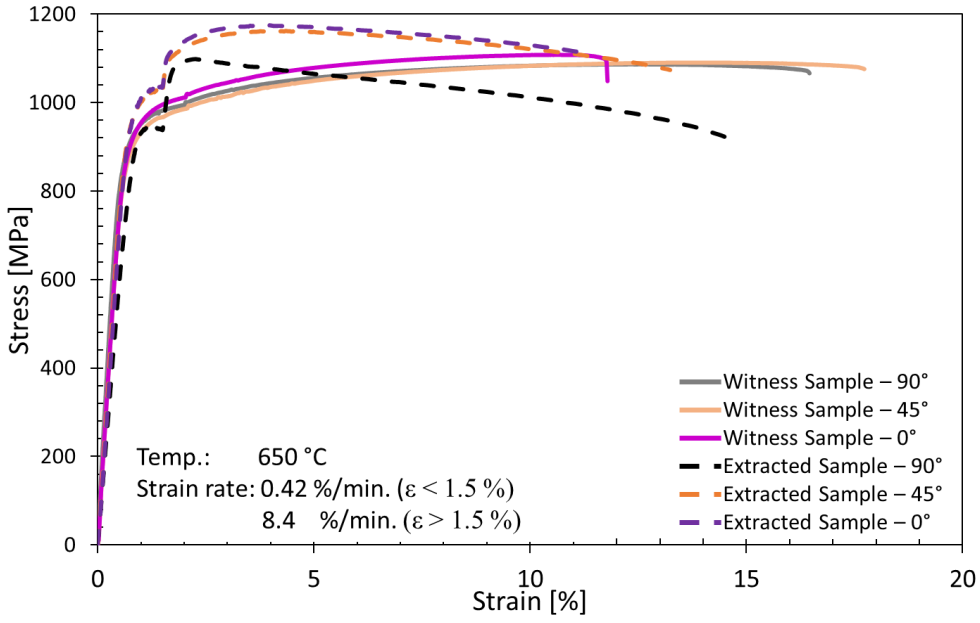

Figure 60 IN718 hot tensile test at 650 °C for witness and extracted samples and all build orientations (0°, 45° and 90°)

Comparing the tensile behavior of witness and extracted samples, a significant difference can be observed: The extracted samples show higher tensile strengths compared to the witness samples. At the same time, the fracture strain of the extracted samples is reduced compared to those of the witness samples.

As seen in Figure 45, the extracted samples contain a significantly higher amount and more evenly distributed δ-phase. The δ-phase has an embrittling effect, which explains the reduced fracture strain seen.

Sanchez et al. [11] published an overview of PBF-LB/M IN718 tensile properties under different testing conditions. Taking the tensile properties obtained under comparable testing conditions as in this study and compiling all data points into one diagram (see Figure 61) allows the evaluation of mechanical properties of witness samples across several research groups and the extracted samples pursued here.

The comparison of reported UTS (see Figure 61a), reported $R_{P0.2}$ (see Figure 61b) and reported tensile elongation (see Figure 61c) with those measured in this thesis for witness and extracted samples shows that all witness samples have similar properties. The extracted samples on the other hand have higher UTS, higher $R_{P0.2}$, and lower elongation values.

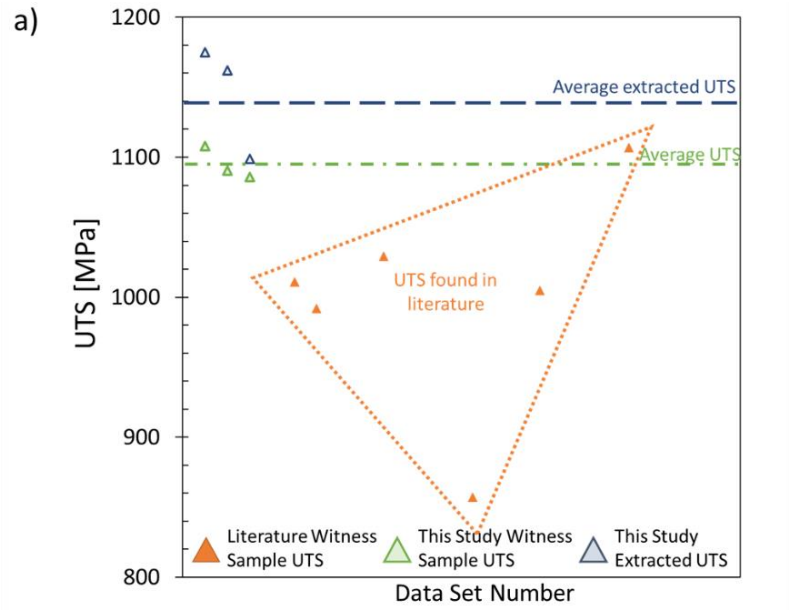

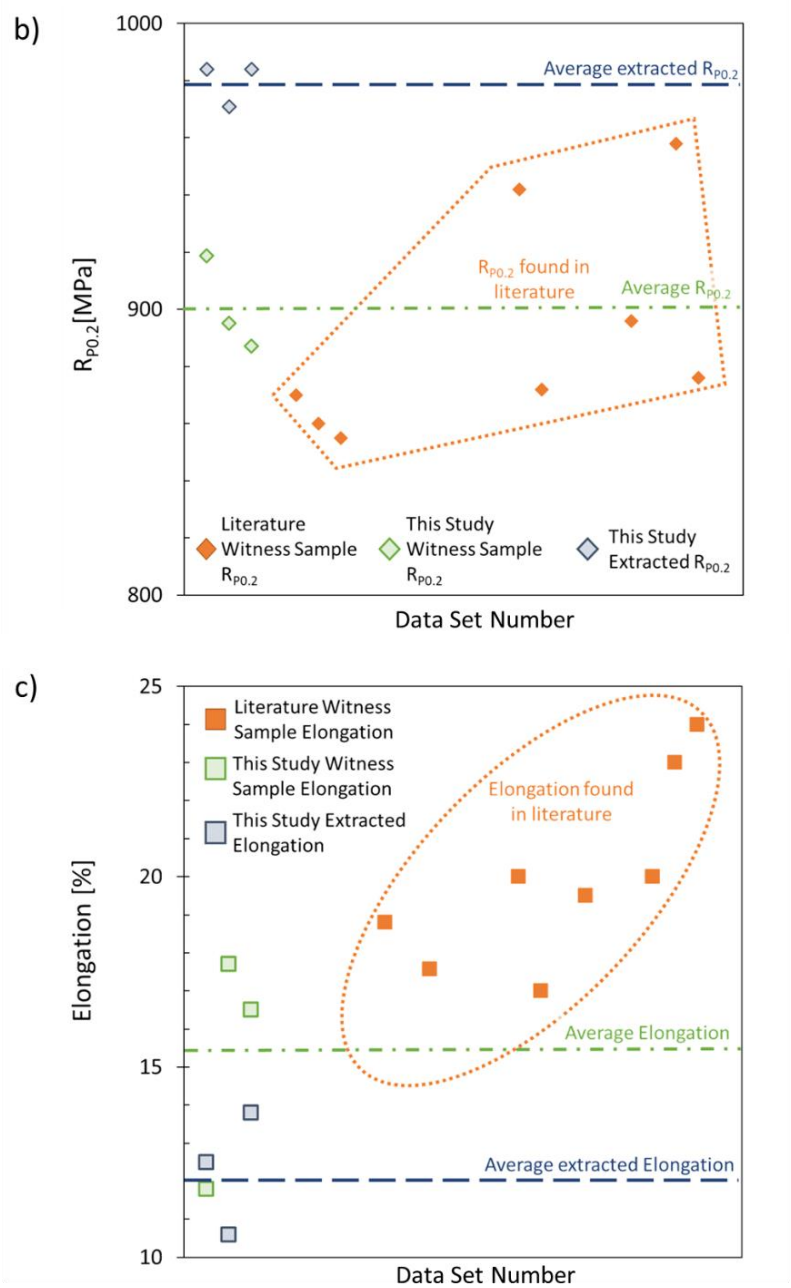

Figure 61 IN718 tensile properties of witness and extracted samples in comparison to data reported in literature: a) UTS; b) $R_{P0.2}$; c) Elongation

Correlation Evaluation

The correlation between UTS and $R_{P0.2}$ and normalized effective cooling rate is characterized in Figure 62. As can be seen with increased normalized effective cooling rate, the UTS and $R_{P0.2}$ values increase. This can be correlated to the grain refinement caused by the faster effective cooling rates (see Chapter 5.2) leading to increased strength according to the Hall-Petch relation [202]. A normalized effective cooling rate threshold of 0.6 can be identified, when an increase in UTS and $R_{P0.2}$ can be seen.

A similar correlation can be seen between UTS and $R_{P0.2}$ and average grain size in Figure 63. This result is expected, since grain size and normalized effective cooling rate are dependent on each other.

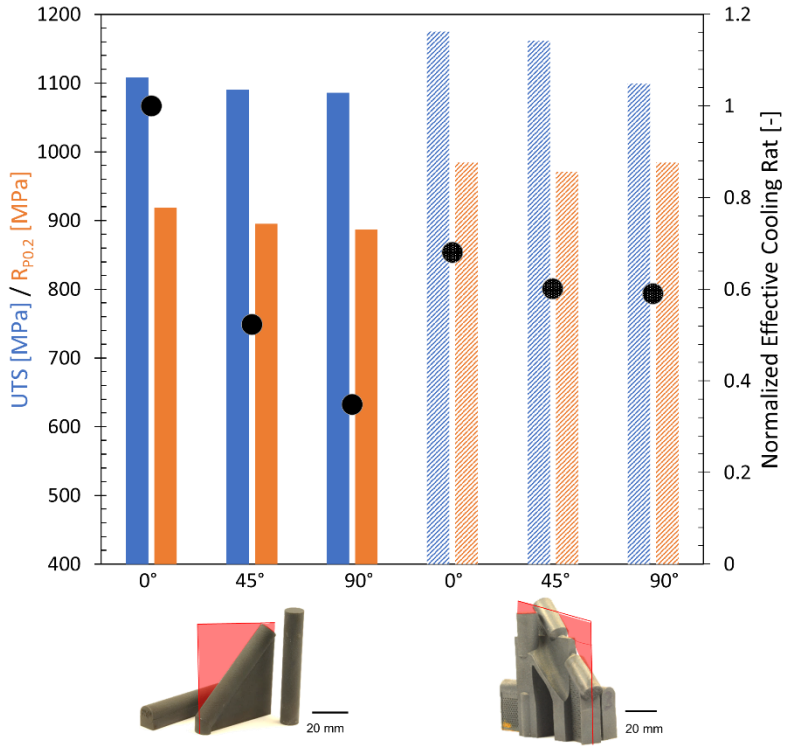

Figure 62 Correlation between IN718 UTS and $R_{P0.2}$ and normalized effective cooling rate

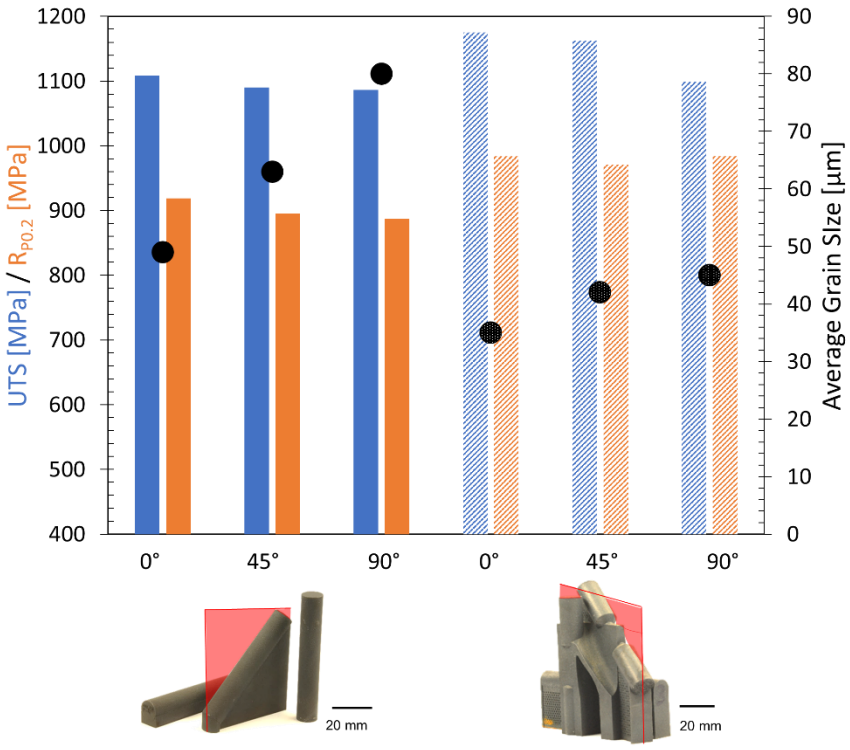

Figure 63 Correlation between IN718 UTS and $R_{P0.2}$ and average grain size

The same correlation evaluation was carried out for elongation, normalized effective cooling rate and average grain size (see Figure 64 and Figure 65). Based on literature [11,57], the 90° build orientation should show the largest elongation values due to the larger average grain sizes. The opposite behavior (i.e. 0° should show the shortest elongation due to smallest grain size) is expected for the 0° build orientation. The 45° build orientation should lie inbetween. While the differences in elongation between the build orientations do not completely agree with the expectation, the differences are below 5% and are therefore considered negligible. The same discrepancies seen in Figure 64 can be found in Figure 65.

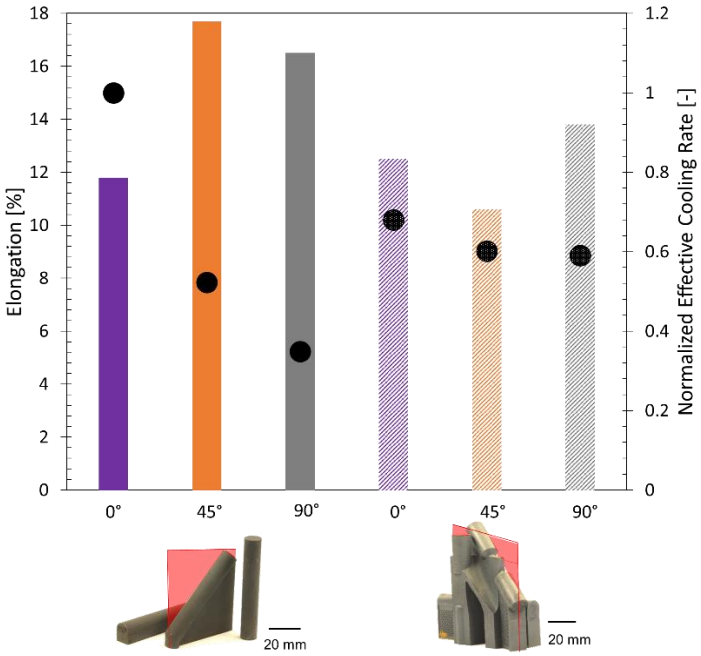

Figure 64 Correlation between IN718 elongation and normalized effective cooling rate

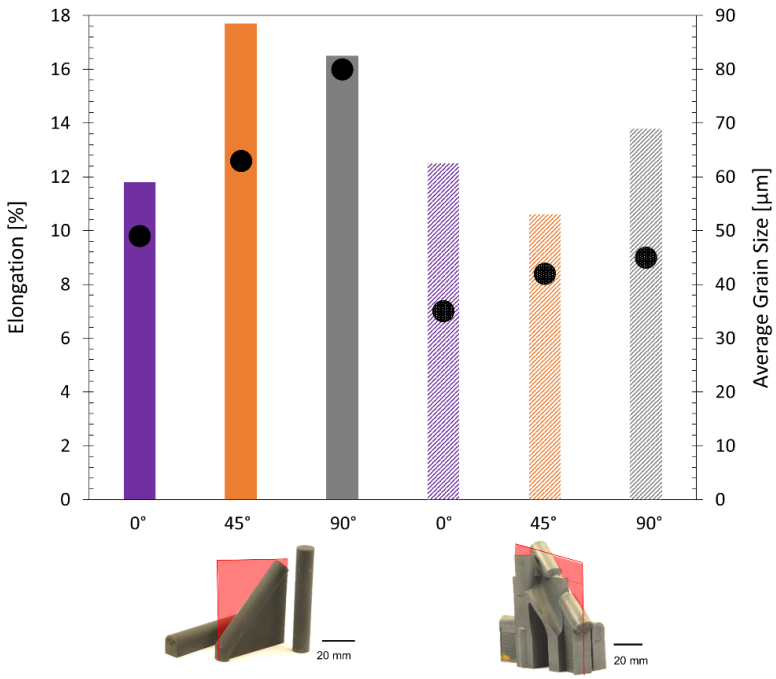

Figure 65 Correlation between IN718 elongation and average grain size

An analysis was carried out to identify the correlation between $R_{P0.2}$ and average grain size (see Figure 66). Based on the data plotted and the Hall-Petch relation, a linear relationship for the respective sample condition is expected. While a near linear relationship can be identified for the witness samples, this is not the case for the extracted samples, meaning that the microstructure (i.e. phase formation) plays a significant role in the tensile properties. As discussed in Chapter 5.2.2.1, the microstructure between witness and extracted samples differ. While the same phases form (γ, γ', γ'' and δ), the shape and distribution differ. The witness samples show a continuous film of δ-phase along grain boundaries, whereas the extracted samples showed needle-shaped δ-phase homogeneously distributed. Even though all extracted samples show needle-shaped δ-phase, the δ-phase within the 90° build orientation was the finest. These thin needle-like increase stress concentrations and cause crack initiation; thinner needles more so than thicker needles. This would explain the 90° discrepancy within the extracted samples. The continuous δ-phase in the witness samples form a weak spot, since they embrittle the grain boundaries in all witness samples.

A summary of the above discussed correlations is listed in Table 14.

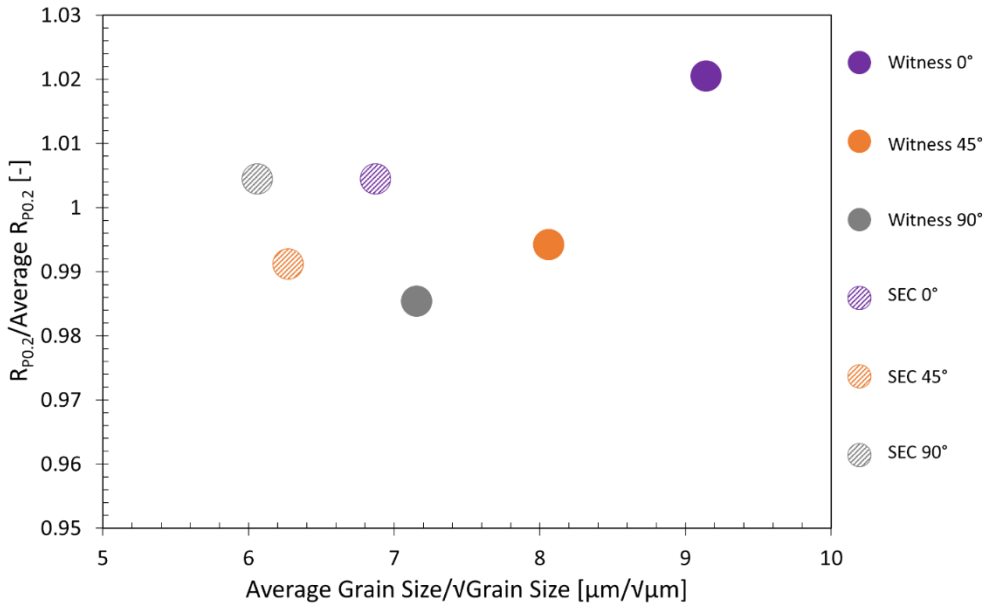

Figure 66 Correlation between IN718 $R_{P0.2}$ and average grain size

Table 14 Correlation evaluation of IN718 tensile properties, normalized effective cooling rates, average grain size and phases

Factors	Strength of Correlation
Normalized effective cooling rate and UTS/$R_{P0.2}$	++
Normalized effective cooling rate and Elongation	0
Average grain size and UTS/$R_{P0.2}$	++
Average grain size and Elongation	0
$R_{P0.2}$ and √average grain size	+
Phases and UTS/$R_{P0.2}$	+
Phases and Elongation	+

5.3.2.2 IN738LC Tensile Properties

Figure 67 shows the hot tensile tests of IN738LC witness and extracted samples, carried out at 850 °C. Similar to IN718, the IN738LC tensile results agree with the expected build orientation behavior. Figure 67 shows that the 90° sample (extracted and witness) show the largest tensile fracture strain compared to 0° and 45° build orientation. The tensile strains (extracted and witness) increase from 0° to 45° to 90°.

In Figure 67, it can clearly be identified that extracted samples (dashed lines) show higher strengths and lower failure strains compared to the witness samples.

The finer average grain size of the extracted samples inhibits dislocation mobility reducing plasticity and thereby strain but increasing strength. However, the microstructural texture (see Figure 52 and Figure 53) and phases formed (refer to Table 10) should also be considered. The extracted samples contain TCP-phases (as seen in Table 10 and Figure 53), which further reduce ductility.

While the UTS and $R_{P0.2}$ for the extracted samples lie above those of the witness samples, which can be attributed to the phases formed, the behavior of the build orientation relative to one another differs compared to the tensile strain. The difference in UTS in witness samples between 0° and 90° lies below 3% and is therefore considered negligible. The same applies for the extracted samples.

Comparable yield and tensile stresses for IN738LC witness samples at 850 °C were reported by Wang et al. [192]. In this study, the 90° samples show a higher ductility compared to 0° and 45°. The 0° and 45° samples show the same tensile ductility of 21.9%. Wang et al. [192] achieved a ductility of ~14.4%. This difference might be caused by a difference in average

grain size. The grain size reported by Wang et al. [192] is roughly half the grain size obtained in this study, presumably due to differences in applied heat treatment.

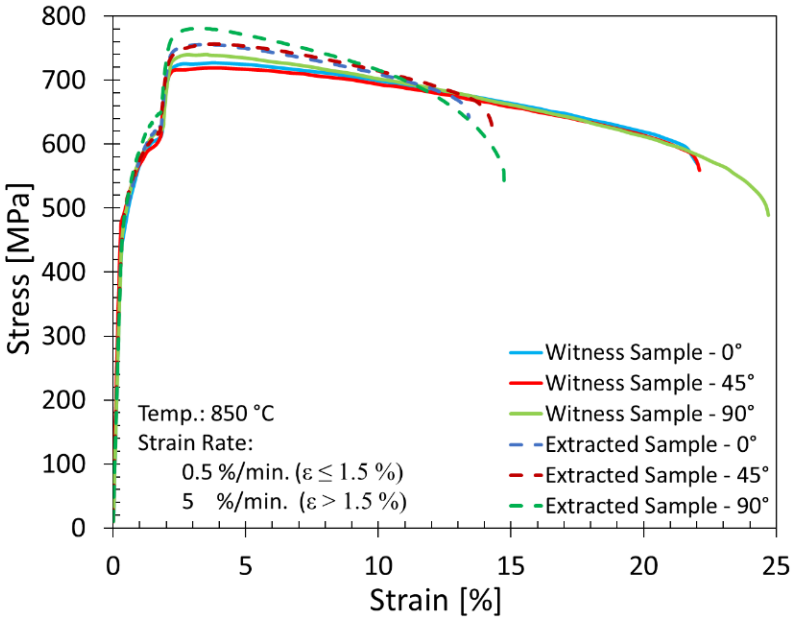

Figure 67 IN738LC hot tensile stress-strain curves for witness and extracted samples at 850 °C

Correlation Evaluation

The correlation between UTS and $R_{P0.2}$ and normalized effective cooling rate is characterized for IN738LC in Figure 69. Similar to IN718 discussed above, with increased normalized effective cooling rate, the UTS and $R_{P0.2}$ values increase. This can be correlated to the grain refinement caused by the faster effective cooling rates (see Chapter 5.2) leading to increased strength according to the Hall-Petch relation [202]. A normalized effective cooling rate threshold of 0.65 can be identified, when an increase in UTS and $R_{P0.2}$ can be seen.

A similar correlation can be seen between UTS and $R_{P0.2}$ and average grain size in Figure 69. This result is expected, since grain size and normalized effective cooling rate are dependent on each other.

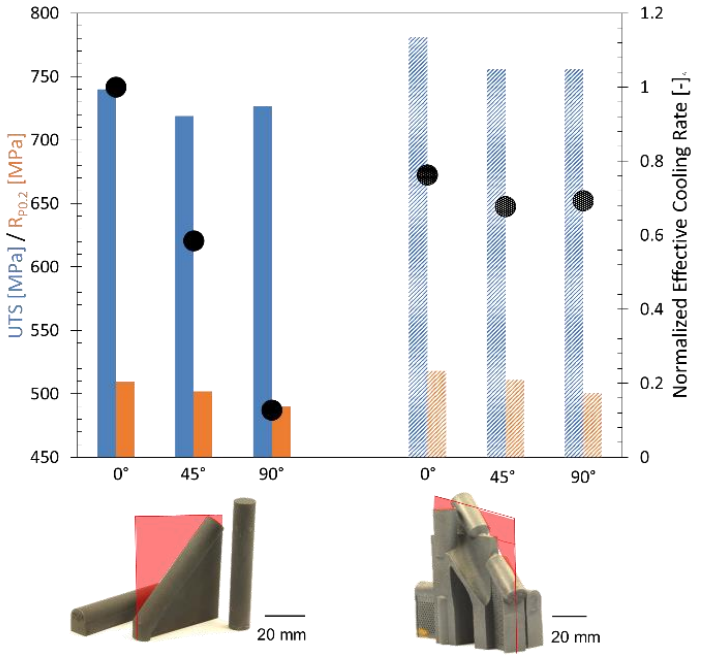

Figure 68 Correlation between IN738LC UTS and $R_{P0.2}$ and normalized effective cooling rate

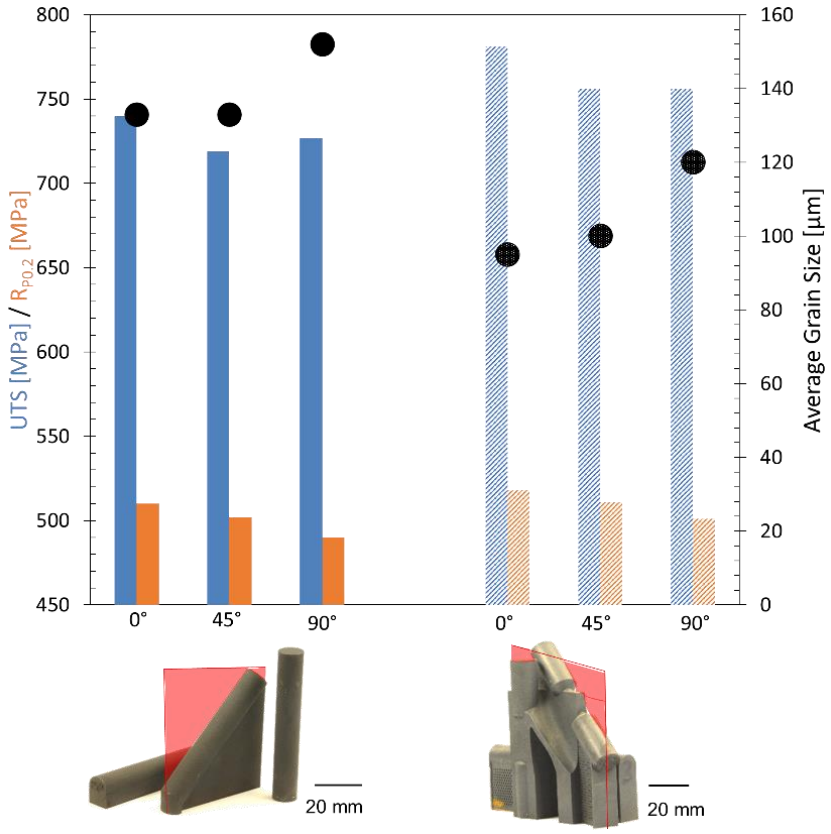

Figure 69 Correlation between IN738LC UTS and $R_{P0.2}$ and average grain size

The same correlation evaluation was carried out for the IN738LC elongation, normalized effective cooling rate and average grain size (see Figure 70 and Figure 71). As can be seen, with decreasing effective cooling rate, the elongation also decreases. This trend is identified

for witness and extracted samples. Similarly, with increasing average grain size, the elongation increases. This strong correlation is listed in Table 15.

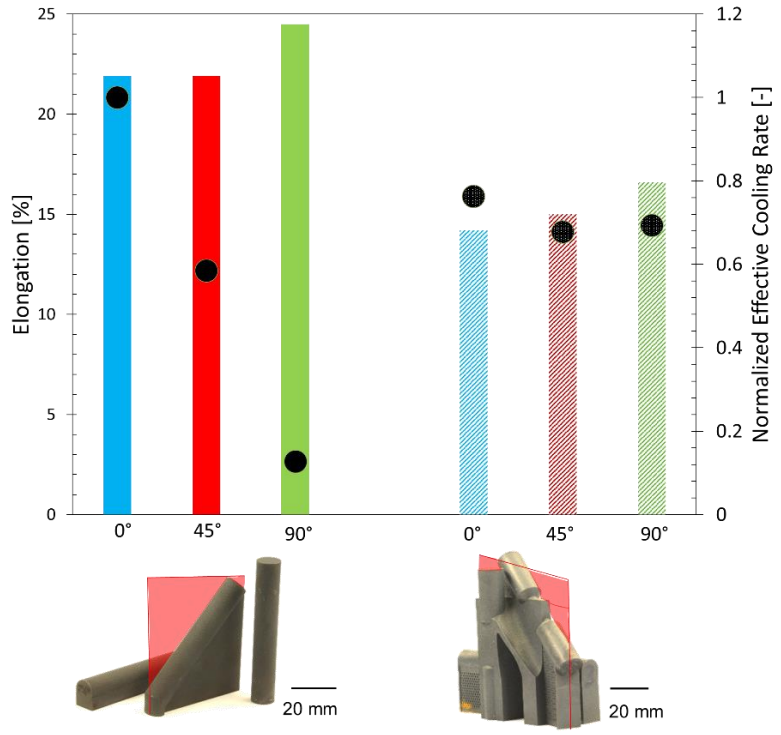

Figure 70 Correlation between IN738LC elongation and normalized effective cooling rate

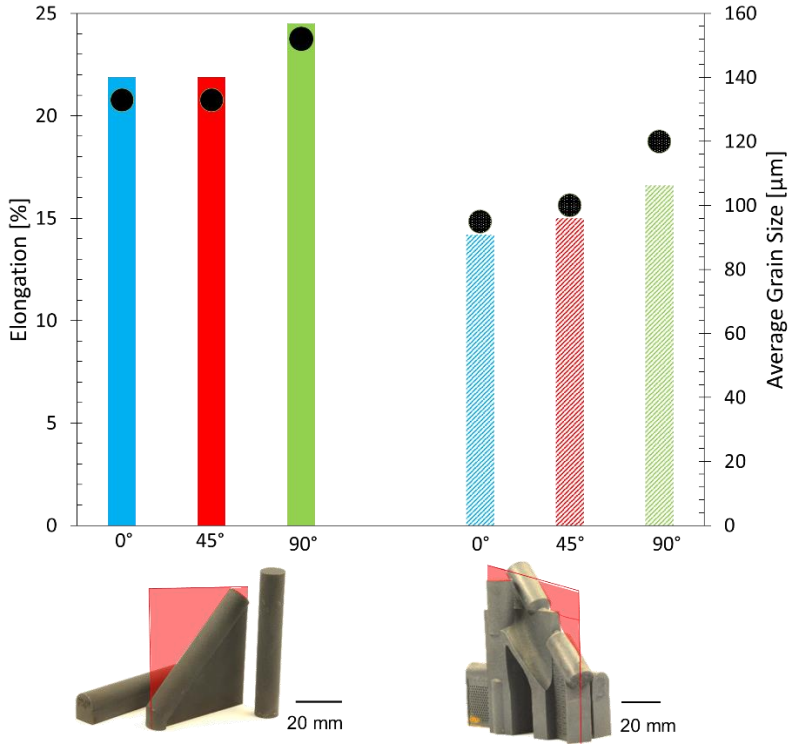

Figure 71 Correlation between IN738LC elongation and average grain size

To determine the effect of the Hall-Petch relation, an analysis was carried out to identify the correlation between $R_{P0.2}$ and average grain size (see Figure 72). A linear relationship for the

respective sample condition is expected. For IN738LC, both the witness samples and the extracted samples show a near-linear relationship, meaning that grain size is the root cause for the documented difference in $R_{P0.2}$ values. The difference in phase formation in witness (γ, γ', carbide) and extracted samples (γ, γ', TCP) is the reason behind the gradient of the correlation. The TCP-phases are also a partial reason for the reduced elongation in extracted samples.

A summary of the above discussed correlations is listed in Table 15.

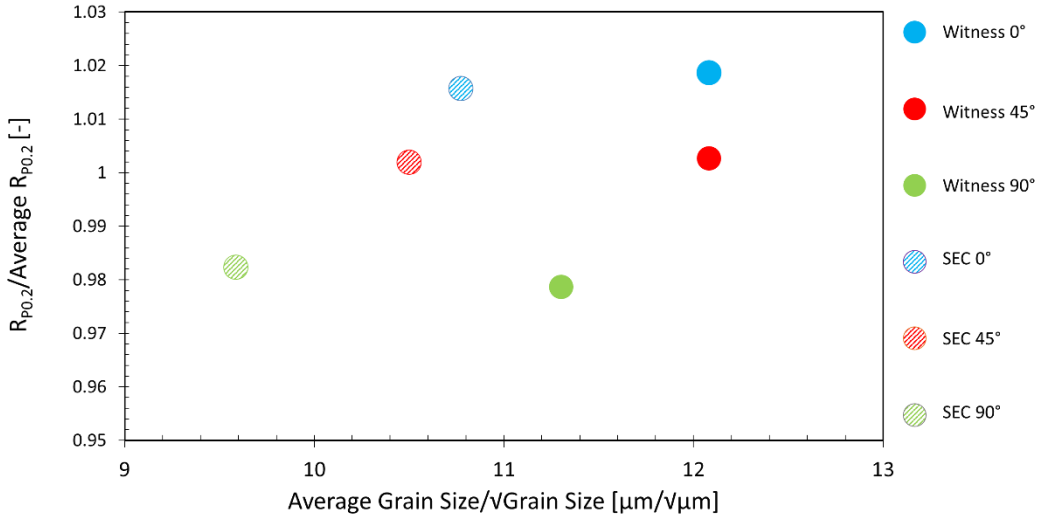

Figure 72 Correlation between IN738LC $R_{P0.2}$ and average grain size

Table 15 Correlation evaluation of IN738LC tensile properties, normalized effective cooling rates, average grain size and phases

Factors	Strength of Correlation
Normalized effective cooling rate and UTS/$R_{P0.2}$	++
Normalized effective cooling rate and Elongation	++
Average grain size and UTS/$R_{P0.2}$	++
Average grain size and Elongation	++
$R_{P0.2}$ and √average grain size	++
Phases and UTS/$R_{P0.2}$	0
Phases and Elongation	0

5.3.3 Mechanical Properties of IN718 versus those of IN738LC

IN718 and IN738LC show similar tensile behaviors. The extracted samples have higher UTS and $R_{P0.2}$ values than witness samples and the tensile failure strains are smaller compared to those of witness samples.

The γ''-phase is responsible for the increased strength of IN718, while the δ-phase causes a decrease in failure strain.
For IN738LC, the higher UTS and $R_{P0.2}$ are attributed to nano-scale TCP-phases. Simultaneously, the TCP-phases are also the reason for the comparatively brittle behavior of the extracted samples.

5.4 Response to Research Question 1

From the results presented above, it can be summarized that a direct transfer of properties from witness samples to those of extracted samples is not possible. Witness samples do not follow the same thermal history leading to differences in phase distribution, microstructure or mechanical properties of voluminous PBF-LB/M components.

The root cause of these differences lies in the differences in geometry height, geometry volume and interface area between sample/component and substrate plate, which acts as the main heat sink in PBF-LB/M processes. The resulting differences in solidification behavior led to identified differences between witness samples and (samples extracted from) components.

The following paragraph quotes DIN EN ISO/ASTM 52920:
‘’…The process qualification forms the basis for both the identification of reproducible material properties as well as evaluation of the current process quality. *This requires testing of reference samples (i.e. witness samples)*, to a statistically significant extent, that includes all qualified process steps defined by the manufacturing plan…The scope and frequency for controlling the process quality shall be defined and documented in the manufacturing process monitoring plan and records. Where required, co-built test artifacts (i.e. witness samples) serve *the quantitative determination of material characteristics*, for *comparison to the control chart*, as specified by the process qualification. Property specific tolerance bands, used for acceptance, are based on the value and dispersion parameters of the material characteristics, …’’ [14].
Based on the results presented, it is therefore highly questionable whether witness samples can be directly used to quantify component properties for qualification purposes as mentioned in DIN EN ISO/ASTM 52920 [14]. However, witness samples might be used to qualitatively ensure that the printing process is yielding similar quality across multiple build jobs. In order to qualify a print job, the component and witness samples would have to be characterized and correlated to one another beforehand. If witness samples of the new print job correspond to those of the qualified job, one might postulate that the part fulfills qualification requirements.

6 Results and Discussion for Research Question 2: How do Build Orientation and Microstructure Affect Creep Mechanisms?

The previous chapter on the transferability of witness samples to components irrevocably showed a dependence of thermal history, microstructure and mechanical properties on build orientation. Literature indicates a general knowledge gap of PBF-LB/M IN738LC creep behavior, and its orientation dependent creep behavior in particular. This chapter is dedicated to filling that gap using publicly available information about PBF-LB/M IN718 creep behavior as a reference for Ni superalloys. As discussed in Chapter 2, creep mechanisms are complex and affected by multiple factors. Conclusions regarding research question 2 therefore require a systematic analysis of different influencing factors.

The effect of creep test temperature, applied stress and different build orientations on creep behavior is studied. Creep deformation mechanisms are identified within research question 2.

The difference between witness and extracted samples is also characterized. The response to research question 1 is accordingly extended with creep results.

6.1 Creep Behavior of PBF-LB/M Witness Samples

6.1.1 Creep Behavior in IN718

Sanchez et al. analyzed the IN718 creep behavior of 0°, 45° and 90° build orientations. The creep curves are shown in Figure 73. The data was extracted from reference number [67]. Similar to the IN718 tensile results, the expected results are seen:

- 0° shows the least creep failure strain and time to rupture,
- 90° shows the highest creep failure strain and longest time to rupture,
- 45° lies within the bounds of 0° and 90° build orientation regarding both creep failure strain and time to rupture.

The IN718 microstructure after creep for the samples shown in Figure 73 can be seen in Figure 74. Similar to the microstructures obtained in this study (see Figure 45), the 0° sample shows the finer grain size compared to the 45° and 90° build orientations. Additionally, it can be seen, that the δ-phase precipitated along the grain boundaries, similar to the microstructure shown for witness samples (see Figure 45).

Due to the faster effective cooling rate of the 0° witness samples (see Chapter 5.2), the precipitation size compared to 45° and 90° witness samples is smaller. The applied heat treatment (AMS5662, see Figure 28) leads to the (partial) dissolution of γ'' forming δ-phase in all build orientations.

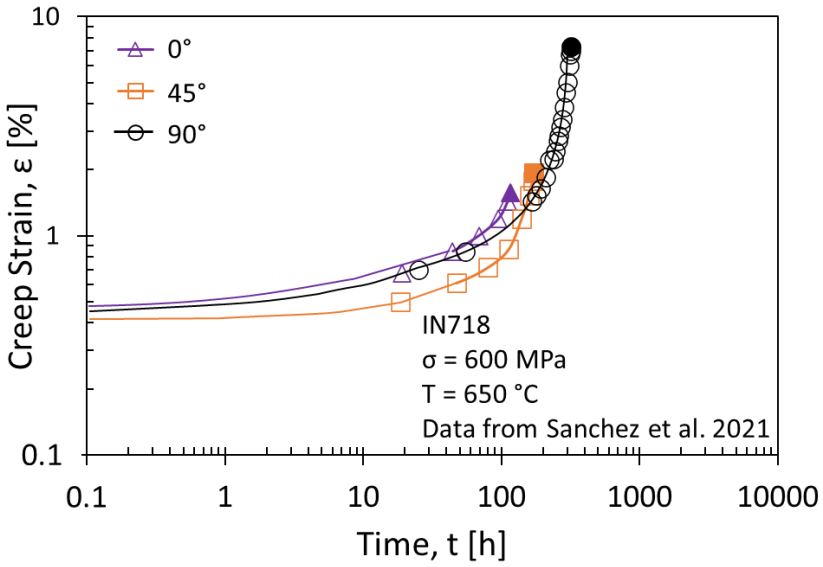

Figure 73 IN718 creep curves, data from Sanchez et al. [12]

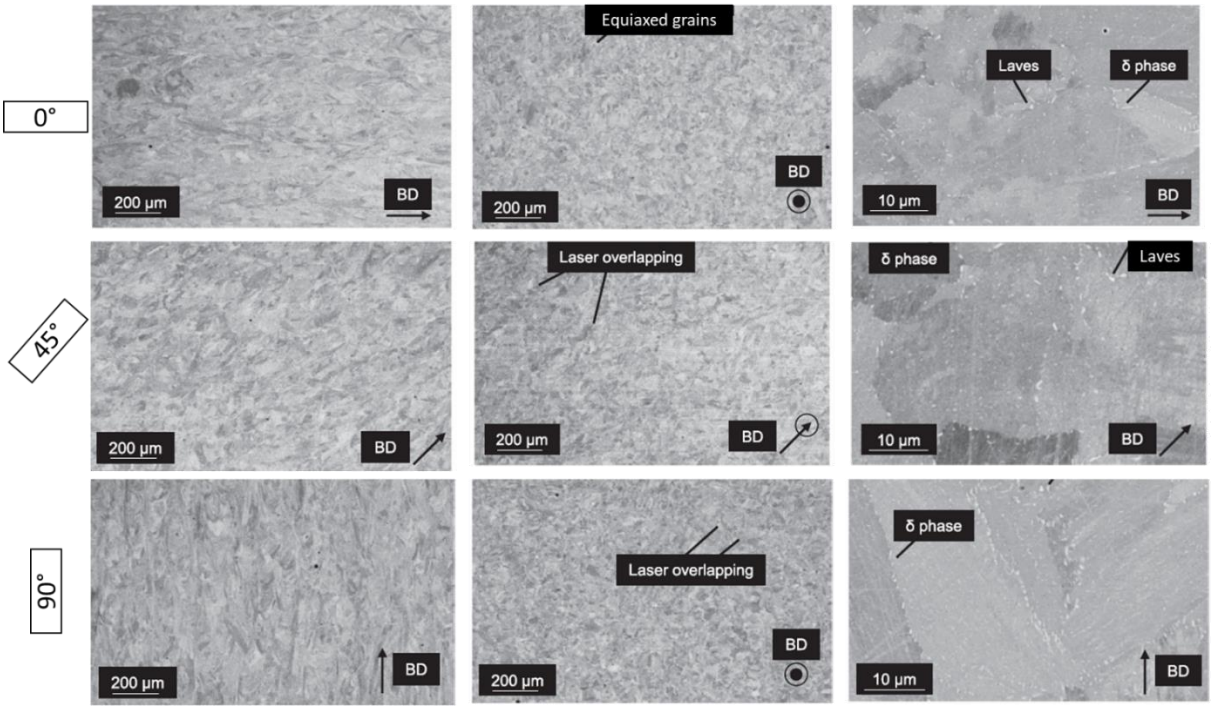

Figure 74 IN718 microstructures after creep (650 °C/600 MPa) for all build orientations, taken and adjusted from [12]

6.1.2 Creep Behavior of IN738LC

The creep results of witness samples for 750 °C at 350 MPa and for 850 °C at 200 MPa are shown in Figure 75a and Figure 75b respectively. For both temperatures, the creep failure strains increase from build orientation angle 0° to 45° to 90°. At 750 °C, the longest time to rupture is that of the 90° sample with 8,803 h and the creep failure strain lies at 3.48%. The 0° sample has a significantly lower time to rupture of 3,076 h and a creep failure strain of 2.23%. The 45° sample shows the lowest time to rupture after 2,808 h and a creep failure strain of 2.75%. An overview of the 750 °C/350 MPa results can be found in Figure 76a.

The difference in tertiary stage should also be noted. Whereas the tertiary stage of the 90° sample is extended, the 0° and 45° show significantly smaller tertiary stages. The difference in tertiary stage between the build orientations was also found for IN718 by Sanchez et al. [67].

A similar behavior is shown at 850 °C. Creep failure strains of 8.61%, 1.72% and 3.37% and times to rupture of 5,362 h, 912 h and 534 h are recorded for 90°, 0° and 45° build orientation respectively. An overview of the 850 °C/200 MPa results can be found in Figure 76b.

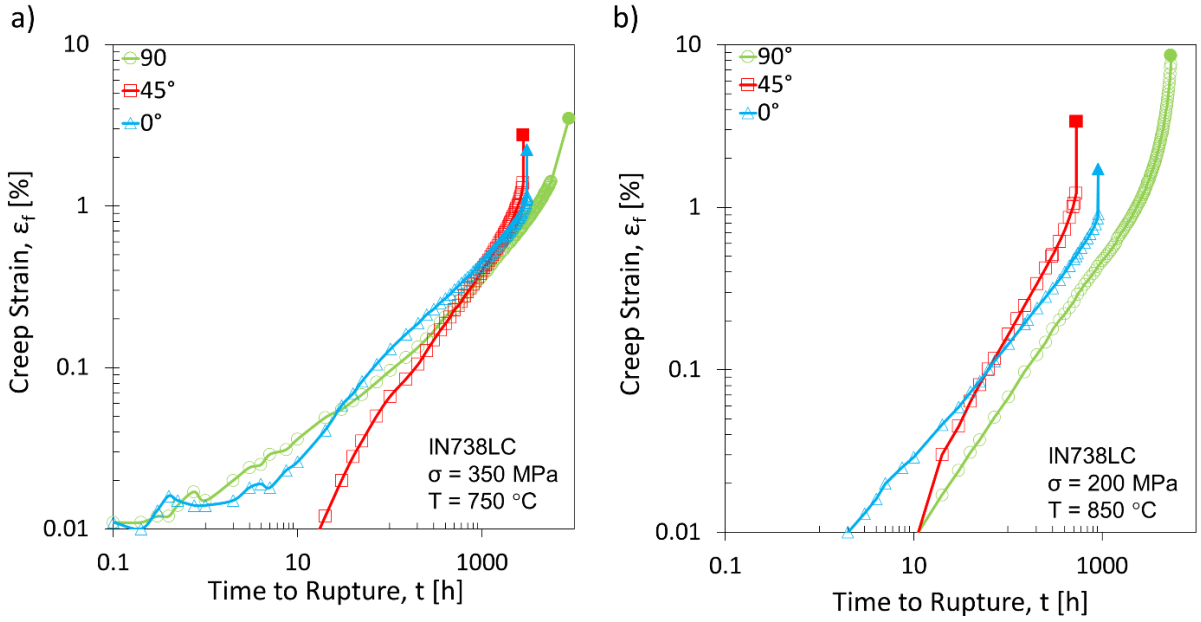

Figure 75 IN738LC creep results for a) 750 °C/350 MPa witness samples and b) 850 °C/200 MPa witness samples

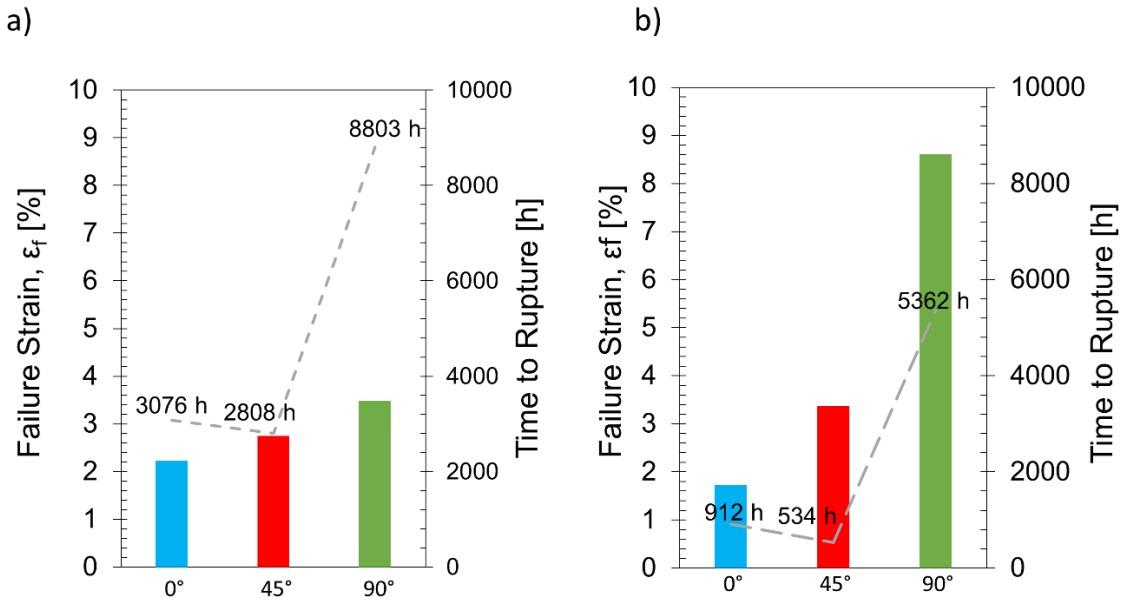

Figure 76 IN738LC overview of creep results for a) 750 °C/350 MPa witness samples and b) 850 °C/200 MPa witness samples

Even though, each creep loading parameter set was only tested once, the creep results show that similar material trends are seen at different temperatures and at different load levels. It can therefore be assumed that this creep behavior is representative. The 90° build orientation achieves the largest creep failure strain, followed by the 45° and 0° build orientation respectively. The creep rate is highest in the 45° build orientation compared to the other two build orientations. Accordingly, the time to rupture of 45° build orientation is lowest compared to the other two build orientations.

The creep behavior seen in Figure 75 is material specific, since the IN738LC 45° creep results do not agree with the IN738LC tensile results (see Figure 67) or the IN718 creep behavior (compare Figure 73). Based on the tensile results and the IN718 creep results reported in literature, it is expected that the 45° build orientation lies within the bounds of the 0° and 90° build orientation. While the creep failure strains do agree with the expectations (compare Figure 76), the time to rupture of the 45° build orientation is significantly lower compared to the other two build orientations. Accordingly, the creep rate of the 45° build orientation is significantly higher compared to the 0° and 90° build orientation.

The IN738LC 45° time to rupture does not agree with those of IN718 as it does not lie between those of 0° and 90° samples. Such a behavior was not observed in microstructure or in hot tensile testing, as shown in Figure 67. The root cause of this anomaly must therefore be found in the creep behavior itself.

6.2 Effect of Creep Test Temperature and Applied Stress on IN738LC Microstructure

As seen in the chapter above (6.1.2), similar creep trends are seen at different creep test temperatures. A difference in macroscopic fracture surfaces can be identified between the build orientations. Macroscopic images of the fractured samples at 750 °C/350 MPa and 850 °C/200 MPa and 850 °C/240 MPa are shown in Figure 77. The 90° and 0° oriented samples show planar fracture surfaces perpendicular to the maximum normal stress. The 45° samples show shear failure oriented at a 45° angle. This fracture behavior holds true for both temperatures 750 °C and 850 °C (both loads: 200 MPa and 240 MPa).

Also noticeable is the fracture location: All build orientations break in a similar region of the samples for the respective creep test temperature. However, the failure locations of the samples tested at 850 °C are located lower (on average 10 mm difference) compared to those tested at 750 °C. The fracture location of the 750 °C samples occurred in the sample center.

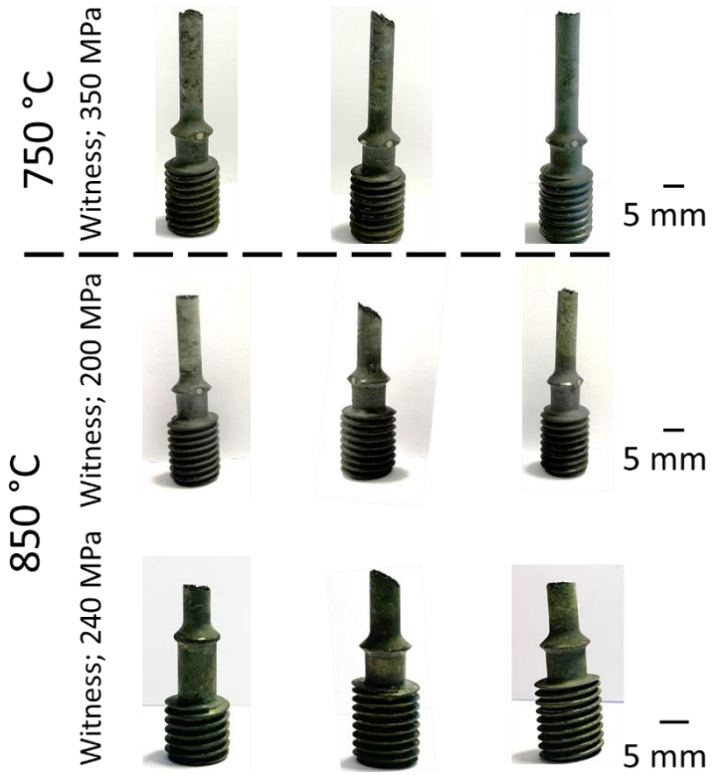

Figure 77 Fractured IN738LC creep witness samples750 °C (top); 850 °C (bottom)

To explore the root causes for the IN738LC creep behavior and macroscopic fracture surfaces, the microstructural changes due to temperature and stress exposure are investigated. The IPF-poles for witness samples tested at 750 °C/350 MPa and 850 °C/200 MPa, 850 °C/240 MPa are shown in Figure 78. At 750 °C, a strong anisotropy in 0° build orientation is seen with a mixture of dominant grain orientations mainly between [111] and [001]. The 90° build orientation shows a dominant grain orientation of [001]. There is no dominant grain orientation in 45°. At 850 °C/200 MPa and 850 °C/240 MPa, the grain orientation in the 0° sample is a mixture of [111] and [101]. Similar to 750 °C, the 90° sample still shows a dominant grain orientation of [001]. The 45° build orientation remains without dominant grain orientation.

While the grain orientation of 90° samples remains mostly oriented in [001] direction for both creep testing temperatures, the dominant build orientation of the 0° samples differs from one temperature to the other. At 750 °C the dominant grain orientation is shown to be [001] and [111], whereas at 850 °C the dominant grain orientations of 0° samples are [001] and [101]. The change in grain orientation depending on creep test temperature indicates that the temperature plays a significant role for grain rotation and final grain orientation.

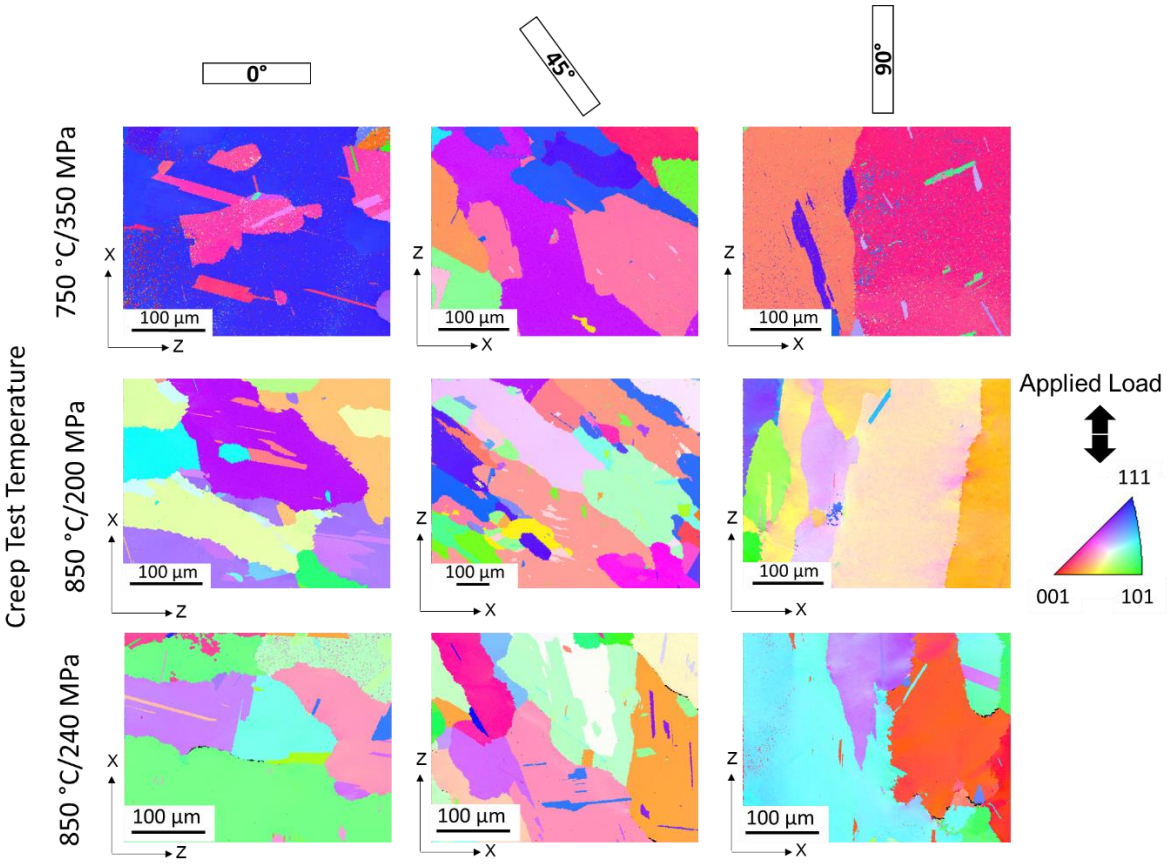

Figure 78 Inverse pole figures (IPF-Z) taken near the fracture surface in all build orientations (0°, 45°, 90°) for 750 °C/350 MPa and 850 °C/200 MPa, 850 °C/240 MPa

The grain boundary angles for creep samples tested at 750 °C/350 MPa and 850 °C/200 MPa, 850 °C/240 MPa are shown in Figure 79. High Angle Grain Boundaries (>12°; HAGBs) are shown in red, while Low Angle Grain Boundaries (<12°; LAGBs) are shown in black. Both creep test temperatures show similar trends: The 0° and 90° build orientations show a mixture of high and low angle grain boundaries, with LAGBs being most dominant. In comparison, 45° shows mostly HAGBs, identifiable by the dominant red lines and lack of black lines. Again, the grain boundary angles of the 850 °C/200 MPa samples are similar to those seen in samples tested at 850 °C/240 MPa.

As shown in Figure 79, the build orientations tested at 750 °C contain a larger amount of LAGBs, which can accommodate the stresses more evenly compared to HAGBs. The high amount of HAGBs found in the build orientations tested at 850 °C cannot accommodate the stresses as evenly as LAGBs, due to the lattice mismatch causing defect initiation. As mentioned above, the sample failure locations differ between the creep test temperatures. The dominant HAGB frequency in the 850 °C samples cause defect initiation leading to non-central sample failure as compared to the 750 °C samples containing more LAGBs, which accommodate the applied stress more evenly leading to central sample failure.

A reduction in LAGBs can be noticed in the 0° and 90° build orientations at 850 °C (200 MPa and 240 MPa) compared to the 750 °C samples. The reduction in LAGBs combined with the change in dominant grain orientation indicates that dynamic recrystallisation is occurring. Representative TEM-images of creep samples at 750 °C and 850°C are shown in Figure 80. Bulging grain boundaries are seen at 850 °C, while grain boundaries do not bulge at 750 °C. The bulging grain boundaries are an indication of discontinuous dynamic recrystallization (DDRX). Based on the TEM-images, it is assumed that while both continuous dynamic recrystallization (CDRX) and DDRX are occurring, at higher temperatures (i.e. 850 °C in this study) DDRX is more dominant. The bulging grain boundaries are the cause for the reduction in LAGBs seen in Figure 79 and the change in dominant grain orientation.

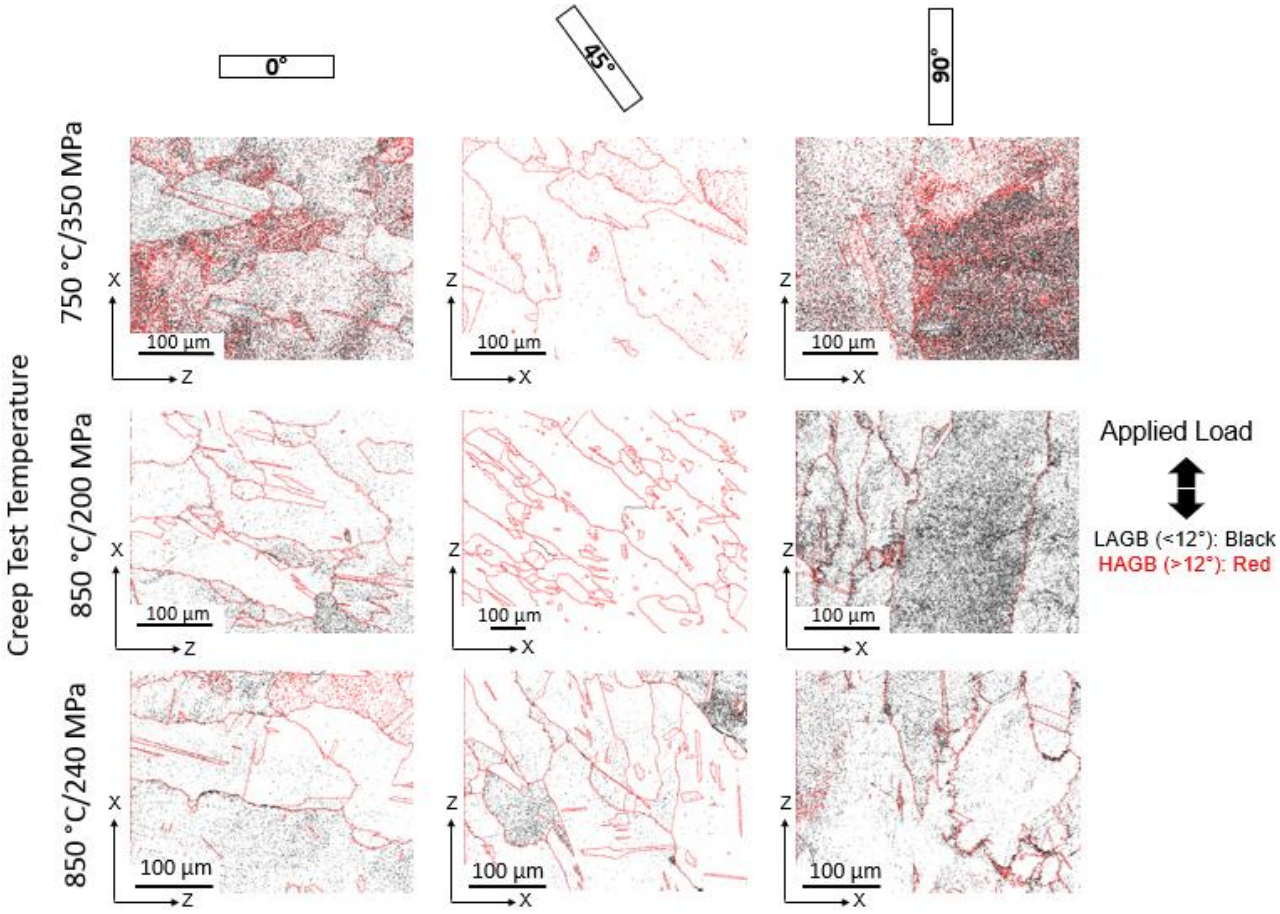

Figure 79 Grain boundary angles for creep samples close to the fracture surface in all build orientations (0°, 45°, 90°) for 750 °C/350 MPa and 850 °C/200 MPa, 850 °C/240 MPa

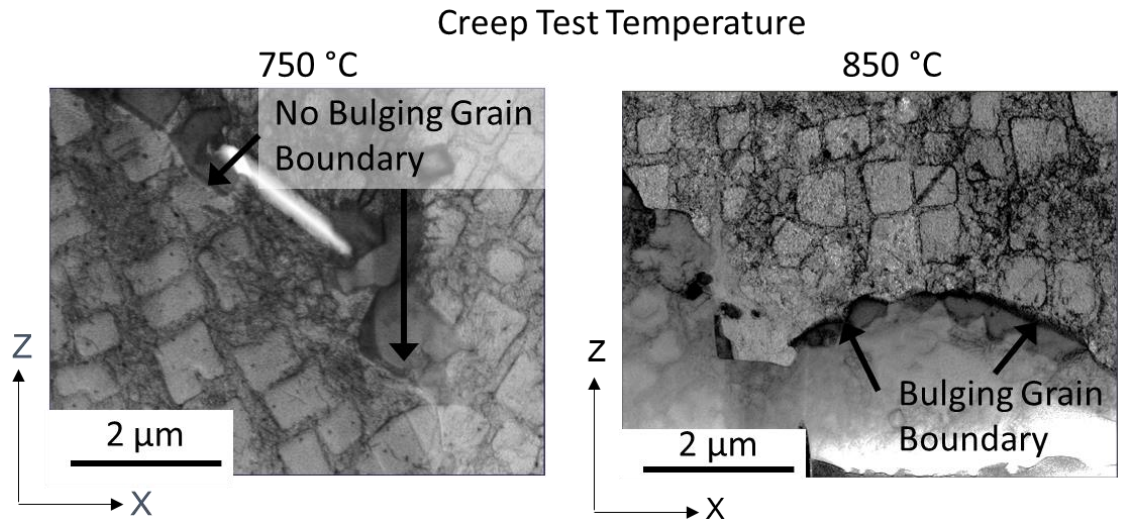

Figure 80 Representative TEM-images of witness creep samples tested at 750 °C/350 MPa showing no bulging grain boundaries (left) and 850 °C/200 MPa showing bulging grain boundaries (right)

From this chapter, it can be concluded that the PBF-LB/M IN738LC creep behavior at 850 °C is similar at different loads. Both at 200 MPa and 240 MPa, similar dominant grain orientations, grain boundary angles, macroscopic fracture surfaces and fracture locations were documented.

With regards to creep temperature, differences are observed at 750 °C and 850 °C. The dominant grain orientations in the build orientations and the grain boundary angles at 750 °C differ compared to 850 °C affecting the recrystallisation during creep and fracture location.

6.3 Effect of Build Orientation on IN738LC Creep Deformation Mechanisms

Creep deformation mechanisms are complex and often occur simultaneously. It is therefore important to identify the active deformation mechanisms to understand the resulting creep properties.

As discussed in Chapter 6.1.2, the IN738LC creep failure strains follow the expected trend, whereas the times to rupture and thus creep rates do not for the different build orientations. This chapter discusses the different creep deformation mechanisms to explain the creep failure strains and creep rates within the build orientations.

6.3.1 Creep Mechanisms affecting Creep Failure Strain

Grain rotation is a common mechanism during creep to accommodate the applied stress. In order to identify how and to what extent grains rotated, Euler angles were determined using EBSD-scans (see Figure 81). The cube wire frames drawn for each grain indicate how the respective grain is oriented (see Figure 81a).

For the 90° build orientation, the dominant orientation prior to and after creep testing is [001], which is parallel to the applied load. Comparing the Euler angles prior to and after creep, no

significant change can be identified. Grain rotation is therefore limited in the 90° build orientation.

The 0° build orientation shows a dominant orientation of [011] prior to creep. After creep, a dominant orientation of [$\bar{1}$11] can be seen. The number of grains oriented parallel to load direction in [001] does not change significantly after creep. The rotation in the 0° build orientation focusses from [011] to [$\bar{1}$11] (see Figure 81b). The inferior creep behavior related to [011] orientations has previously been reported [204].

For the 45° build orientation, grains oriented at [011]-angles rotated towards [001] and [$\bar{1}$11]-angles rotated towards [011] (see Figure 81b). The rotation towards the [001] orientation, that is parallel to the applied loading direction, allows for the accommodation of the applied stress. By contrast the 0° sample shows a Euler angle combination of [$\bar{1}$11] and [011] and the 90° oriented sample shows Euler angles mostly oriented in [001] (i.e., parallel to applied load direction) after creep (see Figure 81c). The Euler angles thus provide a preliminary explanation of the 45° behavior and its relation to 0° and 90° orientations.

As can be seen in Figure 81a, for all samples, grains become longer and thinner during creep, confirming the simultaneous occurrence of CDRX and DDRX. The difference in average grain size is visualized in Figure 82.

a)

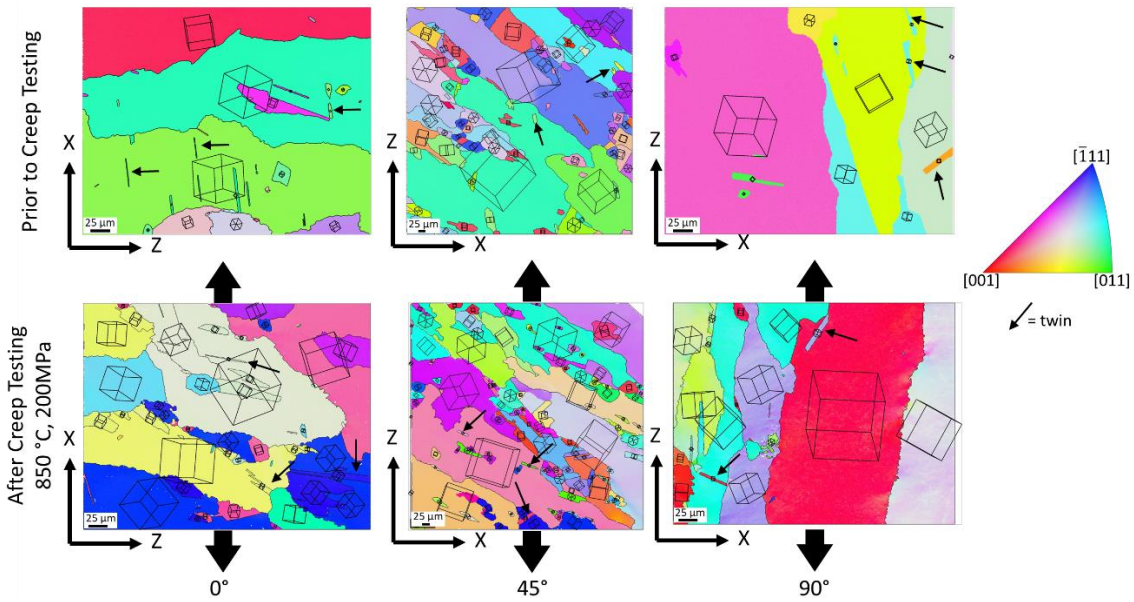

b)

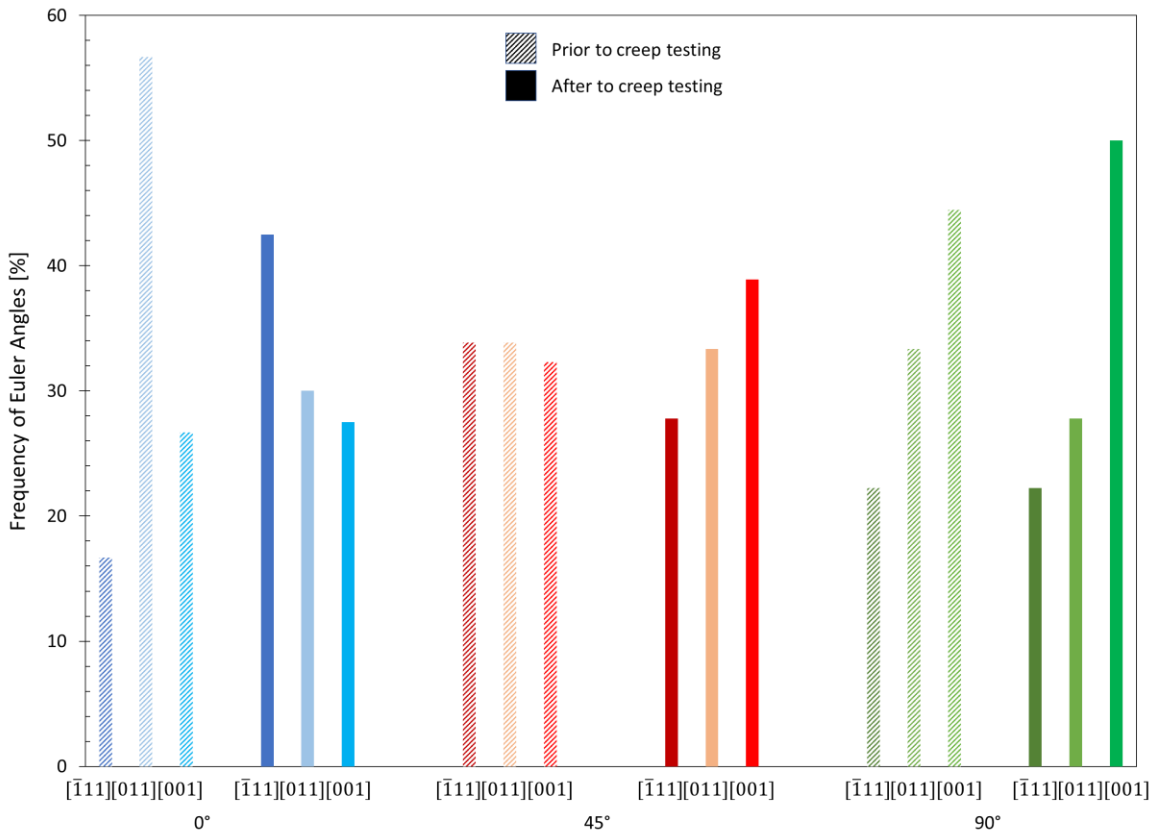

Figure 81 a) Euler angles for IN738LC witness samples oriented in 0°, 45°, 90° tested at 850 °C/200 MPa. The arrows indicate the load direction; b) Frequency of Euler angles for all build orientation prior to and after creep testing (850 °C/200 MPa) determined from a)

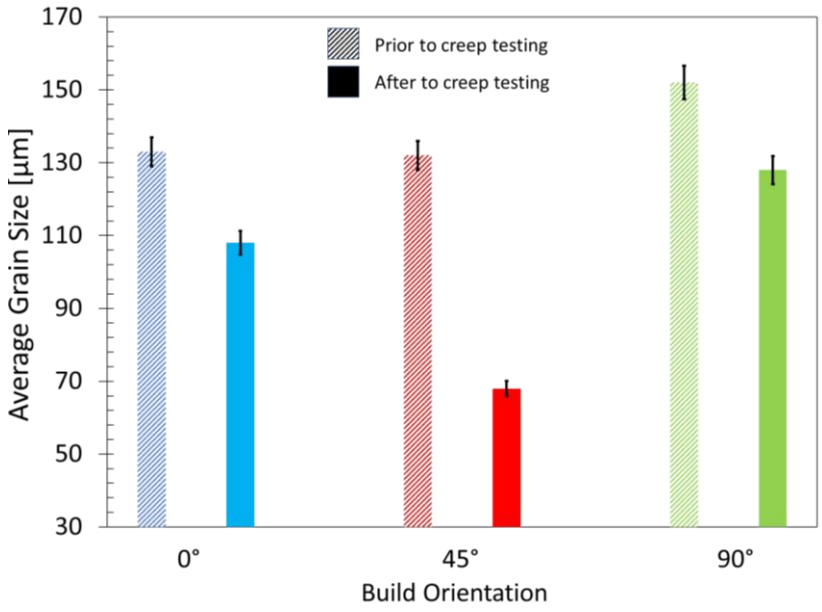

Figure 82 Average heat-treated grain size for witness samples with build orientations 0°, 45°, 90° prior to and after creep testing at 850 °C and 200 MPa

6.3.2 Creep Mechanisms affecting Creep Rate

In a first step, the deformation mechanisms map (see Figure 83) is used to determine the expected creep deformation mechanisms. Based on the creep deformation mechanisms map, the expected dominant deformation mechanism at 850 °C/200 MPa are:

- Grain Boundary Sliding,
- Dislocation Climb and
- Micro-twinning.

The following chapters examine these three deformation mechanisms to determine the reason behind the faster creep rate seen in the 45° build orientation.

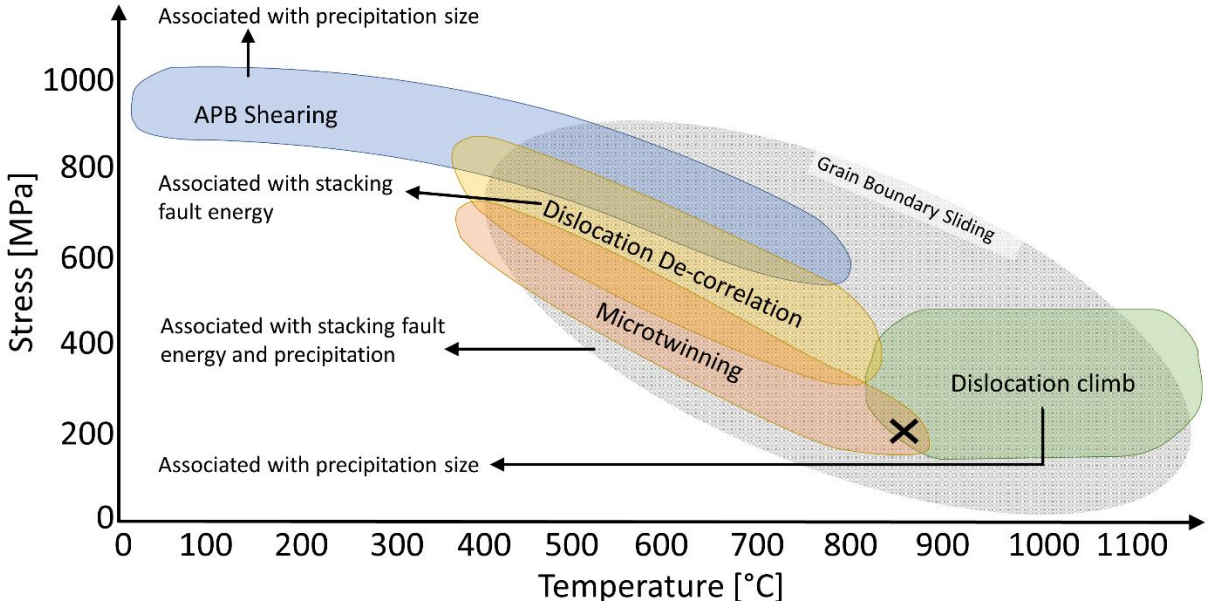

Figure 83 Creep deformation mechanism map to determine expected creep deformation mechanisms at 850 °C and 200 MPa

IN738LC creep tests were carried out at multiple applied net stresses at 850 °C. Figure 84 shows the Norton plot at 850 °C for stresses ranging from 150 MPa – 240 MPa. For a detailed description about the Norton plot refer to [205]. Norton's law is inserted in Figure 84, where $\dot{\varepsilon}$ is the secondary creep rate, A is a material constant and a function of temperature, σ is the stress and n is the stress exponent. The gradient of the dotted lines in Figure 84 is equivalent to the stress exponent. As can be seen, all build orientations were described with Norton exponents between 3 and 5, confirming dislocation creep as a possible creep deformation mechanism [205].

It should be noted that the 45° build orientation shows the lowest value for the stress exponent, indicating that grain boundary sliding is also a possible creep deformation mechanism [206,207].

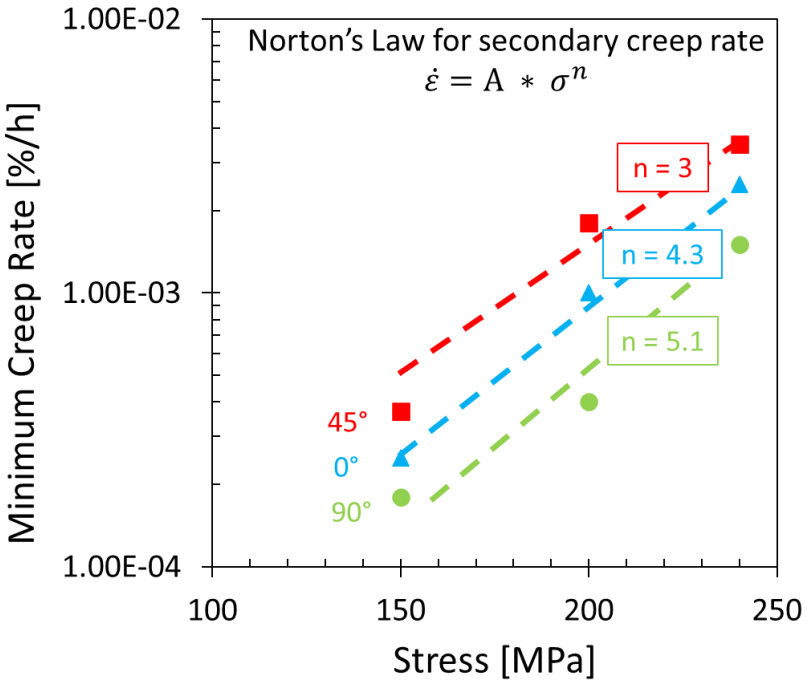

Figure 84 Norton plot for 850 °C IN738LC witness samples for 150 – 240 MPa

6.3.2.1 Grain Boundary Sliding

As a possible active deformation mechanism, grain boundary sliding should be discussed. The difference in grain size was already shown above (see Figure 82). The 45° build orientation shows a significant smaller grain size after creep compared to the other two build orientations. The change in grain size not only indicates CDRX, but also increases the grain boundary area allowing grain boundary sliding to occur.

Besides the grain size and grain orientation, grain boundary sliding is also affected by carbides pinning the grain boundaries. Prior to creep testing all build orientations showed carbides accumulating at grain boundaries (see witness samples in Figure 52). Representative SEM-images of the microstructure after creep testing (at 850 °C/200 MPa) for 0°, 45° and 90° witness samples are shown in Figure 85. Twins can be found in all build orientations. The γ' precipitates can be seen in the enlarged images in Figure 85b, d and f for all build orientations. After creep, carbides can be identified primarily at the grain boundaries in Figure 85a and e for the build orientations 90° and 0° respectively. The presence of carbides is further confirmed with Cr-EDX mappings. Figure 86 shows that the 0° and 90° build orientations exhibit Cr along the grain boundaries. Correlating the EDX maps to the SEM images in Figure 85, these precipitates are $Cr_{23}C_6$ type carbides. These carbides pin the grain boundaries, thereby reducing the creep rate. In comparison, no carbides can be identified at the grain boundaries after creep for the 45° build orientation (see Figure 85c). The 45° build orientation does not show Cr segregations either (refer to Figure 86). Therefore, a microstructural change occurred during creep testing in the 45° build orientation.

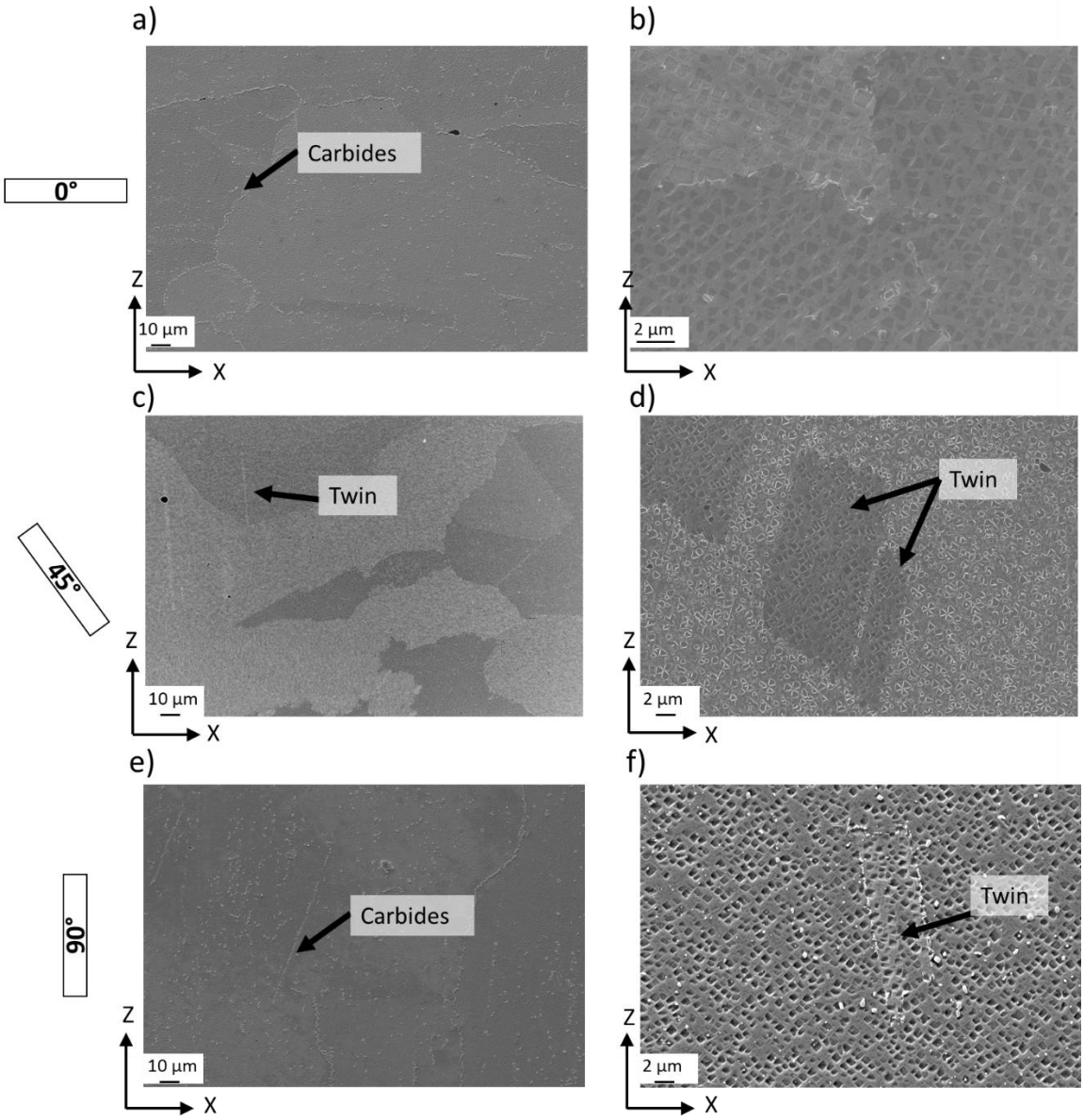

Figure 85 IN738LC SEM-images of witness samples after creep testing (850 °C/200 MPa): a) 90° sample in XZ-plane; b) Detailed image of a; c) 0° sample in XZ-plane; d) Detailed image of c; e) 45° sample in XZ-plane; f) Detailed image of e

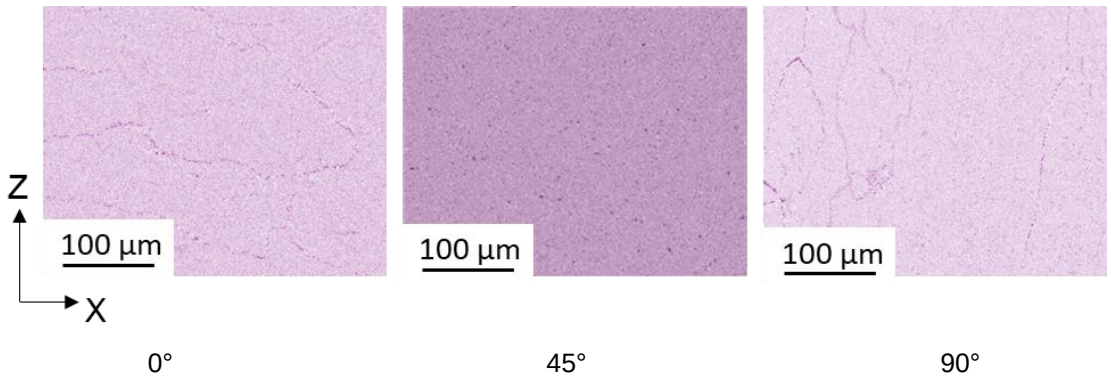

Figure 86 Cr elemental distribution in witness samples for 0°, 45° and 90° build orientation tested at 850 °C/200 MPa

In order to characterize the change in microstructure during creep testing in the 45° build orientation further, the phases are investigated by means of EBSD (see Figure 87). The 0° and 90° build orientations show a combination of face center cubic (fcc) phases (i.e. γ and γ') and carbides. The 45° sample shows a combination of fcc (i.e. γ and γ') phases and hexagonal close packed (hcp) phases.

The hcp-phase in IN738LC includes the η-phase (Ni_3Ti or Ni_3Ta). The η-phase forms only when exposed to temperatures between 850 °C to 950 °C. At that temperature range, Ti- and/or Ta-carbides decompose thereby enriching the grain boundaries with Ti and Ta [20]. Since the formation of the η-phase is dependent on the dissolution of carbides, this hcp-phase forms at grain boundaries. The η-phase is known to increase strength and reduce ductility due to the incoherency of the hcp crystal structure with the γ-matrix [20,21]. The theoretical possibility to form Ni_3Ti for the specific alloy composition was verified by the phase diagram shown in Figure 50. Since grain boundary pinning carbides (i.e., MC) dissolve for the formation of the η-phase, grain boundary sliding can occur more readily.

The reason for the η-phase only forming in the 45° build orientation and not in the other two build orientations can be found when considering the thermal distributions, discussed in Chapter 5.2. The fast solidification of the 0° build orientation does not allow enough time for the η-phase to form, since thermal exposure is required for the decomposition of carbides to occur. The in-situ heat treatment of the 90° build orientation homogenizes elemental distribution of Ti and Ta, hindering η-phase formation. The 45° sample retains temperatures of roughly 1000 K (compare Figure 37b), allowing for optimal η-phase formation conditions.

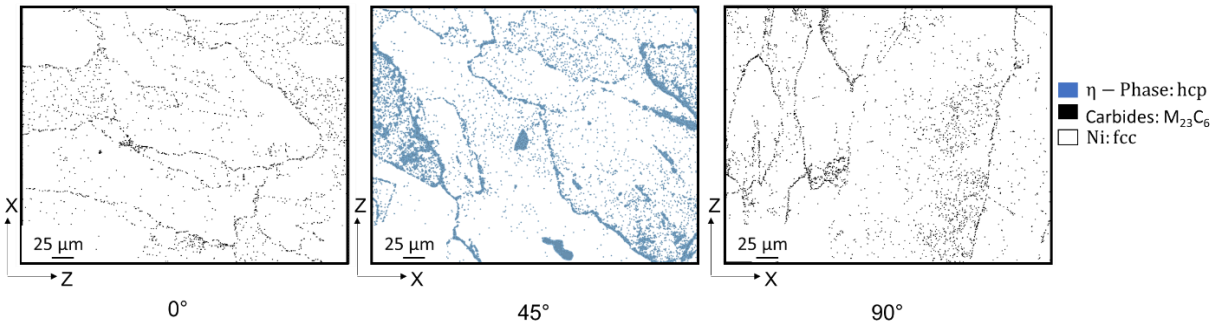

Figure 87 Phase identification in IN738LC witness samples for 0°, 45° and 90° build orientation

Grain boundary sliding is inhibited in 0° and 90° build orientation due to carbide formation at grain boundaries. However, the 45° build orientation does not show carbides due to η-phase formation, allowing for grain boundary sliding.

6.3.2.2 Dislocation Climb

Dislocation climb is a possible creep deformation mechanism according to the creep deformation mechanism map shown in Figure 83. Dislocation climb is based on dislocation mobility, which preferably occurs at high temperatures.

The deformation was analysed using EBSD, as shown in Figure 88. As can be seen, for the 0° build orientation deformation occurs mostly around grain boundaries. This can be correlated to the found $M_{23}C_6$ carbides, which characteristically resolve stresses around them. While the 90° build orientation also shows deformation peaks at grain boundaries (also due to $M_{23}C_6$ carbides), deformation occurred more homogeneously within this build orientation.

The 45° build orientation on the other hand does not show deformation peaks at grain boundaries, but rather at triple points where multiple grains meet. This can be attributed to the lack of $M_{23}C_6$ carbides as well as the dominance of HAGBS (refer to Figure 79).

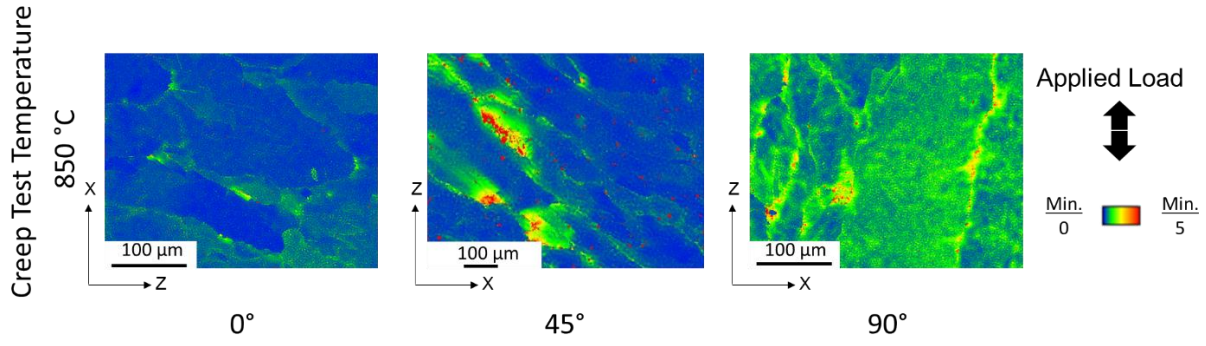

Figure 88 EBSD Deformation maps for witness samples tested at 850 °C/200 MPa

Since the 45° build orientation contains mostly HAGBs, a dislocation pile-up can be expected because these grain boundary types hinder dislocation mobility. The dislocation pile up was confirmed for the 45° build orientation with TEM-analysis, as shown in Figure 89. No dislocation pile-up was found for the 0° or 90° build orientation. TEM-analysis was also used to determine dislocation density within the different build orientations. The difference in dislocation density can clearly be identified in Figure 90. As can be seen, the 45° build orientation shows a significant increase (factor 1000) in dislocation density compared to the other two build orientations. These dislocation pile-ups and increased dislocation density indicate that dislocation mobility is inhibited within the 45° build orientation. Dislocation climb is therefore not a dominant creep deformation mechanism within the 45° build orientation compared to the 0° and 90° build orientation.

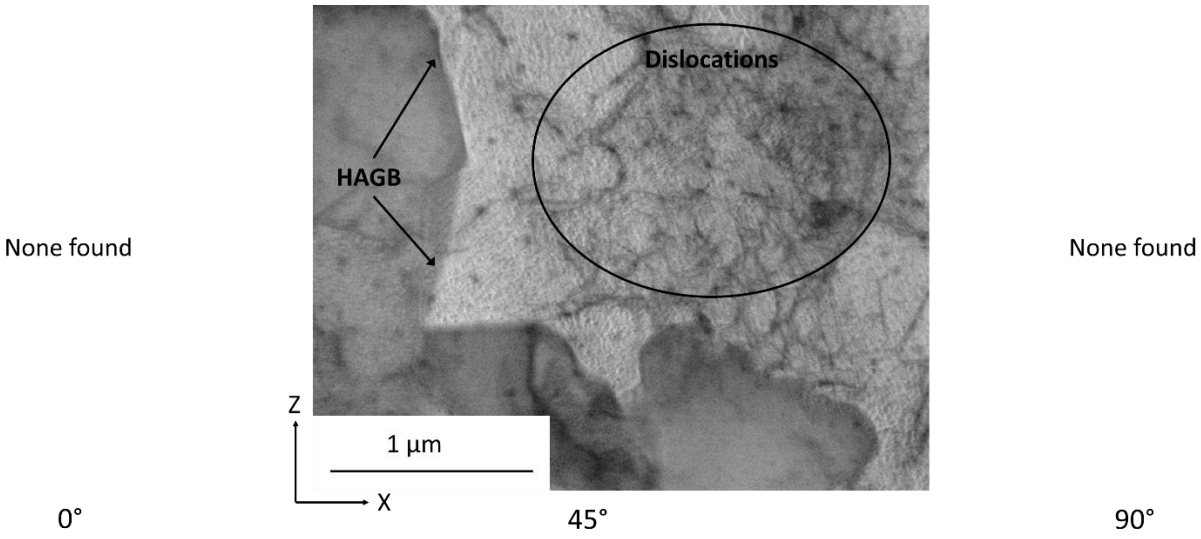

Figure 89 Representative TEM-image of the 45° build orientation showing a dislocation pile-up near HAGBs

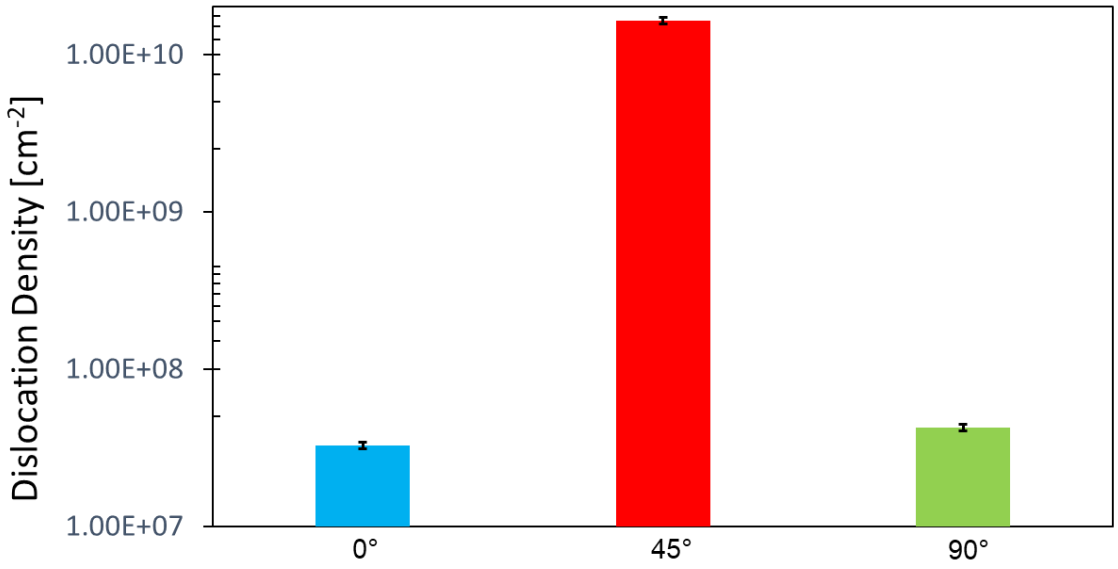

Figure 90 Dislocation density after creep testing at 850 °C and 200 MPa in 0°, 45° and 90° build orientation

6.3.2.3 Micro-Twinning

Micro-twinning is the third expected creep deformation mechanism according to the deformation mechanism map, shown in Figure 83.

Twinning is visible in all build orientations for samples tested at 850 °C/200 MPa (as shown in Figure 91). The twin density increases from 90° to 0° to 45° build orientation, as shown in Figure 92a. As mentioned in Chapter 2, twins can either be mechanical or annealing twins. To determine which twin type formed in this study, the twin density was determined prior to creep testing and after creep testing. As can be seen in Figure 92a, the twin density for the 90° build

orientation is similar prior to and after creep testing, meaning that in the 90° sample, mostly annealing twins formed during the post-processing of the sample prior to creep testing. This result is also in agreement with the results of Sanchez-Mata et al. [144]. The twin density in the 0° build orientation is higher after creep testing compared to that prior to creep testing, meaning there is a mixture of annealing and mechanical twins. The mechanical twins formed during creep testing due to the applied mechanical load. The 45° build orientation shows a significant increase in twin density after creep testing compared to prior to creep testing. This result indicates that while there is a mixture of annealing and mechanical twins, similar to 0° build orientation, the mechanical twins dominate in the 45° build orientation. Mechanical twins are typically found in hcp-phases [150], such as the η-phase, which was found in the 45° build orientation.

Figure 92b shows a clear correlation between twin density and creep rate: With increasing twin density, the creep rate increases.

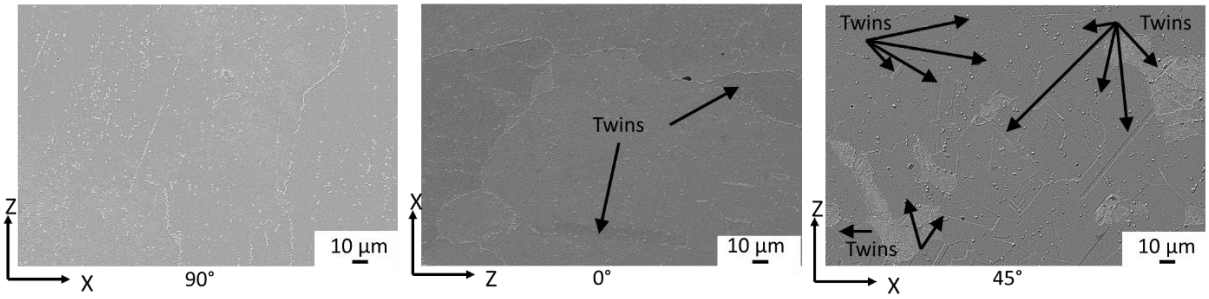

Figure 91 SEM-images of creep samples (witness) tested at 850°C/200 MPa to show the difference in twin density

a)

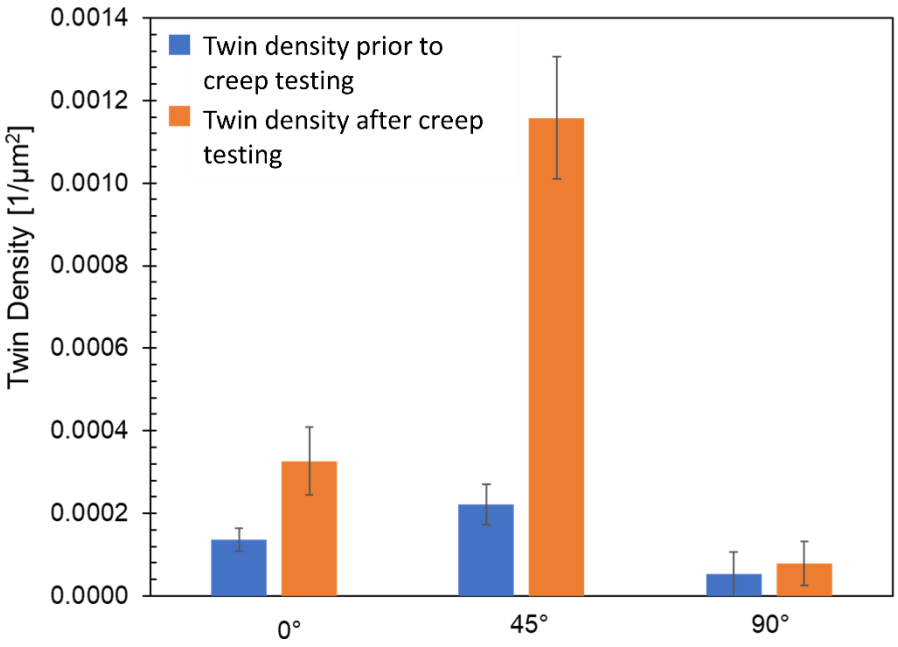

b)

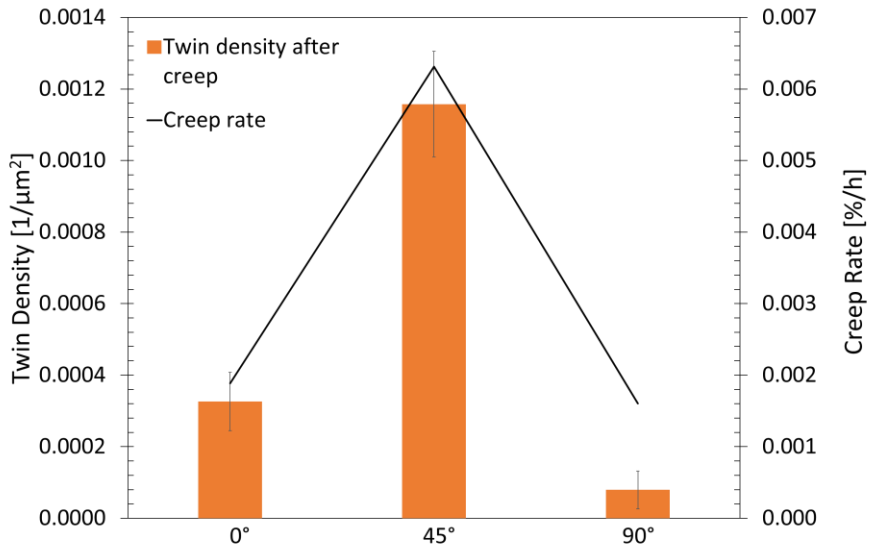

Figure 92 a) Twin density depending on build orientation prior to and after creep testing (850 °C/200 MPa); b) Twin density after creep and creep rate depending on build orientation (850 °C/200 MPa)

Twin dimensions are affected by elemental distribution. As previously shown, Cr distribution was different between the build orientations. Therefore, the distribution of alloying elements was further characterized using EDX (see Figure 93). As can be seen, Nb is homogenously distributed in the 0° and 90° build orientation, while Nb segregations can be found in the 45° build orientation. According to Egan et al., Nb was found to reduce the twin thickness [208,209]. The twin thickness for all build orientations was measured prior to and after creep testing. The results are shown in Figure 94. As can be seen, the twins in the 45° build orientation are thinner compared to 0° and 90° oriented samples.

a)

b)

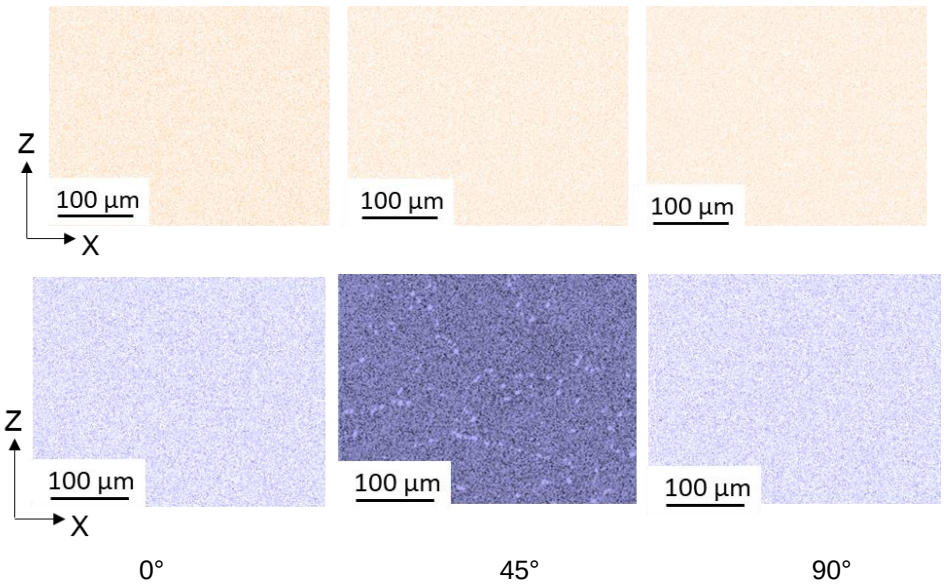

Figure 93 Elemental distribution in witness samples for 0°, 45° and 90° build orientation tested at 850 °C/200 MPa: a) Mo, Al, Fe, Ti, Zr; b) Nb

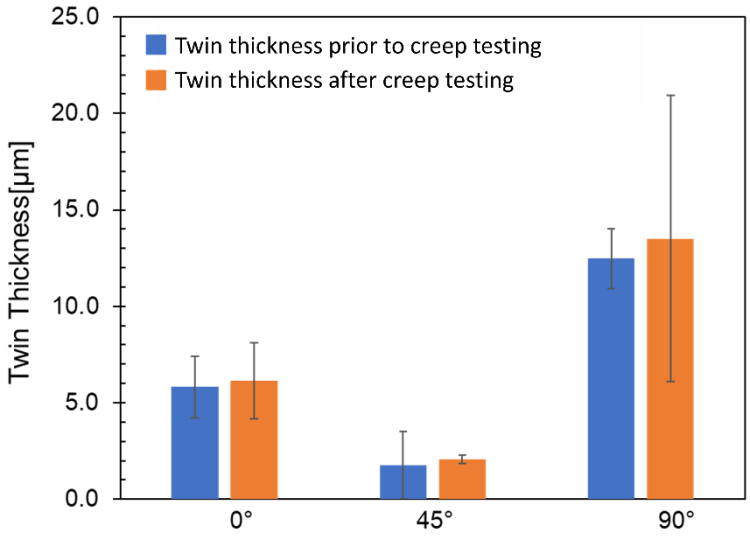

Figure 94 Twin thickness for all build orientations (0°, 45°, 90°) prior to and after creep testing (850 °C/200 MPa)

As mentioned in the introduction, Nb atmospheres increase the formation of micro-twins. The 45° build orientation, which contains Nb clusters, shows significantly thinner twins compared to the other two build orientations, thereby raising the assumption that micro-twins could have formed. Besides Nb reducing twin thickness and increasing the formation of micro-twins, Nb segregations also lead to increased Stacking Faults Energies (SFE) [172,174], which correlates well with the assumption of micro-twin formation. Since higher SFE inhibit dislocation mobility, twinning is energetically favorized compared to slip, which explains the significantly higher twin density in the 45° build orientation. A change in SFE is also suspected due to the local difference in chemical composition found. Clusters of refractory metals, such as Cr and Nb, have also been found to be an indication of increased stacking faults and their respective energies [172,174]. According to Gallagher [210] SFE is heavily dependent on alloying elements and temperature. Small changes in alloying elements even on the atomic scale significantly affect the SFE. Ikeda et al. confirmed that the SFE depends on local concentrations of Cr, Co and Ni [211]. The SFE was found to increase significantly when Cr is either depleted or occupies the crystal structure (almost) completely [211], just as is the case in $M_{23}C_6$ carbides. Since in this study, chemical composition varies locally, the SFE of the 45° build orientation is assumed to be higher compared to the other two build orientations.

Since the Nb clusters reduce twin thickness and thereby the possible operating slip systems [209], the Euler angles discussed above were used to obtain Schmid factor frequency maps for three different slip systems (see Figure 95):

- $\{111\} < 1\bar{1}0 >$ → fcc slip system
- $\{111\} < 2\overline{11} >$ → slip system when Superlattice Intrinsic Stacking Faults (SISF) are present and/or micro-twins are present
- $\{111\} < \bar{2}11 >$ → slip system when Superlattice Extrinsic Stacking Faults (SESF) and/or micro-twins are present

The Schmid factor frequency maps identify how frequent a slip system was active. As seen in Figure 95a, the 90° sample shows a uniform activation of the $\{111\} < 1\bar{1}0 >$ slip system. Contrary to the 90° build orientation, the 0° and 45° build orientation show a non-uniform and lower frequency of the $\{111\} < 1\bar{1}0 >$ slip system.

Figure 95b shows the results for the slip system $\{111\} < 2\overline{11} >$. As can be seen in the 0° sample, no significant change to Figure 95a is identified. For the 90° sample a homogenously activated slip system can still be seen. The 45° sample shows a more homogeneous frequency compared to the slip system shown in Figure 95a. The grains, in which a sudden change occurred for the $\{111\} < 1\bar{1}0 >$ slip system, show an activated Schmid factor for the slip system $\{111\} < 2\overline{11} >$. This indicates that it is likely that SISFs are present, as the slip system $\{111\} < 2\overline{11} >$ is closely linked to SISFs.

Figure 95c shows the results for the slip system $\{111\} < \bar{2}11 >$, which is closely linked to SESFs. The results for 0° and 90° build orientations remain similar to those seen in Figure 95b. In the 45° sample, the grains in which low Schmid Factors are seen in Figure 95a and b, are replaced by a higher Schmid factor frequency in Figure 95c. This indicates the presence of SISF (as seen in Figure 95b) and SESF (as seen in Figure 95c).

As discussed in Chapter 2.3.1, the presence of SISF and SESF increase the SFE and increase the formation of micro-twins during creep. The increased SFE inhibits dislocation mobility. The energy required for dislocation slip in the 45° build orientation is therefore higher compared to twinning.

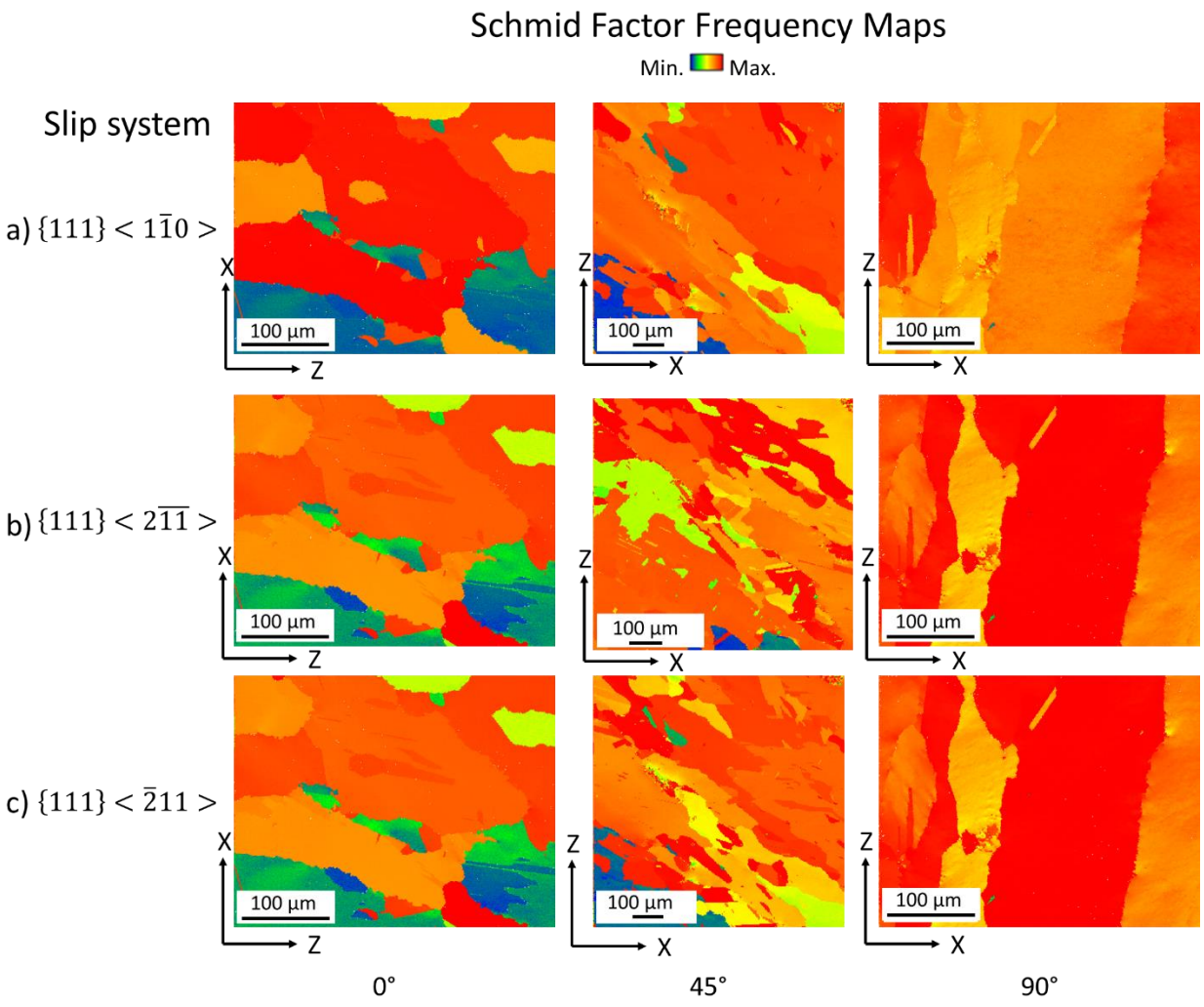

Figure 95 Schmid factor maps for different slip systems in witness samples tested at 850 °C/200 MPa:
a) $\{111\} < 1\bar{1}0 >$***; b)*** $\{111\} < 2\bar{1}\bar{1} >$***; c)*** $\{111\} < \bar{2}11 >$

The dislocation mobility is inhibited in the 45° sample by Nb segregations, a reduced number of slip systems and an increased amount of HAGBs. Once grain boundaries (mostly HAGBs, refer to Figure 79) are met by dislocations, the resulting dislocation pile up will lead to the reduced time to rupture. The dislocation pile up was shown in Figure 89.

Based on the results above and the assumption of micro-twin formation as a possible mechanism to increase the 45° creep rate, the twins present were investigated more closely (see Figure 96). Figure 96 shows representative image of the twins for the respective build orientations. On the right-hand side, the images are labelled for simplified visualization. Whereas the twins in the 0° and 90° build orientations do not show a structure, the 45° twins, do show a structure for the entire length of the twin.

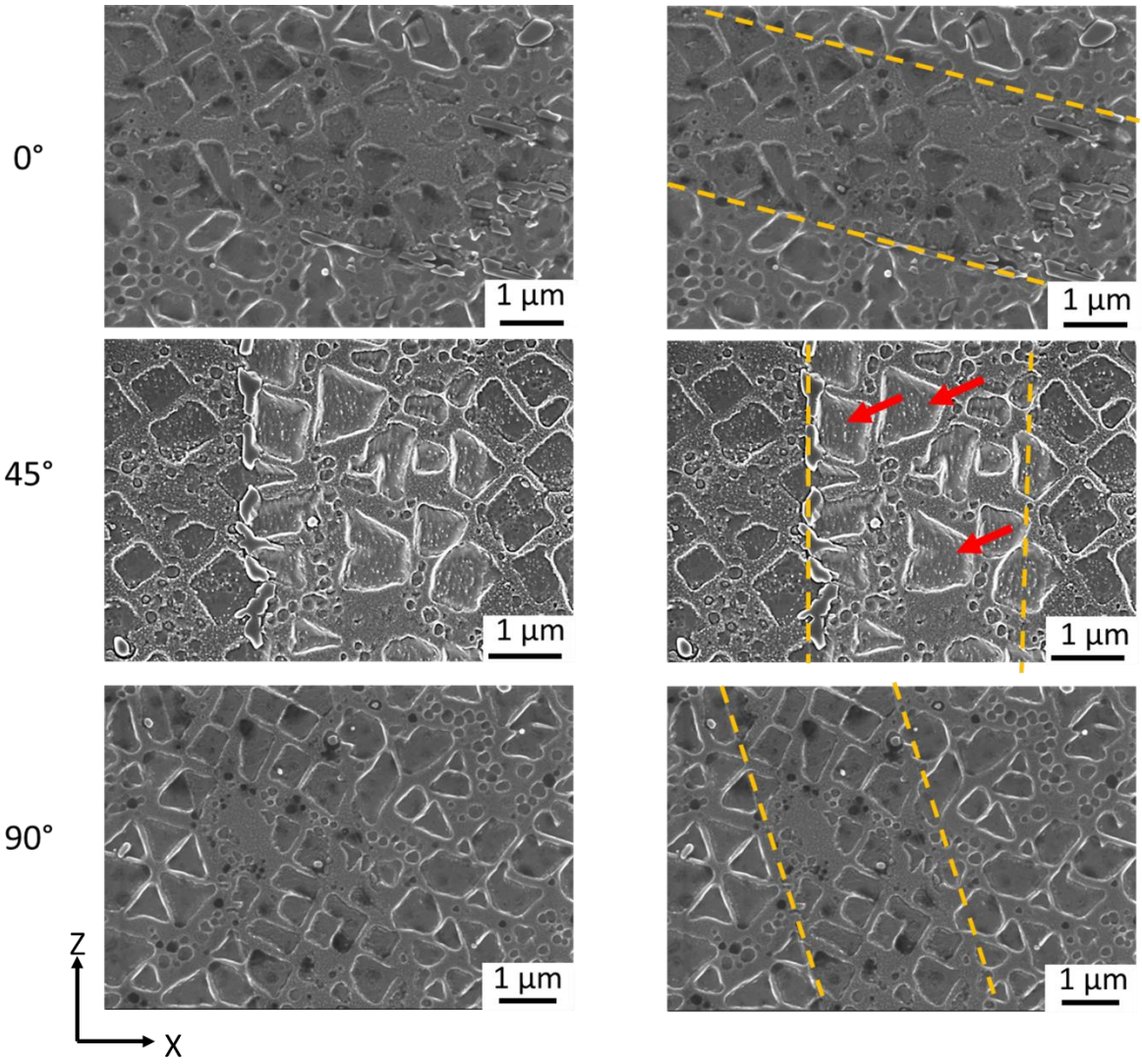

Figure 96 Twin structure for 0°, 45° and 90° build orientation tested at 850 °C/200 MPa. The images on the right are identical to the left images with added visualization aids

The clusters of refractory metals, the expected increased SFE, the Schmid factor frequency maps and the structure within twins are all indicators for micro-twinning within the 45° build orientation. The fracture surface of the 45° build orientation shown in Figure 77, is similar to that reported by Barba et al. for samples containing micro-twins [166]. TEM analysis was carried out to confirm these suspicions. Micro-twins were found for the 45°in the γ/γ'structure (see Figure 97). Close to the micro-twins, a dislocation pile-up can be seen in Figure 97 confirming the reduced number of slip systems. Micro-twins were not found for the other two build orientations, 0° and 90°. This is the first time micro-twins are confirmed in additively manufactured samples [212].

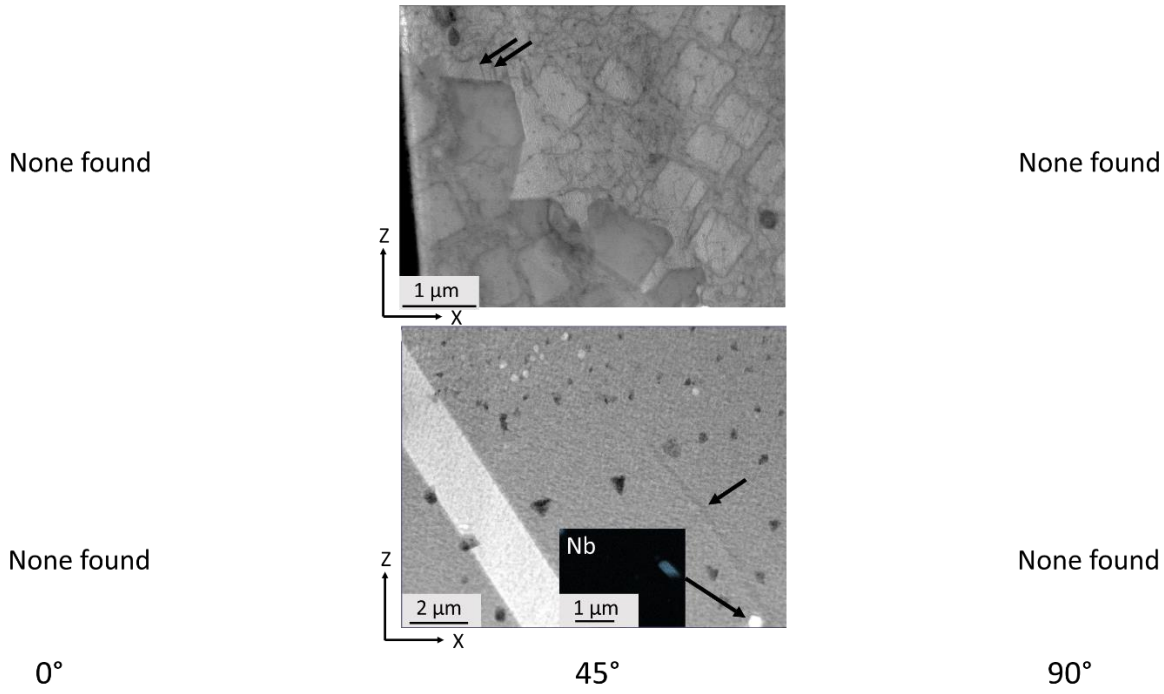

Figure 97 Micro-twins found in 45° build orientation in witness samples tested at 850 °C/200 MPa

Therefore, whereas dislocation creep is the primary creep deformation mechanism in 0° and 90° build orientation, the following creep deformation mechanisms are active in the 45° build orientation:

- Grain boundary sliding
- Micro-twinning

6.4 IN718 vs. IN738LC Creep Behavior

Unlike the reported similar mechanical behavior (hardness and tensile properties) of IN718 and IN738LC (Chapter 5.3), the creep behavior is found to be very different. Whereas for IN718 the 45° orientation lies within the bounds of 0° and 90° regarding creep failure strain and time to rupture, the IN738LC 45° build orientation has the shortest time to rupture and the highest creep rate.

The difference in creep behavior is attributed to phase evolution differences (i.e. η-phase) between both Ni superalloys. In the case of IN718, the phases formed are similar for all build orientations, only the distribution and shape varied. In the case of the IN738LC 45° sample, η-phase formed due to the particular thermal behavior of this build orientation leading to carbide dissolution, increasing creep rate and affecting micro-twin formation. In comparison, the grain boundary strengthening phase in IN718 is the δ-phase (Ni_3Nb). Since the δ-phase already occupies the grain boundaries, the hcp η-phase does not readily form in IN718.

6.5 Response to Research Question 2

It can be generally summarized that creep behavior varies significantly depending on alloy composition. Hence the response to research question 2 is not the same for the alloys considered IN718 and IN738LC.

IN718 creep behavior is not sensitive to build orientation.

The IN738LC composition however responds differently to the different thermal conditions identified for the different build orientations during PBF-LB/M processing. Whereas the 0° and 90° behave similar to IN718, the creep rate of the IN738LC 45° build orientation is faster compared to the other two build orientations. The differences found in elemental distribution and phase formation lead to multiple active creep deformation mechanisms within the 45° build orientation.

6.6 IN738LC Creep Properties of Witness and Extracted Samples

To examine differences in creep behavior between IN738LC witness and extracted samples, creep tests at 850 °C and 240 MPa were carried out for both sample types. Figure 98 shows the creep results for extracted and witness samples. As can be seen, the witness and extracted samples follow the same trend. For witness samples, the longest time to rupture for the 90° sample is 1,342 h and the creep failure strain is 5.27%. The 0° sample has a lower time to rupture of 335 h and a creep failure strain of 2.42%. The 45° sample shows the lowest time to rupture after 194 h and a creep failure strain of 2.78%. A similar behavior is seen for extracted samples. Creep failure strains of 3.97%, 1.65% and 2.38% and times to rupture of 2.348 h, 309 h and 171 h are recorded for 90°, 0° and 45° build orientation respectively.

Similar to the IN738LC creep results observed for witness samples at 750 /350 MPa and 850 °C/200 MPa, the creep rate of the 45° specimens is higher compared to the other two build orientations, also the difference in the tertiary stage is similar to that seen in Figure 75.

Figure 99 summarizes these creep characteristics of extracted and witness samples and their respective build orientations. In general, the extracted samples follow the same trend as the witness samples (discussed above): The 0° samples show the lowest creep failure strains, whereas the 90° samples show the largest creep failure strain (see Figure 99a). The 45° samples show creep failure strains inbetween those of 0° and 90° samples. The time to rupture of the 45° samples shows the lowest values compared to the 0° and 90° samples (see Figure 99b). The creep rates of the 45° build orientation are accordingly highest compared to 0° and 90° build orientations.

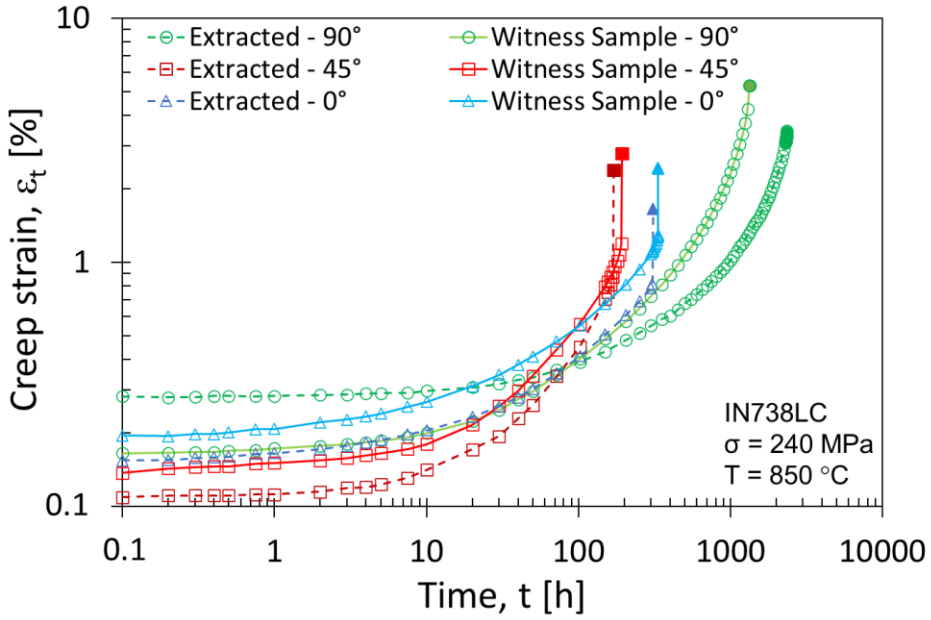

Figure 98 Creep curves of IN738LC at 850 °C at 240 MPa for extracted and witness samples

a) b)

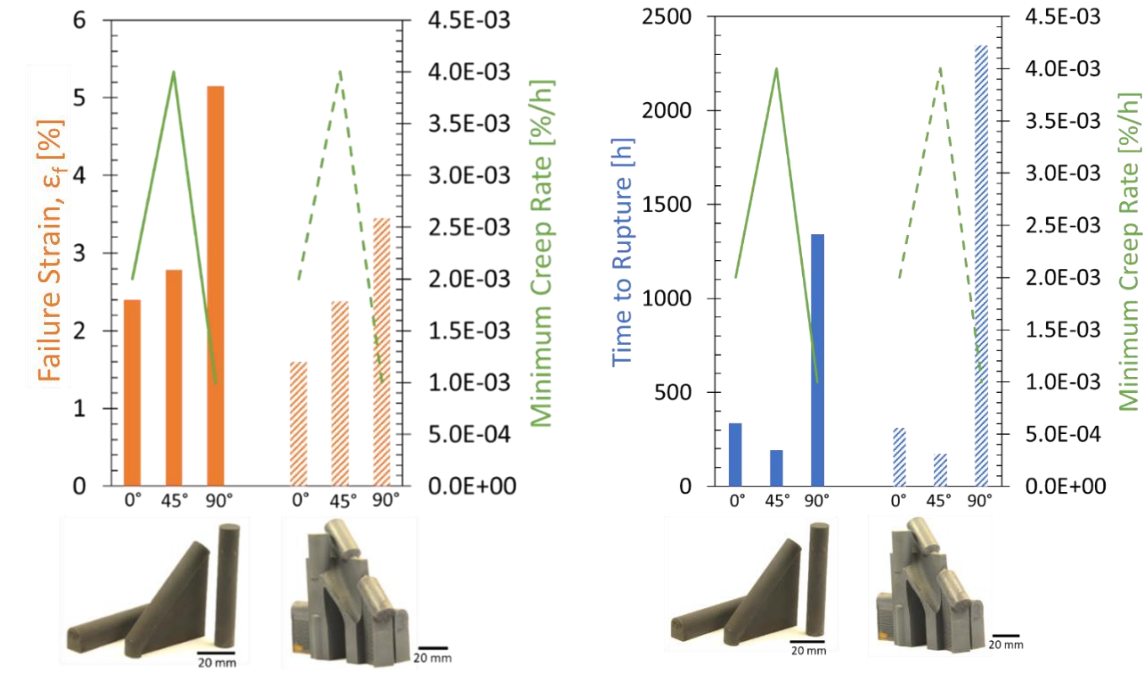

Figure 99 a) Overview of creep failure strain and minimum creep rate for IN738LC for witness and extracted samples tested at 850 °C/240 MPa; b) Overview of time to rupture and minimum creep rate for IN738LC for witness and extracted samples tested at 850 °C/240 MPa

The witness and extracted samples are analyzed using EBSD. IPF-Z poles for the creep tested witness and extracted samples (tested at 850 °C and 240 MPa) are shown in Figure 100. Oriented grains parallel to build direction can clearly be identified for 90° witness and extracted samples. The grain size difference discussed in Chapter 5.2.2 can also be clearly identified in Figure 100. The extracted samples show finer grain sizes compared to witness samples.

For witness samples, the dominant grain orientation in the 90° orientation can be identified as a combination of [111] and [001], whereas in the 90° extracted sample the dominant grain orientation is [001]. The 45° build orientation for both witness and extracted samples do not show a dominant grain orientation. The 0° build orientation for witness samples shows a dominant grain orientation combination of [111] and [101], whereas for the extracted sample, similar to the 45° build orientation, no dominant grain orientation can be identified.

The grain orientation of the extracted 0° sample can be explained by considering the solidification conditions (see Figure 37b and Figure 39b). The 0° sample experiences the faster effective cooling rates (see Chapter 5.2.4). This not only leads to a refined grain size but also, the favorable grain orientations along the vertical thermal gradient do not have a chance to overgrow non-favorable grain orientations.

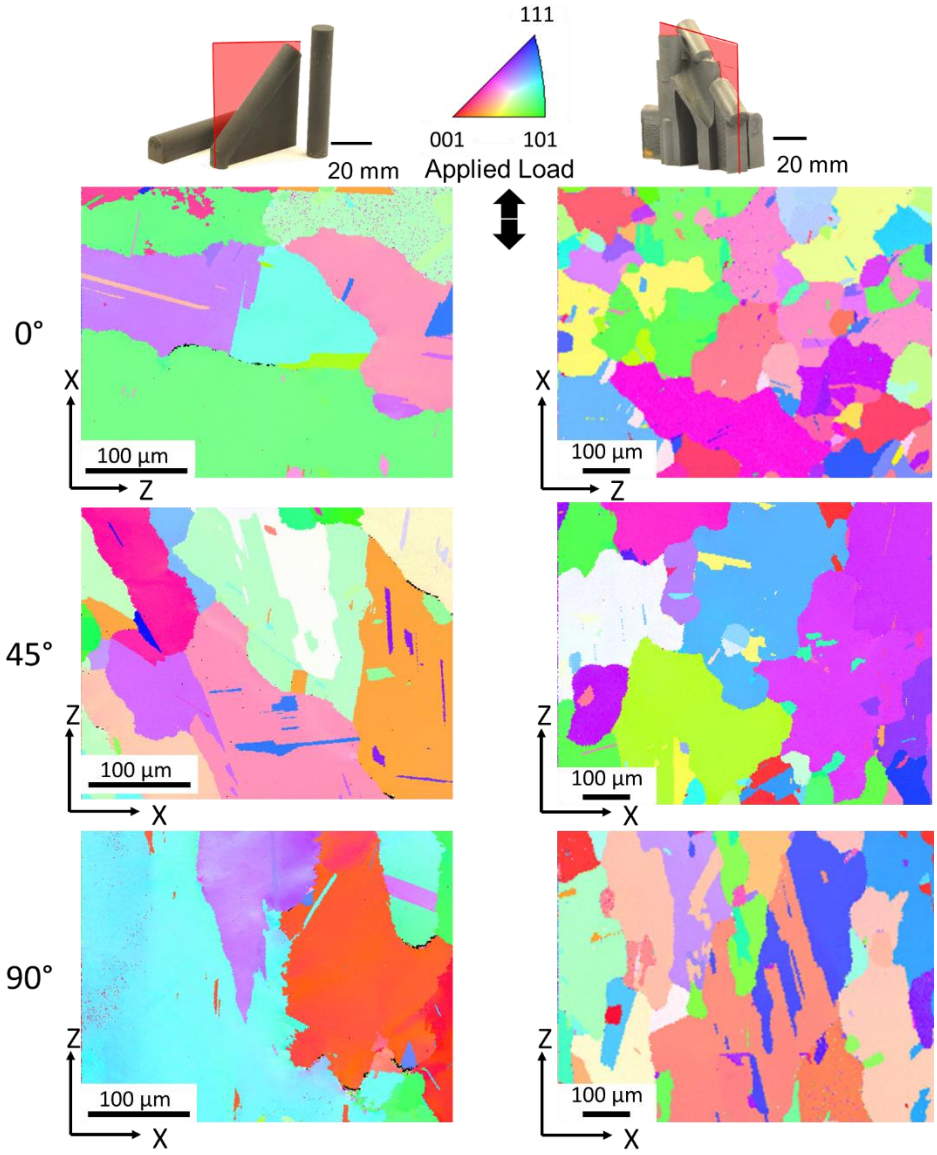

Figure 100 IPF-Z poles (parallel to build direction) after creep for witness and extracted samples tested at 850 °C and 240 MPa

Similar to the witness samples discussed above, the distinct twinning in all samples in Figure 100 is noteworthy. The twin density and twin thickness is presented in Figure 101. While twin density is highest for the 45° build orientation for both extracted and witness samples, the general twin density of extracted samples is lower compared to those of witness samples. The opposite trend can be seen for the twin thickness. The 45° build orientation (witness and extracted) shows the smallest twin thickness compared to 0° and 90°.

The lower twin density in extracted samples is attributed to the smaller grain sizes (see Figure 54 in Chapter 5.2.2) due to higher effective cooling rates (see Figure 39 in Chapter 5.2). The energy necessary for twin formation is higher in fine grained materials. Instead, dislocation slip is energetically more favorable.

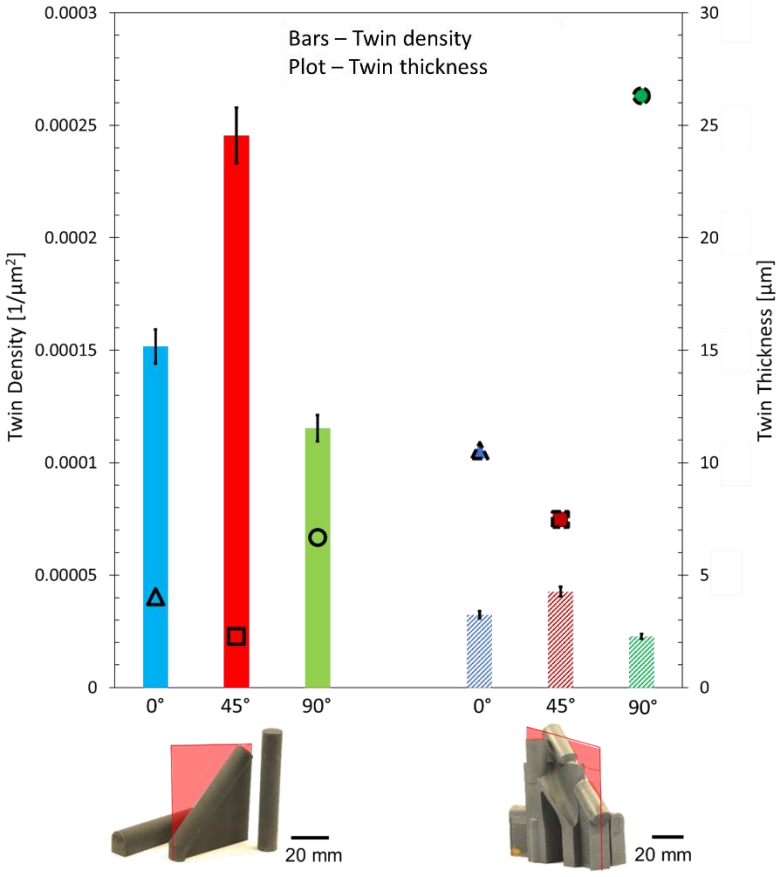

Figure 101 Twin thickness (bars) and twin thickness (plots) after creep for witness and extracted samples tested at 850 °C and 240 MPa

When considering the microstructure further, grain orientation after creep should be considered. For this purpose, Euler angles after creep were determined for witness and extracted samples.

Figure 102 shows the frequency of Euler angles after creep for witness and extracted samples and the respective build orientations. Similar to the witness samples discussed in the chapters above, the frequency of Euler angles after creep provides an explanation for the creep failure

strains documented in Figure 98. Grain orientations parallel to the load direction accommodate the applied load more evenly than grain orientations perpendicular to build direction. Therefore, a dominant grain orientation of [001] leads to increased creep failure strains. As can be seen from Figure 98, the 0° build orientations (witness and extracted) show the lowest creep failure strains. Accordingly, the 0° build orientations show the lowest accumulation of [001] grain orientations. The extracted 45° sample shows a minimal lower creep failure strain compared to the witness sample (the difference is negligible). Even so, the extracted 45° sample shows less [001] grain orientations compared to the witness sample.

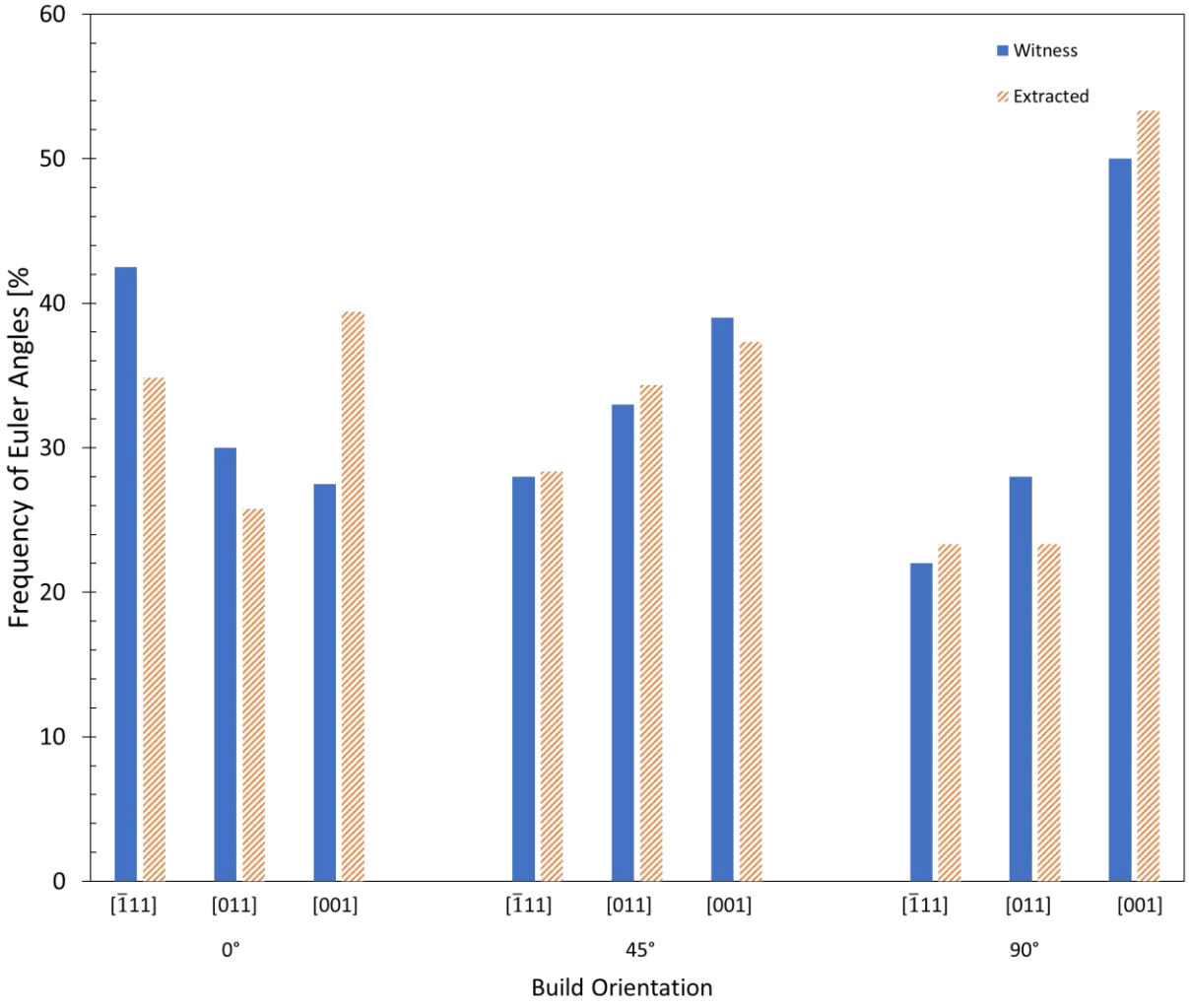

Figure 102 Frequency of Euler angles after creep for witness and extracted samples tested at 850 °C and 240 MPa

The respective Euler angles are shown as Inverse Pole Figures (IPF measured in Z-direction) in Figure 103. Again, the cube wire frames drawn in Figure 103 for each grain indicate how the respective grain is oriented. The grain orientation with regard to the respective neighboring grains differs significantly, as verified by the grain boundary angles (see Figure 104). In general, the 45° build orientation shows mostly High Angle Grain Boundaries (HAGBs >12°; shown in red), while the 0° and 90° build orientations show a combination of HAGBs (more

dominant) and Low Angle Grain Boundaries (LAGBs <12°; shown in black). The HAGBs are at least partially caused by twin boundaries. The reorientation associated with twins causes an increase in the surrounding grain boundary angles [150].The misorientation caused by HAGBs within the lattice also introduces a strain, which increases strength [150]. The misalignment within the lattice due to the HAGBs hinder dislocation movement reducing ductility [150].

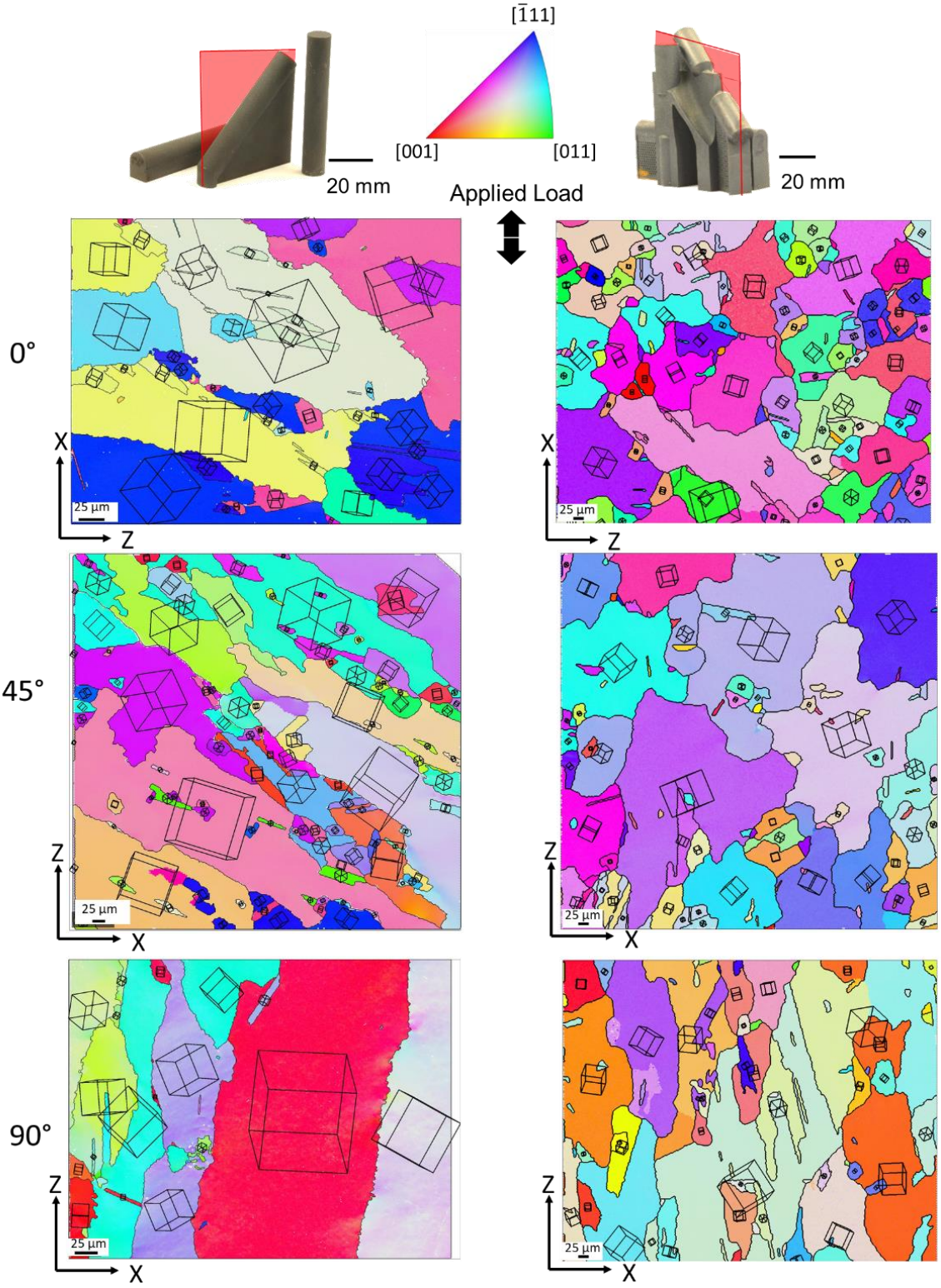

Figure 103 Euler angles after creep for witness and extracted samples tested at 850 °C and 240 MPa

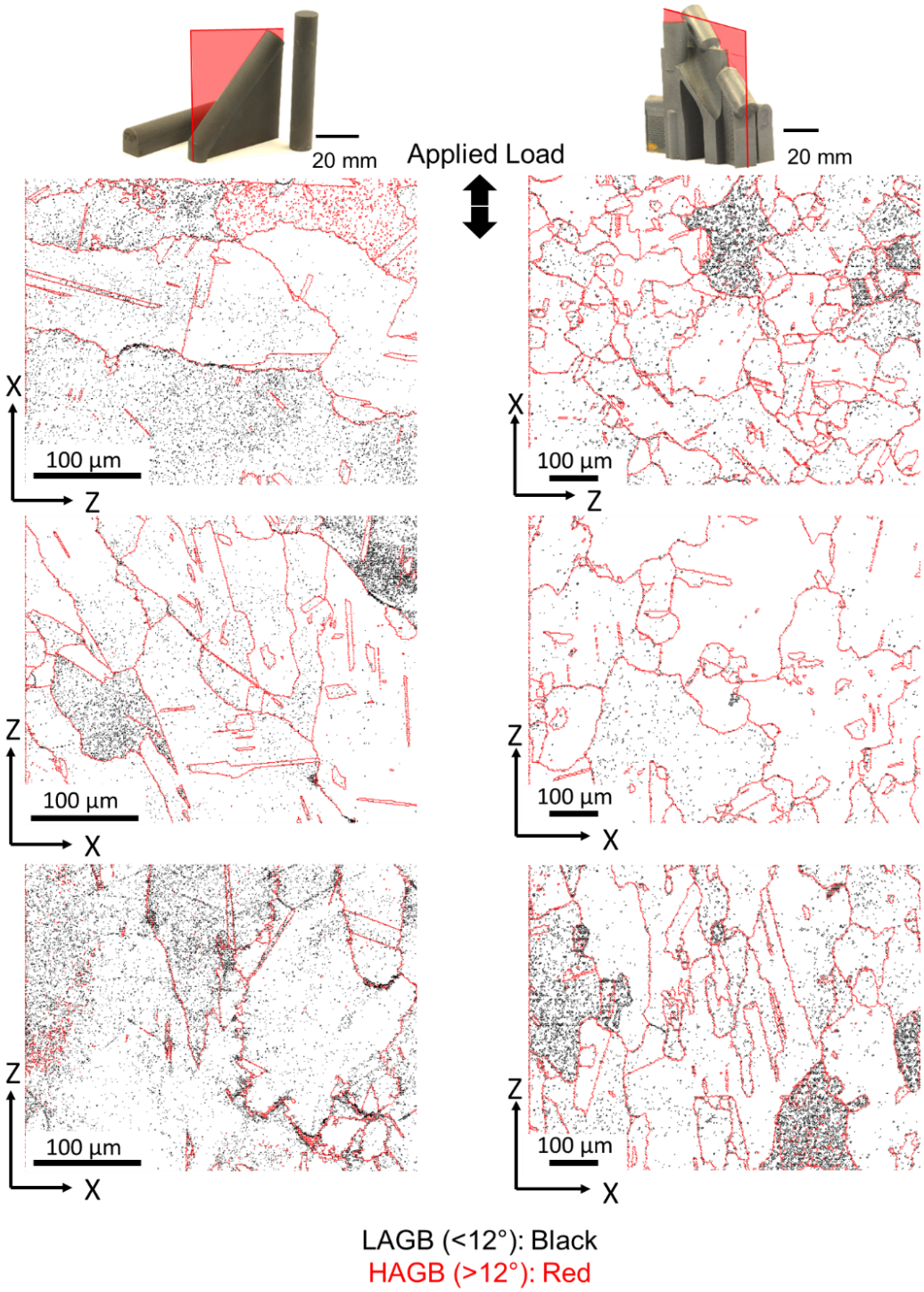

Figure 104 Grain boundary angles after creep for witness and extracted samples tested at 850 °C and 240 MPa

For research question 1, it was concluded that witness samples do not fully represent (samples extracted from) components microstructurally and in turn in mechanical properties (Vickers hardness and tensile properties).

The creep results discussed showed that while witness and extracted samples do show similar trends, the creep results (e.g. times to rupture) differ, indicating that the smaller grain sizes in

extracted samples lead to generally shorter creep life. Therefore, the response to research question 1 does not need to be amended.

It should be noted that further creep results should be performed to verify the similar trends between witness and extracted samples. Creep results in due course of this thesis are ongoing and yield promising results confirming the conclusions to research question 1. A summary of the documented comparison between witness and extracted samples is presented in Figure 105.

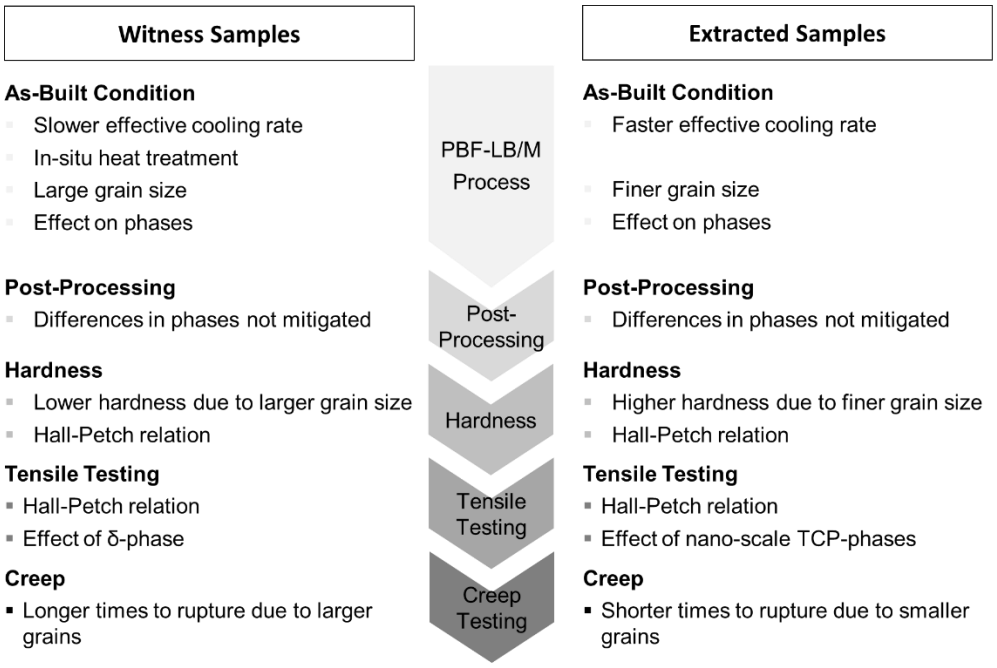

Figure 105 Comparative representation of results for witness and extracted samples

7 Conclusion and Outlook

The aim of this thesis was to identify correlations between the PBF-LB/M microstructure and (long-term) mechanical properties of IN718 and IN738LC for the reliable use in high temperature applications. In order to fulfill this aim, two research questions were studied based on the knowledge gaps identified in the literature review:

1. To what extent are microstructural and mechanical properties of witness samples representative of large-scale components?
2. How do build orientation and microstructure affect creep mechanisms?

In this study, a Sample Extraction Component (SEC) was developed that allows sample extraction in three orientations: 0°, 45° and 90°. Witness samples in the same build orientations were manufactured for comparison. The investigated materials were IN718 and IN738LC. The solidification conditions and microstructure for extracted and witness samples as well as for the three build orientations were characterized to determine the effect on mechanical properties. Based on the results of this study, the following conclusions can be drawn with regards to the studied research questions:

1. To what extent are microstructural and mechanical properties of witness samples representative of large-scale components?

From the results of this study, the microstructure and mechanical properties of witness samples are not directly transferrable to components due to the following reasons:

- The SEC and witness samples experience different solidification conditions. The witness samples (90° and 45°) experience an in-situ heat treatment, while the SEC and 0° witness sample cool significantly faster in comparison. The different solidification conditions cause differences in grain size, phase formation and segregation behavior. For a faster estimation of the solidification conditions, an analytical model was proposed, which agrees with the results of the numerical model and experimental microstructures but requires further validation.
- Based on CALPHAD calculations, a difference in phases formed is predicted. This difference was verified with XRD and SEM analysis.
- The smallest grain size was found for extracted samples from the SEC. Witness samples (45° and 90°) were found to show larger grain sizes. Since grain sizes differ, mechanical properties are also affected. Due to the small grain size, the hardness of extracted samples exceeds the hardness of witness samples. Extracted samples show higher UTS and $R_{P0.2}$ and lower elongations compared to witness samples in this study, but also compared to studies found in literature.

- IN738LC creep behavior of witness and extracted samples show similar trends with generally lower creep lives of extracted samples, which is correlated to the reduced average grain sizes. This result should however be verified with further test parameters.

Further studies regarding research question 1 that are worth deeper analysis include (but are not limited to):

- The microstructural difference between witness and extracted samples was not mitigated with the applied heat treatments. Adaptations of post-processing (e.g. including a quenching step) should be considered to achieve a microstructural similarity between witness and extracted samples.
- The use of different support structures for components and witness samples should be studied, to analyze the effect on thermal history and whether the documented differences in solidification conditions could be mitigated by using different support structures for the different build orientations.
- The analytical model, presented in Chapter 5.2.4, must be validated using different geometries to be used universally. The applicability of different materials should also be investigated.
- This thesis studied round samples and voluminous components. The effect of thermal conditions on thin-walled structures and fine features should be investigated.

The qualification standard (DIN EN ISO/ASTM 52920) states that witness samples should be printed alongside the component to be used in application. The witness samples should be analyzed according to the qualification properties (e.g. relative density, static or dynamic properties) depending on the application to qualify the component for qualification. While witness samples can be used to assess the repeatability of the build quality, the results of this thesis show that the microstructure and mechanical properties of witness samples cannot be readily transferred to samples extracted from voluminous components.

Depending on the application, PBF-LB/M components should be qualified by using microstructural and mechanical results of extracted samples rather than witness samples. In order to assess component quality reliably, witness samples should have comparable volumes and solidifications conditions. Corresponding considerations for PBF-LB/M component qualification requires further work and research.

2. How do build orientation and microstructure affect creep mechanisms

Based on the results of this study, the effect of build orientation on creep properties is strongly dependent on alloy composition and PBF-LB/M thermal history:

- The creep behavior of IN718 and IN738LC build orientations does not follow the same trend. While the creep behavior of IN718 is as expected (45° lies within the bounds of 0°

and 90° build orientation) and agrees with the tensile behavior, the creep behavior of IN738LC is not as expected since the 45° build orientation shows the highest creep rate. This unexpected IN738LC result, was confirmed at different temperatures and applied stresses. The cause behind this 45° behavior is explained by the phases formed and the microstructure leading to different creep mechanisms taking place in comparison to 0° and 90° build orientation.

- The solidification conditions of the 45° orientation and the long-term exposure to high temperatures causes the formation of different phases dependent on alloy composition. In IN738LC, η-phase is formed due to the increased exposure of the 45° build orientation to temperatures ranging between 850 °C – 950 °C during PBF-LB/M processing leading to the dissolution of grain boundary pinning carbides.
- The solidification conditions in 45° samples lead to energetically favorable twinning rather than dislocation slip, causing the twin density in the 45° build orientation to be significantly higher compared to the other two build orientations. Due to the different solidification conditions, elemental distribution (i.e. Nb segregations) results in reduced twin thickness in the 45° build orientation. Micro-twins were found in the 45° build orientations but not in 0° or 90°.
- Multiple slip systems are active in 45° samples. Based on the type of active slip systems, SISFs and SESFs are suspected, which would raise the SFE. The presence of these stacking faults will need to be investigated in future work.

Further studies regarding research question 2 that are worth deeper analysis include (but are not limited to):

- The preliminary creep results of the extracted samples should be validated with more creep tests at different temperatures with different applied stresses.
  In a second step, the creep deformation mechanisms of (samples extracted from) components should be analyzed and identified.
- The formation of the η-phase should be studied in other Ni-superalloys with a similar chemical composition as IN738LC.
- The results of this thesis highlight the importance of creep databases for different materials and processing routes. Based on an established database, categorizing alloys based on their chemical composition and on their susceptibility of η-formation might be considered for simplified identification whether additional build orientations are required for creep characterization.

In summary, the build orientation does have a significant influence on creep behavior. It is however dependent on the specific alloy composition dictating the phases formed during solidification, heat treatment and testing at elevated temperatures.

The identified correlations and results clearly show that further research is required in the qualification of PBF-LB/M components for reliable use in high temperature applications. Thermal conditions during the PBF-LB/M process for the samples should be numerically simulated prior to manufacturing to ensure that solidification conditions are comparable. This could also speed up the qualification process.

In terms of build orientation, the 45° build orientation is worth characterizing to describe the creep behavior. The creep deformation mechanisms are heavily dependent on the phase formation and microstructure, which undergoes changes during creep leading to different creep mechanisms for the different build orientations.

8 Appendix

8.1 Appendix A: Role of Alloying Elements

Table 16 Nominal material compositions of IN18 and IN738LC and role of alloying elements [4,8,32,36–39]

Element	IN718 [wt.%]	IN738LC [wt.%]	Effect
Al	0.8	3.7	• Precipitation strengthening • Improves oxidation resistance
B	0.0015	0.012	• Prevents grain boundary sliding increasing strength • Increases crack susceptibility
C	0.08	0.13	• Carbides prevent grain boundary sliding • Increases crack susceptibility
Co	1	9	• Reduction in precipitate size with increased Co • Reduces the overall number of carbides • Affects carbide morphology
Cr	21	16.3	• Provides corrosion resistance • Carbide former
Cu	0.3	0	• Improves thermal conductivity
Fe	11.14	0.05	• Solid solution strengthener
Mn	0.35	0.02	• Provides corrosion resistance • Acts as a solid solution strengthener
Mo	3.3	2	• Provides corrosion resistance • Acts as a solid solution strengthener
Nb	5	0.9	• Acts as a solid solution strengthener • Contributes to precipitation
Ni	55	58.6	• Base
Si	0.35	0.3	• Segregation at grain boundaries → embrittlement
Ta	0.05	1.75	• Encourages phase precipitation
Ti	1.15	3.7	• Provides corrosion resistance • Carbide former
W	-	2.8	• Acts as a solid solution strengthener
Zr	-	0.08	• Improves strength through grain boundary pinning • Increases crack susceptibility

8.2 Appendix B: PBF-LB/M Feedstock

The feedstock of the PBF-LB/M process is metal powder. The build quality of PBF-LB/M components is strongly affected by the properties of the metal powder used [194,213–215].

Powders can be water-, gas- or plasma-atomized. Gas- and plasma-atomized powders achieve a higher powder particle sphericity, which improves powder flowability [216] and thereby improves the recoating process.

PBF-LB/M powder size distribution usually ranges from 15 µm to 63 µm and is typically characterized by a D_{10} to D_{90} range. D_{10} and D_{90} values indicate the percentiles (10%, 90%) of the cumulative powder distribution (i.e. 10% of the cumulative powder distribution lie below the D_{10} value).

The large surface area to volume ratio of the powder particles increases the risk of oxygen uptake from the atmosphere leading to defects during PBF-LB/M manufacturing. Increased oxygen content can be found in recycled powders [217], which are economically recommended. However, provided that proper handling is ensured such that oxidation and entrainment of impurities are avoided, no consensus about the recycling effect on mechanical properties has been drawn [194,218,219].

8.3 Appendix C: Weldability of Ni Superalloys

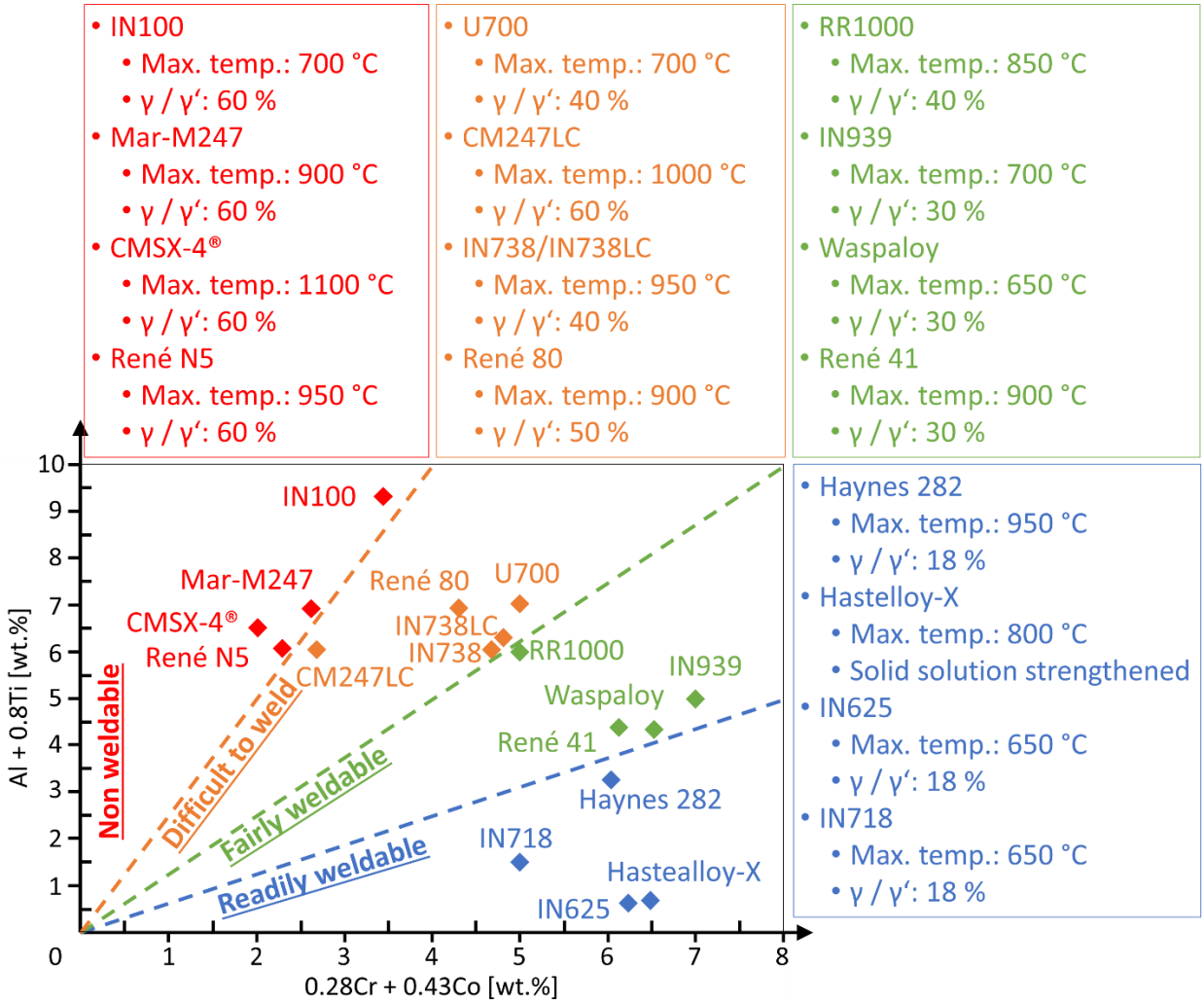

Figure 106 Weldability assessment diagram of Ni superalloy, compiled using [8,61,220–235]

8.4 Appendix D: Overview of PBF-LB/M Process Parameters for IN718 and IN738LC

Table 17 Overview of IN718 and IN738LC process parameters found in literature [11,236,237]

Material	Process Parameter			Range		
				Min.	Max.	E_V [J/mm³]
IN718	Laser Power	P	W	100	250	50- 150
	Scan Speed	v_{scan}	mm/s	80	850	
	Hatch Distance	h	µm	50	160	
	Preheating	T_{pre}	°C	RT	200	
IN738LC	Laser Power	P	W	180	280	50- 150
	Scan Speed	v_{scan}	mm/s	200	1100	
	Hatch Distance	h	µm	80	120	
	Preheating	T_{pre}	°C	RT	1000	

8.5 Appendix E: Typical Cracking Mechanisms in Ni Superalloys

There are four typical cracking mechanisms in Ni superalloys [4,100,238–243]:.

Solidification Cracking – Hot crack

During solidification the cooling material shrinks exerting a tensile stress on the melt pool. The high solid fraction inhibits backfilling of interdendritic regions, which act as crack initiation point [244,245]. The susceptibility to solidification cracking increases with an increased solidification range (i.e. larger mushy zone) [246]. Ergbewande et al. [247] suggest, that solidification cracks occur at high energy input and was able to reduce solidification cracks by reducing energy input, leading to smaller melt pools and a larger fraction of low angle grain boundaries

Liquation Cracking – Hot crack

This type of cracking occurs during rapid heating of the solid material to a temperature below the overall liquidus temperature. The grain boundary phases will melt first; these liquid films act as crack initiation point [41,248]. Heat Affected Zones (HAZ) can also act as a crack initiation site for liquation cracking [249].

Ductility Dip Cracking – Hot Crack

At intermediate temperatures, a reduction in material ductility occurs. This ductility reduction coupled with thermal stresses introduced by material shrinkage could induce cracking within the material. There is still a debate about the exact mechanism of ductility dip cracking (DDC). Literature suggests that DDC is caused by stress concentration around grain-boundary carbides, which act as crack initiation points. It has been reported that DDC tends to form at grain boundary angles greater than 15° [245].

Hot cracks are generally found near grain boundaries due to segregations and shrinkage [99,100]. The differentiation between hot crack types is often challenging [4]. Zhong et al. found five different grain boundary/interface cracks, where three out of five crack mechanisms could not be named [99].

Strain Age Cracking – Cold Crack

Repeated re-heating of the material leads to Strain Age Cracking (SAC). The residual stresses already present within the part combined with the shrinkage due to volume changes and/or heat treatment form cracks [240]. Heat treatment would be required for this cracking to occur [41,250]. The x-axis of the weldability graph shown in Figure 106 is correlated to the susceptibility to SAC. The higher the value on the x-axis, the higher the susceptibility to SAC.

9 List of Figures

10 List of Tables

11 List of Equations

12 Abbreviations

γ	Gamma Phase
γ'	Gamme Prime Phase
γ''	Gamma Double Prime Phase
δ	Delta Phase
η	Eta Phase
σ	Sigma Phase (Type of Topologically Close Packed Phases)
μ	Mu Phase (Type of Topologically Close Packed Phases)
ε	Strain
ρ	Density in g/cm^3
ν	Laser Scan Velocity
λ	Thermal conductivity $\frac{W}{m \cdot K}$
°C	Degrees Celsius
2D	Two (2) dimensional
3D	Three (3) dimensional
2L	Two (2) Layer
3L	Three (3) Layer
A	Interface area between sample/component and substrate plate
AB	As Built
Al	Aluminium
AM	Additive Manufacturing
APB	Anti Phase Boundary
APT	Atom Probe Tomography
B	Boron
BCC	Body Center Cubic
BCT	Body Center Tetragonal
BD	Build Direction
BO	Build Orientation

C	Carbon
c_p	Specific heat (capacity)
CAD	Computer Aided Design
CALPHAD	CALculation of PHAse Diagrams
Co	Cobalt
Cr	Chromium
CSF	Complex Stacking Fault
CT	Computer Tomography
Cu	Copper
DDC	Ductility Dip Cracking
E_A	Area Energy Density
E_L	Linear Energy Density
E_V	Volume Energy Density
EBM	Electron Beam Melting
EBSD	Electron Back Scatter Diffraction
EDX	Energy Dispersive X-Ray Spectroscopy
f_L	Fraction Liquid
f_S	Fraction Solid
Fe	Iron
FCC	Face Center Cubic
GB	Grain Boundary
h	Layer thickness
H	Sample/component height
HAGB	High Angle Grain Boundary
HAZ	Heat Affected Zone
HCP	Hexagonal Close Packed
HIP	Hot Isostatic Pressure
HT	Heat Treatment / heat treated
K	Kelvin

k	Partition Coefficient
LAGB	Low Angle Grain Boundary
LMD	Laser Metal Deposition
LOF	Lack of Fusion
LOM	Laminate Object Manufacturing
LPT	Local Phase Transformation
Mo	Molybdenum
Mn	Manganese
Nb	Niobium
NDT	Non Destructive Testing
Ni	Nickel
P	Phosphorus
P_L	Laser Power
PBF-LB/M	Metal Laser Powder Bed Fusion
ps	pseudo
PSD	Particle Size Distribution
PX	Poly crystal/Polycrystalline
Q_v	Volumetric heat source.
RT	Room Temperature
S	Sulfur
SAC	Strain Age Cracking
SEC	Sample Extraction Component
SEM	Scanning Electron Microscope
SF	Stacking Fault
SFE	Stacking Fault Energy
Si	Silicon
SISF	Superlattice Intrinsic Stacking Fault
SESF	Superlattice Extrinsic Stacking Fault
SLA	Stereolithography

STA	Solution Treatment and Ageing
SX	Single Crystal/Single crystalline
t	Time
Δt	Build time
T	Temperature
ΔT	Temperature difference between average build temperature and chamber temperature
$T_{Liquidus}$	Liquidus Temperature
$T_{Solidus}$	Solidus Temperature
Ta	Tantalum
TCP	Topologically Close Packed
TEM	Transmission Electron Microscope
Ti	Titanium
UTS	Ultimate Tensile Strength
W	Tungsten
X_0	Alloy of interest
X_L	Mole Fraction Liquid
X_S	Mole Fraction Solid
XRD	X-Ray Diffractometry
y	Hatch distance
Zr	Zirconium

13 List of Publications

Journals (Peer-Reviewed)

- Kaveh, K.; Kamachali, R.D.; Khedkar, A.; Manzoni, A.; Jácome, L.A.; Schriever, S.; Saliwan-Neumann, R.; **Megahed, S.**; Kamrani, S.; Heinze, C.; Fedelich, B. Creep anisotropy of additively manufactured Inconel-738LC: Combined experiments and microstructure-based modeling, *Materials Science and Engineering: A*, 2024, 907, 146690, doi: 10.1016/j.msea.2024.146690
- **Megahed, S**.; Krämer, K.M.; Heinze, C.; Kontermann; C; Udoh, A.; Weihe, S.; Oechsner, M., Development and evaluation of generic test pieces for creep property assessment of Laser Powder Bed Fusion components, *Journal of Engineering for Gas Turbines and Power,* 2024, 146(6), doi: 10.1115/1.4065267
- **Megahed, S**.; Krämer, K.M.; Heinze, C.; Kontermann; C; Udoh, A.; Weihe, S.; Oechsner, M.; Creep of LPBF IN738LC: Effect of Build Orientation and Twinning. *Materials at High Temperatures* 2023, doi: 10.1080/09603409.2023.2261665
- **Megahed, S.**; Krämer, K.M.; Kontermann, C.; Heinze, C.; Udoh, A.; Weihe, S.; Oechsner, M. Micro-Twinning in IN738LC Manufactured with Laser Powder Bed Fusion. *Materials* 2023, 16, 5918. https://doi.org/10.3390/ma16175918
- **Megahed, S.**; Krämer, K.M.; Heinze, C.; Kontermann, C.; Udoh, A.; Weihe, S.; Oechsner, M. Influence of build orientation on the creep behavior of IN738LC manufactured with laser powder bed fusion, *Materials Science and Engineering A,* 2023, 878, 145197, doi: 10.1016/j.msea.2023.145197
- **Megahed, S**.; Fischer, F.; Nell, M.; Forsmark, J.; Leonardi, F.; Zhu, L.; Hameyer, K.; Schleifenbaum, J.H. Manufacturing of Pure Copper with Electron Beam Melting and the Effect of Thermal and Abrasive Post-Processing on Microstructure and Electric Conductivity. *Materials* 2023, 16, 73. https://doi.org/10.3390/ma16010073
- **Megahed S**, Koch R, Schleifenbaum JH. Laser Powder Bed Fusion Tool Repair: Statistical Analysis of 1.2343/H11 Tool Steel Process Parameters and Microstructural Analysis of the Repair Interface. *Journal of Manufacturing and Materials Processing*. 2022; 6(6):139. https://doi.org/10.3390/jmmp6060139
- **Megahed, S.**; Aniko, V.; Schleifenbaum, J.H. Electron Beam-Melting and Laser Powder Bed Fusion of Ti6Al4V: Transferability of Process Parameters. *Metals* 2022, *12*, 1332. doi: 10.3390/met12081332
- **Megahed, S.**; Bühring, J.; Duffe, T.; Bach, A.; Schröder, K.-U.; Schleifenbaum, J.H. Effect of Heat Treatment on Ductility and Precipitation Size of Additively Manufactured AlSi10Mg. *Metals* 2022, *12*, 1311. doi: 10.3390/met12081311

- Voshage, M.; **Megahed, S**.; Schückler, P.G.; Wen, P.; Qin, Y.; Jauer, L.; Poprawe, R.; Schleifenbaum, J.H. Additive manufacturing of biodegradable Zn-xMg alloys: Effect of Mg content on manufacturability, microstructure and mechanical properties. *Materials Today Communications 2022*, 32, 103805, doi: 10.1016/j.mtcomm.2022.103805.

Conference Publications (Peer-Reviewed)

- **Megahed, S**.; Krämer, K.M.; Heinze, C.; Kontermann; C; Udoh, A.; Weihe, S.; Oechsner, M., ASME Turbo 2023, Development and evaluation of generic test pieces for creep property assessment of Laser Powder Bed Fusion components, June 2023, Boston (Mi), USA
- Koß, S; Holzer, A.; **Megahed, S**; Ziegler, S.; Schleifenbaum, J. H.; Schmitz, K.; Investigation of the coating of hydrodynamic plain bearing contact surfaces by means of Extreme High-Speed Laser Material Deposition (EHLA), 2021, IOP Conf. Ser.: Mater. Sci. Eng. 1097 012016, doi:10.1088/1757-899X/1097/1/012016

Conference Publications

- **Megahed, S.**; Krämer, K.M.; Heinze, C.; Kontermann; C; Udoh, A.; Weihe, S.; Oechsner, M.; Einfluss der Mikrostruktur auf die Kriecheigenschaften von mittels selektiven Laserstrahlschmelzen hergestellten IN718 und IN738LC, November 2023, Proceedings of FVWHT „Langzeitverhalten warmfester Stähle und Hochtemperaturwerkstoffe“, Düsseldorf, Deutschland
- **Megahed, S.**; Krämer, K.M.; Heinze, C.; Kontermann; C; Udoh, A.; Weihe, S.; Oechsner, M.; Kriechverhalten von LPBF IN738LC: Einfluss der Aufbauorientierung auf Zwillingsbildung, November 2023, DVM Seminar Arbeitskreis Additiv gefertigte Strukturen und Bauteile, Berlin, Deutschland, doi: 10.48447/ADD-2023-BB
- **Megahed, S**.; Krämer, K.M.; Herzog, R..; Kontermann; C; Udoh, A.; Oechsner, M.; Vergleich Mechanischer Eigenschaften von LPBF-Proben und Generischer Bauteile, November 2022, DVM Seminar Arbeitskreis Additiv gefertigte Strukturen und Bauteile, Berlin, Deutschland, doi: 10.48447/ADD-2022-BB
- **Megahed, S**.; Krämer, K.M.; Herzog, R..; Kontermann; C; Udoh, A.; Oechsner, M.; Bewertung generischer Bauteile zur Beurteilung von mechanischen Eigenschaften von LPBF-Bauteilen, DVM-Nachrichten DVM-N 74 Frühjahr 2023, Berlin, Deutschland, https://dvm-berlin.de/publikationen/dvm-nachrichten

Under Review

- **Megahed, S**.; Udoh, A.; Herzog, R.; Krämer, K.M.; Kontermann, C.; Weihe, S.; Oechsner, M.; Mechanical Evaluation of Generic Components for Property Assessment of Laser Powder Bed Fusion
- **Megahed, S**.; Kontermann, C.; Krämer, K.M.; Heinze, C.; Herzog, R.; Udoh, A.; Weihe, S.; Oechsner, M., Effect of Component Geometry on Solidification Conditions during Laser Powder Bed Fusion

Conference Presentations

- **Megahed, S**.; Kontermann, C.; Krämer, K.M.; Heinze, C.; Udoh, A.; Weihe, S.; Oechsner, M.: Kriechverhalten von mittels Selektiven Laserstrahlschmelzen hergestellten IN738LC: Einfluss der Aufbauorientierung auf Zwillingsbildung, DVM Arbeitskreis Additive gefertigte Strukturen und Bauteile, November 2023, Berlin, Germany
- **Megahed, S**.; Kontermann, C.; Krämer, K.M.; Heinze, C.; Herzog, R.; Udoh, A.; Weihe, S.; Oechsner, M., Effect of Microstructure on IN718 and IN738LC Creep Properties manufactured with Laser Powder Bed Fusion, FVWHT, November 2023, Düsseldorf, Germany
- **Megahed, S**.; Kontermann, C.; Krämer, K.M.; Heinze, C.; Udoh, A.; Weihe, S.; Oechsner, M., ASTM ESIS Symposium 2023, Effect of Microstructure on Creep Properties of IN738LC Witness Samples and Generic Components manufactured with Laser Powder Bed Fusion, November 2023, Washington D.C., USA
- **Megahed, S**.; Kontermann, C.; Krämer, K.M.; Heinze, C.; Udoh, A.; Weihe, S.; Oechsner, M., ICAM 2023, Effect of Microstructure on Creep Properties of IN738LC Witness Samples and Samples extracted from components manufactured with Laser Powder Bed Fusion, October 2023, Washington D.C., USA
- **Megahed, S**.; Kontermann, C.; Krämer, K.M.; Heinze, C.; Udoh, A.; Weihe, S.; Oechsner, M., ASME Turbo 2023, Development and evaluation of generic test pieces for creep property assessment of Laser Powder Bed Fusion components, June 2023, Boston (Mi), USA
- **Megahed, S**.; Kontermann, C.; Krämer, K.M.; Heinze, C.; Udoh, A.; Weihe, S.; Oechsner, M. ECCC2023, Creep of LPBF IN738LC: Effect of Build Orientation and Twinning, May 2023, Edinburgh, Scotland
- **Megahed, S**.; Kontermann, C.; Krämer, K.M.; Herzog, R..; Udoh, A.; Weihe, S.; Oechsner, M.; Bewertung generischer Bauteile zur Beurteilung von Kriecheigenschaften von LPBF Bauteilen, DVM Arbeitskreis Additive gefertigte Strukturen und Bauteile, November 2022, Berlin, Germany

- **S Megahed, S**.; Kontermann, C.; Krämer, K.M.; Heinze, C.; Udoh, A.; Weihe, S.; Oechsner, M.10. Werkstofftagung VAIS 2022, Influence of LPBF Build Direction on IN738LC Creep Behavior, October 2022, Düsseldorf, Germany
- **Megahed, S**.; Kontermann, C.; Krämer, K.M.; Heinze, C.; Udoh, A.; Weihe, S.; Oechsner, M.; 48. Jahrestagung Schadensanalyse, Entwicklung von Prüfkonzepten zur Bewertung additiv gefertigter Bauteile für den Hochtemperatureinsatz, Oktober 2022, Düsseldorf, Germany
- Brune, T.; Krämer, K.M.; **Megahed S.**; Kontermann, C.; Oechsner, M.; MSE 2022, Correlations between microstructural characteristics of IN718 from different manufacturing routes and mechanical properties under static and cyclic loading, September 2022, Darmstadt, Germany
- **Megahed, S**.; Kontermann, C.; Krämer, K.M.; Heinze, C.; Udoh, A.; Weihe, S.; Oechsner, M.; Influence of LPBF Build Direction on IN738LC Creep Behavior, September 2022, Bamberg, Germany
- Kontermann, K.; **Megahed, S.**; Brune, T.; Krämer, K.M, Gast Vortrag ZHAW Zürich, Additive Fertigung im Bereich von Hochtemperaturwerkstoffen, 21.06.2022, Zürich, Switzerland
- **Megahed, S.**; V. Aniko, V.; Ziegler, S.: Schleifenbaum, J.H.; Manufacturing Constraints of Electron Beam Melting (EBM) and Laser Powder Bed Fusion (LPBF) and their effects on final component quality, EBAM, October 2020, Erlangen, Germany
- **Megahed S.**; Koch**,** R.; Brenker, T.; Ziegler, S.; Schleifenbaum, J.H., LUS4Metals: Hybrid Tooling using Laser Powder Bed Fusion: Possible Applications of Laser Ultrasonic Systems, September 2019, Linz, Austria
- **Megahed S.**; Koch**,** R.; Brenker, T.; Ziegler, S.; Schleifenbaum, J.H., MS&T2019: Tool Repair using Laser Powder Bed Fusion: Microstructural Analysis of the Interface, October 2019, Portland, Oregon, USA
- Fromm, T.; Xuan, Y., **Megahed, S**.; Borchardt, R. Durst, K. Rosiwal, S.M., Damage Tolerant Diamond Foil Laminates Inspired by Nacre, International Conference on Material Innovation, June 2018, Nuremberg, Germany

14 References

[1] Rolls-Royce Ltd, and Rolls-Royce plc, 2015. *The jet engine*, Wiley, Chichester, West Sussex.

[2] Farhat H., 2021, Lifetime extension: Assessment and considerations, *Operation, Maintenance, and Repair of Land-Based Gas Turbines*, Elsevier, pp. 175–196.

[3] Song P.,“Influence of material and testing parameters on the lifetime of TBC systems with MCrAlY and NiPtAl bondcoats: Fachgruppe für Metallurgie und Werkstofftechnik / Lehrstuhl für Werkstoffe der Energietechnik (FZ Jülich) / Lehrstuhl für Werkstoffchemie,” Dissertation, Publikationsserver der RWTH Aachen University; Aachen, Techn. Hochsch., Diss., 2011, https://publications.rwth-aachen.de/record/82701.

[4] Carter L. N., 2013,“Selective laser melting of nickel superalloys for high temperature applications,” Ph.D., School for Metallurgy and Materials, University of Birmingham, Birmingham, UK.

[5] “DIN EN ISO 17296-3:2016-12, Additive Fertigung_- Grundlagen_- Teil_3: Haupteigenschaften und entsprechende Prüfverfahren (ISO_17296-3:2014); Deutsche Fassung EN_ISO_17296-3:2016,”

[6] “DIN EN ISO 17296-4:2016-12, Additive Fertigung_- Grundlagen_- Teil_4: Überblick über die Datenverarbeitung (ISO_17296-4:2014); Deutsche Fassung EN_ISO_17296-4:2016,”

[7] “DIN EN ISO/ASTM 52900:2017-06, Additive Fertigung_- Grundlagen_- Terminologie (ISO/ASTM 52900:2015); Deutsche Fassung EN_ISO/ASTM 52900:2017,”

[8] Risse J., 2019,“Additive Fertigung der Nickelbasis-Superlegierung IN738LC mittels selektivem Laserstrahlschmelzen,” Dissertation, RWTH Aachen University, Aachen.

[9] Shassere B., Greeley D., Okello A., Kirka M., Nandwana P., and Dehoff R., 2018,“Correlation of Microstructure to Creep Response of Hot Isostatically Pressed and Aged Electron Beam Melted Inconel 718,” Metall Mater Trans A, **49**(10), pp. 5107–5117.

[10] Dev Singh D., Mahender T., and Raji Reddy A., 2021,“Powder bed fusion process: A brief review,” Materials Today: Proceedings, **46**, pp. 350–355.

[11] Sanchez S., Smith P., Xu Z., Gaspard G., Hyde C. J., Wits W. W., Ashcroft I. A., Chen H., and Clare A. T., 2021,“Powder Bed Fusion of nickel-based superalloys: A review,” International Journal of Machine Tools and Manufacture, **165**, p. 103729.

[12] Sanchez S., Gaspard G., Hyde C. J., Ashcroft I. A., G.A. R., and Clare A. T., 2021,“The creep behaviour of nickel alloy 718 manufactured by laser powder bed fusion,” Materials & Design, **204**(Part 2), p. 109647.

[13] DIN EN ISO 6892 1,“DIN EN ISO 204:2019-04, Metallic materials - Uniaxial creep testing in tension - Method of test (ISO 204:2018),”

[14] “DIN EN ISO/ASTM 52920:2021-08, Additive manufacturing - Qualification principles - Requirements for industrial additive manufacturing sites (ISO/ASTM DIS 52920:2021),”

[15] Bürgel R., 2011. *Handbuch hochtemperatur-werkstofftechnik: Grundlagen, werkstoffbeanspruchungen,*, Morgan Kaufmann, [Place of publication not identified].

[16] Kassner M. E., and Tiley J. S., 2009, 11 - γ/γ′ Nickel-Based Superalloys, *Fundamentals of creep in metals and alloys*, 2nd ed., Kassner M. E., and Pérez-Prado M. T., eds., Elsevier, Amsterdam, pp. 247–259.

[17] Hong J., Ma D., Wang J., Wang F., Sun B., Dong A., Li F., and Bührig-Polaczek A., 2016,“Freckle Defect Formation near the Casting Interfaces of Directionally Solidified Superalloys,” Materials, **9**(11).

[18] Sabol G. P., and Stickler R., 1969,“Microstructure of Nickel-Based Superalloys,” phys. stat. sol. (b), **35**(1), pp. 11–52.

[19] Reed R. C., 2006. *The superalloys: Fundamentals and applications*, Cambridge University Press, Cambridge, UK, New York.

[20] Choi B. G., Kim I. S., Kim D. H., Seo S. M., and Jo C. Y., 2004 - 2004,“ETA Phase Formation During Thermal Exposure and Its Effect on Mechanical Properties in Ni-Base Superalloy GTD 111,” *Superalloys 2004 (Tenth International Symposium)*, TMS, pp. 163–171.

[21] Liu G., Xiao X., Véron M., and Birosca S., 2020,“The nucleation and growth of η phase in nickel-based superalloy during long-term thermal exposure,” Acta Materialia, **185**, pp. 493–506.

[22] Pistor J., and Körner C., 2019,“Formation of topologically closed packed phases within CMSX-4 single crystals produced by additive manufacturing,” Materials Letters: X, **1**, p. 100003.

[23] Sinha A. K., 1972,“Topologically close-packed structures of transition metal alloys,” Progress in Materials Science, **15**(2), pp. 81–185.

[24] Rae C., and Reed R. C., 2001,“The precipitation of topologically close-packed phases in rhenium-containing superalloys,” Acta Materialia, **49**(19), pp. 4113–4125.

[25] Long F., Yoo Y. S., Jo C. Y., Seo S. M., Jeong H. W., Song Y. S., Jin T., and Hu Z. Q., 2009,“Phase transformation of η and σ phases in an experimental nickel-based superalloy,” Journal of Alloys and Compounds, **478**(1-2), pp. 181–187.

[26] Zhang Y., Fu H., He J., and Xie J., 2022,“Formation mechanism and thermal stability of C15-Laves phase in a Hf-containing Co-based superalloy,” Journal of Alloys and Compounds, **891**, p. 162016.

[27] Chlebus E., Gruber K., Kuźnicka B., Kurzac J., and Kurzynowski T., 2015,“Effect of heat treatment on the microstructure and mechanical properties of Inconel 718 processed by selective laser melting,” Materials Science and Engineering: A, **639**, pp. 647–655.

[28] John J. Schirra, Robert H. Caless, and Robert W. Hatala, 1991. *The Effect of Laves phase on the mechanical properties of Wrought and Cast+HIP Inconel 718*, The Minerals, Metals & Materials Society.

[29] Liu G., Zhang X., Wang X., and Qiao Y., 2020,“Precipitation Behavior of the Topologically Close-Packed Phase in the DD5 Superalloy during Long-Term Aging,” Scanning, **2020**, p. 2569837.

[30] Xu Z., Hyde C. J., Thompson A., Leach R. K., Maskery I., Tuck C., and Clare A. T., 2017,“Staged thermomechanical testing of nickel superalloys produced by selective laser melting,” Materials & Design, **133**, pp. 520–527.

[31] Deng D., 2018. *Additively Manufactured Inconel 718 Microstructures and Mechanical Properties*, Linköping University Electronic Press, Linköping.

[32] Donachie M. J., and Donachie S. J., 2002. *Superalloys: A Technical Guide, 2nd Edition*, ASM International.

[33] Umakoshi Y., Hagihara K., and Nakano T., 2005,“Deformation Modes and Anomalous Strengthening of Ni_3X -Type Intermetallic Compounds with the Geometrically Close-Packed Structure,” MSF, **502**, pp. 145–150.

[34] Zhang R. Y., Qin H. L., Bi Z. N., Li J., Paul S., Lee T. L., Nenchev B., Zhang J., Kabra S., Kelleher J. F., and Dong H. B., 2019,“Using Variant Selection to Facilitate Accurate Fitting of γ″ Peaks in Neutron Diffraction,” Metall Mater Trans A, **50**(11), pp. 5421–5432.

[35] Roger C. Reed, 2006. *The Superalloys: Fundamentals and Applications*, Cambridge University Press.

[36] Janowski G. M., Heckel R. W., and Pletka B. J., 1986,“The effects of tantalum on the microstructure of two polycrystalline nickel-base superalloys: B-1900 + Hf and MAR-M247,” Metall and Mat Trans A, **17**(11), pp. 1891–1905.

[37] Nathan, M.V., Maier, R.D. and Ebert, L.J., 1982,“The Influence of Cobalt on the Microstructure of the Nickel-Base Super-Alloy MAR-M247,” Metallurgical and Materials Transactions A.

[38] Rawlings, R.D. and Staton-Bevan, A.E., 1975,“The alloying behaviour and mechanical properties of polycrystalline Ni3Al (' phase) with ternary additions.,” Journal of Materials Scienc.

[39] Maier H. J., Niendorf T., and Bürgel R., 2015. *Handbuch Hochtemperatur-Werkstofftechnik*, Springer Fachmedien Wiesbaden, Wiesbaden.

[40] Huan Q. I., 2012,“Review of INCONEL 718 Alloy: Its History, Properties, Processing and De-veloping Substitutes,” Journal of Materials Engineering(8).

[41] Henderson M. B., Arrell D., Larsson R., Heobel M., and Marchant G., 2004,“Nickel based superalloy welding practices for industrial gas turbine applications,” Science and Technology of Welding and Joining, **9**(1), pp. 13–21.

[42] Helmer H. E., Körner C., and Singer R. F., 2014,“Additive manufacturing of nickel-based superalloy Inconel 718 by selective electron beam melting: Processing window and microstructure,” J. Mater. Res., **29**(17), pp. 1987–1996.

[43] Yu K. O., Domingue J. A., Maurer G. E., and Flanders H. D., 1986,“Macrosegregation in ESR and VAR Processes,” JOM, **38**(1), pp. 46–50.

[44] Carlson, R.G., Radavich, J.F., 1989,“Microstructural Characterization of Cast 718,” Superalloy 718-Metallurgy and Applications.

[45] ASM International, 2007. *Heat treating,* 10th ed., ASM International, Materials Park, Ohio.

[46] Rösler J., Hentrich T., and Gehrmann B., 2019,“On the Development Concept for a New 718-Type Superalloy with Improved Temperature Capability,” Metals, **9**(10), p. 1130.

[47] Geddes B., Leon H., and Huang X., 2010. *Superalloys: Alloying and Performance*, ASM International.

[48] Azadian S., 2004,“Aspects of Precipitation in Alloy Inconel 718,” Dissertation, Luleå tekniska universitet, https://mau.diva-portal.org/smash/record.jsf?aq2=%5B%5B%5D%5D&c=1&af=%5B%5D&searchType=SIMPLE&sortOrder2=title_sort_asc&query=&language=en&pid=diva2%3A1404718&aq=%5B%5B%7B%22localid%22%3A%224919%22%7D%5D%5D&sf=all&aqe=%5B%5D&sortOrder=author_sort_asc&onlyFullText=false&noOfRows=50&dswid=-1138.

[49] W. Hoffelner, L. E. Kny, R. Stickler, and W. J. McCall, 1979,“Effects of aging treatments on the Microstructure of the Ni-base superalloy IN-738,” Materialwissenschaft und Werkstofftechnik, **10**(3), pp. 84–92.

[50] Christoph Turk, 2018,“Ausscheidungsverhalten der Ni-Basis-Superlegierung 718,” University of Leoben, https://pure.unileoben.ac.at/portal/en/publications/ausscheidungsverhalten-der-nibasissuperlegierung-718(dc7235f2-caf4-4b33-9f3b-84d422715b28).html.

[51] Rong Y., Chen S., Hu G.-X., Gao M., and Wei R. P., 1999,“Prediction and characterization of variant electron diffraction patterns for γ″ and δ precipitates in an INCONEL 718 alloy,” Metall Mater Trans A, **30**(9), pp. 2297–2303.

[52] Bieber C.G. G. J., 1967,“Cast Nickel-Base Alloy,”

[53] C. Sims, 1984,“A History of Superalloy Metallurgy for Superalloy Metallurgists,” Superalloys, pp. 399–419.

[54] Divya V. D., Muñoz-Moreno R., Messé O., Barnard J. S., Baker S., Illston T., and Stone H. J., 2016,“Microstructure of selective laser melted CM247LC nickel-based superalloy and its evolution through heat treatment,” Materials Characterization, **114**, pp. 62–74.

[55] Cloots M., Uggowitzer P. J., and Wegener K., 2016,“Investigations on the microstructure and crack formation of IN738LC samples processed by selective laser melting using Gaussian and doughnut profiles,” Materials & Design, **89**(Part B), pp. 770–784.

[56] Wang X., Carter L. N., Pang B., Attallah M. M., and Loretto M. H., 2017,“Microstructure and yield strength of SLM-fabricated CM247LC Ni-Superalloy,” Acta Materialia, **128**, pp. 87–95.

[57] Rickenbacher L., Etter T., Hövel S., and Wegener K., 2013,“High temperature material properties of IN738LC processed by selective laser melting (SLM) technology,” Rapid Prototyping Journal, **19**(4), pp. 282–290.

[58] Linn S., Scholz A., Oechsner M., Berger C., and Luesebrink O., 2011,“Evaluation of property scatter of Ni-base alloy in 738 LC,” Materials Science and Engineering: A, **528**(13-14), pp. 4676–4682.

[59] Koul A. K., Immarigeon J.-P., Castillo R., Lowden P., and Liburdi J., 1988,“Rejuvenation of Service-Exposed in 738 Turbine Blades,” *Superalloys: 6th International symposium Papers*, The Metallurgical Society, pp. 755–764.

[60] Carter L. N., Attallah M. M., and Reed R. C., 2012, Laser Powder Bed Fabrication of Nickel-Base Superalloys: Influence of Parameters; Characterisation, Quantification and Mitigation of Cracking, *Superalloys 2012*, Huron E. S., Reed R. C., Hardy M. C., Mills M. J., Montero R. E., Portella P. D., and Telesman J., eds., John Wiley & Sons, Inc, Hoboken, NJ, USA, pp. 577–586.

[61] Megahed S., Krämer K. M., Heinze C., Kontermann C., Udoh A., Weihe S., and Oechsner M., 2023,“Influence of build orientation on the creep behavior of IN738LC manufactured with laser powder bed fusion,” Materials Science and Engineering: A, p. 145197.

[62] Körner C., Attar E., and Heinl P., 2011,“Mesoscopic simulation of selective beam melting processes,” Journal of Materials Processing Technology, **211**(6), pp. 978–987.

[63] David A. Porter, and Kenneth E. Easterling, 2009. *Phase Transformations in Metals and Alloys (Revised Reprint)*, CRC Press.

[64] Helmer H. E., 2016. *Additive Fertigung durch Selektives Elektronenstrahlschmelzen der Ni-ckelbasis Superlegierung IN718: Prozessfenster, Mikrostruktur und mechanische Eigenschaften*, Dissertation.

[65] Gargani M., 2019. *Homogenization of Inconel 718 Made by Additive Manufacturing and Suction Casting*.

[66] Wei H. L., Mazumder J., and DebRoy T., 2015,“Evolution of solidification texture during additive manufacturing,” Scientific reports, **5**, p. 16446.

[67] Sanchez S., Hyde C. J., Ashcroft I. A., G.A. R., and Clare A. T., 2021,“Multi-laser scan strategies for enhancing creep performance in LPBF,” Additive Manufacturing, **41**(11), p. 101948.

[68] Yadroitsev I., 2009. *Selective laser melting: Direct manufacturing of 3D-objects by selective laser melting of metal powders*, LAP Lambert Academic Publishing.

[69] Wang X., Gong X., and Chou K., 2017,“Review on powder-bed laser additive manufacturing of Inconel 718 parts,” Proceedings of the Institution of Mechanical Engineers, Part B: Journal of Engineering Manufacture, **231**(11), pp. 1890–1903.

[70] Ur Rehman A., Pitir F., and Salamci M. U., 2021,“Laser Powder Bed Fusion (LPBF) of In718 and the Impact of Pre-Heating at 500 and 1000 °C: Operando Study,” Materials (Basel, Switzerland), **14**(21).

[71] Caiazzo F., Alfieri V., Corrado G., and Argenio P., 2017,“Laser powder-bed fusion of Inconel 718 to manufacture turbine blades,” Int J Adv Manuf Technol, **93**(9-12), pp. 4023–4031.

[72] Uhlmann E., Düchting J., Petrat T., Krohmer E., Graf B., and Rethmeier M., 2021,“Effects on the distortion of Inconel 718 components along a hybrid laser-based additive manufacturing process chain using laser powder bed fusion and laser metal deposition,” Prog Addit Manuf, **6**(3), pp. 385–394.

[73] Choi J.-P., Shin G.-H., Yang S., Yang D.-Y., Lee J.-S., Brochu M., and Yu J.-H., 2017,“Densification and microstructural investigation of Inconel 718 parts fabricated by selective laser melting,” Powder Technology, **310**, pp. 60–66.

[74] Bi G., Sun C.-N., Chen H., Ng F. L., and Ma C. C. K., 2014,“Microstructure and tensile properties of superalloy IN100 fabricated by micro-laser aided additive manufacturing,” Materials & Design, **60**, pp. 401–408.

[75] Dadbakhsh S., Hao L., and Sewell N., 2012,“Effect of selective laser melting layout on the quality of stainless steel parts,” Rapid Prototyping Journal, **18**(3), pp. 241–249.

[76] Delgado J., Ciurana J., and Rodríguez C. A., 2012,“Influence of process parameters on part quality and mechanical properties for DMLS and SLM with iron-based materials,” Int J Adv Manuf Technol, **60**(5-8), pp. 601–610.

[77] Dinda G. P., Dasgupta A. K., and Mazumder J., 2009,“Laser aided direct metal deposition of Inconel 625 superalloy: Microstructural evolution and thermal stability,” Materials Science and Engineering: A, **509**(1-2), pp. 98–104.

[78] Li J., Wang H. M., and Tang H. B., 2012,“Effect of heat treatment on microstructure and mechanical properties of laser melting deposited Ni-base superalloy Rene′41,” Materials Science and Engineering: A, **550**, pp. 97–102.

[79] Murr L. E., Martinez E., Amato K. N., Gaytan S. M., Hernandez J., Ramirez D. A., Shindo P. W., Medina F., and Wicker R. B., 2012,“Fabrication of Metal and Alloy Components by

Additive Manufacturing: Examples of 3D Materials Science," Journal of Materials Research and Technology, **1**(1), pp. 42–54.

[80] Schwab H., Prashanth K., Löber L., Kühn U., and Eckert J., 2015,"Selective Laser Melting of Ti-45Nb Alloy," Metals, **5**(2), pp. 686–694.

[81] Scipioni Bertoli U., Wolfer A. J., Matthews M. J., Delplanque J.-P. R., and Schoenung J. M., 2017,"On the limitations of Volumetric Energy Density as a design parameter for Selective Laser Melting," Materials & Design, **113**(1), pp. 331–340.

[82] Megahed S., Fischer F., Nell M., Forsmark J., Leonardi F., Zhu L., Hameyer K., and Schleifenbaum J. H., 2022,"Manufacturing of Pure Copper with Electron Beam Melting and the Effect of Thermal and Abrasive Post-Processing on Microstructure and Electric Conductivity," Materials (Basel, Switzerland), **16**(1).

[83] Arısoy Y. M., Criales L. E., Özel T., Lane B., Moylan S., and Donmez A., 2017,"Influence of scan strategy and process parameters on microstructure and its optimization in additively manufactured nickel alloy 625 via laser powder bed fusion," Int J Adv Manuf Technol, **90**(5-8), pp. 1393–1417.

[84] Hilal H., Lancaster R., Jeffs S., Boswell J., Stapleton D., and Baxter G., 2019,"The Influence of Process Parameters and Build Orientation on the Creep Behaviour of a Laser Powder Bed Fused Ni-based Superalloy for Aerospace Applications," Materials (Basel, Switzerland), **12**(9).

[85] DebRoy T., Wei H. L., Zuback J. S., Mukherjee T., Elmer J. W., Milewski J. O., Beese A. M., Wilson-Heid A., De A., and Zhang W., 2018,"Additive manufacturing of metallic components – Process, structure and properties," Progress in Materials Science, **92**(5), pp. 112–224.

[86] Megahed S., Bühring J., Duffe T., Bach A., Schröder K.-U., and Schleifenbaum J. H., 2022,"Effect of Heat Treatment on Ductility and Precipitation Size of Additively Manufactured AlSi10Mg," Metals, **12**(8), p. 1311.

[87] Wang W., Takata N., Suzuki A., Kobashi M., and Kato M., 2022,"Microstructural Variations in Laser Powder Bed Fused Al-15%Fe Alloy at Intermediate Temperatures," Materials (Basel, Switzerland), **15**(13).

[88] Attard B., Cruchley S., Beetz C., Megahed M., Chiu Y. L., and Attallah M. M., 2020,"Microstructural control during laser powder fusion to create graded microstructure Ni-superalloy components," Additive Manufacturing, **36**, p. 101432.

[89] Yu C.-H., Peng R. L., Luzin V., Sprengel M., Calmunger M., Lundgren J.-E., Brodin H., Kromm A., and Moverare J., 2020,"Thin-wall effects and anisotropic deformation mechanisms of an additively manufactured Ni-based superalloy," Additive Manufacturing, **36**, p. 101672.

[90] Gaikwad A., 2020,“On Geometric Design Rules and In-Process Build Quality Monitoring of Thin-Wall Features Made Using Laser Powder Bed Fusion Additive Manufacturing Process,” Mechanical (and Materials) Engineering -- Dissertations, Theses, and Student Research.

[91] Wu Z., Narra S. P., and Rollett A., 2020,“Exploring the fabrication limits of thin-wall structures in a laser powder bed fusion process,” Int J Adv Manuf Technol, **110**(1-2), pp. 191–207.

[92] Rickenbacher L. E., 2012,“Additive Reparaturstrategien für Strömungschmaschinenkomponenten,” ETH Zurich.

[93] Engeli, R., Etter, T., Geiger, F., Stankowski, A., Wegener, K., 2015, Effect of Si on the SLM processability of IN738LC SFF Proceedings, 2015.

[94] Engeli R., Etter T., Hövel S., and Wegener K., 2016,“Processability of different IN738LC powder batches by selective laser melting,” Journal of Materials Processing Technology, **229**(816), pp. 484–491.

[95] Cloots M., 2017,“Empirische und simulative Studie über die Verarbeitbarkeit von IN738LC mittels SLM,” ETH Zurich.

[96] Kan W. H., Chiu L. N. S., Lim C. V. S., Zhu Y., Tian Y., Jiang D., and Huang A., 2022,“A critical review on the effects of process-induced porosity on the mechanical properties of alloys fabricated by laser powder bed fusion,” J Mater Sci, **57**(21), pp. 9818–9865.

[97] Huynh T., Mehta A., Graydon K., Woo J., Park S., Hyer H., Le Zhou, Imholte D. D., Woolstenhulme N. E., Wachs D. M., and Sohn Y., 2022,“Microstructural Development in Inconel 718 Nickel-Based Superalloy Additively Manufactured by Laser Powder Bed Fusion,” Metallogr. Microstruct. Anal., **11**(1), pp. 88–107.

[98] Kunze, K., Etter, T., Grässlin, J., Shklover, V., 2015,“Texture, anisotropy in microstructure and mechanical properties of IN738LC alloy processed by selective laser melting (SLM),” Materials Science and Engineering: A(620), pp. 213–222.

[99] Zhong M., Sun H., Liu W., Zhu X., and He J., 2005,“Boundary liquation and interface cracking characterization in laser deposition of Inconel 738 on directionally solidified Ni-based superalloy,” Scripta Materialia, **53**(2), pp. 159–164.

[100] Attallah M. M., Jennings R., Wang X., and Carter L. N., 2016,“Additive manufacturing of Ni-based superalloys: The outstanding issues,” MRS Bulletin, **41**(10), pp. 758–764.

[101] Carter L. N., Wang X., Read N., Khan R., Aristizabal M., Essa K., and Attallah M. M., 2016,“Process optimisation of selective laser melting using energy density model for nickel based superalloys,” Materials Science and Technology, **32**(7), pp. 657–661.

[102] Aboulkhair N. T., Everitt N. M., Ashcroft I., and Tuck C., 2014,“Reducing porosity in AlSi10Mg parts processed by selective laser melting,” Additive Manufacturing, **1-4**, pp. 77–86.

[103] Antonella Sola, and Alireza Nouri, 2019,“Microstructural porosity in additive manufacturing: The formation and detection of pores in metal parts fabricated by powder bed fusion,” Journal of Advanced Manufacturing and Processing, **1**(3), e10021.

[104] Roland Berger Strategy Consultants Holding GmbH, 2013. *Additive manufacturing A game changer for the manufacturing industry?*, Munich.

[105] I.E. Anderson, E.M.H. White, J.A. Tiarks, T.R. Riedemann, J.D. Regele, D.J. Byrd, R., 2017, Fundamental Progress Toward Increased Powder Yields from Gas Atomization for Additive Manufacturing, *Advances in Powder Metallurgy and Particulate Materials-2017, Metal Powder Industries Federation*, Ryuichiro Goto, J.T. Strauss (Eds.), ed., Princeton, NJ, pp. 136–146.

[106] Tammas-Williams S., Withers P. J., Todd I., and Prangnell P. B., 2016,“Porosity regrowth during heat treatment of hot isostatically pressed additively manufactured titanium components,” Scripta Materialia, **122**, pp. 72–76.

[107] Withers P. J., and Bhadeshia H., 2001,“Residual stress. Part 1 – Measurement techniques,” Materials Science and Technology, **17**(4), pp. 355–365.

[108] Mercelis P., and Kruth J.-P., 2006,“Residual stresses in selective laser sintering and selective laser melting,” Rapid Prototyping Journal, **12**(5), pp. 254–265.

[109] Withers P. J., and Bhadeshia H., 2001,“Residual stress. Part 2 – Nature and origins,” Materials Science and Technology, **17**(4), pp. 366–375.

[110] Gu D. D., Meiners W., Wissenbach K., and Poprawe R., 2012,“Laser additive manufacturing of metallic components: materials, processes and mechanisms,” International Materials Reviews, **57**(3), pp. 133–164.

[111] Colegrove P., Ikeagu C., Thistlethwaite A., Williams S., Nagy T., Suder W., Steuwer A., and Pirling T., 2009,“Welding process impact on residual stress and distortion,” Science and Technology of Welding and Joining, **14**(8), pp. 717–725.

[112] Dai K., and Shaw L.,“Distortion minimization of laser-processed components through control of laser scanning patterns,” Rapid Prototyping Journal.

[113] Shamsaei N., Yadollahi A., Bian L., and Thompson S. M., 2015,“An overview of Direct Laser Deposition for additive manufacturing; Part II: Mechanical behavior, process parameter optimization and control,” Additive Manufacturing, **8**, pp. 12–35.

[114] Gåård A., Krakhmalev P., and Bergström J., 2006,“Microstructural characterization and wear behavior of (Fe,Ni)–TiC MMC prepared by DMLS,” Journal of Alloys and Compounds, **421**(1), pp. 166–171.

[115] Rangaswamy P., Griffith M. L., Prime M. B., Holden T. M., Rogge R. B., Edwards J. M., and Sebring R. J., 2005,“Residual stresses in LENS® components using neutron diffraction and contour method,” Materials Science and Engineering: A, **399**(1), pp. 72–83.

[116] Casavola C., Campanelli S. L., and Pappalettere C., 2009,“Preliminary investigation on distribution of residual stress generated by the selective laser melting process,” The Journal of Strain Analysis for Engineering Design, **44**(1), pp. 93–104.

[117] Beuth J., and Klingbeil N., 2001,“The role of process variables in laser-based direct metal solid freeform fabrication,” JOM, **53**(9), pp. 36–39.

[118] Moat R. J., Pinkerton A. J., Li L., Withers P. J., and Preuss M., 2011,“Residual stresses in laser direct metal deposited Waspaloy,” Materials Science and Engineering: A, **528**(6), pp. 2288–2298.

[119] Wang L., Felicelli S. D., and Pratt P., 2008,“Residual stresses in LENS-deposited AISI 410 stainless steel plates,” Materials Science and Engineering: A, **496**(1), pp. 234–241.

[120] Klingbeil N., Beuth J., Chin R., and Amon C., 2002,“Residual stress-induced warping in direct metal solid freeform fabrication,” International Journal of Mechanical Sciences, **44**(1), pp. 57–77.

[121] Nickel A. H., Barnett D. M., and Prinz F. B., 2001,“Thermal stresses and deposition patterns in layered manufacturing,” Materials Science and Engineering: A, **317**(1), pp. 59–64.

[122] Prabhakar P., Sames W. J., Dehoff R., and Babu S. S., 2015,“Computational modeling of residual stress formation during the electron beam melting process for Inconel 718,” Additive Manufacturing, **7**, pp. 83–91.

[123] Aggarangsi P., and Beuth J. L., 2006,“Localized Preheating Approaches for Reducing Residual Stress in Additive Manufacturing,”

[124] Li C., Fu C. H., Guo Y. B., and Fang F. Z., 2015,“Fast Prediction and Validation of Part Distortion in Selective Laser Melting,” Procedia Manufacturing, **1**(1), pp. 355–365.

[125] Ding J., Colegrove P., Mehnen J., Ganguly S., Sequeira Almeida P. M., Wang F., and Williams S., 2011,“Thermo-mechanical analysis of Wire and Arc Additive Layer Manufacturing process on large multi-layer parts,” Computational Materials Science, **50**(12), pp. 3315–3322.

[126] Megahed M., Mindt H.-W., N’Dri N., Duan H., and Desmaison O., 2016,“Metal additive-manufacturing process and residual stress modeling,” Integr Mater Manuf Innov, **5**(1), pp. 61–93.

[127] Khairallah S. A., Anderson A. T., Rubenchik A., and King W. E., 2016,“Laser powder-bed fusion additive manufacturing: Physics of complex melt flow and formation mechanisms of pores, spatter, and denudation zones,” Acta Materialia, **108**, pp. 36–45.

[128] Zielinski J., Theunissen J., Kruse H., Rittinghaus S.-K., Schleifenbaum J. H., Zhu D., and Megahed M., 2023,“Understanding Inhomogeneous Mechanical Properties in PBF-LB/M Manufactured Parts Due to Inhomogeneous Macro Temperature Profiles Based on Process-Inherent Preheating,” JMMP, **7**(3), p. 88.

[129] Wolfer A. J., Aires J., Wheeler K., Delplanque J.-P., Rubenchik A., Anderson A., and Khairallah S., 2019,“Fast solution strategy for transient heat conduction for arbitrary scan paths in additive manufacturing,” Additive Manufacturing, **30**, p. 100898.

[130] Moran T. P., Warner D. H., and Phan N., 2021,“Scan-by-scan part-scale thermal modelling for defect prediction in metal additive manufacturing,” Additive Manufacturing, **37**, p. 101667.

[131] Liu B., Fang G., and Lei L., 2021,“An analytical model for rapid predicting molten pool geometry of selective laser melting (SLM),” Applied Mathematical Modelling, **92**, pp. 505–524.

[132] Duong E., Masseling L., Knaak C., Dionne P., and Megahed M., 2022,“Scan path resolved thermal modelling of LPBF,” Additive Manufacturing Letters, **3**, p. 100047.

[133] Ji X., Wang Y., and Liang S. Y., 2022,“Analytical modeling of temperature evolution in laser powder bed fusion considering the size and shape of the build part,” Journal of Materials Processing Technology, **301**, p. 117452.

[134] Zielinski J., Theunissen J., Kruse H., Rittinghaus S., Schleifenbaum J. H., Zhu D., and Megahed M., 2023. *Understanding inhomogeneous mechanical properties in PBF-LB/M manufactured parts due to inhomogeneous macro temperature profiles based on process-inherent preheating*, Aachen, Germany.

[135] Gulliver G. H., 1921. *Metallic alloys: their structure and constitution*.

[136] Scheil E., 1942,“Bemerkungen zur Schichtkristallbildung,” International Journal of Materials Research(3), pp. 70–72.

[137] Serrano-Munoz I., Ulbricht A., Fritsch T., Mishurova T., Kromm A., Hofmann M., Wimpory R. C., Evans A., and Bruno G., 2021,“Scanning Manufacturing Parameters Determining the Residual Stress State in LPBF IN718 Small Parts,” Advanced Engineering Materials, **23**(7), p. 2100158.

[138] Serrano-Munoz I., Fritsch T., Mishurova T., Trofimov A., Apel D., Ulbricht A., Kromm A., Hesse R., Evans A., and Bruno G., 2021,“On the interplay of microstructure and residual stress in LPBF IN718,” J Mater Sci, **56**(9), pp. 5845–5867.

[139] Gokcekaya O., Ishimoto T., Hibino S., Yasutomi J., Narushima T., and Nakano T., 2021,“Unique crystallographic texture formation in Inconel 718 by laser powder bed fusion and its effect on mechanical anisotropy,” Acta Materialia, **212**, p. 116876.

[140] Zhao J.-R., Hung F.-Y., and Lui T.-S., 2020,“Microstructure and tensile fracture behavior of three-stage heat treated inconel 718 alloy produced via laser powder bed fusion process,” Journal of Materials Research and Technology, **9**(3), pp. 3357–3367.

[141] Carter L. N., Martin C., Withers P. J., and Attallah M. M., 2014,“The influence of the laser scan strategy on grain structure and cracking behaviour in SLM powder-bed fabricated nickel superalloy,” Journal of Alloys and Compounds, **615**, pp. 338–347.

[142] Brune T., Schueckler P., Krämer K. M., Kontermann C., and Oechsner M., 2020,“Mechanische Kurz- und Langzeiteigenschaften von additiv hergestellten Bauteilen für den Hochtemperatureinsatz am Beispiel der Legierung IN718,” 43. Vortragsveranstaltung zum Langzeitverhalten warmfester Stähle und Hochtemperaturwerkstoffe.

[143] Liu S. Y., Li H. Q., Qin C. X., Zong R., and Fang X. Y., 2020,“The effect of energy density on texture and mechanical anisotropy in selective laser melted Inconel 718,” Materials & Design, **191**(3), p. 108642.

[144] Sanchez-Mata O., Wang X., Muñiz-Lerma J. A., Atabay S. E., Attarian Shandiz M., and Brochu M., 2021,“Dependence of mechanical properties on crystallographic orientation in nickel-based superalloy Hastelloy X fabricated by laser powder bed fusion,” Journal of Alloys and Compounds, **865**, p. 158868.

[145] Han Q., Gu Y., Setchi R., Lacan F., Johnston R., Evans S. L., and Yang S., 2019,“Additive manufacturing of high-strength crack-free Ni-based Hastelloy X superalloy,” Additive Manufacturing, **30**, p. 100919.

[146] Mehdi Tofighi Naeem, Seyed Ali Jazayeri, Nesa Rezamahdi, 2008. *Failure analysis of gas turbine blades*.

[147] Kuo Y.-L., Horikawa S., and Kakehi K., 2017,“Effects of build direction and heat treatment on creep properties of Ni-base superalloy built up by additive manufacturing,” Scripta Materialia, **129**, pp. 74–78.

[148] Hovig E. W., Azar A. S., Grytten F., Sørby K., and Andreassen E., 2018,“Determination of Anisotropic Mechanical Properties for Materials Processed by Laser Powder Bed Fusion,” Advances in Materials Science and Engineering, **2018**(4), pp. 1–20.

[149] Jaimyun Jung, Jae Ik Yoon, Jung Gi Kim, Marat I. Latypov, and Hyoung Seop Kim, 2017,“Continuum understanding of twin formation near grain boundaries of FCC metals with low stacking fault energy,” 2057-3960, **3**(1), p. 21.

[150] Callister W. D., and Rethwisch D. G., 2013. *Fundamentals of materials science and engineering,* 4th ed., Wiley, Hoboken, N.J.

[151] Mohsin Raza M., and Lo Y.-L., 2021,“Experimental investigation into microstructure, mechanical properties, and cracking mechanism of IN713LC processed by laser powder bed fusion,” Materials Science and Engineering: A, **819**(12), p. 141527.

[152] Azarbarmas M., Aghaie-Khafri M., Cabrera J. M., and Calvo J., 2016,“Dynamic recrystallization mechanisms and twining evolution during hot deformation of Inconel 718,” Materials Science and Engineering: A, **678**, pp. 137–152.

[153] Popovich A. A., Sufiiarov V. S., Polozov I. A., and Borisov E. V., 2015,“Microstructure and Mechanical Properties of Inconel 718 Produced by SLM and Subsequent Heat Treatment,” KEM, **651-653**, pp. 665–670.

[154] E28 Committee,“Test Methods for Conducting Creep, Creep-Rupture, and Stress-Rupture Tests of Metallic Materials,”

[155] da Costa Andrade E. N., 1910,“On the viscous flow in metals, and allied phenomena,” Proc. R. Soc. Lond. A, **84**(567), pp. 1–12.

[156] da Costa Andrade E. N., 1914,“The flow in metals under large constant stresses,” Proc. R. Soc. Lond. A, **90**(619), pp. 329–342.

[157] Altenbach H., and Eisenträger J., 2020, Introduction to Creep Mechanics, *Encyclopedia of Continuum Mechanics*, Altenbach H., and Öchsner A., eds., Springer, Berlin, Heidelberg, pp. 1–9.

[158] Courtney T. H., 2005. *Mechanical behavior of materials,* 2nd ed., Waveland Press, Long Grove, IL.

[159] Cottrell A., 2019. *An Introduction to Metallurgy*, CRC Press.

[160] Li M., and Zinkle S. J., 2005,“Deformation Mechanism Maps of Unirradiated and Irradiated V-4Cr-4Ti,” J. ASTM Int., **2**(10), p. 12462.

[161] Murty K., Ed., 2013. *Materials' ageing and degradation in light water reactors*, Woodhead Publishing Limited.

[162] Viswanathan G. B., Sarosi P. M., Whitis D. H., and Mills M. J., 2005,“Deformation mechanisms at intermediate creep temperatures in the Ni-base superalloy René 88 DT,” Materials Science and Engineering: A, **400-401**, pp. 489–495.

[163] Kovarik L., Unocic R. R., Li J., Sarosi P., Shen C., Wang Y., and Mills M. J., 2009,“Microtwinning and other shearing mechanisms at intermediate temperatures in Ni-based superalloys,” Progress in Materials Science, **54**(6), pp. 839–873.

[164] Ghosh S., Weber G., and Keshavarz S., 2016,“Multiscale modeling of polycrystalline nickel-based superalloys accounting for subgrain microstructures,” Mechanics Research Communications, **78**, pp. 34–46.

[165] Unocic R. R., Zhou N., Kovarik L., Shen C., Wang Y., and Mills M. J., 2011,“Dislocation decorrelation and relationship to deformation microtwins during creep of a γ′ precipitate strengthened Ni-based superalloy,” Acta Materialia, **59**(19), pp. 7325–7339.

[166] Barba D., Alabort E., Pedrazzini S., Collins D. M., Wilkinson A. J., Bagot P., Moody M. P., Atkinson C., Jérusalem A., and Reed R. C., 2017,“On the microtwinning mechanism in a single crystal superalloy,” Acta Materialia, **135**, pp. 314–329.

[167] Smith T. M., Unocic R. R., Deutchman H., and Mills M. J., 2016,“Creep deformation mechanism mapping in nickel base disk superalloys,” Materials at High Temperatures, **33**(4-5), pp. 372–383.

[168] B. H. KEAR, and J. M. OBLAK, 1974,“DEFORMATION MODES γ' PRECIPITATION HARDENED NICKEL-BASE ALLOYS,” J. Phys. Colloques, **35**(C7), C7-35-C7-45.

[169] M.Kolbe, 2001,“The high temperature decrease of the critical resolved shear stress in nickel-base superalloys,” Materials Science and Engineering: A, pp. 383–387.

[170] D.M. Knowles, and Q:Z: Chen, 2003,“Superlattice stacking fault formation and twinning during creep in γ/γ′ single crystal superalloy CMSX-4,” Materials Science and Engineering: A(340), pp. 88–102.

[171] Smith T. M., Esser B. D., Antolin N., Carlsson A., Williams R. E. A., Wessman A., Hanlon T., Fraser H. L., Windl W., McComb D. W., and Mills M. J., 2016,“Phase transformation strengthening of high-temperature superalloys,” Nat Commun, **7**(1), pp. 1–7.

[172] Barba D., Pedrazzini S., Vilalta-Clemente A., Wilkinson A. J., Moody M. P., Bagot P., Jérusalem A., and Reed R. C., 2017,“On the composition of microtwins in a single crystal nickel-based superalloy,” Scripta Materialia, **127**, pp. 37–40.

[173] Smith T. M., Esser B. D., Antolin N., Viswanathan G. B., Hanlon T., Wessman A., Mourer D., Windl W., McComb D. W., and Mills M. J., 2015,“Segregation and η phase formation along stacking faults during creep at intermediate temperatures in a Ni-based superalloy,” Acta Materialia, **100**, pp. 19–31.

[174] Titus M. S., Mottura A., Babu Viswanathan G., Suzuki A., Mills M. J., and Pollock T. M., 2015,“High resolution energy dispersive spectroscopy mapping of planar defects in L12-containing Co-base superalloys,” Acta Materialia, **89**, pp. 423–437.

[175] Gubicza Jeno, Line Profiles Caused by Planar Faults, *X-Ray Line Profile Analysis in Materials Science*, IGI Global, pp. 101–141.

[176] Xu Z., Hyde C. J., Tuck C., and Clare A. T., 2018,“Creep behaviour of inconel 718 processed by laser powder bed fusion,” Journal of Materials Processing Technology, **256**, pp. 13–24.

[177] Davies S. J., Jeffs S. P., Coleman M. P., and Lancaster R. J., 2018,“Effects of heat treatment on microstructure and creep properties of a laser powder bed fused nickel superalloy,” Materials & Design, **159**, pp. 39–46.

[178] Balachandramurthi A. R., Moverare J., Dixit N., Deng D., and Pederson R., 2019,“Microstructural influence on fatigue crack propagation during high cycle fatigue testing of additively manufactured Alloy 718,” Materials Characterization, **149**, pp. 82–94.

[179] Kuo Y.-L., Horikawa S., and Kakehi K., 2017,“The effect of interdendritic δ phase on the mechanical properties of Alloy 718 built up by additive manufacturing,” Materials & Design, **116**, pp. 411–418.

[180] Černý I., Kec J., Vlasák T., Remar L., Jersák M., and Zetek M., 2018,“Mechanical Properties and Fatigue Resistance of 3D Printed Inconel 718 in Comparison with Conventional Manufacture,” KEM, **774**, pp. 313–318.

[181] ASTM E1835-14,“Test Method for Analysis of Nickel Alloys by Flame Atomic Absorption Spectrometry,”

[182] ASTM B637,“Specification for Precipitation-Hardening and Cold Worked Nickel Alloy Bars, Forgings, and Forging Stock for Moderate or High Temperature Service,”

[183] Inco, The Internactional Nickel Company, Inc.,“Alloy IN-738 Technical Data,” https://www.nickelinstitute.org/media/1709/in_738alloy_preliminarydata_497_.pdf.

[184] Mohr G., Altenburg S. J., and Hilgenberg K., 2020,“Effects of inter layer time and build height on resulting properties of 316L stainless steel processed by laser powder bed fusion,” Additive Manufacturing, **32**, p. 101080.

[185] Verhülsdonk M., Vervoort S., Dionne P., and Megahed M., LPBF thermal history of IN718 part and metallurgical considerations Additive Manufacturing.

[186] Hosaeus H., Seifter A., Kaschnitz E., and Pottlacher G., 2001,“Thermophysical properties of solid and liquid inconel 718 alloy,” High Temperures - High Pressures(33), pp. 405–410.

[187] Pottlacher G., Hosaeus H., Wilthan B., Kaschnitz E., and Seifter A., 2002,“Thermophysikalische Eigenschaften von festem und flüssigem Inconel 718,” Thermochimica Acta, **382**(1-2), pp. 255–267.

[188] DIN, 2019. *Materials testing standards for metallic materials 1: Mechanical-technological test methods (independent of product form), testing machines,* 18th ed., Beuth Verlag, Berlin.

[189] “DIN EN ISO 6892 1, Metallic materials - Tensile testing (ISO 6892-1:2019),”

[190] “DIN EN 15305 Berichtigung 1:2009-04, Non-destructive testing - Test method for residual stress analysis by X-ray diffraction; German version EN 15305:2008, Corrigendum to DIN EN 15305:2009-01,”

[191] Zhong Q., Wei K., Lu Z., Yue X., Ouyang T., and Zeng X., 2023,“High power laser powder bed fusion of Inconel 718 alloy: Effect of laser focus shift on formability, microstructure and mechanical properties,” Journal of Materials Processing Technology, **311**, p. 117824.

[192] Wang H., Zhang X., Wang G. B., Shen J., Zhang G. Q., Li Y. P., and Yan M., 2019,“Selective laser melting of the hard-to-weld IN738LC superalloy: Efforts to mitigate

defects and the resultant microstructural and mechanical properties," Journal of Alloys and Compounds, **807**(11), p. 151662.

[193] Yin J., Zhang W., Ke L., Wei H., Wang D., Yang L., Zhu H., Dong P., Wang G., and Zeng X., 2021,"Vaporization of alloying elements and explosion behavior during laser powder bed fusion of Cu–10Zn alloy," International Journal of Machine Tools and Manufacture, **161**, p. 103686.

[194] Santecchia E., Spigarelli S., and Cabibbo M., 2020,"Material Reuse in Laser Powder Bed Fusion: Side Effects of the Laser—Metal Powder Interaction," Metals, **10**(3), p. 341.

[195] Hebert R. J., 2016,"Viewpoint: metallurgical aspects of powder bed metal additive manufacturing," J Mater Sci, **51**(3), pp. 1165–1175.

[196] Kruth J. P., Froyen L., van Vaerenbergh J., Mercelis P., Rombouts M., and Lauwers B., 2004,"Selective laser melting of iron-based powder," Journal of Materials Processing Technology, **149**(1-3), pp. 616–622.

[197] Fine M. E., and Starke E. A., 1986. *Rapidly solidified powder aluminum alloys: A Symposium*, American Society for Testing and Materials, Philadelphia, Pa.

[198] Serrano-Munoz I., Mishurova T., Thiede T., Sprengel M., Kromm A., Nadammal N., Nolze G., Saliwan-Neumann R., Evans A., and Bruno G., 2020,"The residual stress in as-built Laser Powder Bed Fusion IN718 alloy as a consequence of the scanning strategy induced microstructure," Sci Rep, **10**(1), p. 14645.

[199] Kümmel F., Fritton M., Solís C., Kriele A., Stark A., and Gilles R., 2022,"Near-Surface and Bulk Dissolution Behavior of γ′ Precipitates in Nickel-Based VDM® Alloy 780 Studied with In-Situ Lab-Source and Synchrotron X-ray Diffraction," Metals, **12**(7), p. 1067.

[200] Antonov S., Huo J., Feng Q., Isheim D., Seidman D. N., Helmink R. C., Sun E., and Tin S., 2017,"σ and η Phase formation in advanced polycrystalline Ni-base superalloys," Materials Science and Engineering: A, **687**, pp. 232–240.

[201] Nie P., Ojo O. A., and Li Z., 2014,"Numerical modeling of microstructure evolution during laser additive manufacturing of a nickel-based superalloy," Acta Materialia, **77**, pp. 85–95.

[202] HALL E. O., 1954,"Variation of Hardness of Metals with Grain Size," Nature, **173**(4411), pp. 948–949.

[203] Angus H. T., and Summers P. T., 1925. *THE EFFECT OF GRAIN-SIZE UPON HARDNESS AND ANNEALING TEMPERATURE*, J.Inst. Metals.

[204] Jingui Yu, Shiming Zhang, Qiaoxin Zhang, Rong Liu, Mingkai Tang, and Xuewu Li, 2016,"Simulation study and experiment verification of the creep mechanism of a nickel-based single crystal superalloy obtained from microstructural evolution," RSC Adv., **6**(109), pp. 107748–107758.

[205] Norton F. H., 1929. *The creep of steel at high temperatures*, McGraw-Hill Book Company, Inc., New York, USA.

[206] Lei C., Wang Q., Tang H., Liu T., Li Z., Jiang H., Wang K., Ebrahimi M., and Ding W., 2021,“Hot deformation constitutive model and processing maps of homogenized Al–5Mg–3Zn–1Cu alloy,” Journal of Materials Research and Technology, **14**, pp. 324–339.

[207] Ma J., Wang S., Yang J., Zhang W., Chen W., Cui G., and Chu G., 2022,“Hot Deformation Behavior, Processing Maps and Microstructural Evolution of the Mg-2.5Nd-0.5Zn-0.5Zr Alloy,” Materials, **15**(5), p. 1745.

[208] Egan A. J., Rao Y., Viswanathan G. B., Smith T. M., Ghazisaeidi M., Tin S., and Mills M. J., 2020, Effect of Nb Alloying Addition on Local Phase Transformation at Microtwin Boundaries in Nickel-Based Superalloys, *Superalloys 2020*, Springer, Cham, pp. 640–650.

[209] Egan A. J., Xue F., Rao Y., Sparks G., Marquis E., Ghazisaeidi M., Tin S., and Mills M. J., 2022,“Local Phase Transformation Strengthening at Microtwin Boundaries in Nickel-Based Superalloys,” Acta Materialia, **238**, p. 118206.

[210] Gallagher P. C. J., 1970,“The influence of alloying, temperature, and related effects on the stacking fault energy,” Metall Mater Trans B, **1**(9), pp. 2429–2461.

[211] Ikeda Y., Körmann F., Tanaka I., and Neugebauer J., 2018,“Impact of Chemical Fluctuations on Stacking Fault Energies of CrCoNi and CrMnFeCoNi High Entropy Alloys from First Principles,” Entropy, **20**(9), p. 655.

[212] Megahed S., Krämer K. M., Kontermann C., Heinze C., Udoh A., Weihe S., and Oechsner M., 2023,“Micro-Twinning in IN738LC Manufactured with Laser Powder Bed Fusion,” Materials, **16**(17), p. 5918.

[213] Denti L., Sola A., Defanti S., Sciancalepore C., and Bondioli F., 2019,“Effect of Powder Recycling in Laser-based Powder Bed Fusion of Ti-6Al-4V,” Manufacturing Technology, **19**(2), pp. 190–196.

[214] Bricin D., and Kriz A., 2018,“Assessment of Usability of WC-Co Powder Mixtures for SLM,” Manufacturing Technology, **18**(5), pp. 719–726.

[215] Zhao X., Chen J., Lin X., and Huang W., 2008,“Study on microstructure and mechanical properties of laser rapid forming Inconel 718,” Materials Science and Engineering: A, **478**(1-2), pp. 119–124.

[216] Schulze D., 2021. *Powders and Bulk Solids*, Springer International Publishing, Cham.

[217] Gruber K., Smolina I., Kasprowicz M., and Kurzynowski T., 2021,“Evaluation of Inconel 718 Metallic Powder to Optimize the Reuse of Powder and to Improve the Performance and Sustainability of the Laser Powder Bed Fusion (LPBF) Process,” Materials (Basel, Switzerland), **14**(6).

[218] Vock S., Klöden B., Kirchner A., Weißgärber T., and Kieback B., 2019,“Powders for powder bed fusion: a review,” Prog Addit Manuf, **4**(4), pp. 383–397.

[219] Lutter-Günther M., Gebbe C., Kamps T., Seidel C., and Reinhart G., 2018,“Powder recycling in laser beam melting: strategies, consumption modeling and influence on resource efficiency,” Prod. Eng. Res. Devel., **12**(3), pp. 377–389.

[220] Basak A., and Das S., 2017,“Additive Manufacturing of Nickel-Base Superalloy René N5 through Scanning Laser Epitaxy (SLE) − Material Processing, Microstructures, and Microhardness Properties,” Adv Eng Mater, **19**(3), p. 1600690.

[221] MacDonald J. E., Khan R., Aristizabal M., Essa K., Lunt M. J., and Attallah M. M., 2019,“Influence of powder characteristics on the microstructure and mechanical properties of HIPped CM247LC Ni superalloy,” Materials & Design, **174**, p. 107796.

[222] Jahangiri M. R., Arabi H., and Boutorabi S. M. A., 2012,“Development of wrought precipitation strengthened IN939 superalloy,” Materials Science and Technology, **28**(12), pp. 1470–1478.

[223] Mignanelli P. M., Jones N. G., Pickering E. J., Messé O., Rae C., Hardy M. C., and Stone H. J., 2017,“Gamma-gamma prime-gamma double prime dual-superlattice superalloys,” Scripta Materialia, **136**, pp. 136–140.

[224] Goodfellow A. J., Galindo-Nava E. I., Schwalbe C., and Stone H. J., 2019,“The role of composition on the extent of individual strengthening mechanisms in polycrystalline Ni-based superalloys,” Materials & Design, **173**, p. 107760.

[225] Liu D., Ding Q., Zhou Q., Zhou D., Wei X., Zhao X., Zhang Z., and Bei H., 2023,“Microstructure, Mechanical Properties and Thermal Stability of Ni-Based Single Crystal Superalloys with Low Specific Weight,” Crystals, **13**(4), p. 610.

[226] Montero-Sistiaga M. L., Liu Z., Bautmans L., Nardone S., Ji G., Kruth J.-P., van Humbeeck J., and Vanmeensel K., 2020,“Effect of temperature on the microstructure and tensile properties of micro-crack free hastelloy X produced by selective laser melting,” Additive Manufacturing, **31**, p. 100995.

[227] Barrett P. R., Ahmed R., Menon M., and Hassan T., 2016,“Isothermal low-cycle fatigue and fatigue-creep of Haynes 230,” International Journal of Solids and Structures, **88-89**, pp. 146–164.

[228] Wang Y., Dong J., Zhang M., and Yao Z., 2016,“Stress relaxation behavior and mechanism of AEREX350 and Waspaloy superalloys,” Materials Science and Engineering: A, **678**, pp. 10–22.

[229] Jena A., Atabay S. E., Gontcharov A., Lowden P., and Brochu M., 2021,“Laser powder bed fusion of a new high gamma prime Ni-based superalloy with improved weldability,” Materials & Design, **208**, p. 109895.

[230] Bensch M., Preußner J., Hüttner R., Obigodi G., Virtanen S., Gabel J., and Glatzel U., 2010,“Modelling and analysis of the oxidation influence on creep behaviour of thin-walled structures of the single-crystal nickel-base superalloy René N5 at 980 °C,” Acta Materialia, **58**(5), pp. 1607–1617.

[231] Kozar R. W., Suzuki A., Milligan W. W., Schirra J. J., Savage M. F., and Pollock T. M., 2009,“Strengthening Mechanisms in Polycrystalline Multimodal Nickel-Base Superalloys,” Metall and Mat Trans A, **40**(7), pp. 1588–1603.

[232] Viswanathan G. B., Sarosi P. M., Henry M. F., Whitis D. D., Milligan W. W., and Mills M. J., 2005,“Investigation of creep deformation mechanisms at intermediate temperatures in René 88 DT,” Acta Materialia, **53**(10), pp. 3041–3057.

[233] Monajati H., Jahazi M., Bahrami R., and Yue S., 2004,“The influence of heat treatment conditions on γ′ characteristics in Udimet® 720,” Materials Science and Engineering: A, **373**(1-2), pp. 286–293.

[234] Kelekanjeri, V. Siva Kumar G., Moss L. K., Gerhardt R. A., and Ilavsky J., 2009,“Quantification of the coarsening kinetics of γ′ precipitates in Waspaloy microstructures with different prior homogenizing treatments,” Acta Materialia, **57**(16), pp. 4658–4670.

[235] Penkalla H., Wosik J., and Czyrska-Filemonowicz A., 2003,“Quantitative microstructural characterisation of Ni-base superalloys,” Materials Chemistry and Physics, **81**(2-3), pp. 417–423.

[236] Hosseini E., and Popovich V. A., 2019,“A review of mechanical properties of additively manufactured Inconel 718,” Additive Manufacturing, **30**(10), p. 100877.

[237] Vilanova M., Escribano-García R., Guraya T., and San Sebastian M., 2020,“Optimizing Laser Powder Bed Fusion Parameters for IN-738LC by Response Surface Method,” Materials (Basel, Switzerland), **13**(21).

[238] Charlotte Amelia Boig, 2018,“The Application of Additive Manufacturing to Nickel-bae Superalloys for Turboscharger Applications,” Dissertation, University of Sheffield, https://webcache.googleusercontent.com/search?q=cache:35kNLZ5NdDwJ:https://etheses.whiterose.ac.uk/23416/1/Boig_Thesis_Final_Submission.pdf+&cd=10&hl=de&ct=clnk&gl=de&client=firefox-b-d.

[239] Dye D., Hunziker O., and Reed R. C., 2001,“Numerical analysis of the weldability of superalloys,” Acta Materialia, **49**(4), pp. 683–697.

[240] Kayacan R., Varol R., and Kimilli O., 2004,“The effects of pre- and post-weld heat treatment variables on the strain-age cracking in welded Rene 41 components,” Materials Research Bulletin, **39**(14-15), pp. 2171–2186.

[241] Ramirez A., and Lippold J., 2004,“High temperature behavior of Ni-base weld metal,” Materials Science and Engineering: A, **380**(1-2), pp. 245–258.

[242] Shi Z., Li J., and Liu S., 2012,“Effect of long term aging on microstructure and stress rupture properties of a nickel based single crystal superalloy,” Progress in Natural Science: Materials International, **22**(5), pp. 426–432.

[243] Young, G.A, Capobianco, T.E., Penik, M.A., Morris, B.W., McGee, J.J., 2008. *The mechanism of ductility dip cracking in nickel-chromium alloys*.

[244] D. Dye, O. Hunziker, and R.C. Reed, 2001,“Numerical analysis of the weldability of superalloys,” Acta Materialia, **49**(4), pp. 683–697.

[245] Lippold J. C., 2009. *Welding Metallurgy and Weldability of Nickel-Base Alloys,* 1st ed., Wiley, Hoboken.

[246] Kou S., 2003. *Welding metallurgy,* 2nd ed., Wiley-Interscience, Hoboken, N.J.

[247] Egbewande A. T., Buckson R. A., and Ojo O. A., 2010,“Analysis of laser beam weldability of Inconel 738 superalloy,” Materials Characterization, **61**(5), pp. 569–574.

[248] Attallah M. M., Terasaki H., Moat R. J., Bray S. E., Komizo Y., and Preuss M., 2011,“In-situ observation of primary γ′ melting in Ni-base superalloy using confocal laser scanning microscopy,” Materials Characterization, **62**(8).

[249] Sidhu R. K., Ojo O. A., and Chaturvedi M. C., 2009,“Microstructural Response of Directionally Solidified René 80 Superalloy to Gas-Tungsten Arc Welding,” Metallurgical and Materials Transactions A, **40**(1), pp. 150–162.

[250] M. Rowe, 2006,“Ranking the resistance of wrought superalloys to strain-age cracking,” undefined.